



**HAL**  
open science

# Synthesis and properties of mono and bi- metallic nanoparticles of noble metals; towards fabrication of novel functional nanoparticles assemblies

Suyeon Lee

► **To cite this version:**

Suyeon Lee. Synthesis and properties of mono and bi- metallic nanoparticles of noble metals; towards fabrication of novel functional nanoparticles assemblies. Catalysis. Sorbonne Université, 2021. English. NNT: 2021SORUS580 . tel-04001713

**HAL Id: tel-04001713**

**<https://theses.hal.science/tel-04001713>**

Submitted on 24 Feb 2023

**HAL** is a multi-disciplinary open access archive for the deposit and dissemination of scientific research documents, whether they are published or not. The documents may come from teaching and research institutions in France or abroad, or from public or private research centers.

L'archive ouverte pluridisciplinaire **HAL**, est destinée au dépôt et à la diffusion de documents scientifiques de niveau recherche, publiés ou non, émanant des établissements d'enseignement et de recherche français ou étrangers, des laboratoires publics ou privés.

# Sorbonne Université

Ecole doctorale 388 (Chimie Physique et Chimie Analytique de Paris Centre)

*Laboratoire De la Molécule au Nano-objet : Réactivité, Interactions et Spectroscopies  
(MONARIS)*

## **Synthesis and properties of mono and bi- metallic nanoparticles of noble metals; towards fabrication of novel functional nanoparticles assemblies**

Par Suyeon Lee

Thèse de doctorat de Chimie physique et chimie analytique

Présentée et soutenue publiquement le 18 janvier 2021

Devant un jury composé de:

Mme. Mona Tréguer-Delapierre	Pr., Université de Bordeaux	Rapporteur
M. Emmanuel Cottancin	Pr., Université Claude Bernard Lyon1	Rapporteur
Mme. Katia Fajerweg	MDC., Université Toulouse	Examinateur
M. Ahmed Nataibdi	MDC., Sorbonne Université	Examinateur
Mme. Christine Ménager	Pr., Sorbonne Université	Examinateur
Mme. Alexa Courty	Pr., Sorbonne Université	Directeur de thèse
Mme. Isabelle Lisiecki	DR., CNRS/Sorbonne Université	Co-encadrant



## **Acknowledgement**

First, I would like to thank all members of jury, Pr. Mona Tréguer-Delapierre, Pr. Emmanuel Cottancin, Mme. Katia Fajerweg, M. Ahmed Nataibdi, and Pr. Christine Ménager for agreeing to judge this work and to be present at the defence.

I appreciate Professors Christophe Petit for welcoming me to MONARIS (From MOlecule to NAno-objects: Reactivity, Interactions and Spectroscopies). I want to thank my thesis director, Pr. Alexa Courty in MONARIS for all the discussion that we had and helping me a lot during three years of study. Also, I want to thank to my co-encadrant, Dr. Isabelle Lisiecki for also having supervised this thesis and helping me to finish the thesis. Thank you for your patience, support, and advice that you provided during these 3 years of study.

My thanks also go to the people with whom I had the chance to collaborate during this thesis. I would therefore like to thank Michael Walls (LPS, Université Paris Saclay), Pierre-Antoine Albouy (LPS, Université Paris Saclay), Patricia Beaunier (LRS, SU), Vincent Noël (ITODYS, Université de Paris), Jérémie Margueritat (ILM, Université Claude Bernard), Jean-François Lemineur (ITODYS, Université de Paris), Hervé Portalès, Caroline Salzemann, Anh-Tu Ngo, Adrien Girard, Benoît Tremblay, and Nicolas Goubet (MONARIS, SU).

I also thank all people that I shared my 3 years at the MONARIS laboratories: Patrice, Mylène, Garry, Thierry, Imad, Sylvie, Caroline, and all the doctoral students and internship students: Alter, Sassi, Romain, Mario, Marie, Imène, in particular, my special officemates Arthur, Yinan, Liyan, Margarita, and ma twix à gauche, Sonia.

I thank my family, my parents, my sister Wooyeon and Junsoo for their support throughout these 3 years.



# Table of Contents

<b>List of acronyms</b> .....	<b>1</b>
<b>General Introduction</b> .....	<b>3</b>
<b>Chapter I. State-of-art</b> .....	<b>5</b>
1. Noble metal nanomaterials .....	5
2. Bimetallic nanoparticles .....	6
2.1. Various structures of bimetallic nanoparticles .....	7
2.2. Synergetic effect of bimetallic nanoparticles .....	9
2.3. Segregation/mixing rules .....	10
2.4. Synthesis of bimetallic nanoparticles.....	12
2.4.1. Coreduction.....	12
2.4.2. Thermal decomposition .....	12
2.4.3. Seed mediated growth.....	13
2.4.4. Galvanic replacement.....	14
2.5. Properties of bimetallic nanoparticles.....	16
2.5.1. Plasmonic properties .....	16
2.5.2. Vibrational properties .....	18
2.5.3. Catalytic properties .....	21
2.5.4. Combination of optical and catalytic properties .....	22
2.6. Applications of bimetallic nanoparticles .....	24
3. Self-assemblies of nanoparticles .....	25
3.1. Interaction between nanoparticles .....	26
3.2. Self-assembly methods.....	28
3.3. Collective properties of NPs 3D self-assemblies .....	30
4. The concept and interest of binary superlattices .....	31
4.1. Structures of binary superlattices .....	32
4.2. Collective properties of binary superlattices .....	35
4.2.1. Optical properties.....	35
4.2.2. Magnetic properties .....	36
4.2.3. Mechanical properties.....	37
5. Conclusion .....	37
6. References .....	39
<b>Chapter II. Synthesis of core-shell nanoparticles composed of plasmonic/catalytic materials with controlled size, composition, and crystallinity</b> .....	<b>47</b>
1. Introduction .....	47

2. Synthesis of Au@Ag core-shell NPs .....	48
2.1. First step: Synthesis of Au NPs .....	49
2.2. Intermediate step: <i>Nanocrystallinity selection</i> .....	51
2.3. Second step: Ag shell growth on Au seeds .....	53
3. Control of Au@Ag nanoparticles size, composition, and crystallinity.....	55
3.1. Effect of Au(PC) seed initial size, concentration and nature of the ligands .....	55
3.2. Effect of Au seed crystallinity .....	60
3.3. Effect of silver precursor initial concentration and reaction temperature .....	62
4. Self-assembly of Au@Ag core-shell nanoparticles .....	66
5. Replacement of core and shell materials: towards new properties .....	69
5.1. Replacement of shell material: synthesis of Au@Pd and Au@Pt core-shell nanoparticles .....	70
5.2. Replacement of core materials: synthesis of Ag@Pt and Ag@Pd core-shell nanoparticles .....	74
5.3. 3D organization of the metallic/catalytic core-shell nanoparticles .....	79
6. Conclusion .....	81
7. References .....	83
<b>Chapter III. Physical and chemical properties of bimetallic core-shell nanoparticles....</b>	<b>87</b>
1. Introduction .....	87
2. Optical properties .....	88
2.1. Au@Ag core-shell nanoparticles .....	88
2.2. Au@M (M=Ag, Pt or Pd) core-shell nanoparticles .....	92
2.3. Ag@M (M=Ag, Pt or Pd) core-shell nanoparticles.....	93
3. Vibrational properties of Au@Ag core-shell NPs .....	95
4. Catalytic Properties of Au@M (M=Ag, Pt or Pd) core-shell NPs.....	99
4.1. Experimental setup .....	99
4.1.1. Preparation of NPs and ligand exchange.....	100
4.1.2. Catalytic reduction of 4-nitrophenol (4-NP) in 4-aminophenol (4-AP) by NPs .....	108
4.2. Catalytic activity of Au NPs: size effects .....	110
4.3. Catalytic activity of Au@M(M=Ag, Pt or Pd) core-shell nanoparticles .....	111
4.4. Influence of crystallinity of NPs on their catalytic performance .....	115
4.5. Influence of reaction temperature on catalytic activity of Au and Au@Ag core-shell nanoparticles.....	117
5. Conclusion .....	120
6. References .....	122

<b>Chapter IV. Fabrication of multifunctional binary nanoparticle superlattices: mixing plasmonic and magnetic or catalytic nanoparticles .....</b>	<b>127</b>
1. Introduction .....	127
2. Fabrication of binary superlattices by mixing $\gamma$ -Fe <sub>2</sub> O <sub>3</sub> and Au NPs .....	128
2.1. Preparation of nanoparticles (NPs).....	128
2.2. Preparation of binary assemblies .....	130
3. Control of binary superlattices structure: case of mixing $\gamma$ -Fe <sub>2</sub> O <sub>3</sub> and Au NPs .....	131
3.1. Influence of effective size ratios .....	131
3.2. Influence of [ $\gamma$ -Fe <sub>2</sub> O <sub>3</sub> ]/[Au] concentration ratio and deposition temperature .....	134
3.3. Influence of the nature of the solvent .....	136
3.4. Influence of deposition method .....	140
3.5. Structural and magnetic characterizations of 2D organization of BNSLs ( $\gamma$ -Fe <sub>2</sub> O <sub>3</sub> NPs-Au NPs) and $\gamma$ -Fe <sub>2</sub> O <sub>3</sub> NPs .....	142
3.5.1. Structural characterization of 2D organization of BNSLs ( $\gamma$ -Fe <sub>2</sub> O <sub>3</sub> NPs-Au NPs) and $\gamma$ -Fe <sub>2</sub> O <sub>3</sub> NPs .....	142
3.5.2. Magnetic characterization of 2D organization of BNSLs ( $\gamma$ -Fe <sub>2</sub> O <sub>3</sub> NPs-Au NPs) and $\gamma$ -Fe <sub>2</sub> O <sub>3</sub> NPs .....	144
4. Fabrication of binary superlattices by mixing Pd and Au NPs .....	146
5. Macroscopic 3D organization of binary superlattices formed by mixing $\gamma$ -Fe <sub>2</sub> O <sub>3</sub> and Au nanoparticles.....	149
6. Conclusion .....	153
7. References .....	155
<b>Conclusion and perspectives .....</b>	<b>159</b>
<b>Annex .....</b>	<b>163</b>
Annex 1. Electronic microscopy techniques .....	163
Annex 2. Spectroscopy techniques .....	169
Annex 3. Discrete dipole approximation (DDA) simulations and size-corrected dielectric functions of Au and Ag .....	173
Annex 4. Comparison of experimental and DDA calculated absorption spectra of core-shell NPs .....	179
Annex 5. NPs control conditions of catalytic activity test .....	181
Annex 6. Ligands on core-shell NPs in XPS analysis .....	183
Annex 7. Catalytic test of 4-NP to 4-AP UV-visible absorption spectrum.....	187
Annex 8. Crystalline structure information of representative types of BNSLs .....	189
Annex 9. TEM image of NaCl, AlB <sub>2</sub> , and NaZn <sub>13</sub> -type of BNSL structure .....	191
References .....	192





## List of acronyms

NPs	nanoparticles
M@N NP	Core-shell nanoparticle with core M and shell N
LSPR	Localized Surface Plasmon resonance
TEM	Transmission electron microscopy
STEM	Scanning Transmission electron microscopy
HR-TEM	High resolution Transmission electron microscopy
HAADF	Annular dark-field imaging
EELS	Electron Energy Loss Spectroscopy
SEM	scanning electron microscopy
EDX	Energy Dispersive X-Ray spectroscopy
SEM-FEG	Scanning Electron Microscopy-Field Emission Gun
UV-vis spectroscopy	UV-vis ultraviolet-visible spectroscopy
IR spectroscopy	infrared spectroscopy
LFRS	Low frequency Raman spectroscopy
PC	Poly crystal
SC	Single crystal
DDA	Discrete dipolar approximation
SERS	Surface Enhanced Raman Scattering
LSPR	Localized Surface Plasmon Resonance
4-NP	4-Nitrophenol
4-AP	4-Aminophenol
XPS	X-ray Photoelectron Spectroscopy
SL	SuperLattice
BNSL	BiNary SuperLattice
SQUID	Superconducting QUantum Interference Device
SAXS	Small-angle X-ray scattering
ZFC	zero field cooled



## **General Introduction**

Nano-sized noble metals (NPs) synthesized by various routes show their own distinct physical and chemical properties such as optical, catalytic or magnetic properties. Their high surface-to-volume ratio leads indeed to novel properties that are not observed in their bulk state.

Interest in bimetallic nanoparticles has increased significantly in recent years with the identification of many potential applications for which they may be suited, and in particular for their use as efficient catalysts. They allow to combine the novel nanoscale properties of more than one component within one nanoparticle, and to gain enhancement of the properties through synergistic interactions between those components. Bimetallic NPs present thus significant advantages over their monometallic counterparts. Their greatest advantage lies in the tunability of their properties. Their properties can be controlled by controlling the structure and chemical composition, as well as their size and shape. In the case of sequentially synthesized systems, size and shape can be influenced both by the seed particle and by the deposition of the second metal. This tunability means that bimetallic nanoparticles are ideal candidates for achieving the goal of rationally designed nanocatalysts.

Furthermore, binary NP superlattices, which are composed of two complementary components have also emerged. Compared to the limited phase structures formed in the single-component NP superlattices (SLs), a variety of phase structures such as  $\text{AlB}_2$ ,  $\text{NaZn}_{13}$ ,  $\text{NaCl}$  of binary NP SLs can be produced, and the prediction of these phase structures mainly relies on the space-filling principles. The binary SLs constitute ideal candidates to favor coupling between two types of nanomaterials (e.g. plasmonic/plasmonic, magnetic/magnetic and magnetic/plasmonic), which is expected to result in tunable and/or novel collective properties.

The main objective of this thesis work is thus the integration of two different types of metals into one system based on NPs, either through bimetallic core-shell NPs or binary superlattices. The synergistic interaction between both components will be studied through their properties (optical, catalytic and magnetic).

**In chapter I**, recent advances one hand in the synthesis and properties of bimetallic core-shell NPs and on the other hand in the fabrication and properties of binaries SLs are reviewed.

**Chapter II** is focused on the development of a two steps synthesis process of bimetallic core-shell NPs such as  $\text{Au/Ag@M}$  ( $\text{M}=\text{Ag, Pd, Pt}$ ). The central point of this strategy is to solubilize the shell precursor in oleylamine and to induce the growth of the shell on selected

seeds under heating. The shell thickness is thus controlled by various parameters (temperature, annealing time, the [shell precursor] / [seed] concentration ratio, seed size and crystallinity). Au or Ag nanoparticles (NPs) characterized by distinct surface chemistry, different sizes and crystallinities are chosen as seeds to demonstrate the versatility and robustness of the approach. The combination of two plasmonic materials into core-shell NPs (Au@Ag NPs) is developed to tune their localized surface plasmon (LSPR). Then, the change of shell materials with representative catalytic properties (Pd or Pt) is studied. Au@Pd, Au@Pt with controlled composition and crystallinity are synthesized. The Au core is also exchanged by silver, which exhibits intrinsically stronger plasmonic performance than gold. Finally, the ability of core-shell nanoparticles to organize in 3D superlattices is studied.

**In Chapter III**, the optical and catalytic properties of core-shell NPs are studied. The combination of Au@Ag NPs, as both materials having plasmonic properties, are expected to tune their localized surface plasmon resonance (LSPR). By combining UV-visible spectrophotometry measurements and DDA calculations, we show significant changes in the plasmonic response depending on the core size and silver thickness. These experiments are extended to Au/Ag@Pt and Pd NPs. Blue shift and damping are observed, depending on the nature of the two components, core size and shell thickness. Finally, we present results in the catalytic activity of core-shell Au@M (M=Ag, Pd, Pt) NPs studied through a model reaction based on the reduction of 4-nitrophenol to 4-aminophenol by NaBH<sub>4</sub>. The effects of size, composition and crystallinity on the bimetallic core-shell NP catalytic performance are discussed.

**Chapter IV** is related to the fabrication of binary nanoparticle superlattices (BNSLs). Two cooperative and complementary components such as  $\gamma$ -Fe<sub>2</sub>O<sub>3</sub>/Au or Pd/Au NPs are used to grow the BNSLs. The effects of different parameters like deposition temperature, effective size ratio or concentration ratio on the formation of BNSLs from  $\gamma$ -Fe<sub>2</sub>O<sub>3</sub>/Au or Pd/Au mixtures are discussed. Finally, the magnetic properties of  $\gamma$ -Fe<sub>2</sub>O<sub>3</sub>/Au NP binary superlattices were studied by SQUID measurements and compared to those of pure  $\gamma$ -Fe<sub>2</sub>O<sub>3</sub> NPs superlattices. The  $\gamma$ -Fe<sub>2</sub>O<sub>3</sub> interparticle distance modulated by the insertion of Au NPs is shown to effectively impact their magnetic properties.

# Chapter I. State-of-the-art

## 1. Noble metal nanomaterials

The term of noble metal was determined in fourteenth century as a type of metal that is not reactive with air, resistant from the oxidation and corrosion. Generally, the list of noble metals consists of ruthenium (Ru), rhodium (Rh), palladium (Pd), silver (Ag), iridium (Ir), platinum (Pt) and gold (Au). In physics, there is a strict definition of noble metal having a filled electronic layer (d-band) and including only copper (Cu), Ag and Au. The applications of noble metals are in various domains such as medicine, catalyst, mechanics, electronics, and nanotechnologies. In this Ph.D work, nano-sized noble metals such as Au and Ag nanoparticles (NPs) were synthesized by chemical route which allow the control of their size, crystalline structure, shape, and chemical composition.

Magnetic metals				Plasmonic metals
26 <b>Fe</b> Iron	27 <b>Co</b> Cobalt	28 <b>Ni</b> Nickel	29 <b>Cu</b> Copper	
44 <b>Ru</b> Ruthenium	45 <b>Rh</b> Rhodium	46 <b>Pd</b> Palladium	47 <b>Ag</b> Silver	
76 <b>Os</b> Osmium	77 <b>Ir</b> Iridium	78 <b>Pt</b> Platinum	79 <b>Au</b> Gold	
Catalytic metals				

Figure 1.1. Schematic image in part of periodic table, list of metals which divide into three major parts depending on their representative physical properties (plasmonic, magnetic, catalytic) and applications covered in this Ph.D work.

Compared to the bulk phase, NPs have an increased surface area per unit volume and higher density of low-coordination atom on the surface. They are not in a thermodynamically favored state compared from bulk phase<sup>1</sup>. They show specific chemical and physical properties

such as a localized surface plasmon resonance (LSPR) or superparamagnetism (in assemblies of non-interacting NPs). The optical properties of plasmonic NPs (Cu, Au and Ag NPs in Fig 1.1) are especially interesting because they can be controlled by their composition, size, and shape. For instance, Au bulk metal exhibits a high reflectivity, while Au nanocrystal absorbs visible light by stimulating LSPR around 500 nm showing vivid wine color. This phenomenon is due to the collective oscillation of conduction electrons stimulated from the oscillating electric field of incident light.

The platinum group metals (green area in in Figure 1.1) are most extensively investigated for catalytic properties. These metals can catalyze a variety of chemical reactions such as hydrogenation, dehydrogenation, and coupling reactions<sup>2,3</sup>. Their catalytic activities depend on various characteristics such as surface area/volume ratio, coordination number, their d-band location, and even plasmonic properties. Optimizing some of these characteristics can lead to develop effective heterogeneous catalyst. The physical properties described above can be integrated, tuned, and/or enhanced by alloying with another metals.

## **2. Bimetallic nanoparticles**

Bimetallic metals have been used since Bronze Age. The humankind found out that mixing two metals can produce an alloy showing an enhanced property as compared to one of the two metals. Interestingly, steelmakers are still using a similar process to make an alloy. For example, Fe is known as an element with a rapid surface oxidation in the presence of oxygen. Alloying Fe with a minimum 11 wt. % of chromium (Cr) and a maximum of 1.2 wt. % carbon (C), stainless steel, the most well-known alloy, can be produced. This alloying can keep the structural and chemical stability of the surface for a long time.

In case of NPs, synthesizing bimetallic or more complex NPs can enhance the physical properties upgraded from the monometallic system. For instance, development of a bimetallic system can lead to heterogeneous catalysts with higher performance. Among the different candidates of catalytic materials, Pt group metals (Pt, Pd, and Rh in Figure 1.1) are the most investigated materials for catalytic purpose. The NPs maximize the specific surface area to access the more effective catalytic reactions. Also, a practical catalytic system often requires more than one metal for a complicated reaction. In case of optical properties, the LSPR properties can be modified and even enhanced through alloying process with other type of

metals. The novel optical properties of bimetallic NPs give rise to various applications such as sensing, imaging, catalysts, and spectroscopy<sup>4-13</sup>.

The development of different types of bimetallic NPs allow us to control the physical properties and merge new ones from the individual monometallic NPs. The properties are in some cases highly dependent on their atomic ordering and composing structure. Therefore, several synthesis protocols to make bimetallic NPs have been studied to produce different types of bimetallic NPs<sup>14,15</sup>.

### 2.1. Various structures of bimetallic nanoparticles

The structure of bimetallic NPs depends on the synthesis conditions and the miscibility of the two components. The possible architecture of bimetallic NPs can be diverse up to atomic ordering (alloyed or intermetallic), crystal structure, shape, facet type and configuration (dimeric, dendritic, or core-shell, concentric/non-concentric). Figure 1.2 shows schematic images of possible structures of bimetallic NPs. They can be categorized in three main families: alloys, Janus, and core-shell.

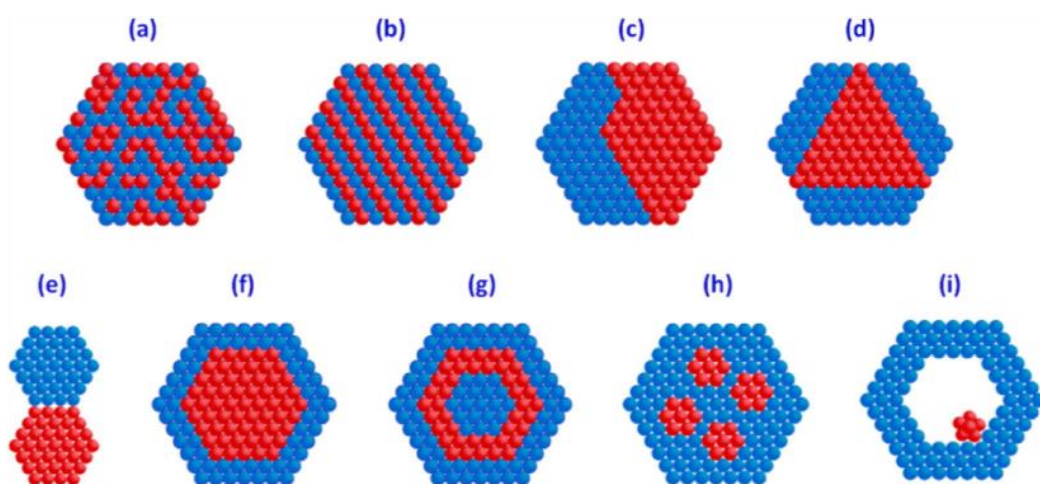


Figure 1.2. Schematic images of structures of representative bimetallic NPs into three families: (a-b) alloys, (c-e) Janus, and (f-i) core-shell. In detail, (a) disordered alloys; (b) ordered alloys; (c) subclusters with two interfaces; (d) subclusters with three interfaces; (e) subclusters with a small number of A–B bonds; (f) core-shell NPs; (g) multi-shell core-shell NPs; (h) multiple small core material coated by single shell material, (i) movable core within hollow shell NPs (Zhao, W. et al. 2013)<sup>16</sup>.



An alloyed NP can be either disordered (solid solution Figure 1.2 (a)) or ordered (Figure 1.2 (b)). Metal combination such as Au/Cu or Pt/Ni can form an ordered alloy with a specific lattice parameter, far from original monometallic system. Typical example of this structure is  $\text{Au}_3\text{Cu}$  and  $\text{PtNi}_2$ <sup>14,17</sup>. In most cases, bimetallic compounds tend to form disordered alloys, hence an additional step such as post-synthesis annealing is needed to transform disordered alloy into intermetallic compound exhibiting defined stoichiometry and ordered crystal structure<sup>18</sup>.

Janus NPs are made up of two parts where each part is enriched with one of the two components and two parts are contacted with two distinct faces: Sides red and blue represent two surfaces with different physical or chemical properties (Figures 1.2 (c), (d) and (e)) (Ferrando, R. *et al.* 2008).<sup>19</sup> It is then possible to have for example a nanomaterial with opposite physico-chemical properties such as a strong difference in affinity with water and/or organic solvents<sup>20,21</sup>.

The core-shell NPs are composed of a core surrounded by a shell, of different materials (Figure 1.2 (f)). It is possible to have a configuration called "onion", e.g. alternating layers of two materials (Figure 1.2 (g)) or a configuration where few small core materials are coated by a single shell material (Fig. 1.2 (h)). Core-shell structures, offer the possibility to observe different and new physical and/or chemical properties in regards to the properties of the materials taken alone<sup>19,20</sup>. The development of core-shell NPs has a great interest for several reasons; i) enhanced chemical stability, ii) tuning optical properties, iii) increasing catalytic efficiency through the electronic coupling. The physical properties of core-shell NPs are tunable through the thickness of the shell<sup>24</sup>. Also, the derivatives of core-shell NPs are nanocage or nanobox. Those systems are variously studied for different applications such as biomedicine including cancer therapy, drug delivery and sensing system<sup>22,23</sup>. Finally, it is also possible to synthesize a movable core particle within a uniformed hollow shell particle (Figure 1.2 (i)).

Some of these structures allow their individual components to keep their own original physical properties. Moreover, new physical properties (or modified ones) can emerge from their original properties (related to the two components) in favor of merging from the synergy between the components in the bimetallic structures.

## 2.2. Synergetic effect of bimetallic nanoparticles

There are various possibilities to integrate two different metals into one system as previously introduced in Section 2.1. Bimetallic NPs with core-shell structure have intermetallic effect between core and shell, hence they show their own optical or catalytic properties, different from the sum of two individual properties. This intermetallic effect depends on the bimetallic structure, the core-shell structure in this PhD work. Especially, we focused on synthesizing core-shell structure of NPs by integrating plasmonic materials with another plasmonic or catalytic materials.

Making a core-shell structure composed of two plasmonic metals (e.g. Ag, Au, Cu) enable us to tune the LSPR, which creates intense localized electric fields enhancing a variety of lift-matter and light-molecule interaction at the nanoparticle surface. In this work, we focus on the case that a thin Ag shell covers the Au core NPs surface (Chapter II). Monometallic Au or Ag NPs have maximum LSPR band around 500 nm or 400 nm respectively. The LSPR response of bimetallic core-shell structure shows a distinct behavior as compared to the disordered alloy structure of the same metallic components. The optical coupling between core and shell induces a blue shift of LSPR band and increases of its intensity. However, the LSPR band shows two peaks due to the Au core and the Ag shell unlike LSPR peak from the alloy which shows only one LSPR peak dependent on the mole fraction of the Au and Ag atoms<sup>25</sup>.

When we combine the plasmonic metal (as a core) with catalytic metal (as a shell), the intermetallic effects between optical (core) and catalytic (shell), promise enhanced reactivity and products specify. This effect significantly depends on the bimetallic structure, and results in plasmon hybridization (optical coupling), to charge transfer (electronic coupling), to a new electronic structure (atomic coupling)<sup>26</sup>.

Plasmonic and catalytic metals have different electronic band structure (Figure 1.3). Plasmonic metals have a d-band far from the Fermi level, and catalytic metals have a d-band center close to the Fermi level. Intense plasmonic properties need a d-band far from Fermi level, however, d-band close to Fermi level is required for the catalytic properties. For the core-shell structure, the catalytic shell covers the plasmonic core achieving the optical coupling and contacts to the chemical environment. Integrating catalytic metals on the plasmonic core metals surface modifies the d-band center relative to Fermi level. This induces a change of the adsorption of a molecule. Moreover, this d-band shift is induced from two ways; mechanical strain or/and charge transfer between core and shell. Table 3 shows the lattice parameter of the metals investigated in this PhD work. When the shell materials have smaller lattice parameter

than the core materials, it causes a narrower d-band width and d-band shift closer to the Fermi level. For the larger lattice parameter of shell than core, opposite effect is caused. A charge transfer reaction, named as ligand effect, may also occur from the different Fermi level caused through the interface between two metals (core and shell) and shift the Fermi level possibly to both directions<sup>26</sup>.

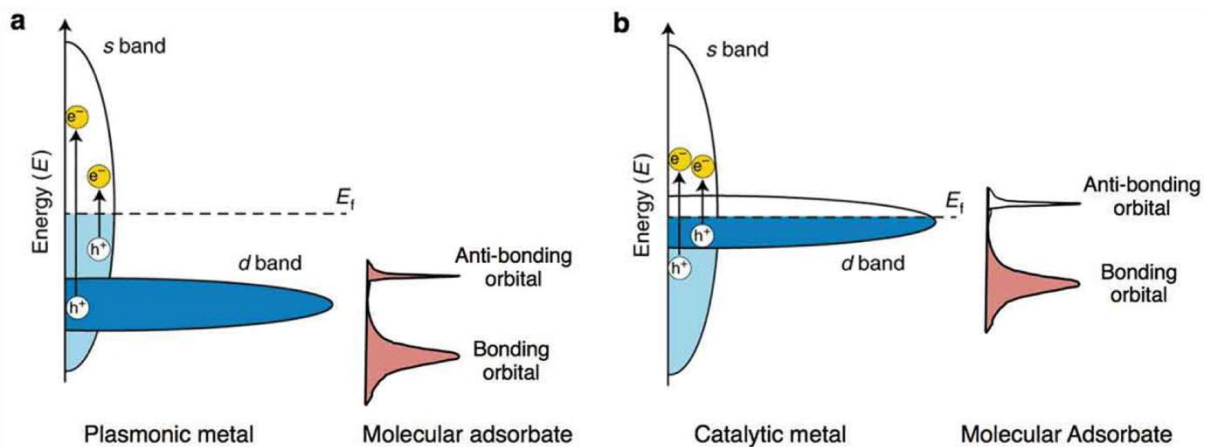


Figure 1.3. Electronic properties of plasmonic and catalytic metals. (a,b) Electronic band structure of typical plasmonic metals (a) and catalytic metals (b). To the right of each diagram is the density of states of a simple molecular adsorbate (Sytwu et al. 2019)<sup>26</sup>.

### 2.3. Segregation/mixing rules

The equilibrium shape of bimetallic NPs are described by different rules (Ferrando, R. et al. 2008)<sup>19</sup>; i) element with the highest cohesion energy will preferentially occupy the core of the particle while the species with the lowest surface energy will be placed on the surface to minimize the total surface energy; ii) ionic character of the different species establishing metal-metal bonds. The ionic bond is caused by the difference in electronegativity between two elements. In this case, the system tends to maximize the number of heterogeneous bonds. In the case of small NPs, the more electronegative elements would preferentially occupy the surface of the NP; iii) local elastic tension when atoms of different sizes are present within a NP. The elasticity of energy may be relaxed by promoting the segregation of the larger atoms towards the surface; iv) This rule is related to environmental effects. This applies, for example, to NPs synthesized in presence of ligands (to prevent coalescence) as it is the case in my PhD work. The element which will have the strongest binding with the ligand will then be pulled to the surface of the NP; v) An alloy is favored if the attraction between the different metallic

atoms is stronger than between the same metallic atoms. On the other hand, segregation is favored by strong homonuclear interactions which tend to be at the center of the cluster; vi) the atomic arrangement is stabilized by electron spin interaction.

Tables 1.1, 1.2 and 1.3 summarize the most important properties of metals used in this PhD work determining the final bimetallic core-shell NP structure. Au@Ag, Au@Pd and Ag@Pt NPs are considered in this PhD work. The structure of bimetallic NPs obtained by simultaneous reduction of ions of both metals could be initially predicted based on the difference of the reduction potential. In the case of Au-Ag NPs, a simultaneous reduction may lead to alloyed NPs while a sequential reduction (seeded growth) allows to obtain core-shell NPs. This last synthesis method was thus chosen in this work. Ag and Au have relatively low surface energy in mixture with other metals such as Pt or Pd, thus they tend to migrate to the surface. Nevertheless, the strength of the Au-Au bonding is higher than Au-Pd and Au-Ag and favors the formation of an Au-rich core.

Table 1.1. Physicochemical properties of selected metals<sup>16</sup>.

Metal	Atom radius (pm)	Surface energy (J/m <sup>2</sup> )	Standard reduction potential (V)	
Ag	144	1.246/1.250	$\text{Ag}^+ + \text{e}^- \rightleftharpoons \text{Ag}$	0.7996
Au	144	1.506/1.500	$\text{Au}^{3+} + 3\text{e}^- \rightleftharpoons \text{Au}$	1.498
Pd	137	2.003/2.050	$\text{Pd}^{2+} + 2\text{e}^- \rightleftharpoons \text{Pd}$	0.951
Pt	138	2.489/2.475	$\text{Pt}^{2+} + 2\text{e}^- \rightleftharpoons \text{Pt}$	1.18

Table 1.2: Strength of selected homonuclear and heteronuclear metallic bonds<sup>16</sup>.

Bond	Dissociation energy (kJ/mol)	
	0 K	298 K
Ag-Ag	159 ± 8	163 ± 8
Ag-Au	199.2 ± 9.2	203 ± 9
Au-Au	215.5 ± 6.3	218.5 ± 5
Au-Pd	n/a	142.7 ± 21
Pd-Pd	105-141.8	>136
Pt-Pt	n/a	306.7 ± 1.9

Table 1.3: Lattice constant of metals with fcc structure<sup>16</sup>.

	Lattice parameter (pm)	Atomic radius (pm)
Au	407.82	144
Ag	408.53	144
Pt	392.42	137
Pd	389.07	138

## 2.4. Synthesis of bimetallic nanoparticles

Different protocols have been established to synthesize the various bimetallic system and often require using multiple synthesis steps up to the targeted structure. The structure of bimetallic NPs significantly depends on the preparation condition, kinetics of reduction process, miscibility<sup>16</sup>. The most well-known protocols for efficient bimetallic NPs synthesis is introduced in following subsections.

### 2.4.1. Coreduction

Coreduction is well-known as a simple approach to synthesize alloy structure, but it is also possible to make core-shell structure. This process is based on the simultaneous reduction of two metal precursors to atoms  $A^0$  and  $B^0$ . The nucleation and growth processes involving both atoms may induce the formation of disordered A-B alloy NPs. To produce an ordered alloys such as  $AuCu_3$ , an additional annealing step is required<sup>27</sup>. As the coreduction is simultaneous reduction of two metals, the final structure depends on several experimental parameters, such as reduction potential of metal ions, strength of the reducing agent, or nature of the ligand. It is assumed that a small difference in the reduction potentials usually leads to alloyed NPs while a large difference results in a core-shell structure (Tojo, C. *et al.* N Mater, 2014)<sup>28</sup>.

### 2.4.2. Thermal decomposition

Another way to synthesize the bimetallic system is the thermal decomposition. This method is well-known route to promote the formation of either monometallic or bimetallic NPs<sup>15</sup>. Thermal decomposition is a conventionally applied method when a metallic precursor has relatively low reduction potential and is not easily reduced such as Fe, Co and Ni<sup>29-31</sup>.

The use of thermal decomposition to synthesize the bimetallic NPs is through one-pot decomposition of two precursors with time difference. First reaction occurs at a temperature

slightly below than the reduction temperature of the less stable metal precursor, inducing the formation of the first monometallic NPs. Then, the initially formed monometallic NPs becomes an active site for heterogeneous growth of shell. This method was reported for the synthesis of Pd@Ni NPs through decomposition of Pd and Ni precursors in a sequence (Son, S.U. *et al.* 2004)<sup>32</sup>. Trioctylphosphine (TOP) forms Pd-TOP and Ni-TOP complexes, then Ni-TOP is firstly decomposed at 205°C during 30 min. The temperature is increased to 235°C, then finally Pd-TOP complex is decomposed and formed Pd shell.

It is difficult to accurately control the decomposition rate of two different metal precursors is entered to complicate the decomposition and induce the unexpected results. For example, thermal decomposition using bimetallic precursor  $\text{Pt}_3\text{Fe}_3(\text{CO})_{15}$  in presence of oleic acid and oleylamine, gives rise to the formation of 5.8 nm diameter FePt alloys (Lukehart *et al.* 2006).<sup>33</sup> Another study shows that the use of different types of PtFe precursors with different carbonyl cluster anions such as  $[\text{Pt}_3\text{Fe}_3(\text{CO})_{15}]^{-1}$  and  $[\text{Fe}_4\text{Pt}(\text{CO})_{16}]^{2-}$ , allows to form different alloy NPs FePt and  $\text{Fe}_4\text{Pt}$  (Robinson. I. *et al.* 2009)<sup>34</sup> (Figure 1.4).

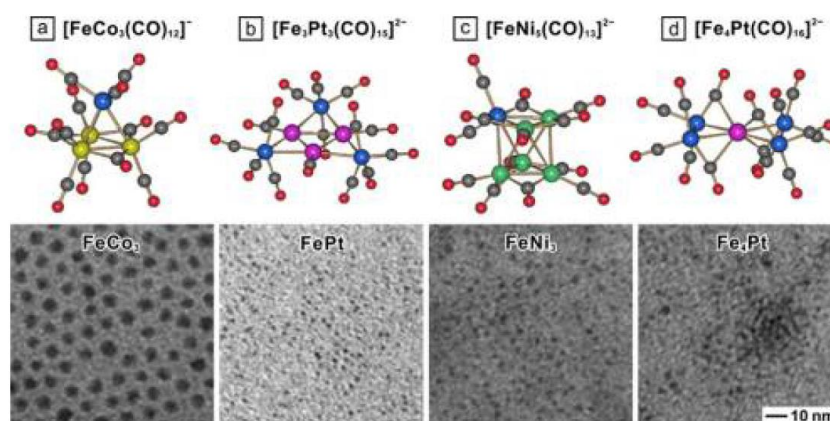


Figure 1.4. (a–d) Atomic models of bimetallic carbonyl complexes that have been explored as precursors for the synthesis of bimetallic NPs (red = O, grey = C, yellow = Co, blue = Fe, purple = Pt, and green = Ni). Below each model is a TEM image of the corresponding Fe-based NPs derived from the precursor. (Thanh *et al.* 2009)<sup>34</sup>.

### 2.4.3. Seed mediated growth

Seed mediated growth is a well-established route to fabricate the core-shell NPs<sup>15</sup>. This process consists of separated steps:

- First step: nucleation and growth of metallic NPs, the future core.
- Second step: heterogeneous nucleation of the shell at the core surface.

This methodology was used in a first place in 2001 by Murphy and their group. They used Au NPs as seeds and grew an additional Au to form nanorods (Jana, N. R. *et al.* 2001)<sup>35-37</sup>. This method was then used by several research groups to synthesize bimetallic NPs especially core-shell structure. For example, Ag nanowire grown from Pt seeds (Sun, Y. *et al.* 2002)<sup>38</sup> and Pt@Pd core-shell NPs (Habas, S. E. *et al.* 2007)<sup>39</sup> could be synthesized in this way.

The main advantage of seed mediated growth method is well-controlled architecture of bimetallic NPs such as distribution in size, shape, composition and structure. This result is strongly linked to the quality of the germs synthesized (distribution of size, shape, crystalline structure etc). In MONARIS laboratory, various synthesis methods to make NPs were developed as i) reverse-micelle synthesis for Co NPs (Lisiecki. I. *et al.* 2003)<sup>40</sup>, Ag NPs (Taleb. A. *et al.* 1997)<sup>41</sup>, Cu NPs (Lisiecki. I. *et al.* 1995)<sup>42</sup>; ii) organometallic synthesis for Au NPs (Goubet. N. *et al.* 2011)<sup>43-45</sup>, Ag NPs (Andrieux-Ledier. A. *et al.* 2013)<sup>46</sup>, Copper (Courty. A. *et al.* 2015)<sup>47</sup> or Co NPs (Meziane. L. *et al.* 2016)<sup>48</sup>; iii) thermal decomposition for  $\gamma$ -Fe<sub>2</sub>O<sub>3</sub> NPs (Ngo. A-T. *et al.* 2013)<sup>49</sup>; iv) direct reduction in oleylamine for Au NPs (Chapus. L. *et al.* 2017)<sup>50</sup>. All NPs listed previously can be used as a seed that allows to have different core materials. In this PhD work, we have used silver and gold nanoparticles as seeds for the overgrowth of Ag, Pt or Pd layers. Ag [OIA]<sub>n</sub>, Pt[Acac]<sub>2</sub> and Pd[Acac]<sub>2</sub> have been used as precursors for the second synthesis step. More details are given in chapter II and III.

#### 2.4.4. Galvanic replacement

Galvanic replacement can be used for making bimetallic NPs. Galvanic replacement reaction is a redox process between a metal (NP) reacting as a sacrificial template and metal ions in solution. The difference in the reduction potential between the sacrificial NP and the metal ions in solution is the driving force for the reaction; oxidation and dissolution of the template together with reduction of metal ions from solution and deposition at the surface of the template. Then, this reaction requires a higher redox potential in the metallic shell compared to the sacrificial metallic core. The standard reduction potentials of representative metals are shown in table 2. The change of Gibbs free energy ( $\Delta G$ ) is expressed as:

$$\Delta G = -nFE \quad (1.1)$$

where  $n$  is the number of moles of electron,  $F$  is Faraday constant, and  $E$  is potential difference of electrochemical half reactions. The potential difference can be re-written by the Nernst equation as:

$$E = E^\circ + \frac{RT}{nF} \ln Q \quad (1.2)$$

where  $E^\circ$  is the standard reduction potential at 25°C shown in Table 1.1,  $R$  is ideal gas constant,  $T$  is temperature, and  $Q$  is reaction quotient from the concentration of reactants and products. Positive potential difference gives a negative Gibbs free energy, leading to a spontaneous reduction. It is reverse in case of negative potential difference. Galvanic replacement is using different materials with the different redox potentials.

The most common way for galvanic replacement involves separate stages; i) synthesis of certain shape of NPs; ii) adding the metal ions with higher reduction potentials than that of the metallic core. If the reaction continues, it is possible to make a nanocage as shown in Figure 1.5 (b) and this final structure is maintained as initial shape of NPs.

It is possible to build core-shell NPs (not hollow) using two step reaction when shell materials ( $M_D$ ) has a higher reduction potential than core materials ( $E_D^0 > E_A^0$ ); i) reduction of metallic precursor ( $C^{X+}$ ) on core surface (seed mediated growth); ii) galvanic replacement from metal ( $C$ ) to materials of the shell ( $D$ ) ( $E_D^0 > E_C^0$ ) as shown in Figure 1.4 (b). Theoretically, core-shell NPs synthesis is impossible when shell materials ( $M_D$ ) have higher reduction potentials than core materials ( $E_D^0 > E_A^0$ ). By introducing intermediate step (i), the shell overgrowth can occur by galvanic replacement (ii) (Figure 1.5 (b)).

A seed mediated growth is mainly studied in this PhD work. Galvanic replacement is thus the phenomenon which must be avoided as it interferes shell overgrowth. If redox potential of metal precursor is higher than core NPs metal, hollow NPs may be synthesized instead of core-shell NPs. Hence, the redox potential of each core and shell metal must be considered before the shell overgrowth reaction.



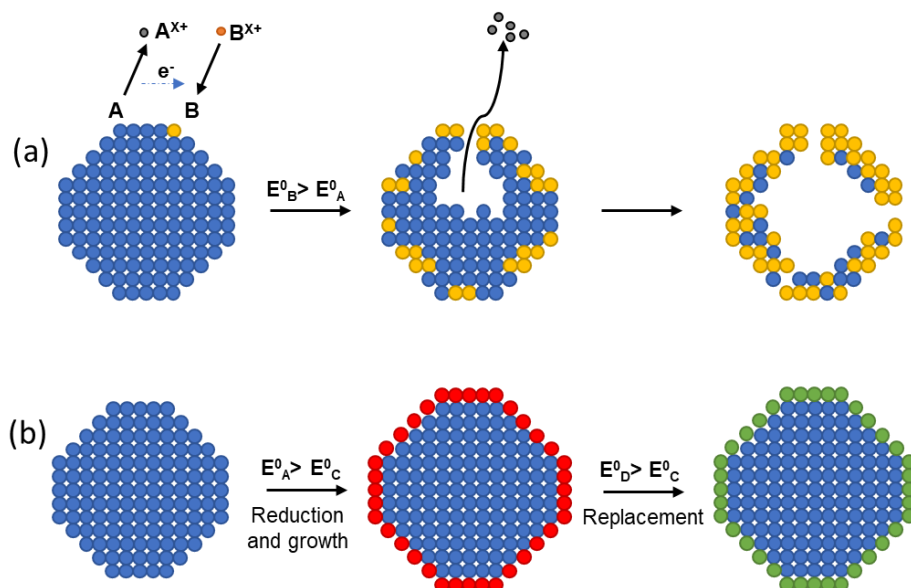


Figure 1.5. Schematic description of (a) mechanism of galvanic replacement between metal A and B for forming the hollow NPs (nanocage),<sup>51</sup> (b) 2-step reaction to build core-shell structure involved with reduction and replacement to another metals.<sup>52</sup>

## 2.5. Properties of bimetallic nanoparticles

There are lists of metals which have some specific physical properties as shown in Figure 1.1. They can be categorized into three groups depending on their properties; i) Cu, Ag, Au for plasmonic properties; ii) Ru, Rh, Pd, Os, Ir, Pt for catalytic properties; iii) Fe, Co, Ni for magnetism. The most important objective of synthesizing the bimetallic NPs is to combine the properties related to the presence of two individual metals and to obtain new or enhanced properties due to a synergetic effect such as charge transfer between two metals.

### 2.5.1. Plasmonic properties

LSPR of noble metal NPs originate from the strong interaction between conduction electrons of the NP and incident light under specific resonant condition (Figure 1.6). The corresponding plasmon peak is located on the visible range (400-800 nm) in case of plasmonic NPs such as Cu, Ag and Au. NPs such as Ru, Rh, Pd and Pt have their LSPR in the ultraviolet (UV) range. The nature of the metal mainly determines the LSPR wavelength.

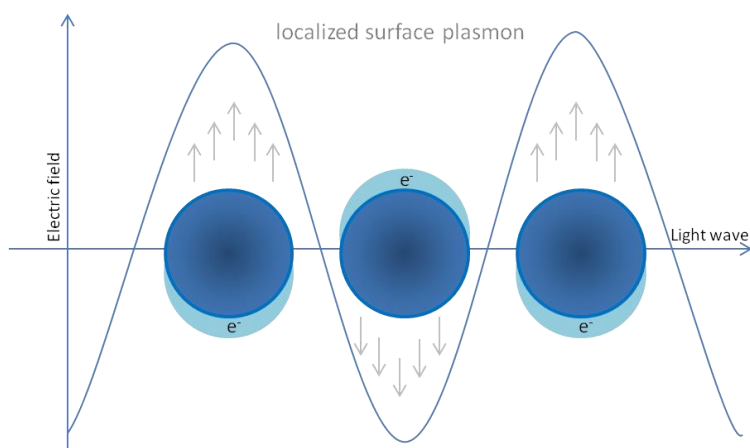


Figure 1.6. Illustration of collective oscillation of electrons of metallic sphere under an electric field called localized surface plasmon (LSP).

LSPR wavelength and their intensity can be tuned through the size and crystallinity of the NPs as shown in Figure 1.7. The increase in Au NPs size from 5 nm to 10 nm induces a slight red shift of LSPR from 520 nm to 530 nm. Their intensity increased proportionally to the diameter of NPs. The crystallinity of NPs also impacts the LSPR. Single crystalline Au NPs shows more intense and better defined SPR band compared to polycrystalline Au NPs with the same diameter (Figure 1.7 (b)). Single crystalline Au NPs consist of cuboctahedron or octahedron that have less defects on their surface than polycrystalline Au NPs. Therefore, single crystalline Au NPs show better collective oscillation resulting in a narrower and more intense plasmon peak<sup>44</sup>.

In this Ph. D work, one of the main objectives is to synthesize core-shell NPs combining two metals (plasmonic-plasmonic or plasmonic-catalytic). The plasmonic properties of Au@Ag core-shell NPs as a function of their core and shell diameter, and crystallinity are described in Chapter III. The plasmonic properties can be tuned by fine control of shell thickness and narrow distribution. The plasmonic properties of core-shell NPs by replacing Ag shell to catalytic materials (Pd or Pt) are then investigated, and eventually replacement of Au core material by Ag. A combination of plasmonic-catalytic metals can upgrade the properties from simple catalytic NPs and become photocatalytic materials<sup>26</sup>. We observe the catalytic properties of these core-shell NPs in Chapter III.

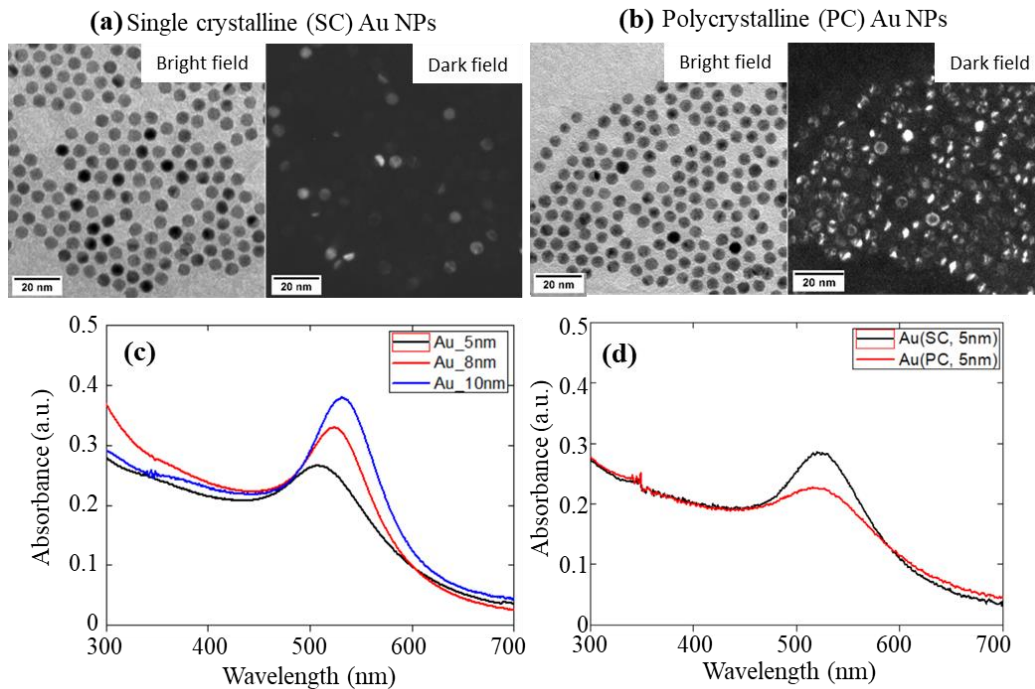


Figure 1.7. Absorption spectra of Au NPs (a) with different sizes black: 5 nm, red: 8 nm, blue: 10 nm, (b) with different crystallinities black; single crystalline (SC), red; poly crystalline (PC).

### 2.5.2. Vibrational properties

Raman scattering is discovered by Chandrashekara Venkata Raman (Raman, C.V. *et al.* 1928)<sup>53</sup>. He observed the scattered light is made up of emitted light, which has two families of band located at greater or lower length than incident wavelength. The difference of energy gives information about the vibrational structure of the molecule. Three possibilities of transmitted frequencies are possible as shown in Figure 1.8:

- Rayleigh scattering
- Raman Stokes scattering
- Raman Anti-Stokes scattering

The intensity of Stokes and Anti-Stokes scattering looks identical, but in experiment, their intensities are not same (Venkateswarlu, K. *et al.* 1941)<sup>54</sup>.

The frequency of the acoustic phonons depends on the direction of the crystals propagates. In case of nanosized object, the reduction of size into nanometer can affect the acoustic phonons behavior. As the NPs cannot support the propagation of vibrational

wavelength ( $D < \lambda/2$ ), they behave like one object that can vibrate. Therefore, we can observe their own individual acoustic vibrational mode.

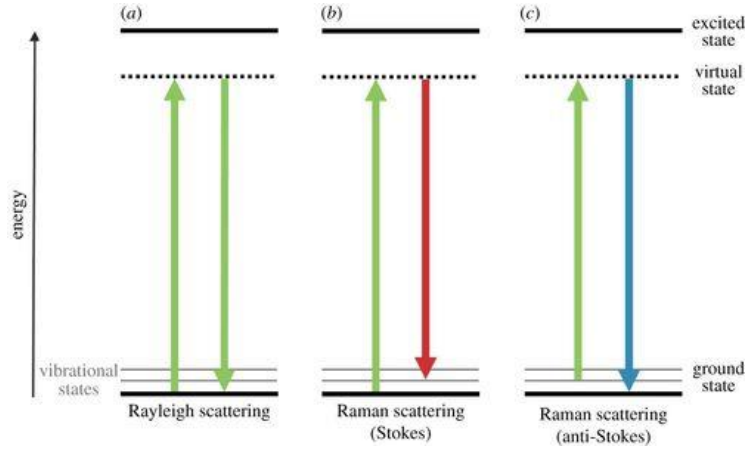


Figure 1.8. Energy diagram of a molecule in excitation and de-excitation of Rayleigh and Raman scattering (Stokes/anti- Stokes).

Horace Lamb described the different modes of vibration of a homogeneous isotropic elastic sphere.<sup>55</sup> Each vibrational mode is distinguished by number  $(l, n)$ ;  $l$  means the vibrational mode with angular moment, and  $n$  is different harmonics in mode  $l$ . We could distinguish different modes of vibrational mode in case of spheroidal modes as shown in Figure 1.9.

- The breathing mode (radial mode) defined by the numbers  $(l=0, n)$
- The quadrupolar mode  $(l=2)$

The breathing mode, another term radial mode, causes change in volume of NPs during vibration. In case of quadrupolar mode, the vibration causes the deformation of sphere by shearing effect and no change in total volume of sphere. The vibrating frequency of sphere object is expressed as:

$$v_{l,n} = S_{l,n} \frac{v_L/v_T}{D} \quad (1.3)$$

$$S_{l,n} \propto \frac{v_L}{v_T} \quad (1.4)$$

where  $v_{l,n}$  is the vibrating frequency,  $v_L$  is longitudinal velocity,  $v_T$  is traverse velocity,  $D$  is diameter of sphere object,  $S_{l,n}$  is the coefficient. As the equation of vibrating frequency is presented in (1.3), their vibrating frequencies ( $v_{l,n}$ ) is associated with longitudinal velocity ( $v_L$ )

and traverse velocity ( $v_T$ ) which are determined by the materials. The coefficient ( $S_{l,n}$ ) is also dependent on the longitudinal and traverse velocity of the materials. Hence, the diameter ( $D$ ) of the sphere object mainly influences the vibrational frequency.

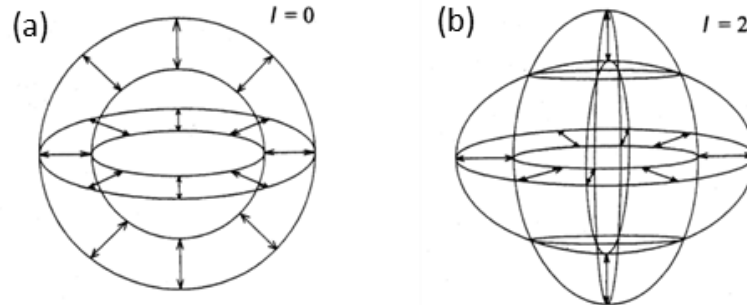


Figure 1.9. Illustration of different vibrational mode of (a) breathing mode ( $l=0$ ), (b) quadrupolar mode ( $l=2$ ). (Lamb, H.I. et al. 1904, Portalés, H. et al. 2001)<sup>55-57</sup>.

The LFRS spectra performed on Au NPs are given in Figure 1.10, showing that different parameters influence the NP vibrational frequency. Maximum vibrational frequency is inversely proportional to the diameter of the NPs (Figure 1.10 (a)) as described in Equation (1.3). For crystalline NPs, we observed a splitting of the quadrupolar mode due to the anisotropic NP shape induced from larger facets as shown in Figure 1.10 (b). In this Ph.D work, the vibrational properties of Au@Ag core-shell NPs characterized by different size, chemical composition, and crystallinity was studied and reported in Chapter III.

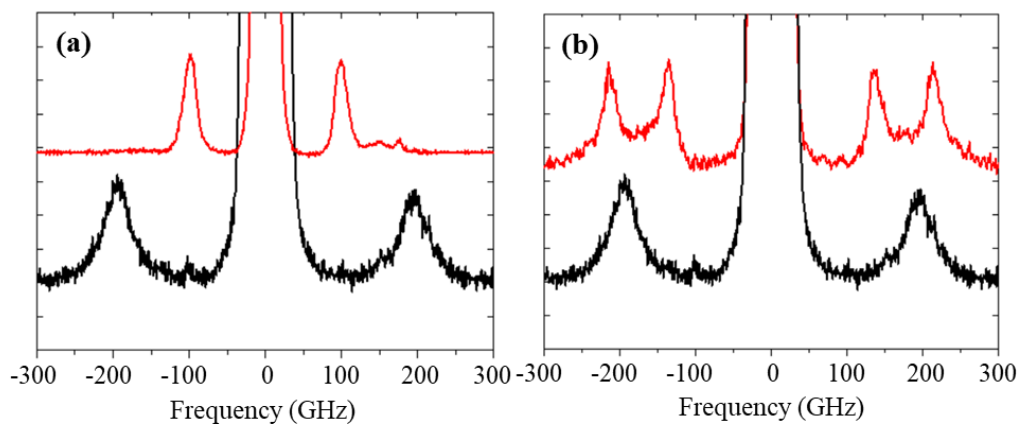


Figure 1.10. Quadrupolar vibrational mode of LFRS spectrum in (a) different sizes of Au NPs red: 10 nm, black: 5 nm, (b) different crystallinity of Au NPs of 5 nm, red: Single crystalline, black: Poly crystalline.

### 2.5.3. Catalytic properties

Heterogeneous catalyst is where the catalyst and the reactants are in different physical phases (gas, liquid, or solid phases). In our case, the catalyst (NP) is solid. The surface reactivity of metals towards molecules (in liquid or gaseous phase) and their ability to catalyze chemical reactions results from a balance between different elementary steps, such as the adsorption of the reagents on the metal surface, ability to react and the desorption of the products formed. The advantage of using metallic NPs rather than larger particles or bulk metals is related to their large surface area per unit volume. The surface-to-volume ratio increases as particle size decreases. As the NPs are smaller, the proportion of "sub-coordinate, edge and corner" atoms are greater. These atoms at the edge are more reactive than atoms on the face. It is accompanied with structural changes that directly influence on the reactivity.

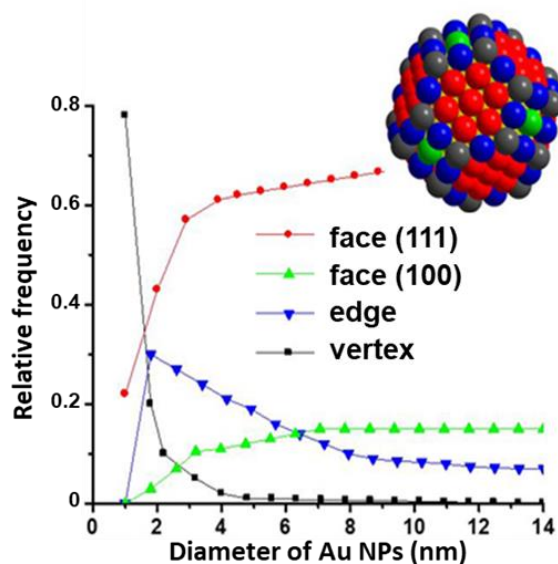


Figure 1.11. Evolution of the proportion of the different surface sites of a metallic NP as a function of diameter; calculation based on a truncated cuboctahedron model (Mohr C *et al.* 2001)<sup>58</sup>

The catalytic properties of Au NPs were discovered in the late 1980s, thanks to the development of small Au NPs synthesis method (< 5 nm) stabilized on oxide supports (M. Haruta *et al.* 1987)<sup>59</sup>. Haruta *et al.* proved that Au NPs smaller than 5 nm exhibit remarkable catalytic properties for the oxidation reaction of CO ( $\text{CO} + 1/2 \text{O}_2 \rightarrow \text{CO}_2$ ). They also showed that Au is the only metal capable of catalyzing this reaction at room temperature, and even at lower temperatures. Following study proved that Au is capable of catalyzing many reactions (Hashmi, A. S. K. *et al.* 2006)<sup>60</sup>.

The surface atoms of a metallic NP are not all equivalent depending on whether they occupy tips, edges or planes (Figure 1.11) and then do not offer the same reactivity. They have fewer close neighbors than volume atoms (twelve first neighbors in the case of Au of *fcc* structure) eight or nine first neighbor's for plane atoms, seven for edge atoms, and six for tips atoms (these are called sub-coordinate low-coordination atoms). As a result, the latter have a greater reactivity than the other atoms on the surface planes.

**The major advantage of bimetallic NPs** over monometallic NPs is the improvement in catalytic properties. The addition of the second metal may show a significant enhancement in terms of the activity, selectivity, and stability of the nanocatalyst<sup>61,62</sup>. It causes modification in the electron density of the system and the alteration of the metal–metal bond length that may lead to an improved catalytic activity<sup>63</sup>. Furthermore, the geometry is important as the charge transfer in core-shell NPs can affect the catalytic activities<sup>15</sup>. It is also possible that a precious metal can be integrated with an inexpensive metal reducing the overall cost. For example, it has been reported that for the hydrogenation of methyl acrylate Ag@Pd NPs had an activity of 1.6 times more than Pd monometallic NPs<sup>64</sup>.

Different types of M@Pd NPs with a core of different metal M, M=Ag, Rh, Ru, Au, Pt has been developed. The formic acid decomposition rate against work function of different core metals showed a linear decrease in order of Ag>Rh>Au=Ru>Pt (Tedsree, K. *et al.* 2011)<sup>65</sup>.

Dimitrov and their group synthesized Pt<sub>x</sub>Cu<sub>100-x</sub> nanocubes and studied their catalytic activities with different atomic composition to find the best candidate as a catalyst (Xu, D. *et al.* 2010)<sup>66</sup>. Another study to build Pd@Pt core-shell NPs was performed by Xia group. Pd@Pt core-shell NPs based on various shapes of Pd core such as cubes, octahedra, decahedra and icosahedra were synthesized (Wang, X. *et al.* 2015)<sup>24</sup>. It is already well-known that Pt(111) shows much higher catalytic activity than Pt(100). Hence, NPs having (111)-facets such as octahedra, decahedra, and icosahedra showed an increase in catalytic activity (Xie, S. 2013)<sup>67</sup>. Depositing several layers of Pt on Pd tune the properties.

#### ***2.5.4. Combination of optical and catalytic properties***

There is a special synergetic effect when integrating plasmonic metals such as Au, Ag and Cu with efficient catalytic metals like Pd, Pt in bimetallic NPs. The catalytic activity may be enhanced with the visible light. At the resonant plasmonic wavelength, NPs absorb the light, then release the energy in two ways, radiatively (photon is re-emitted) or non-radiatively (electron–hole pair is generated). The electron–hole pair has a much larger energy than the

carriers near the Fermi energy, called as “hot” carriers. These hot electrons near the metal surface with enough energy to overcome the barrier can jump up to other materials. It can be, for example, an adsorbed molecule or a semiconductor in contact with metal. This electron transfer activates chemical reactions that usually require high energy input (Gilroy K.D. *et al.* 2016)<sup>15</sup>.

Intermetallic effect between two metals in bimetallic NPs results in optical and catalytic properties distinct from the sum of their parts. Wang *et al.* showed that the extinction spectrum of a bimetallic, core-shell Au@Pd NP was strikingly different than the sum of the extinction spectra of its two components. They observed the blue-shift of LSPR peak, the intensity damping, and broadening in spectral shape (Figure 1.12) (Wang, F. *et al.* 2013)<sup>10</sup>. Despite this dampened plasmonic response, Au@Pd NPs were shown to be more functional than monometallic systems due to their photocatalytic ability. Under illumination, Au@Pd core-shell nanorod system were shown to have a greater catalytic yield at Suzuki coupling than a mixture of its individual components (Figure 1.12 (b)).

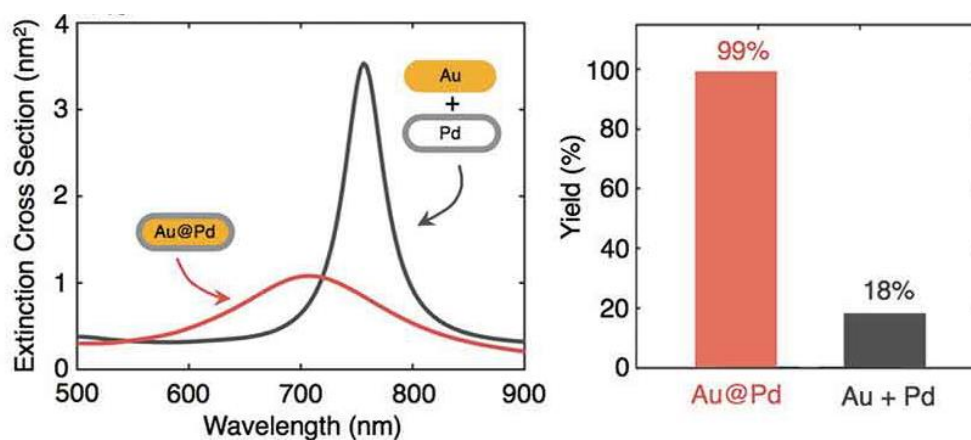


Figure 1.12. (a) Calculated extinction cross section of the sum of a 24 nm × 96 nm Au nanorod and a 2 nm Pd shell (black) versus an Au@Pd core-shell nanorod (red) with the same dimensions. (b) The yield of the Suzuki coupling reaction between bromobenzene and *m*-tolylboronic acid under illumination using either Au@Pd nanorod catalysts (red) or a mixture of Au nanorods and porous Pd NPs (black) with the same metal molarity ratio (Wang, F. *et al.* 2013)<sup>10</sup>.



Yan *et al.* found that Pd and Pt tipped Au nanorods shows an important role in cross-coupling between bromobenzene and m-tolyboronic acid with resonant light (Wang, F. *et al.* 2013)<sup>10</sup>. Majima *et al.* developed Pt tipped Au nanorods for plasmon-enhanced H<sub>2</sub> production from water and methanol (Zheng, Z. *et al.* 2014)<sup>68</sup>.

## 2.6. Applications of bimetallic nanoparticles

Possible application area of bimetallic nanocomposites includes Surface-enhanced Raman spectroscopy (SERS)<sup>69,70</sup>, photocatalysis<sup>9,71,72</sup>, drug delivery<sup>73</sup>, photothermal therapy<sup>74,75</sup> and sensing<sup>76,77</sup> etc.

Bimetallic NPs integrated two different natures can be utilized for bio-diagnostics, biophysical studies, and medical therapy as shown in Figure 1.13 (a)<sup>68</sup>. Strong LSPR scattering attached with specific targeting molecules enables the molecule-specific imaging and diagnosis of diseases such as cancer. Tuning LSPRs of the metal NPs through their composition modification allows chemists to design nanostructures geared for specific bio-applications. Nanostructures such as core-shell type nanorods show an enhanced and tunable LSPRs in targeted wavelength by modifying the rods length, highly suitable for bio-applications<sup>78</sup>.

Integration of plasmonic and plasmonic nanostructures can develop electron-hole charge separation in semiconductor medium, photocatalytic and photovoltaic devices as shown in Figure 1.13 (b). Recent research has been focusing on improving the efficiency of photocatalysts and photovoltaic devices by integration of plasmonic NPs (NPs) with semiconductor materials. The presence of plasmonic NPs increases the absorption cross-section of semiconductors via strong field enhancement and extension of light absorption to longer wavelengths.

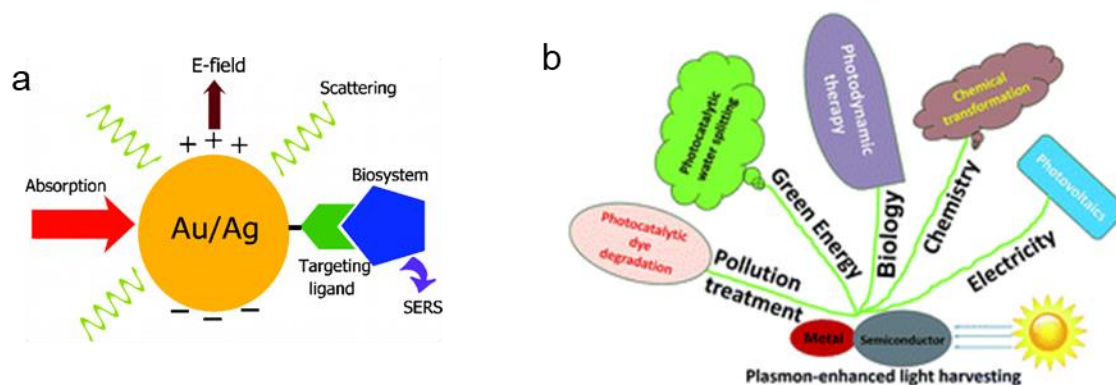


Figure 1.13. Various applications of NPs (a) biological applications such as bioimaging, drug delivery<sup>75</sup> (b) photocatalysis<sup>9</sup>.

### 3. Self-assemblies of nanoparticles

Self-assembly is a process by which inorganic nanoparticles can spontaneously organize themselves into ordered structures. It is a method of choice to control their collective properties and integrate them into materials that will become functional. As a result of these assemblies, new properties may emerge because of the interaction between the magnetic moments and/or plasmon of the surfaces of individual nanoparticles.

NPs can self-organize at 2D or 3D through different growth modes. Heterogeneous growth is occurring layer by layer on the substrate to give rise to supercrystalline films. For the homogeneous growth, the nucleation and the subsequent growth is occurring in the colloidal solution to result in the formation of isolated supercrystals also called colloidal crystals, characterized by well-defined shapes.

Specific conditions are necessary to obtain ordered self-assemblies of NPs in both growth modes; i) narrow size distribution of NPs; ii) suitable growth conditions (temperature, nature of the solvent, and nature of the substrate); iii) ligand inter-digitation. The final crystalline structure of the 3D self-assemblies is also dependent on these conditions (Figure 1.14)<sup>79</sup>.

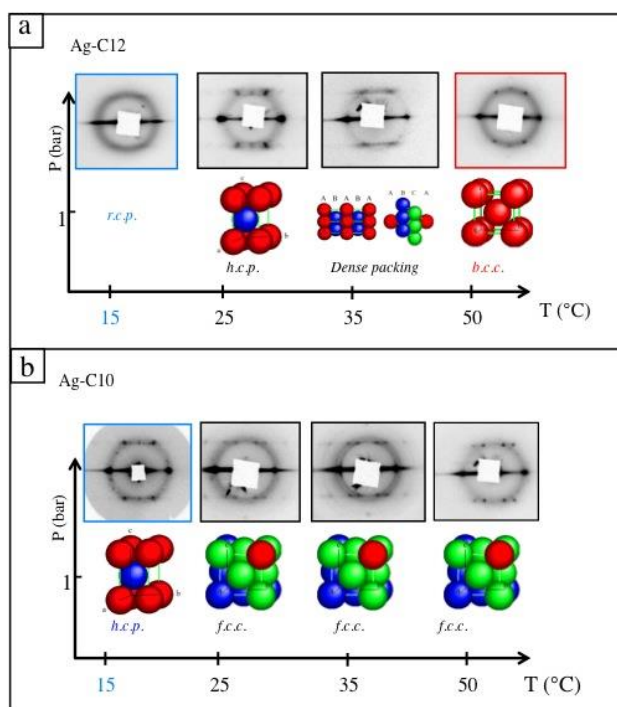


Figure 1.14. Crystalline phase diagram of 3D self-assemblies made of Ag NPs coated by a) dodecanethiols and b) decanethiols. The crystalline order is characterized by small-angle X-ray diffraction (SAXRD) on a 3D film grown by immersion of a polished silicon substrate in colloidal solution and evaporation of the decane solvent at controlled temperature between 15 and 50°C (Courty, A. *et al.* 2008)<sup>79</sup>.

### 3.1. Interaction between nanoparticles

In order to fabricate ordered 3D self-assemblies, nanoparticles interact with each other via different types of forces. The spontaneous organization of uniform metallic coated NPs results from the balance between (i) van der Waals attractive interactions between metallic cores, (ii) steric repulsive interactions between the ligands, (iii) dipolar magnetic interaction between ferro (or anti) magnetic NPs and (iv) ligand-ligand interactions driven by the nature of the solvent. The representative attractive and repulsive interactions between NPs are shown in Figure 1.15.

Korgel, B. A. *et al.* suggested the simple model using dodecanethiol-capped Ag NPs. Interaction is a balance of the attractive energy (van der Waals interactions ( $E_{vdw}$ )) between the metal cores and the repulsive energy (steric repulsive forces ( $E_s$ )) between the ligand (Korgel, B. A. *et al.* 1998)<sup>80</sup> expressed as:

$$E_{vdW} = -\frac{A}{12} \left[ \frac{4R^2}{d^2 - 4R^2} + \frac{4R^2}{d^2} + 2Ln \left[ \frac{d^2 - 4R^2}{d^2} \right] \right] \quad (1.5)$$

$$E_s = \frac{100Rl^2}{(d - 2R)\pi\sigma_l^3} kT \exp\left(\frac{-\pi(d - 2R)}{l}\right) \quad (1.6)$$

where  $d$  is the interparticle distance (center to center),  $R$  the radius of the particles,  $l$  the length of the capping agent,  $\sigma$  its surface per polar head group.  $A$  is the so-called Hamaker constant dependent on the nature of the material.

Interaction with the substrate during the deposition process, could also play an important role in the self-assembly process<sup>81</sup>.

The electrostatic forces can have an important role in self-assembly of NPs. Conversely to Van der Waals, the electrostatic interactions can be attractive or repulsive. Electrostatic repulsion plays a role when the NPs have a same surface charge to each other forming electrical double layer (EDL) outside of the NPs. Directional electrostatic interaction can be detected only when NPs are asymmetrically charged<sup>82</sup>. Repulsive electrostatic force prevents the aggregation of NPs and keeps the stability of colloidal solution. On the other hand, oppositely charged NPs have attractive electrostatic force and favor the self-assembly formation.

If NPs are magnetic, the organization also depends on the dipolar (magnetic) interactions. In that case, uniform colloidal NPs can assemble into long-range ordered superlattices as result of the balance between; i) van der Waals attractions between the metallic cores, ii) magnetic dipolar interactions between the NPs, iii) solvent-mediated interactions between ligands. An external field during the solvent evaporation may control the 3D superlattices morphology<sup>83</sup>.

There is one major force for the formation of assembly structure is entropic effect which can drive ligand molecules to interdigitate each other and stabilize the organization. The entropic effect can be applied to an attractive force when hard spheres of NPs are diluted in colloidal solution.

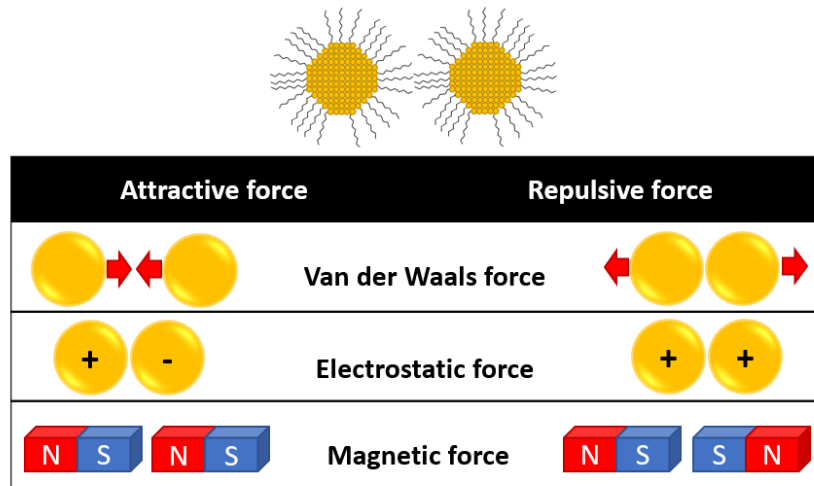


Figure 1.15. Attractive and repulsive interactions between NPs (Yan, C. et al. 2017)<sup>82</sup>.

### 3.2. Self-assembly methods

The assembly of nanoparticles can take place at the liquid-liquid, liquid-air or liquid-solid interfaces. The assembly of nanoparticles can take place at the liquid-liquid, liquid-air or liquid-solid interfaces. It can be realized in different ways namely the Langmuir Blodgett technique, by sedimentation or evaporation, and by adsorption of nanoparticles.

Organization at 2D of silver or golds NPs were obtained by *drop deposition* on a solid substrate. This deposition is performed by using a micropipette, on a TEM grid placed on a filter paper. In that case, the excess of colloidal solution is rapidly drained to the paper, inducing the formation of a homogeneous film<sup>84</sup>.

Also, to favor the 3D self-assembly formation, *anticapillary tweezer* can be used (Figure 1.16 a). The whole one drop of NPs solution is trapped on substrate with the help of tweezer, then this whole drop evaporate on substrate with enough time to organize if a solvent with a low boiling point is used in order to prevent Marangoni effects<sup>85,86</sup>.

Homogeneous ordered films were obtained also by the liquid-liquid interface deposition method (Figure 1.16 c). This assembly method is based on the use of a bad solvent such as ethylene glycol (EG) or diethylene glycol (DEG). It is called a bad solvent because it cannot solubilize the NPs which tend to agglomerate at its surface. Heterogeneous growth mode of NPs lead to the formation of ordered film. This method was established for the formation of a binary superlattice to study the plasmonic tuning effect mixing PbS, PbSe with

Au NPs by Murray group (Ye, X. *et al.* 2013)<sup>87</sup>. EG or DEG is filled in a Teflon beaker, then one drop of NPs colloidal solution is deposited on top of bad solvent. After solvent evaporation, the NPs interface is collected and deposited on a solid substrate.

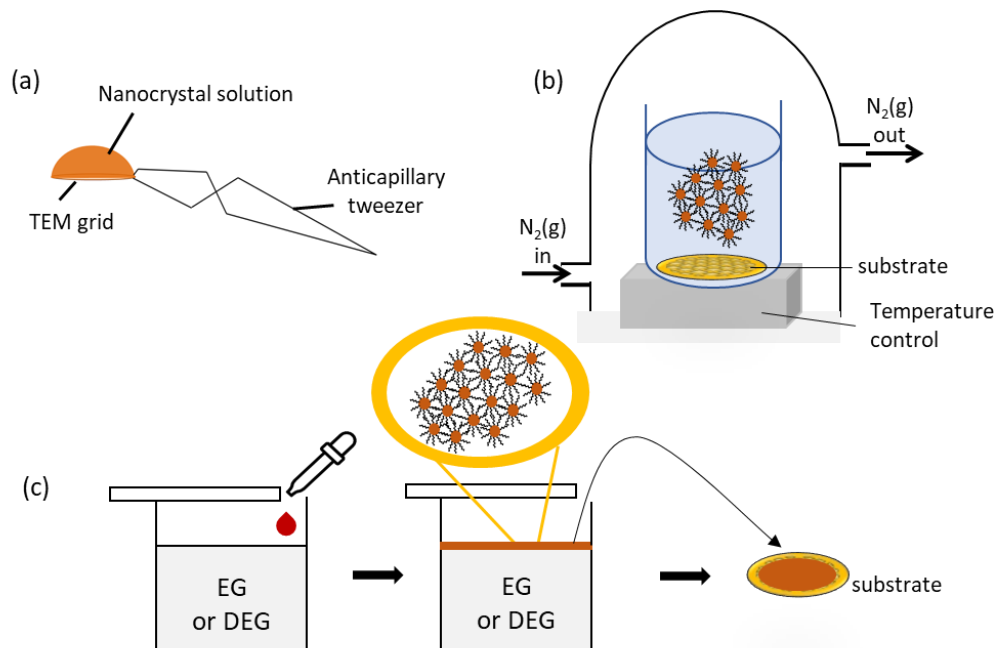


Figure 1.16. Schematic image of different deposition methods to build 3D NPs assemblies through (a) drop deposition method (b) immersion deposition (c) interface deposition using ethylene glycol (EG).

Ordered assemblies at 3D and large scale were obtained also via the solvent evaporation<sup>79,79,86,88</sup> (Figure 1.16 b). The solid substrate (HOPG, silicon etc...) was in this case placed in a glass bottle containing a colloidal solution. This bottle was placed in a temperature-controlled chamber through water circulation and the whole chamber is filled with flowing N<sub>2</sub>. This deposition method allows to obtain long range ordered *fcc* 3D NPs (micrometer scale) of different type of NPs such as Co (Lisiecki, I. *et al.* 2003)<sup>40</sup>, Ag (Ouhenia-Ouadahi, K. *et al.* 2016)<sup>86</sup> and Au (Wan, Y. *et al.* 2013)<sup>89</sup>. For 5 nm Au NPs depending on the nature of the solvent, two types of supercrystal growths were observed; a layer-by-layer growth (heterogeneous) with hexane as a solvent; a nucleation and growth occurring within the colloidal solution (homogeneous) with toluene. Calculation based on a Flory type model showed indeed that the interaction potential between Au NPs coated by dodecanethiol ligands was attractive for toluene and repulsive or weakly attractive for hexane (Goubet, N. *et al.* 2011).

Hexane allowed better solubilization of particles than toluene due to the structure of hexane close to that of the dodecanethiol ligands.

The glass bottle can also be tilted by 60-70° and placed in a low-pressure chamber as shown in Figure 1.17 a. Binary assemblies of  $\gamma$ -Fe<sub>2</sub>O<sub>3</sub> and Au NPs were obtained after evaporation of solvent such as toluene or mixtures of toluene with THF or chloroform (approximately 1:1 by volume), (Figure 1.17 b)<sup>90</sup>. The best assemblies were obtained by evaporating concentrated colloidal solution at 45° under low pressure (around 3.2 kPa).

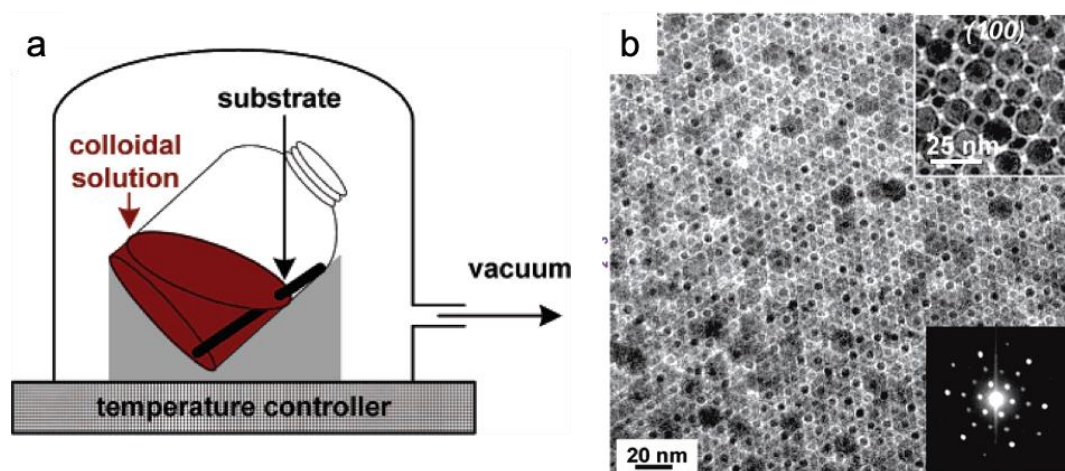


Figure 1.17. low-pressure chamber used for the fabrication of binary assemblies b) example of binary assembly made of  $\gamma$ -Fe<sub>2</sub>O<sub>3</sub> and Au NPs obtained by using this deposition method.

### 3.3. Collective properties of NPs 3D self-assemblies

When NPs are organized in 2D or 3D, collective properties can result from the interactions between neighboring NPs, inducing enhanced chemical and physical properties. The metal NPs have their own size-dependent effect on their electronic and magnetic properties. The collective properties of NPs 3D self-assemblies can be tuned by their structure.

Collective magnetic properties of the 3D superlattices of magnetic NPs have been evidenced in various systems. For example,  $\gamma$ -Fe<sub>2</sub>O<sub>3</sub> showed an increase in blocking temperature from 80 K for the isolated NPs, to ~100K for the aggregate of NPs (Nakata, K. *et al.* 2008)<sup>91</sup>. The 3D *fcc* supercrystalline films of Co NPs were characterized by a higher blocking temperature compared to the disordered assemblies composed of the same NPs

(Figure 1.18 left)<sup>92</sup>. The collective properties can differ by the contact distance between NPs, the shape of NPs assemblies and packing density (Lalatonne, Y. *et al.* 2004)<sup>93</sup>.

Collective optical properties of plasmonic nanoparticles 2D and 3D ordered assemblies were also evidenced (A Courty *J.Phys.Chem* 2010)<sup>94</sup>. Assemblies of Au or Ag NPs allows the coupling between surface plasmon. This coupling strength may be affected by the interparticle distance related to the geometry of assemblies. Coupling brings a red shift of LSPR when NPs and interparticle distances are small enough. This 3D plasmonic NP ordered assemblies can be used as SERS substrate (Aubertin, P. *et al.* 2015; Chapus, L. *et al.* 2017)<sup>95,956</sup>. The SERS enhancement was correlated to the thickness of NP assemblies, the NP sizes, and the interparticle distance (Figure 1.18, right).

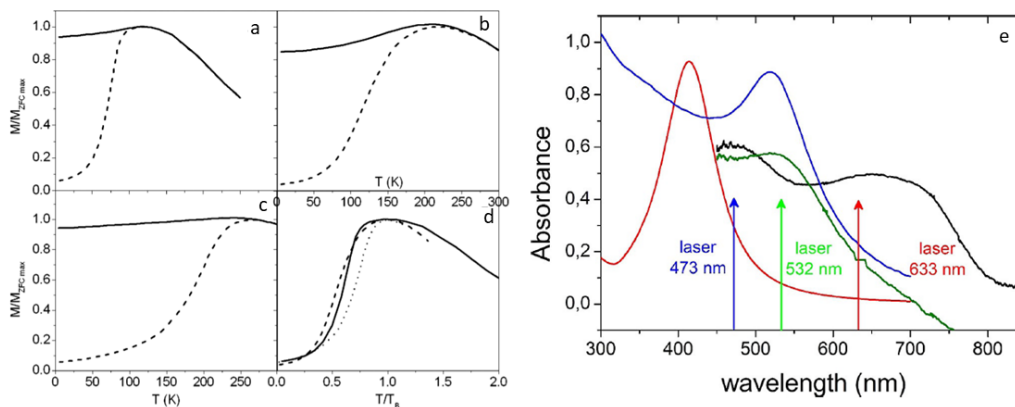


Figure 1.18. (left) FC (full line) and ZFC (dashed line)  $M$  vs  $T$  curves for disordered samples (a) native and (b) annealed at 250 and (c) 350 °C; (d) ZFC  $M$  vs  $T/T_B$  curves for disordered samples, native (full line) and annealed at 250 (dashed line) and 350 °C (dotted line). (right) UV/Vis absorption spectra of  $Ag_{5nm}$  (red) and  $Au_{5nm}$  (blue) nanoparticles dispersed in solution and absorbance spectra of  $Au_{5nm}$  (black) and  $Ag_{5nm}$  (green) 3D NP SLs with thicknesses of 96 and 872 nm, respectively.

#### 4. The concept and interest of binary superlattices

The term binary superlattices (BNSLs) refers to the assemblies of nanomaterials composed of two different cooperative complementary components. Normally, two or more individual components are synthesized separately, then binary superlattices can be fabricated through the methods like fabricate the 3D assemblies of one type of NPs as described



previously. They are obtained in organic solvents. The assembly of NPs can lead to binary 3D superlattices with accurately controlled stoichiometry and symmetry depending on the relative size.

The definition of binary components was established around 1978 with opal which was discovered in two different mixed sizes.<sup>96</sup> In 1998, BNSLs of different size of Au NPs were studied for the first time (Kiely, C. J. *et al.* 1998)<sup>97</sup>. Binary superlattices are characterized by specific superlattices crystalline structures such as AB, AB<sub>2</sub>, or AB<sub>13</sub> (Figure 1.19) with different interparticle distance compared with 3D assemblies of single component NPs. The interparticle distance (between NPs of type A) can be increased and tuned through the insert of NPs of type B (with tunable sizes) in the BNSLs. Consequently, the strategy of the binary superlattices offers a possibility to tune the interactions between the NPs (A), to control the collective properties of the assemblies. The binary superlattices constitute ideal candidates to favor coupling between two types of materials (NPs A and B) (e.g. plasmonic/plasmonic, magnetic/magnetic and magnetic/plasmonic NPs), which is expected to result in tunable and/or novel collective properties.

Despite extensive study and results on the synthesis of binary superlattices, results about their properties are still few. This can be explained by the fact that the binary assemblies obtained today are usually fine (stacking of a few layers) and extend over several tens of nanometers. We will see in chapter IV that we have obtained binary networks at the mesoscopic scale allowing the study of their collective properties and their valorization for application.

#### ***4.1. Structures of binary superlattices***

The mixture of two populations of NPs is often presented as a mixture of hard particles yielding to 3D self-assembly; one of the two components occupies an interstitial position in the compact structure (mainly *fcc*). In entropy-driven crystallization and hard-sphere approximation, it is possible to predict the final binary structures that are thermodynamically stable<sup>98</sup>. Hence, there are two important parameters that can determine the possibility of formation of BNSLs with A and B components differing by their radius ratio  $\gamma = R_B/R_A$  with  $R_A > R_B$ . In addition, the softness parameter (L/R) where the chain length, L, has to be considered in case of hydrocarboned chains capped NPs, and the parameters  $\gamma$  becomes  $\gamma L = (R_B+L_B)/(R_A+L_A)$ . The ratio  $\gamma$  determines the domain of stability of the different structures (Figure 1.19).

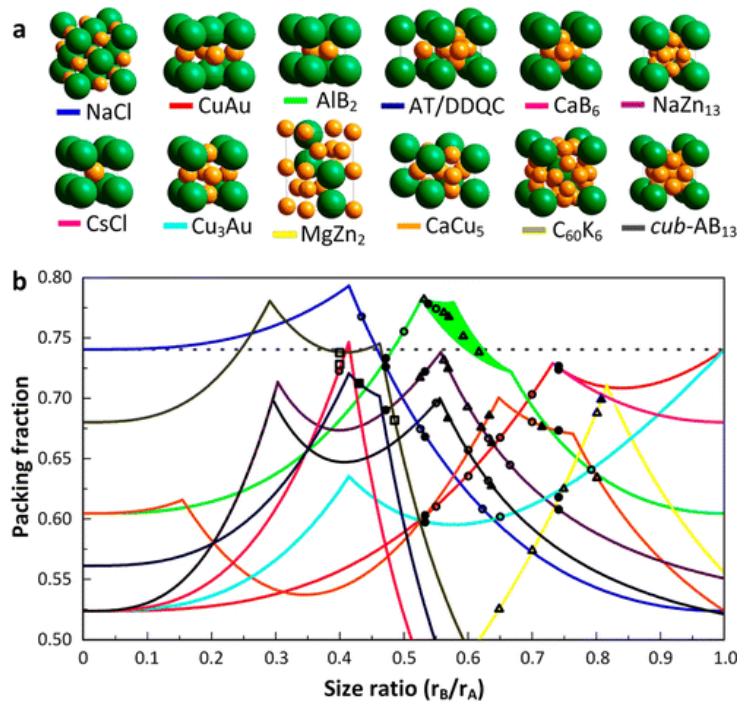


Figure 1.19. Structural diversity of binary NP superlattices and low packing density predictions for most observed phases. (a) Models of 12 commonly observed binary arrangements showing larger A spheres in green and smaller B spheres in orange. Unit cells with AB, AB<sub>2</sub>, AB<sub>3</sub>, AB<sub>5</sub>, AB<sub>6</sub>, and AB<sub>13</sub> stoichiometry as well as the structural motifs of Archimedean tiling (AT) and dodecagonal quasicrystal (DDQC) configurations are shown. (b) Plot of density vs. size ratio for spheres packed in these arrangements. Overlay; data points showing phases observed in several BNSL studies using reported effective size ratios and densities predicted using sphere-packing models. Most observed BNSLs appear to be open arrangements compared with close-packed monodisperse hard spheres (dotted line). (Boles, M.A. *et al.* 2015)<sup>98</sup>.

The entropic model is not perfect even with the correction and some experimental data do not agree with the model. Shevchenko and their group published the formation of more than 15 different binary superlattices structures using semiconducting and metallic NPs, shown in Figure 1.20 (Shevchenko, E.V. *et al.* 2006)<sup>90</sup>. These binary assembly structures include AB, AB<sub>2</sub>, AB<sub>3</sub>, AB<sub>4</sub>, AB<sub>5</sub>, AB<sub>6</sub>, AB<sub>13</sub> and cub-AB<sub>13</sub>. However, AB<sub>3</sub>, AB<sub>4</sub> and AB<sub>5</sub> structures are known as unstable ones. It was concluded that BNSL structure is determined by entropic effect, and thanks to the strong interparticle interaction between the components. It is also reported

that the crystalline structure of binary superlattices could depend also on the nature of the ligands (Wei, J. *et al.* 2015)<sup>99</sup>.

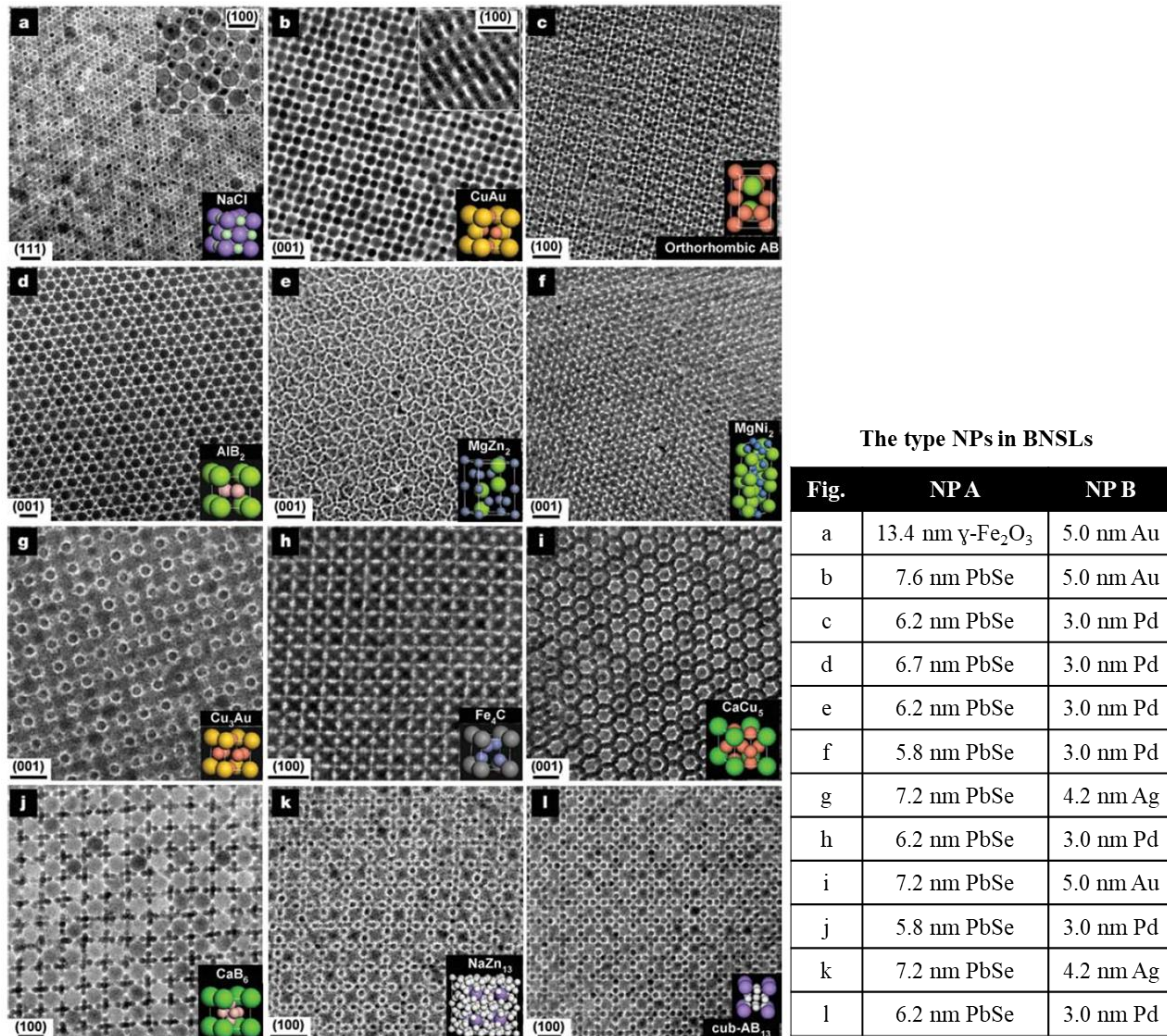


Figure 1.20. TEM images of the characteristic projections of the binary superlattices, self-assembled from different NPs, and modelled unit cells of the corresponding three-dimensional structures. Each superlattice is assembled from two types of NPs listed in table right to TEM images. Scale bars: a–c, e, f, i–l, 20 nm; d, g, h, 10 nm<sup>90</sup>.

There are several studies about the key parameters which determine the BNSLs formation. M.-P. Pileni demonstrated that the Ag/Co NP size ratio  $\gamma_{eff}$  is the dominating factor in their BNSLs formation<sup>100</sup>. The ratio  $\gamma_{eff}$  governs the crystalline structure, even with these hydrocarbon-coated NPs. Following study proved that regardless of the relative ratio concentration of Co and Ag NPs, the deposition temperature markedly changes the crystalline

structure of BNSLs<sup>100</sup>. A change in the polarity of solvent including capping agent change may alter the interaction and vary the BNSLs structure. A new BNSL structure (diamond-like) was thus obtained in polar solvent of oppositely charged 5 nm Au and Ag NPs<sup>101</sup>.

## 4.2. Collective properties of binary superlattices

### 4.2.1. Optical properties

Optical properties of BNSLs composed of semiconductor and metals has been studied by some research groups. It has been shown that the coupling between semiconductor and metallic NPs induces the interaction between excitons and plasmons. This interaction can be controlled by the size of the NPs, the morphology of superlattices, and the interparticle distance between NPs<sup>102,103</sup>.

BNSLs can show distinctive optical properties. For example, Alivisatos and their group fabricated the BNSLs consisting of CdSe and Au NPs. They discovered a drastic decrease in fluorescence intensity and lifetime compared to CdSe NPs assemblies Figure 1.21. This has been explained by energy transfer from CdSe to Au NPs<sup>104</sup>.

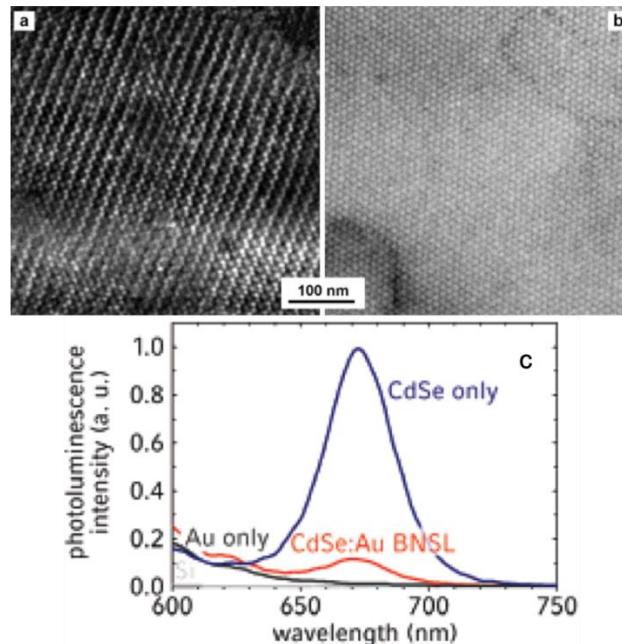


Figure 1.21. HRSEM images of fragments of (a)  $AlB_2$ -type binary superlattice consisting of 8.7 nm CdSe and 5.5 nm Au NPs and (b) CdSe-only superlattice of 8.7 nm CdSe NPs (c) Time integrated fluorescence spectra of CdSe NP only superlattice (blue curve) and of BNSL of CdSe and Au NPs (red curves).

### 4.2.2. Magnetic properties

In magnetic NPs assemblies, the magnitude of magnetic dipolar interactions, which strongly influence the magnetic properties, can be tuned through the interparticle distance. Controlling this last structural characteristic, which is not trivial, is possible thanks to the use of binary superlattices, by adjusting the component size ratio. This strategy could be used to study the superspin glass<sup>105</sup>, which origin is not yet fully elucidated (The magnetic properties has been tuned through the insertion of  $\text{Mo}_{132}$  polyoxometalates (POM) with 2.9 nm diameter between maghemite NPs with 6.2 nm diameter. The interparticle distance between maghemite NPs is slightly increased in the presence of POM inducing the blocking temperature increase<sup>106</sup> (Figure 1.22).

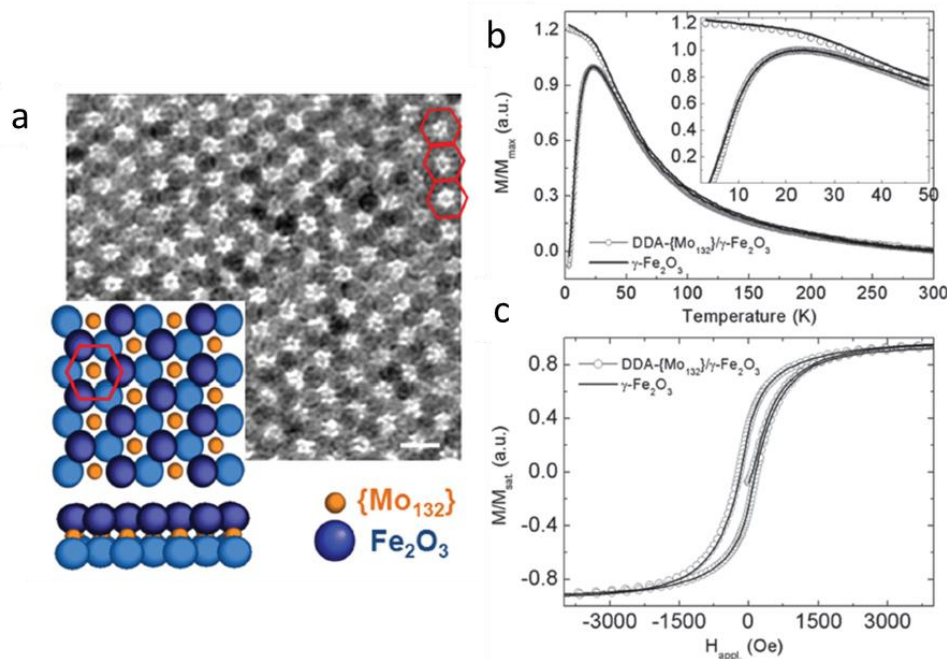


Figure 1.22. (a) Typical TEM image of  $[111]$ -projected AB-type DDA- $\{\text{Mo}_{132}\}/\text{OA}-\gamma\text{-Fe}_2\text{O}_3$  binary superlattice (scale bar: 10 nm) and (b, c) corresponding SQUID measurements binary thin film (open circles) and for a pure  $\gamma\text{-Fe}_2\text{O}_3$  thin film (solid line), in detail, (b) The temperature-dependence (FC and ZFC measured with in-plane field of 100 Oe) and (c) the in-plane field dependence (measured at 3 K).

It has been shown that binary superlattices of two different sizes of  $\text{Fe}_3\text{O}_4$  NPs, one is 14.3 nm and the other is 7.2 nm diameter, displays a single-phase-like magnetization alignment

process. In another study, the collective properties have been compared between  $\text{Fe}_3\text{O}_4$  NPs and binary  $\text{Fe}_3\text{O}_4/\text{FePt}$  superlattices, and a dipolar interaction effect is observed<sup>107</sup>.

### 4.2.3. Mechanical properties

Stoichiometries of binary superlattices can determine packing density such as  $\text{AB}_5$  showing much lower packing density than other binary crystalline structures. It is due to the van der Waals interactions between ligands and entropic driving<sup>108</sup>.

It was observed a shrinkage of the superlattices with perpendicular direction to the solid substrate through the studies of binary  $\gamma\text{-Fe}_2\text{O}_3/\text{Au}$  superlattices with  $\text{AB}_2$  structure. This shrinkage has been determined by small-angle X-ray scattering. It occurred in (210) direction when binary superlattices on (100) plane<sup>109</sup>.

## 5. Conclusions

This bibliography section has allowed us to review the state of the art concerning the synthesis of bimetallic nanoparticles and in particular core-shell nanoparticles. We were interested in the specific case of the combination of two materials with plasmonic and/or catalytic properties. We have also introduced the bases and the principle of self-assembly of metallic nanoparticles and the resulting collective properties. Finally, we treated the case of binary assemblies which offer the possibility of new physical properties (optical, magnetic, etc.) due to couplings between particles. The continuation of this thesis work consists of 3 chapters.

In Chapter II, we focused on the controlled synthesis of core-shell NPs system with two different metals with plasmonic properties (Au or Ag) and/or catalytic properties (Pd and Pt), in Chapter III, we studied their various physical properties such as optical, vibrational, and catalytic activities as a function of their size, chemical composition, and crystallinity.

Finally, Chapter IV deal with the fabrication of BNSLs which is another strategy to integrate two different metals into one system. In case of plasmonic/plasmonic or plasmonic/magnetic NPs, different types of coupling and tunable interparticle distance are expected to give rise to tunable and/or novel collective properties. Figure 1.23 illustrates the different paths used in this thesis to combine the properties of different metals through binary systems (core-shell or BNSL) and the study of the resulting properties.

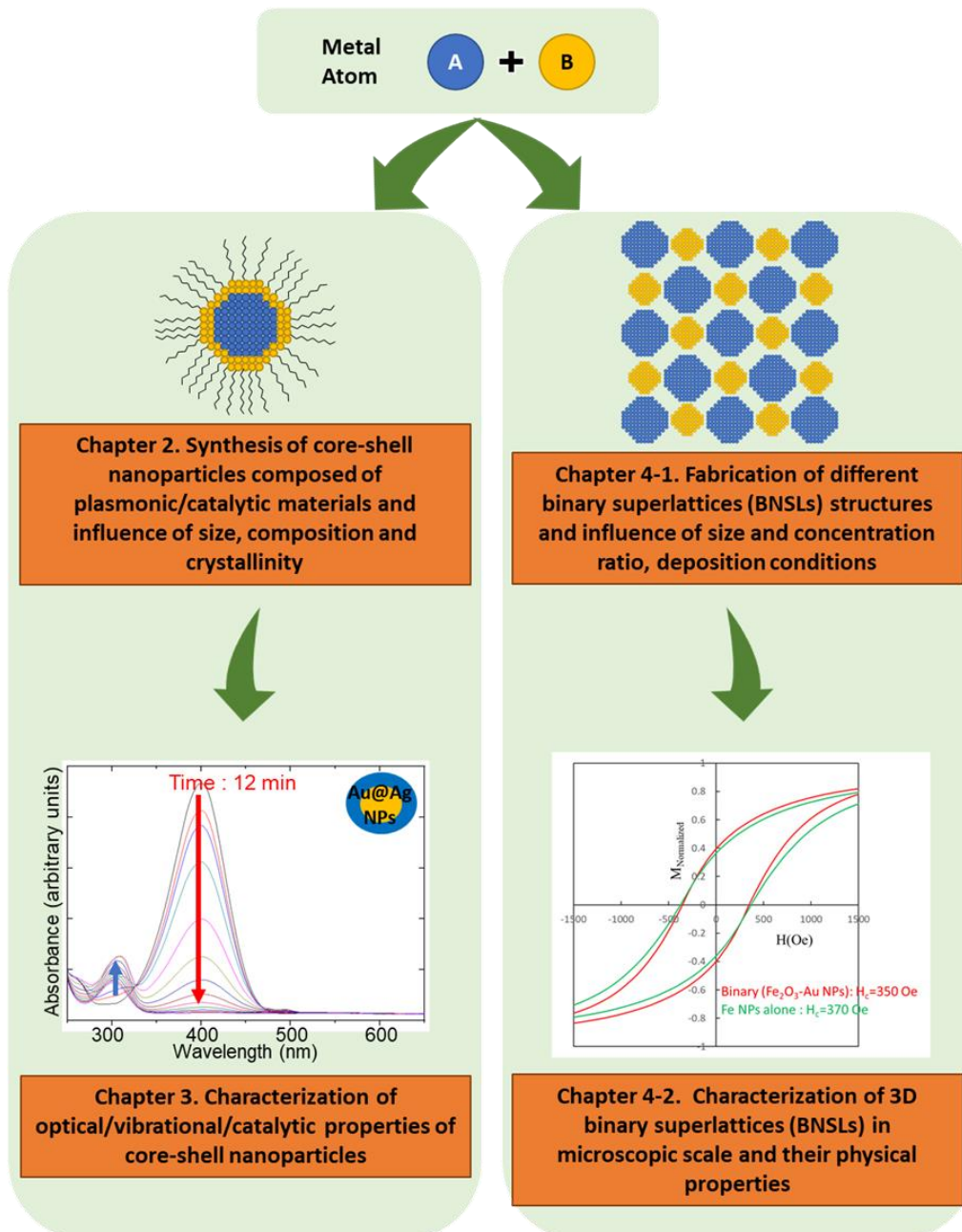


Figure 1.23. The overall guide of this study is illustrated. To integrate two different metals in one system in two ways: one in Chapter II which is about the synthesis of core-shell NPs and chapter III with their characterization of optical, vibrational, and catalytic properties. Second way is via mixing two separate NPs and forming the binary superlattices, and finally, fabrication in microscopic scale of BNSLs and their characterization will be shown in chapter IV.

## 6. References

- (1) Phan, H. T.; Haes, A. J. What Does Nanoparticle Stability Mean? *J. Phys. Chem. C Nanomater. Interfaces* **2019**, *123* (27), 16495–16507. <https://doi.org/10.1021/acs.jpcc.9b00913>.
- (2) Kim, C.; Suh, B. L.; Yun, H.; Kim, J.; Lee, H. Surface Plasmon Aided Ethanol Dehydrogenation Using Ag–Ni Binary Nanoparticles. *ACS Catal.* **2017**, *7* (4), 2294–2302. <https://doi.org/10.1021/acscatal.7b00411>.
- (3) Bedford, R. B.; Hazelwood, S. L.; Albisson, D. A. Platinum Catalysts for Suzuki Biaryl Coupling Reactions. *Organometallics* **2002**, *21* (13), 2599–2600. <https://doi.org/10.1021/om0202524>.
- (4) Mao, K.; Zhou, Z.; Han, S.; Zhou, X.; Hu, J.; Li, X.; Yang, Z. A Novel Biosensor Based on Au@Ag Core-Shell Nanoparticles for Sensitive Detection of Methylamphetamine with Surface Enhanced Raman Scattering. *Talanta* **2018**, *190*, 263–268. <https://doi.org/10.1016/j.talanta.2018.07.071>.
- (5) Xiao, Q.; Sarina, S.; Jaatinen, E.; Jia, J.; Arnold, D. P.; Liu, H.; Zhu, H. Efficient Photocatalytic Suzuki Cross-Coupling Reactions on Au–Pd Alloy Nanoparticles under Visible Light Irradiation. *Green Chem.* **2014**, *16* (9), 4272–4285. <https://doi.org/10.1039/C4GC00588K>.
- (6) Lee, K.-S.; El-Sayed, M. A. Gold and Silver Nanoparticles in Sensing and Imaging: Sensitivity of Plasmon Response to Size, Shape, and Metal Composition. *J. Phys. Chem. B* **2006**, *110* (39), 19220–19225. <https://doi.org/10.1021/jp062536y>.
- (7) Gao, J.; Gu, H.; Xu, B. Multifunctional Magnetic Nanoparticles: Design, Synthesis, and Biomedical Applications. *Acc. Chem. Res.* **2009**, *42* (8), 1097–1107. <https://doi.org/10.1021/ar9000026>.
- (8) Jain, P. K.; Huang, X.; El-Sayed, I. H.; El-Sayed, M. A. Noble Metals on the Nanoscale: Optical and Photothermal Properties and Some Applications in Imaging, Sensing, Biology, and Medicine. *Acc. Chem. Res.* **2008**, *41* (12), 1578–1586. <https://doi.org/10.1021/ar7002804>.
- (9) Zhou, N.; López-Puente, V.; Wang, Q.; Polavarapu, L.; Pastoriza-Santos, I.; Xu, Q.-H. Plasmon-Enhanced Light Harvesting: Applications in Enhanced Photocatalysis, Photodynamic Therapy and Photovoltaics. *RSC Adv.* **2015**, *5* (37), 29076–29097. <https://doi.org/10.1039/C5RA01819F>.
- (10) Wang, F.; Li, C.; Chen, H.; Jiang, R.; Sun, L.-D.; Li, Q.; Wang, J.; Yu, J. C.; Yan, C.-H. Plasmonic Harvesting of Light Energy for Suzuki Coupling Reactions. *J. Am. Chem. Soc.* **2013**, *135* (15), 5588–5601. <https://doi.org/10.1021/ja310501y>.
- (11) Wu, W.; Njoki, P. N.; Han, H.; Zhao, H.; Schiff, E. A.; Lutz, P. S.; Solomon, L.; Matthews, S.; Maye, M. M. Processing Core/Alloy/Shell Nanoparticles: Tunable Optical Properties and Evidence for Self-Limiting Alloy Growth. *J. Phys. Chem. C* **2011**, *115* (20), 9933–9942. <https://doi.org/10.1021/jp201151m>.
- (12) Cortie, M. B.; McDonagh, A. M. Synthesis and Optical Properties of Hybrid and Alloy Plasmonic Nanoparticles. *Chem. Rev.* **2011**, *111* (6), 3713–3735. <https://doi.org/10.1021/cr1002529>.
- (13) Xiao, Q.; Sarina, S.; Bo, A.; Jia, J.; Liu, H.; Arnold, D. P.; Huang, Y.; Wu, H.; Zhu, H. Visible Light-Driven Cross-Coupling Reactions at Lower Temperatures Using a Photocatalyst of Palladium and Gold Alloy Nanoparticles. *ACS Catal.* **2014**, *4* (6), 1725–1734. <https://doi.org/10.1021/cs5000284>.
- (14) Zhao, W.; Yang, L.; Yin, Y.; Jin, M. Thermodynamic Controlled Synthesis of Intermetallic Au<sub>3</sub>Cu Alloy Nanocrystals from Cu Microparticles. *J. Mater. Chem. A* **2013**, *2* (4), 902–906. <https://doi.org/10.1039/C3TA13921B>.



- (15) Gilroy, K. D.; Ruditskiy, A.; Peng, H.-C.; Qin, D.; Xia, Y. Bimetallic Nanocrystals: Syntheses, Properties, and Applications. *Chem. Rev.* **2016**, *116* (18), 10414–10472. <https://doi.org/10.1021/acs.chemrev.6b00211>.
- (16) Zaleska-Medynska, A.; Marchelek, M.; Diak, M.; Grabowska, E. Noble Metal-Based Bimetallic Nanoparticles: The Effect of the Structure on the Optical, Catalytic and Photocatalytic Properties. *Adv. Colloid Interface Sci.* **2016**, *229*, 80–107. <https://doi.org/10.1016/j.cis.2015.12.008>.
- (17) Wu, Y.; Cai, S.; Wang, D.; He, W.; Li, Y. Syntheses of Water-Soluble Octahedral, Truncated Octahedral, and Cubic Pt–Ni Nanocrystals and Their Structure–Activity Study in Model Hydrogenation Reactions. *J. Am. Chem. Soc.* **2012**, *134* (21), 8975–8981. <https://doi.org/10.1021/ja302606d>.
- (18) Peng, Z.; Yang, H. Designer Platinum Nanoparticles: Control of Shape, Composition in Alloy, Nanostructure and Electrocatalytic Property. *Nano Today* **2009**, *4* (2), 143–164. <https://doi.org/10.1016/j.nantod.2008.10.010>.
- (19) Ferrando, R.; Jellinek, J.; Johnston, R. L. Nanoalloys: From Theory to Applications of Alloy Clusters and Nanoparticles. *Chem. Rev.* **2008**, *108* (3), 845–910. <https://doi.org/10.1021/cr040090g>.
- (20) Perro, A.; Reculosa, S.; Ravaine, S.; Bourgeat-Lami, E.; Duguet, E. Design and Synthesis of Janus Micro- and Nanoparticles. *J. Mater. Chem.* **2005**, *15* (35–36), 3745–3760. <https://doi.org/10.1039/B505099E>.
- (21) Binks, B. P. Particles as Surfactants—Similarities and Differences. *Curr. Opin. Colloid Interface Sci.* **2002**, *7* (1), 21–41. [https://doi.org/10.1016/S1359-0294\(02\)00008-0](https://doi.org/10.1016/S1359-0294(02)00008-0).
- (22) Zeng, J.; Zhang, Q.; Chen, J.; Xia, Y. A Comparison Study of the Catalytic Properties of Au-Based Nanocages, Nanoboxes, and Nanoparticles. *Nano Lett.* **2010**, *10* (1), 30–35. <https://doi.org/10.1021/nl903062e>.
- (23) Fang, Z.; Wang, Y.; Liu, C.; Chen, S.; Sang, W.; Wang, C.; Zeng, J. Rational Design of Metal Nanoframes for Catalysis and Plasmonics. *Small* **2015**, *11* (22), 2593–2605. <https://doi.org/10.1002/smll.201402799>.
- (24) Wang, X.; Choi, S.-I.; Roling, L. T.; Luo, M.; Ma, C.; Zhang, L.; Chi, M.; Liu, J.; Xie, Z.; Herron, J. A.; Mavrikakis, M.; Xia, Y. Palladium–Platinum Core-Shell Icosahedra with Substantially Enhanced Activity and Durability towards Oxygen Reduction. *Nat. Commun.* **2015**, *6* (1), 1–8. <https://doi.org/10.1038/ncomms8594>.
- (25) Malathi, S.; Ezhilarasu, T.; Abiraman, T.; Balasubramanian, S. One Pot Green Synthesis of Ag, Au and Au–Ag Alloy Nanoparticles Using Isonicotinic Acid Hydrazide and Starch. *Carbohydr. Polym.* **2014**, *111*, 734–743. <https://doi.org/10.1016/j.carbpol.2014.04.105>.
- (26) Sytwu, K.; Vadai, M.; Dionne, J. A. Bimetallic Nanostructures: Combining Plasmonic and Catalytic Metals for Photocatalysis. *Adv. Phys. X* **2019**, *4* (1), 1619480. <https://doi.org/10.1080/23746149.2019.1619480>.
- (27) Sra, A. K.; Schaak, R. E. Synthesis of Atomically Ordered AuCu and AuCu<sub>3</sub> Nanocrystals from Bimetallic Nanoparticle Precursors. *J. Am. Chem. Soc.* **2004**, *126* (21), 6667–6672. <https://doi.org/10.1021/ja031547r>.
- (28) Tojo, C.; Vila-Romeu, N. Kinetic Study on the Formation of Bimetallic Core-Shell Nanoparticles via Microemulsions. *Materials* **2014**, *7* (11).
- (29) Park, S.-J.; Kim, S.; Lee, S.; Khim, Z. G.; Char, K.; Hyeon, T. Synthesis and Magnetic Studies of Uniform Iron Nanorods and Nanospheres. *J. Am. Chem. Soc.* **2000**, *122* (35), 8581–8582. <https://doi.org/10.1021/ja001628c>.
- (30) Puntès, V. F.; Krishnan, K. M.; Alivisatos, A. P. Colloidal Nanocrystal Shape and Size Control: The Case of Cobalt. *Science* **2001**, *291* (5511), 2115–2117. <https://doi.org/10.1126/science.1058495>.

- (31) Ely, T. O.; Amiens, C.; Chaudret, B.; Snoeck, E.; Verelst, M.; Respaud, M.; Broto, J.-M. Synthesis of Nickel Nanoparticles. Influence of Aggregation Induced by Modification of Poly(Vinylpyrrolidone) Chain Length on Their Magnetic Properties. *Chem. Mater.* **1999**, *11* (3), 526–529. <https://doi.org/10.1021/cm980675p>.
- (32) Son, S. U.; Jang, Y.; Park, J.; Na, H. B.; Park, H. M.; Yun, H. J.; Lee, J.; Hyeon, T. Designed Synthesis of Atom-Economical Pd/Ni Bimetallic Nanoparticle-Based Catalysts for Sonogashira Coupling Reactions. *J. Am. Chem. Soc.* **2004**, *126* (16), 5026–5027. <https://doi.org/10.1021/ja039757r>.
- (33) Rutledge, R. D.; Morris, W. H.; Wellons, M. S.; Gai, Z.; Shen, J.; Bentley, J.; Wittig, J. E.; Lukehart, C. M. Formation of FePt Nanoparticles Having High Coercivity. *J. Am. Chem. Soc.* **2006**, *128* (44), 14210–14211. <https://doi.org/10.1021/ja0633868>.
- (34) Robinson, I.; Zacchini, S.; Tung, L. D.; Maenosono, S.; Thanh, N. T. K. Synthesis and Characterization of Magnetic Nanoalloys from Bimetallic Carbonyl Clusters. *Chem. Mater.* **2009**, *21* (13), 3021–3026. <https://doi.org/10.1021/cm9008442>.
- (35) Jana, N. R.; Gearheart, L.; Murphy, C. J. Wet Chemical Synthesis of Silver Nanorods and Nanowires of Controllable Aspect Ratio. *Chem. Commun.* **2001**, No. 7, 617–618. <https://doi.org/10.1039/B100521I>.
- (36) Jana, N. R.; Gearheart, L.; Murphy, C. J. Seeding Growth for Size Control of 5–40 Nm Diameter Gold Nanoparticles. *Langmuir* **2001**, *17* (22), 6782–6786. <https://doi.org/10.1021/la0104323>.
- (37) Jana, N. R.; Gearheart, L.; Murphy, C. J. Evidence for Seed-Mediated Nucleation in the Chemical Reduction of Gold Salts to Gold Nanoparticles. *Chem. Mater.* **2001**, *13* (7), 2313–2322. <https://doi.org/10.1021/cm000662n>.
- (38) Sun, Y.; Yin, Y.; Mayers, B. T.; Herricks, T.; Xia, Y. Uniform Silver Nanowires Synthesis by Reducing AgNO<sub>3</sub> with Ethylene Glycol in the Presence of Seeds and Poly(Vinyl Pyrrolidone). *Chem. Mater.* **2002**, *14* (11), 4736–4745. <https://doi.org/10.1021/cm020587b>.
- (39) Habas, S. E.; Lee, H.; Radmilovic, V.; Somorjai, G. A.; Yang, P. Shaping Binary Metal Nanocrystals through Epitaxial Seeded Growth. *Nat. Mater.* **2007**, *6* (9), 692–697. <https://doi.org/10.1038/nmat1957>.
- (40) Lisiecki, I.; Pileni, M. P. Synthesis of Well-Defined and Low Size Distribution Cobalt Nanocrystals: The Limited Influence of Reverse Micelles. *Langmuir* **2003**, *19* (22), 9486–9489. <https://doi.org/10.1021/la0301386>.
- (41) Taleb, A.; Petit, C.; Pileni, M. P. Synthesis of Highly Monodisperse Silver Nanoparticles from AOT Reverse Micelles: A Way to 2D and 3D Self-Organization. *Chem. Mater.* **1997**, *9* (4), 950–959. <https://doi.org/10.1021/cm960513y>.
- (42) Lisiecki, I.; Pileni, M. P. Copper Metallic Particles Synthesized “in Situ” in Reverse Micelles: Influence of Various Parameters on the Size of the Particles. *J. Phys. Chem.* **1995**, *99* (14), 5077–5082. <https://doi.org/10.1021/j100014a030>.
- (43) Goubet, N.; Richardi, J.; Albouy, P. A.; Pileni, M. P. How to Predict the Growth Mechanism of Supracrystals from Gold Nanocrystals. *J. Phys. Chem. Lett.* **2011**, *2* (5), 417–422. <https://doi.org/10.1021/jz200004f>.
- (44) Portalès, H.; Goubet, N.; Sirotkin, S.; Duval, E.; Mermet, A.; Albouy, P.-A.; Pileni, M.-P. Crystallinity Segregation upon Selective Self-Assembling of Gold Colloidal Single Nanocrystals. *Nano Lett.* **2012**, *12* (10), 5292–5298. <https://doi.org/10.1021/nl3029009>.
- (45) Goubet, N.; Tempira, I.; Yang, J.; Soavi, G.; Polli, D.; Cerullo, G.; Pileni, M. Size and Nanocrystallinity Controlled Gold Nanocrystals: Synthesis, Electronic and Mechanical Properties. *Nanoscale* **2015**, *7* (7), 3237–3246. <https://doi.org/10.1039/C4NR06513A>.

- (46) Andrieux-Ledier, A.; Tremblay, B.; Courty, A. Synthesis of Silver Nanoparticles Using Different Silver Phosphine Precursors: Formation Mechanism and Size Control. *J. Phys. Chem. C* **2013**, *117* (28), 14850–14857. <https://doi.org/10.1021/jp4040248>.
- (47) Ben Aissa, M. A.; Tremblay, B.; Andrieux-Ledier, A.; Maisonhaute, E.; Raouafi, N.; Courty, A. Copper Nanoparticles of Well-Controlled Size and Shape: A New Advance in Synthesis and Self-Organization. *Nanoscale* **2015**, *7* (7), 3189–3195. <https://doi.org/10.1039/c4nr06893a>.
- (48) Meziane, L.; Salzemann, C.; Aubert, C.; Gérard, H.; Petit, C.; Petit, M. Hcp Cobalt Nanocrystals with High Magnetic Anisotropy Prepared by Easy One-Pot Synthesis. *Nanoscale* **2016**, *8* (44), 18640–18645. <https://doi.org/10.1039/C6NR05792F>.
- (49) Ngo, A.-T.; Richardi, J.; Pileni, M. P. Crack Patterns in Superlattices Made of Maghemite Nanocrystals. *Phys. Chem. Chem. Phys.* **2013**, *15* (26), 10666–10672. <https://doi.org/10.1039/C3CP50276G>.
- (50) Chapus, L.; Aubertin, P.; Joiret, S.; Lucas, I. T.; Maisonhaute, E.; Courty, A. Tunable SERS Platforms from Small Nanoparticle 3D Superlattices: A Comparison between Gold, Silver, and Copper. *ChemPhysChem* **2017**, *18* (21), 3066–3075. <https://doi.org/10.1002/cphc.201700601>.
- (51) Cobley, C. M.; Xia, Y. Engineering the Properties of Metal Nanostructures via Galvanic Replacement Reactions. *Mater. Sci. Eng. R Rep. Rev. J.* **2010**, *70* (3–6), 44–62. <https://doi.org/10.1016/j.mser.2010.06.002>.
- (52) Sasaki, K.; Naohara, H.; Cai, Y.; Choi, Y. M.; Liu, P.; Vukmirovic, M. B.; Wang, J. X.; Adzic, R. R. Core-Protected Platinum Monolayer Shell High-Stability Electrocatalysts for Fuel-Cell Cathodes. *Angew. Chem. Int. Ed Engl.* **2010**, *49* (46), 8602–8607. <https://doi.org/10.1002/anie.201004287>.
- (53) Raman, C. V.; Krishnan, K. S. A New Type of Secondary Radiation. *Nature* **1928**, *121* (3048), 501–502. <https://doi.org/10.1038/121501c0>.
- (54) Venkateswarlu, K. Relative Intensities of Stokes and Anti-Stokes Raman Lines in Crystals. *Proc. Indian Acad. Sci. - Sect. A* **1941**, *13* (1), 64–67. <https://doi.org/10.1007/BF03052534>.
- (55) Lamb, H. I. On the Propagation of Tremors over the Surface of an Elastic Solid. *Philos. Trans. R. Soc. Lond. Ser. Contain. Pap. Math. Phys. Character* **1904**, *203* (359–371), 1–42. <https://doi.org/10.1098/rsta.1904.0013>.
- (56) Duval, E.; Portales, H.; Saviot, L.; Fujii, M.; Sumitomo, K.; Hayashi, S. Spatial Coherence Effect on the Low-Frequency Raman Scattering from Metallic Nanoclusters. *Phys. Rev. B* **2001**, *63* (7), 075405. <https://doi.org/10.1103/PhysRevB.63.075405>.
- (57) Portales, H.; Saviot, L.; Duval, E.; Fujii, M.; Hayashi, S.; Del Fatti, N.; Vallée, F. Resonant Raman Scattering by Breathing Modes of Metal Nanoparticles. *J. Chem. Phys.* **2001**, *115* (8), 3444–3447. <https://doi.org/10.1063/1.1396817>.
- (58) Mohr, C.; Claus, P. Hydrogenation Properties of Supported Nanosized Gold Particles. *Sci. Prog.* **2001**, *84* (4), 311–334. <https://doi.org/10.3184/003685001783238925>.
- (59) Haruta, M.; Kobayashi, T.; Sano, H.; Yamada, N. Novel Gold Catalysts for the Oxidation of Carbon Monoxide at a Temperature Far Below 0 °C. *Chem. Lett.* **1987**, *16* (2), 405–408. <https://doi.org/10.1246/cl.1987.405>.
- (60) Hashmi, A. S. K.; Hutchings, G. J. Gold Catalysis. *Angew. Chem. Int. Ed.* **2006**, *45* (47), 7896–7936. <https://doi.org/10.1002/anie.200602454>.
- (61) Su, F.; Lv, L.; Lee, F. Y.; Liu, T.; Cooper, A. I.; Zhao, X. S. Thermally Reduced Ruthenium Nanoparticles as a Highly Active Heterogeneous Catalyst for Hydrogenation of Monoaromatics. *J. Am. Chem. Soc.* **2007**, *129* (46), 14213–14223. <https://doi.org/10.1021/ja072697v>.

- (62) Lu, F.; Liu, J.; Xu, J. Fast Aqueous/Organic Hydrogenation of Arenes, Olefins and Carbonyl Compounds by Poly(N-Vinylpyrrolidone)-Ru as Amphiphilic Microreactor System. *Adv. Synth. Catal.* **2006**, *348* (7–8), 857–861. <https://doi.org/10.1002/adsc.200505444>.
- (63) Zhang, L.; Xie, Z.; Gong, J. Shape-Controlled Synthesis of Au–Pd Bimetallic Nanocrystals for Catalytic Applications. *Chem. Soc. Rev.* **2016**, *45* (14), 3916–3934. <https://doi.org/10.1039/C5CS00958H>.
- (64) He, J.; Ichinose, I.; Kunitake, T.; Nakao, A.; Shiraishi, Y.; Toshima, N. Facile Fabrication of Ag–Pd Bimetallic Nanoparticles in Ultrathin TiO<sub>2</sub>-Gel Films: Nanoparticle Morphology and Catalytic Activity. *J. Am. Chem. Soc.* **2003**, *125* (36), 11034–11040. <https://doi.org/10.1021/ja035970b>.
- (65) Tedsree, K.; Li, T.; Jones, S.; Chan, C. W. A.; Yu, K. M. K.; Bagot, P. A. J.; Marquis, E. A.; Smith, G. D. W.; Tsang, S. C. E. Hydrogen Production from Formic Acid Decomposition at Room Temperature Using a Ag–Pd Core–Shell Nanocatalyst. *Nat. Nanotechnol.* **2011**, *6* (5), 302–307. <https://doi.org/10.1038/nnano.2011.42>.
- (66) Xu, D.; Bliznakov, S.; Liu, Z.; Fang, J.; Dimitrov, N. Composition-Dependent Electrocatalytic Activity of Pt-Cu Nanocube Catalysts for Formic Acid Oxidation. *Angew. Chem. Int. Ed.* **2010**, *49* (7), 1282–1285. <https://doi.org/10.1002/anie.200905248>.
- (67) Xie, S.; Choi, S.-I.; Xia, X.; Xia, Y. Catalysis on Faceted Noble-Metal Nanocrystals: Both Shape and Size Matter. *Curr. Opin. Chem. Eng.* **2013**, *2* (2), 142–150. <https://doi.org/10.1016/j.coche.2013.02.003>.
- (68) Zheng, Z.; Tachikawa, T.; Majima, T. Single-Particle Study of Pt-Modified Au Nanorods for Plasmon-Enhanced Hydrogen Generation in Visible to Near-Infrared Region. *J. Am. Chem. Soc.* **2014**, *136* (19), 6870–6873. <https://doi.org/10.1021/ja502704n>.
- (69) Willets, K. A.; Van Duyne, R. P. Localized Surface Plasmon Resonance Spectroscopy and Sensing. *Annu. Rev. Phys. Chem.* **2007**, *58* (1), 267–297. <https://doi.org/10.1146/annurev.physchem.58.032806.104607>.
- (70) Yang, M.; Chen, T.; Lau, W. S.; Wang, Y.; Tang, Q.; Yang, Y.; Chen, H. Development of Polymer-Encapsulated Metal Nanoparticles as Surface-Enhanced Raman Scattering Probes. *Small* **2009**, *5* (2), 198–202. <https://doi.org/10.1002/sml.200800777>.
- (71) Liu, Z.; Hou, W.; Pavaskar, P.; Aykol, M.; Cronin, S. B. Plasmon Resonant Enhancement of Photocatalytic Water Splitting Under Visible Illumination. *Nano Lett.* **2011**, *11* (3), 1111–1116. <https://doi.org/10.1021/nl104005n>.
- (72) Sun, M.; Xu, H. A Novel Application of Plasmonics: Plasmon-Driven Surface-Catalyzed Reactions. *Small* **2012**, *8* (18), 2777–2786. <https://doi.org/10.1002/sml.201200572>.
- (73) Dreaden, E. C.; Alkilany, A. M.; Huang, X.; Murphy, C. J.; El-Sayed, M. A. The Golden Age: Gold Nanoparticles for Biomedicine. *Chem. Soc. Rev.* **2012**, *41* (7), 2740–2779. <https://doi.org/10.1039/C1CS15237H>.
- (74) Gobin, A. M.; Lee, M. H.; Halas, N. J.; James, W. D.; Drezek, R. A.; West, J. L. Near-Infrared Resonant Nanoshells for Combined Optical Imaging and Photothermal Cancer Therapy. *Nano Lett.* **2007**, *7* (7), 1929–1934. <https://doi.org/10.1021/nl070610y>.
- (75) Jain, P. K.; El-Sayed, I. H.; El-Sayed, M. A. Au Nanoparticles Target Cancer. *Nano Today* **2007**, *2* (1), 18–29. [https://doi.org/10.1016/S1748-0132\(07\)70016-6](https://doi.org/10.1016/S1748-0132(07)70016-6).
- (76) Sil, D.; Gilroy, K. D.; Niaux, A.; Boulesbaa, A.; Neretina, S.; Borguet, E. Seeing Is Believing: Hot Electron Based Gold Nanoplasmonic Optical Hydrogen Sensor. *ACS Nano* **2014**, *8* (8), 7755–7762. <https://doi.org/10.1021/nn500765t>.

- (77) Anker, J. N.; Hall, W. P.; Lyandres, O.; Shah, N. C.; Zhao, J.; Van Duyne, R. P. Biosensing with Plasmonic Nanosensors. In *Nanoscience and Technology*; Co-Published with Macmillan Publishers Ltd, UK, 2009; pp 308–319. [https://doi.org/10.1142/9789814287005\\_0032](https://doi.org/10.1142/9789814287005_0032).
- (78) Zhang, W.; Goh, H. Y. J.; Firdoz, S.; Lu, X. Growth of Au@Ag Core–Shell Pentatwinned Nanorods: Tuning the End Facets. *Chem. - Eur. J.* **2013**, *19* (38), 12732–12738. <https://doi.org/10.1002/chem.201301753>.
- (79) Henry, A.-I.; Courty, A.; Pileni, M.-P.; Albouy, P.-A.; Israelachvili, J. Tuning of Solid Phase in Supracrystals Made of Silver Nanocrystals. *Nano Lett.* **2008**, *8* (7), 2000–2005. <https://doi.org/10.1021/nl8010947>.
- (80) Korgel, B. A.; Fullam, S.; Connolly, S.; Fitzmaurice, D. Assembly and Self-Organization of Silver Nanocrystal Superlattices: Ordered “Soft Spheres.” *J. Phys. Chem. B* **1998**, *102* (43), 8379–8388. <https://doi.org/10.1021/jp981598o>.
- (81) Motte, L.; Lacaze, E.; Maillard, M.; Pileni, M. P. Self-Assemblies of Silver Sulfide Nanocrystals on Various Substrates. *Langmuir* **2000**, *16* (8), 3803–3812. <https://doi.org/10.1021/la9908283>.
- (82) Yan, C.; Wang, T. A New View for Nanoparticle Assemblies: From Crystalline to Binary Cooperative Complementarity. *Chem. Soc. Rev.* **2017**, *46* (5), 1483–1509. <https://doi.org/10.1039/C6CS00696E>.
- (83) Salzemann, C.; Richardi, J.; Lisiecki, I.; Weis, J.-J.; Pileni, M. P. Mesoscopic Void Structures in Cobalt Nanocrystal Films Formed from Drying Concentrated Colloidal Solutions. *Phys. Rev. Lett.* **2009**, *102* (14), 144502. <https://doi.org/10.1103/PhysRevLett.102.144502>.
- (84) Taleb, A.; Petit, C.; Pileni, M. P. Optical Properties of Self-Assembled 2D and 3D Superlattices of Silver Nanoparticles. *J. Phys. Chem. B* **1998**, *102* (12), 2214–2220. <https://doi.org/10.1021/jp972807s>.
- (85) Maillard, M.; Motte, L.; Ngo, A. T.; Pileni, M. P. Rings and Hexagons Made of Nanocrystals: A Marangoni Effect. *J. Phys. Chem. B* **2000**, *104* (50), 11871–11877. <https://doi.org/10.1021/jp002605n>.
- (86) Ouhenia-Ouadahi, K.; Andrieux-Ledier, A.; Richardi, J.; Albouy, P.-A.; Beaunier, P.; Sutter, P.; Sutter, E.; Courty, A. Tuning the Growth Mode of 3D Silver Nanocrystal Superlattices by Triphenylphosphine. *Chem. Mater.* **2016**, *28* (12), 4380–4389. <https://doi.org/10.1021/acs.chemmater.6b01374>.
- (87) Ye, X.; Chen, J.; Diroll, B. T.; Murray, C. B. Tunable Plasmonic Coupling in Self-Assembled Binary Nanocrystal Superlattices Studied by Correlated Optical Microspectrophotometry and Electron Microscopy. *Nano Lett.* **2013**, *13* (3), 1291–1297. <https://doi.org/10.1021/nl400052w>.
- (88) Courty, A.; Fermon, C.; Pileni, M.-P. “Supra Crystals” Made of Nanocrystals. *Adv. Mater.* **2001**, *13* (4), 254–258. [https://doi.org/10.1002/1521-4095\(200102\)13:4<254::AID-ADMA254>3.0.CO;2-P](https://doi.org/10.1002/1521-4095(200102)13:4<254::AID-ADMA254>3.0.CO;2-P).
- (89) Wan, Y.; Goubet, N.; Albouy, P.-A.; Schaeffer, N.; Pileni, M.-P. Hierarchy in Au Nanocrystal Ordering in a Supracrystal: II. Control of Interparticle Distances. *Langmuir* **2013**, *29* (44), 13576–13581. <https://doi.org/10.1021/la403583q>.
- (90) Shevchenko, E. V.; Talapin, D. V.; Kotov, N. A.; O’Brien, S.; Murray, C. B. Structural Diversity in Binary Nanoparticle Superlattices. *Nature* **2006**, *439*, 55.
- (91) Nakata, K.; Hu, Y.; Uzun, O.; Bakr, O.; Stellacci, F. Chains of Superparamagnetic Nanoparticles. *Adv. Mater.* **2008**, *20* (22), 4294–4299. <https://doi.org/10.1002/adma.200800022>.
- (92) Parker, D.; Lisiecki, I.; Salzemann, C.; Pileni, M.-P. Emergence of New Collective Properties of Cobalt Nanocrystals Ordered in Fcc Supracrystals: II, Magnetic

- Investigation. *J. Phys. Chem. C* **2007**, *111* (34), 12632–12638. <https://doi.org/10.1021/jp071821u>.
- (93) Lalatonne, Y.; Richardi, J.; Pileni, M. P. Van Der Waals versus Dipolar Forces Controlling Mesoscopic Organizations of Magnetic Nanocrystals. *Nat. Mater.* **2004**, *3* (2), 121–125. <https://doi.org/10.1038/nmat1054>.
- (94) Courty, A. Silver Nanocrystals: Self-Organization and Collective Properties. *J. Phys. Chem. C* **2010**, *114* (9), 3719–3731. <https://doi.org/10.1021/jp908966b>.
- (95) Aubertin, P.; Aissa, M. A. B.; Raouafi, N.; Joiret, S.; Courty, A.; Maisonhaute, E. Optical Response and SERS Properties of Individual Large Scale Supracrystals Made of Small Silver Nanocrystals. *Nano Res.* **2015**, *8* (5), 1615–1626. <https://doi.org/10.1007/s12274-014-0650-5>.
- (96) Sanders, J. V.; Murray, M. J. Ordered Arrangements of Spheres of Two Different Sizes in Opal. *Nature* **1978**, *275* (5677), 201–203. <https://doi.org/10.1038/275201a0>.
- (97) Kiely, C. J.; Fink, J.; Brust, M.; Bethell, D.; Schiffrin, D. J. Spontaneous Ordering of Bimodal Ensembles of Nanoscopic Gold Clusters. *Nature* **1998**, *396* (6710), 444–446. <https://doi.org/10.1038/24808>.
- (98) Boles, M. A.; Talapin, D. V. Many-Body Effects in Nanocrystal Superlattices: Departure from Sphere Packing Explains Stability of Binary Phases. *J. Am. Chem. Soc.* **2015**, *137* (13), 4494–4502. <https://doi.org/10.1021/jacs.5b00839>.
- (99) Wei, J.; Schaeffer, N.; Pileni, M.-P. Ligand Exchange Governs the Crystal Structures in Binary Nanocrystal Superlattices. *J. Am. Chem. Soc.* **2015**, *137* (46), 14773–14784. <https://doi.org/10.1021/jacs.5b09959>.
- (100) Yang, Z.; Wei, J.; Pileni, M.-P. Metal–Metal Binary Nanoparticle Superlattices: A Case Study of Mixing Co and Ag Nanoparticles. *Chem. Mater.* **2015**, *27* (6), 2152–2157. <https://doi.org/10.1021/acs.chemmater.5b00123>.
- (101) Bodnarchuk, M. I.; Erni, R.; Krumeich, F.; Kovalenko, M. V. Binary Superlattices from Colloidal Nanocrystals and Giant Polyoxometalate Clusters. *Nano Lett.* **2013**, *13* (4), 1699–1705. <https://doi.org/10.1021/nl4002475>.
- (102) Govorov, A. O.; Bryant, G. W.; Zhang, W.; Skeini, T.; Lee, J.; Kotov, N. A.; Slocik, J. M.; Naik, R. R. Exciton–Plasmon Interaction and Hybrid Excitons in Semiconductor–Metal Nanoparticle Assemblies. *Nano Lett.* **2006**, *6* (5), 984–994. <https://doi.org/10.1021/nl0602140>.
- (103) Lee, J.; Hernandez, P.; Lee, J.; Govorov, A. O.; Kotov, N. A. Exciton–Plasmon Interactions in Molecular Spring Assemblies of Nanowires and Wavelength-Based Protein Detection. *Nat. Mater.* **2007**, *6* (4), 291–295. <https://doi.org/10.1038/nmat1869>.
- (104) Shevchenko, E. V.; Ringler, M.; Schwemer, A.; Talapin, D. V.; Klar, T. A.; Rogach, A. L.; Feldmann, J.; Alivisatos, A. P. Self-Assembled Binary Superlattices of CdSe and Au Nanocrystals and Their Fluorescence Properties. *J. Am. Chem. Soc.* **2008**, *130* (11), 3274–3275. <https://doi.org/10.1021/ja710619s>.
- (105) Andersson, M. S. Nanoparticle Magnetism: Superspin Glasses. *J. Nanosci. Nanotechnol.* **2019**, *19* (8), 4903–4910. <https://doi.org/10.1166/jnn.2019.16798>.
- (106) Breitwieser Romain; Auvray Thomas; Volatron Florence; Salzemann Caroline; Ngo Anh-Tu; Albouy Pierre-Antoine; Proust Anna; Petit Christophe. Binary Superlattices from {Mo132} Polyoxometalates and Maghemite Nanocrystals: Long-Range Ordering and Fine-Tuning of Dipole Interactions. *Small* **2016**, *12* (2), 220–228. <https://doi.org/10.1002/sml.201502127>.
- (107) Chen, J.; Dong, A.; Cai, J.; Ye, X.; Kang, Y.; Kikkawa, J. M.; Murray, C. B. Collective Dipolar Interactions in Self-Assembled Magnetic Binary Nanocrystal Superlattice Membranes. *Nano Lett.* **2010**, *10* (12), 5103–5108. <https://doi.org/10.1021/nl103568q>.

- (108) Chen, Z.; Moore, J.; Radtke, G.; Siringhaus, H.; O'Brien, S. Binary Nanoparticle Superlattices in the Semiconductor–Semiconductor System: CdTe and CdSe. *J. Am. Chem. Soc.* **2007**, *129* (50), 15702–15709. <https://doi.org/10.1021/ja076698z>.
- (109) Smith, D. K.; Goodfellow, B.; Smilgies, D.-M.; Korgel, B. A. Self-Assembled Simple Hexagonal AB<sub>2</sub> Binary Nanocrystal Superlattices: SEM, GISAXS, and Defects. *J. Am. Chem. Soc.* **2009**, *131* (9), 3281–3290. <https://doi.org/10.1021/ja8085438>.

## Chapter II. Synthesis of core-shell nanoparticles composed of plasmonic/catalytic materials with controlled size, composition, and crystallinity.

### 1. Introduction

We developed a synthesis in two steps of bimetallic core-shell NPs combining a plasmonic core (Au or Ag) and a plasmonic (Ag) or catalytic (Pt or Pd) shell. This synthesis presents a great flexibility because it makes it possible to start from spherical seeds of different crystallinity, size or capped with different ligands. It is based on the use of oleylamine to solubilize and reduce the metallic precursor for the shell under annealing for a controlled time at the surface of the core, itself synthesized by different synthesis pathways in an organic medium.

Bimetallic Au@Ag core-shell nanoparticles have received extensive interest for many years due to the possibility of tuning their properties through the size of the core, the thickness of the shell and the structural coupling between the core and the shell. In this way, it becomes possible to modify and control the plasmon resonances for SERS application, catalysis, and chemical sensing<sup>1-7</sup>. The synthesis of alloys or core-shells is facilitated for gold and silver by their similar crystal structure (*fcc*) and lattice constants ( $a = 0.408$  nm for Au and 0.409 nm for Ag)<sup>4</sup>. The fabrication of Au@Ag core-shell structures results in most cases from the reduction of gold to form a core followed by the reduction of silver ions to coat it<sup>2,8-14</sup>. Due to the close match of the lattice constants an epitaxial growth of Ag on the Au seeds is expected<sup>15</sup>. However, the morphology of the gold seeds can evolve after the deposition of the silver shell depending on experimental conditions such as the type of Au seeds (size, shape, crystalline structure and coating agent)<sup>3,11,12</sup>, the precursor of silver ions, the reductant, the capping agent present in the reaction solution<sup>2,3,12</sup>, the solvent and the temperature<sup>10</sup>. A wide variety of synthesis protocols were thus developed in recent years that play on these multiple parameters. Different morphologies of Au@Ag NPs were obtained including sphere, cube, nanorod, octahedron, decahedron or cornlike shapes<sup>3,5,6,10,11,16</sup>

In this chapter, we were first interested in the synthesis of spherical Au@Ag NPs with a fine control of core size and crystallinity and also of shell thickness. Au NPs characterized by distinct surface chemistry (including dodecanethiol or oleylamine as capping agent), different



sizes (~5 and ~10 nm) and crystallinities (polycrystalline or single crystalline), were chosen as seeds to demonstrate the versatility of our synthetic route in two steps. We then studied the influence of the temperature, annealing time, [shell precursor] / [seed] concentration ratio, seed size and crystallinity on the shell growth.

Then, we replaced the silver layer by platinum or palladium which are well known for their strong catalytic activity. This combination – when efficiently tuned – can lead to plasmonic-driven enhancement of NPs catalytic activities<sup>17–19</sup>. It is known that various applications of Au–Pd(or Pt) catalysts and the significance of preparing shape-controlled Au–Pd (or Pt) NPs, followed by an overview of synthetic strategies for structural effect of Au–Pd (or Pt) bimetallic catalysts: a core–shell structure different from an alloy structure<sup>19</sup>. Finally, the Au core was exchange by silver, which exhibits intrinsically stronger plasmonic performance than gold. The overgrowth of Pd and Pt shells on Ag or Au core was studied in function of the nature of the core and [shell precursor] / [seed] concentration ratio.

SEM, STEM-HAADF, HR-TEM, EELS, UV-Visible and low-frequency Raman spectroscopies are used to characterize the crystallinity, chemical composition of the NPs and their organization. The last two spectroscopic techniques mentioned above allow to probe the large uniformity of the samples in terms of structure, chemical composition, and size.

## **2. Synthesis of Au@Ag core-shell NPs**

Within the framework of this thesis work, the synthesis of Au@Ag core-shell NPs is done in two main steps (Figure 2.1).

- **1st step: Synthesis of Au NPs of 5 and 10 nm in diameter** is done via organometallic route or direct reduction in oleylamine, respectively. (see section 2.1 and Figure 2.3).
- Intermediate step: **Nanocrystallinity selection** is performed for 5 nm Au NPs, through a process based on the preferential self-assembly of Au single crystals (SC). Either SC or polycrystals (PC) Au NPs can then be obtained. (see section 2.2 and Figure 2.4)
- **2nd step: Ag shell growth** on Au seeds is performed from the reduction of silver nitrate by oleylamine at a controlled temperature. (see section 2.3 and Figure 2.5)

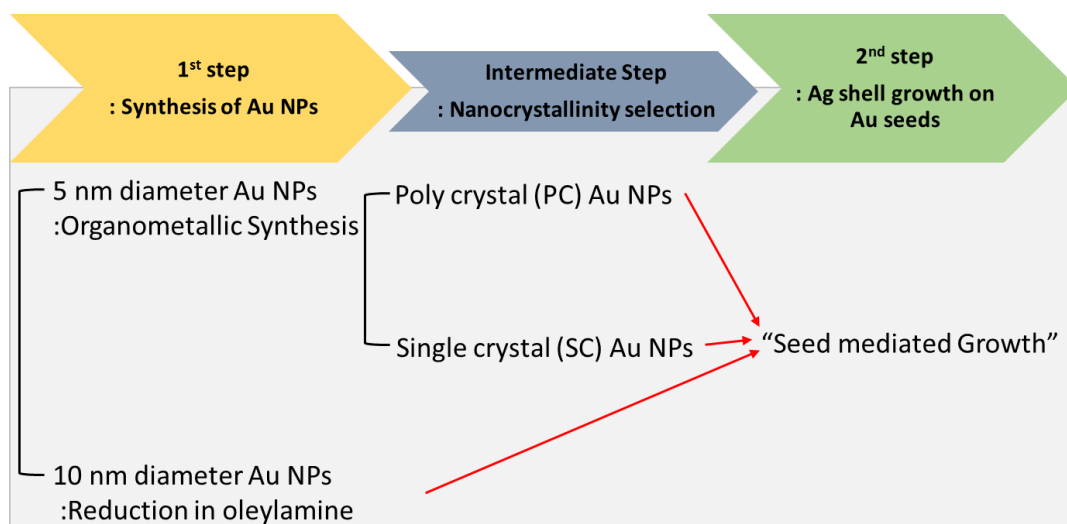


Figure 2.1. Outline of overall synthesis pathways to synthesize Au@Ag core-shell NPs. In seed mediated growth method, it consists of two main steps i) Au core NPs synthesis and ii) Ag shell growth on Au core NPs. Here, as an intermediate step, the crystallinity of Au NPs can be selected before Ag shell growth.

### 2.1. First step: Synthesis of Au NPs

**5 nm Au NPs** are synthesized through a revisited method from the Stucky group<sup>20,21</sup>. Briefly, 0.25 mmol of gold(I) chlorotriphenylphosphine (AuClPPh<sub>3</sub>) complex is dissolved in 25 mL of toluene with 500  $\mu$ L of 1-dodecanethiol. The gold precursor is reduced by adding a solution of tert-butylamine borane (TBAB) complex (2.5 mmol dissolved in 5 mL of toluene). The reaction takes place at 100°C under vigorous stirring for 5 min. The formation of Au NPs is evidenced by the color change of the solution from colorless to dark red. After the reaction, a washing step is necessary to remove all by-products. First, all the solvent is evaporated, and the same amount of ethanol is added, then the solution is centrifuged at 5000 rpm for 5 min. The precipitate is then dispersed in toluene or hexane. These NPs corresponding to a mixture of polycrystals (PC) (decahedra and icosahedra) and single crystals (SC)<sup>22</sup> were used for the selection in crystallinity and the obtaining of polycrystal (PC) or single crystal (SC) Au seeds.

**10nm Au(PC) NPs** are synthesized by using only two reagents: oleylamine and gold(III) chloride trihydrate. The ability of oleylamine to act as surfactant, solvent and reducing agent is well known<sup>23,24</sup>. The reduction process is carried out via the amine which can undergo induced oxidation by the metal ions to nitrile<sup>25,26</sup>. By dissolving 25 mmol of gold(III) chloride

trihydrate in 5 mL oleylamine at 30°C under magnetic stirring for 30 min, Au-oleylamine complex is formed. The complex formation was evidenced by IR spectroscopy (Figure 2.2 (a) and (b)), which showed that Au ions were bonded through N-H functional groups to oleylamine. The N-H stretching vibration can be detected at about 3340  $\text{cm}^{-1}$ , which is the characteristic peak of oleylamine. Two new peaks appear around 3290 and 3380  $\text{cm}^{-1}$  which may be due to the coordination of  $\text{Au}^{3+}$  with the amine group of oleylamine.<sup>27</sup> We observe also a blue shift on the N-H<sub>2</sub> scissoring band in the  $\text{Au}^{3+}$  oleylamine complexes (around 1610  $\text{cm}^{-1}$ ) compared to that in oleylamine (1588  $\text{cm}^{-1}$ )<sup>28</sup>.

Subsequently, the temperature was increased to 110°C (4°C  $\text{min}^{-1}$ ) and maintained there for 30 min. The solution was cooled to room temperature and the nanoparticles were precipitated by adding an excess of ethanol and centrifuging at 5000 rpm for 5 min to remove all the by-products. The supernatant was discarded and the precipitate was dispersed in toluene.

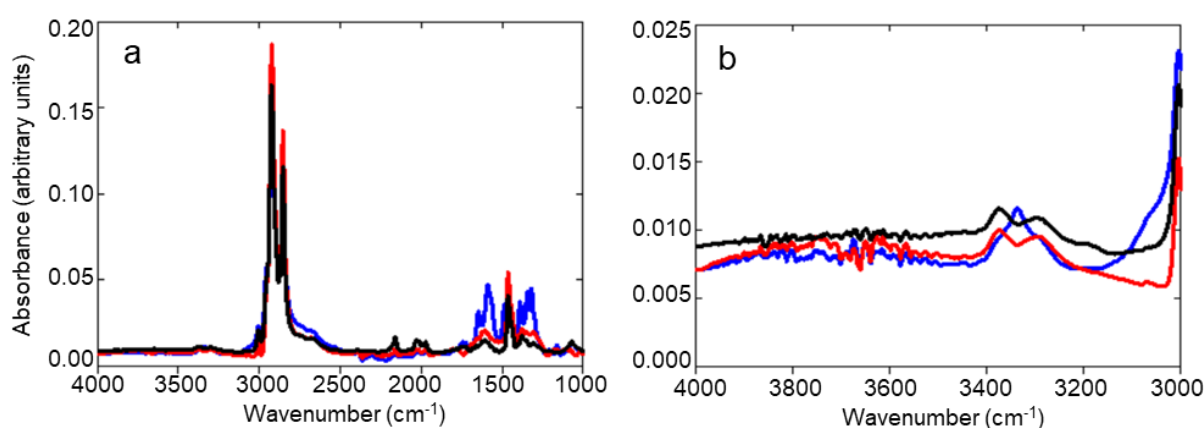


Figure 2.2. IR spectra of Oleylamine (blue curve),  $\text{Ag}^+$ -Oleylamine (red curve) and  $\text{Au}^{3+}$ -Oleylamine complexes (black curve) at frequency ranges (a) 4000-1000  $\text{cm}^{-1}$  and (b) 4000 - 3000  $\text{cm}^{-1}$ .

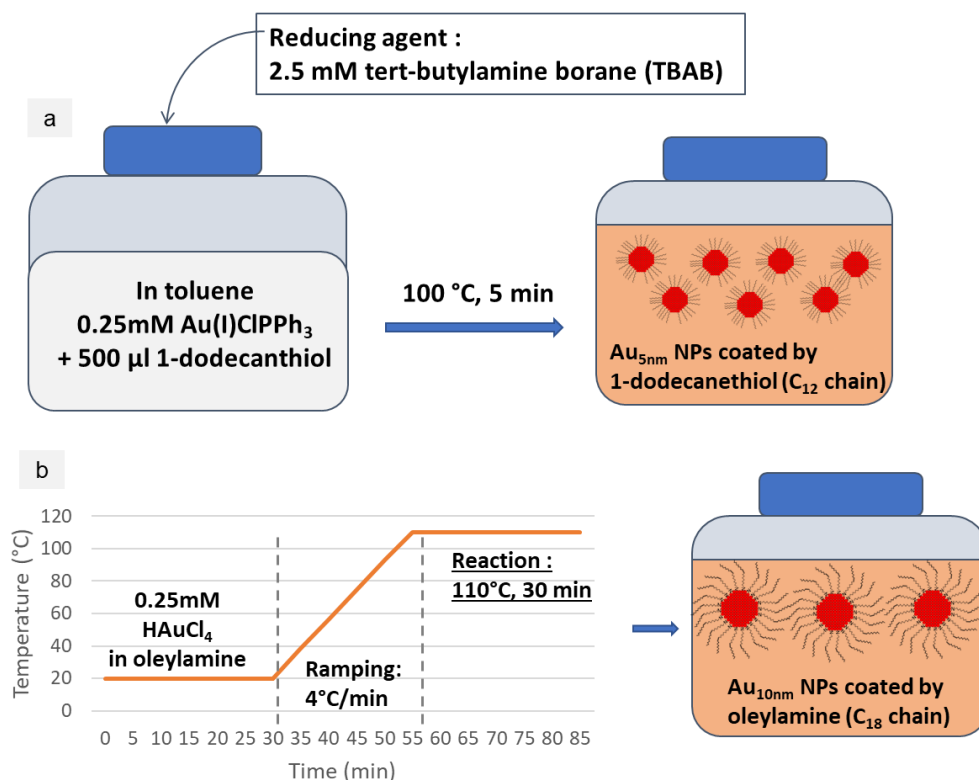


Figure 2.3. Description of Au NP core synthesis processes (a) via organometallic route to produce 5 nm diameter Au NPs, (b) via direct reduction of Au<sup>3+</sup> ion in oleylamine to produce 10 nm diameter Au NPs

## 2.2. Intermediate step: Nanocrystallinity selection

The crystallinity selection of 5nm Au NPs was carried out through a process based on the preferential self-assembly of gold single crystals (Figure 2.4). This process was followed from the protocol of H. Portalés *et al.*<sup>29</sup>. Nanocrystals of single-crystalline forms (cuboctahedra and truncated octahedra) have larger facet surfaces than polycrystals (icosahedra and decahedra). Knowing that the intensity of van der Waals interactions of flat surfaces is proportional to their areas; single crystals will preferentially associate with each other contrary to polycrystals by orienting themselves in such a way as to have their facets facing each other. In addition, the configuration and interaction of the molecules that dress the nanocrystals has to be considered. Indeed, it is well known that the molecules of 1-dodecanethiol form organized and compact layers on the gold surfaces. When these layers are on the surfaces of nanocrystals, their interactions allow the aggregation of the latter. However, the organized and compact arrangement of 1-dodecanethiol molecules can be very altered by the presence of crystal defects in the case of polycrystalline nanocrystals, which decreases their interactions.

The crystallinity segregation protocol is as follows: 20 ml of Au NPs colloidal solution in toluene is washed firstly with ethanol. Detailed washing protocol is that all solvent is evaporated by nitrogen flow, then 10 ml of ethanol are added and centrifuged for 4 minutes by 5000 rpm. All precipitates are re-dispersed in 20 ml of toluene. Washed Au NPs in toluene placed in a closed vessel to avoid solvent evaporation. After 8 days, a black precipitate corresponding to the single crystal (SC) NP superlattices was recovered after centrifugation and dispersed in isooctane. This solution was then used as Au(SC) seeds. The supernatant contains the Au(PC) seeds.

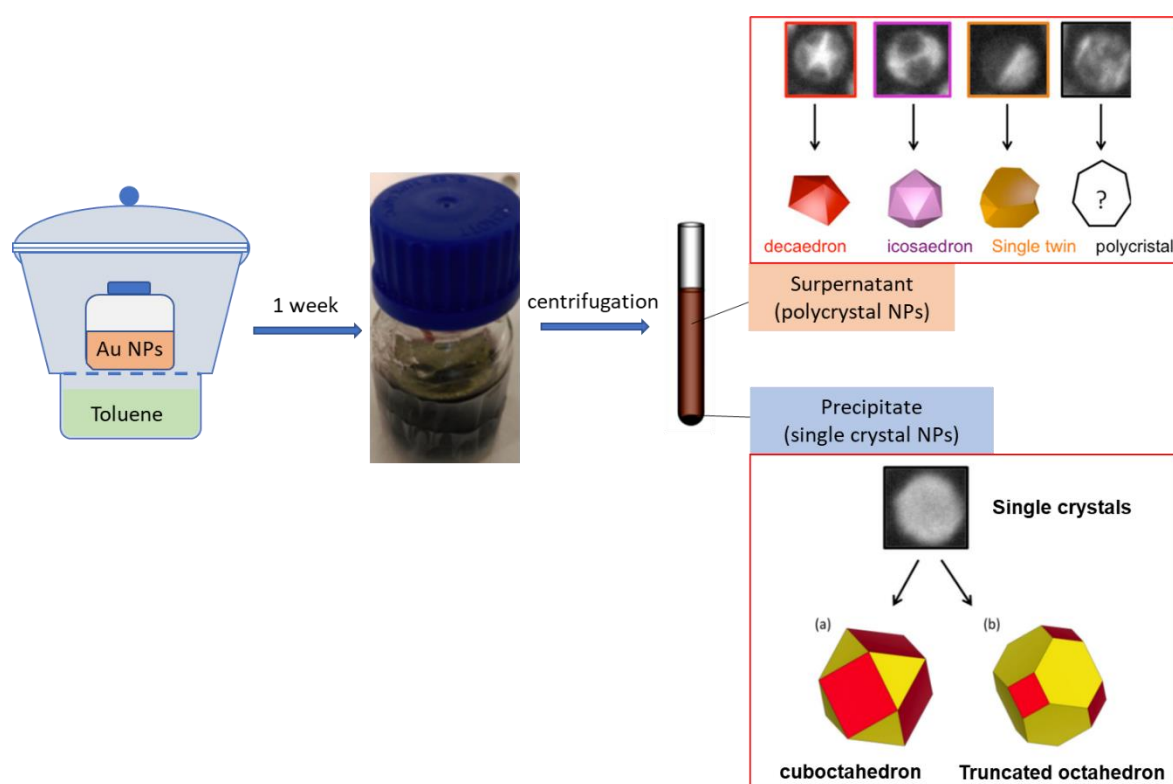


Figure 2.4. Schematic description of crystallinity segregation process. Separated single crystalline Au NPs consists of (a) cuboctahedron and (b) truncated octahedron with two color, red-(111) facets, yellow-(100) facets.<sup>30</sup> and polycrystalline Au NPs consist of a mixture of decahedron icosahedron or single twin.

### 2.3. Second step: Ag shell growth on Au seeds

Whatever their size or crystallinity (PC or SC), the Au NP seeds must be washed before the silver growth to remove the excess of ligands (oleylamine or dodecanethiols). After adding ethanol, the solution was centrifuged at 2000 rpm for 4 min and the resulting precipitates were dispersed in 2 mL of toluene or isooctane for Au(PC) or Au(SC) seeds respectively. Isooctane

replaced toluene for Au(SC) NPs to avoid their self-assembly into superlattices and thus their precipitation<sup>29,31,32</sup>. This step was repeated one more time. The growth of the silver shell was then induced in a solution of Ag-oleylamine complex. This solution is produced by a method adapted from Shen *et al*<sup>24</sup>. 0.055 mmol of AgNO<sub>3</sub> were dissolved in 5 mL pure oleylamine at 30°C and stirred during 30 min. After dissolution, the solution was used immediately. As in the case of Au-oleylamine, the complex formation was evidenced by IR spectroscopy shown in Figures 2.2 (a) and (b), which showed that Ag ions, like Au ions, in a gold oleylamine complex are bonded through an N-H functional group to oleylamine. The N-H stretching vibration can be detected at about 3340 cm<sup>-1</sup>, which is the characteristic peak of oleylamine. Two new peaks appear around 3290 and 3380 cm<sup>-1</sup> which may be due to the coordination of Ag<sup>+</sup> with the amine group of oleylamine.<sup>27</sup> We observe also a blue shift on the N-H<sub>2</sub> scissoring band in the Ag<sup>+</sup> oleylamine complexes (around 1610 cm<sup>-1</sup>) compared to that in oleylamine (1588 cm<sup>-1</sup>).<sup>28</sup>

Then 100 μL of Au seed suspension was mixed with 150 μL Ag-oleylamine complex solution and the volume was completed to 2 mL with toluene or isooctane. The final concentration C<sub>Ag<sup>+</sup></sub> of silver precursors is equal to 0.825 mmol L<sup>-1</sup> but could also be changed and multiplied thus by 2 or 4 for a fixed concentration of Au seed (C<sub>seed</sub>= 1.4 μmol L<sup>-1</sup>). Furthermore, the final concentration of Au seeds can be also tuned from C<sub>seed</sub> to C<sub>seed</sub>/2 or C<sub>seed</sub>/4. The silver shell overgrowth takes place under annealing at 90°C during 5 hours for dodecanethiol functionalized AuNPs and 2 hours for oleylamine functionalized AuNPs. A slight lower temperature of 80°C was also used for 5nm dodecanethiol functionalized single crystalline AuNPs. The NPs are finally washed with 1 mL of acetone and dispersed in chloroform.

This method can be adapted for different metallic seeds and shells which will be handled in section 5. The change of materials used on shell overgrowth can be also same materials as seed to obtain a bigger size of monometallic NPs.

The core-shell Au@Ag NPs are schematically presented in figure 2.6 and are characterized by a diameter of core NPs as  $D_{CORE}$ , a total diameter as  $D_{CS}$  and a shell thickness expressed as  $e = (D_{CS}-D_{CORE})/2$ .

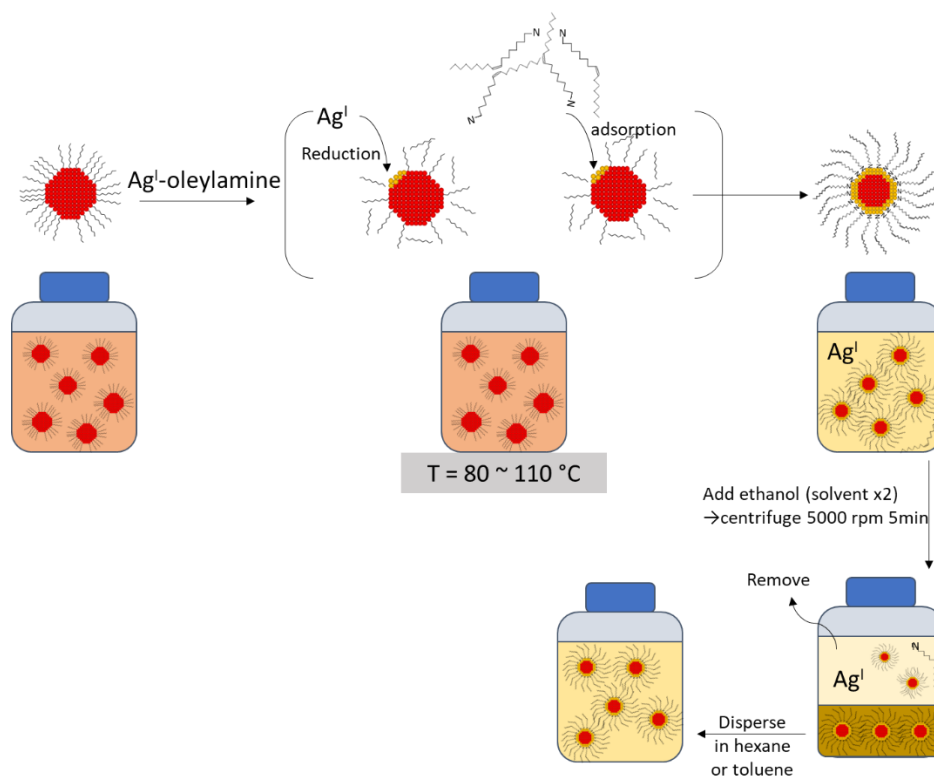


Figure 2.5. Schematic description to synthesize Au@Ag core-shell NPs via seed mediated growth (Reaction condition can be varied from this to obtain different final size.)

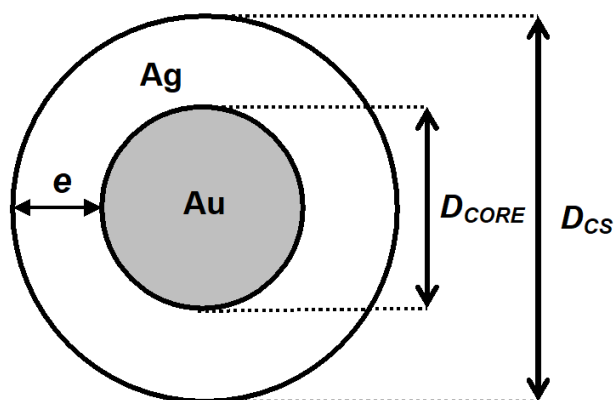


Figure 2.6. Schematic diagram of a core-shell Au@Ag nanoparticle made of a Au core with a diameter  $D_{CORE}$ , a total diameter  $D_{CS}$  and a Ag shell thickness  $e = (D_{CS} - D_{CORE})/2$ .

### 3. Control of Au@Ag nanoparticle size, composition and crystallinity.

#### 3.1. Effect of Au(PC) seed initial size, concentration and nature of the ligands

Figures. 2.7 (a) and (b) shows typical TEM images of Au(PC) NPs with diameters around 5 and 10 nm and functionalized by dodecanethiols or oleylamine respectively. They are characterized by a narrow size distribution (both <8%) (figures. 2.7 (a), (b), (e) and (f)) and an average diameter  $D_{\text{core}}$  of  $5.3 \pm 0.4$  or  $10.6 \pm 0.8$  nm depending on the synthesis process used (Tables 2.1 and 2.2). They have a rather spherical shape and are polycrystalline as seen in the dark-field TEM images (figures 2.7 (c) and (d)) in which a significant proportion of NPs exhibiting inhomogeneous contrast are present. The different seeds are referred to as Au<sub>5nm</sub>(PC)-C<sub>12</sub> and Au<sub>10nm</sub>(PC)-C<sub>18</sub>.

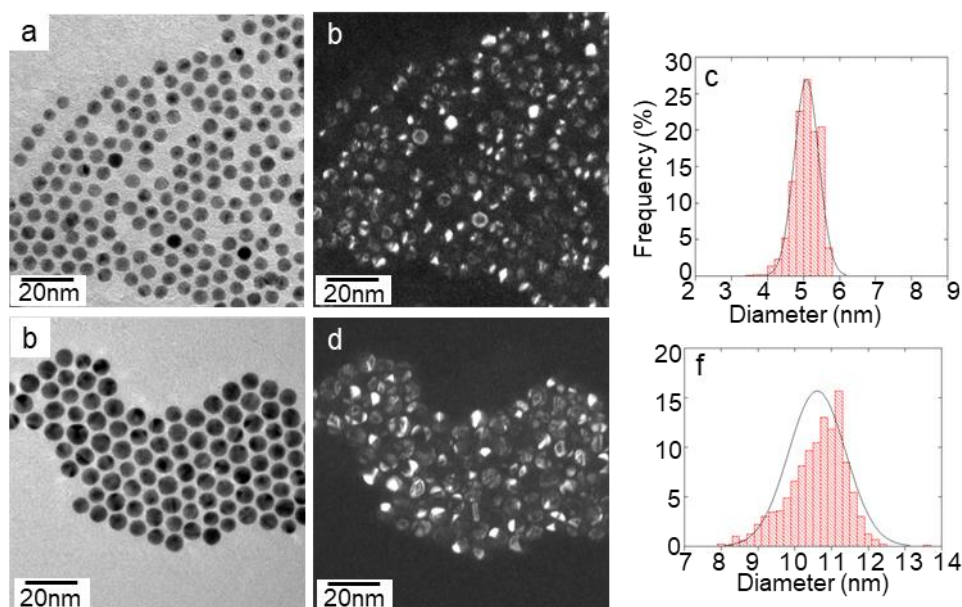


Figure 2.7. Representative TEM images (a) Au<sub>5nm</sub>(PC)-C<sub>12</sub>, (b) Au<sub>10nm</sub>(PC)-C<sub>18</sub> seeds and (c) the corresponding dark field TEM images and (e, f) the corresponding size histograms.

The silver shell overgrowth on gold cores was induced by mixing the colloidal solution with a solution of Ag-oleylamine complex under annealing at 90°C during 2 or 5 hours depending on the core size (for more details see section 2.3). The silver growth on the Au seeds takes place via a surface catalyzed reaction of Ag<sup>+</sup> by oleylamine at 90°C<sup>33</sup>. A much higher



temperature is indeed required to reduce silver nitrate directly in oleylamine and to form nanoparticles<sup>34</sup>. At 90°C, any nucleation of new silver NPs can thus be avoided.

**Au<sub>5nm</sub>(PC)@Ag NPs** obtained from three different Au seed concentrations ( $C_{seed}$ ,  $C_{seed}/2$  and  $C_{seed}/4$ ) and an annealing time fixed of 5 hours were observed by TEM (Figures 2.8 (a)-(c)). As the gold seed concentration decreases, the overall size of Au<sub>5nm</sub>(PC)@Ag NP increases from  $6.3 \pm 0.5$  to  $6.6 \pm 0.5$  and  $7 \pm 0.6$  nm in diameter and the obtained polydispersity remains low (around 8%) (figures. 2.8 (d)-(f)) with a Gaussian profile characteristic of a homogeneous growth of silver at the surface of the seeds. The values of the shell thickness  $e$  were estimated assuming that the average size of gold cores was  $D_{core} = 5.3 \pm 0.4$  nm and the deposited silver layer was uniform (Table 2.1).

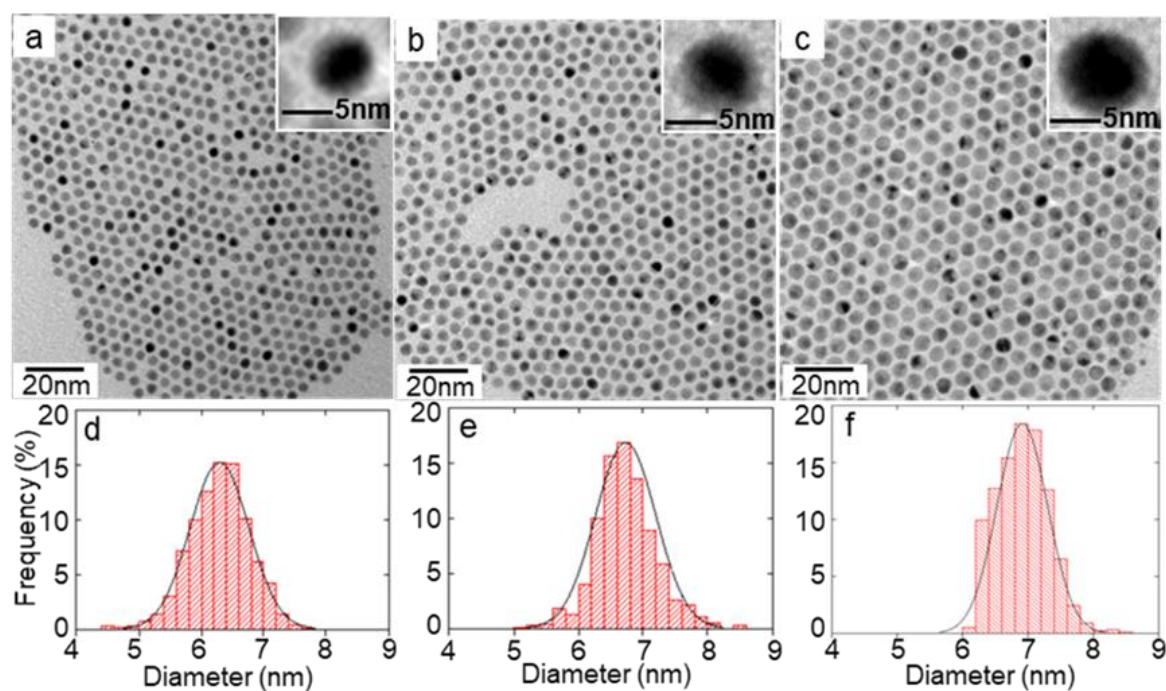


Figure 2.8. Representative TEM images of Au<sub>5nm</sub>(PC)@Ag NPs obtained from different seed concentrations (a)  $C_{seed}$ , (b)  $C_{seed}/2$  and (c)  $C_{seed}/4$  where  $C_{seed} = 1.4 \mu\text{mol L}^{-1}$  and (d, e, f) the corresponding histogram. In inset: TEM images at higher magnification.

Table 2.1. Experimental conditions used for the preparation of  $Au_{5nm}(PC)@Ag$  NPs, where  $R$  is the  $[Ag \text{ precursor}] / [Au \text{ seed}]$  concentration ratio.

Samples	[Au seed ] ( $\mu\text{mol L}^{-1}$ )	[Ag <sup>+</sup> ] ( $\text{mmol L}^{-1}$ )	$e$ (nm)	R
1	1.4	0.825	0.5	6
2	0.7	0.825	0.65	12
3	0.35	0.825	0.85	24
4	1.4	1.65	0.45	12
5	1.4	3.3	0.8	24

Furthermore, the TEM images (insets in figures. 2.8 (a)-(c)) confirm the formation of  $Au_{5nm}(PC)@Ag$  core-shell NPs, as most of the particles have a dark central part and a bright outer part, in agreement with a gold core and a silver shell since gold atoms scatter electrons more strongly than silver. However, strong diffraction contrast affects the visibility of the shell, which is somewhat variable as a function of particle crystallinity and orientation<sup>35</sup>. The two elements Au and Ag have the same lattice structure (*fcc*), similar lattice parameters (lattice mismatch less than 0,1%) and very close electronegativities (2.5 and 1.9 for Au and Ag respectively)<sup>4</sup>. These metals thus satisfy the Hume-Rothery's rules and are therefore highly miscible<sup>36</sup>. Core-shell Au@Ag nanoparticles are often obtained by depositing silver on Au seeds. Their conversion to homogeneous alloys is then possible by heating at high temperatures (250-1000°C)<sup>37,38</sup>. Our synthesis process in two steps and at low temperature (90°C) is thus favorable to the formation of core-shell NPs in agreement with the obtained results. Further morphology observations were performed by HAADF-STEM. The HAADF approach can detect the variation in chemical composition of the multi-component sample with an atom-level resolution due to the contrast difference between different elements (Z-contrast imaging). As the atomic number difference between Ag(47) and Au(79) is rather high, Z-contrast imaging can distinguish the Au and Ag within the nanoparticles<sup>10</sup>. Figures 2.9(a) present a typical HAADF-STEM images of quasi-spherical core-shell  $Au_{5nm}(PC)@Ag$  (sample 1 in table 2.1) with Au core and Ag shell in a bright and dark contrast respectively. This can be further verified by corresponding EELS maps (figure 2.9 (b)). A silver thickness  $e = 0.6$  nm is estimated in agreement with the value deduced from TEM images ( $e = 0.5$  nm see Table 2.1). Nevertheless, this latter value is less precise, due to a sampling difference. In fact, a minimum of 500 particles were measured by TEM compared to about ten particles by STEM-HAADF. More generally,

we observe polycrystalline NPs including multiply-twinned particles (MTP) with tetrahedral sub-units corresponding to an icosahedron (see arrow on figure 2.9 (a)). Furthermore, it is important to note that because of their low size distribution, the Au<sub>5nm</sub>(PC)@Ag NPs self-organize into a 2D hexagonal network<sup>39</sup>.

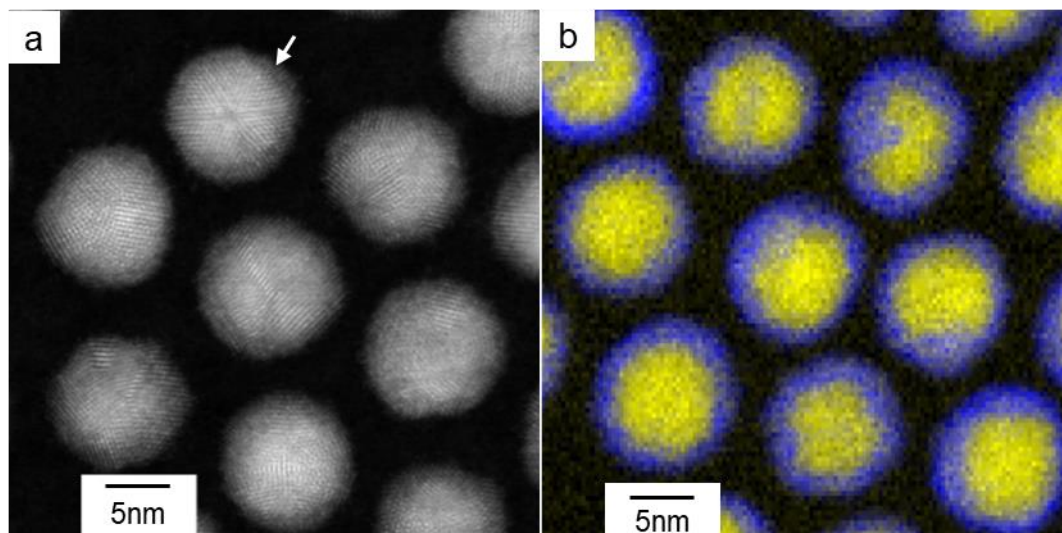


Figure 2.9. Electron microscopy characterization of Au@Ag core-shell NPs (a) Typical HAADF-STEM dark field image of Au<sub>5nm</sub>(PC)@Ag NPs obtained for  $C_{seed}=1.4 \mu\text{mol L}^{-1}$ , white arrow pointed an icosahedral NP (b) corresponding EELS map showing the Au core (yellow) and the silver shell (blue).

By using Au<sub>10nm</sub>(PC)-C<sub>18</sub> NPs as seeds, the silver shell overgrowth takes place during annealing at 90°C of only 2 hours. The TEM images confirm the formation of core-shell Au<sub>10nm</sub>(PC)@Ag NPs with a total diameter  $D_{CS} = 12.2 \pm 1.0$ ,  $14 \pm 1.0$  or  $14.8 \pm 1.2$  nm obtained for three seed concentrations  $C_{seed}$ ,  $C_{seed}/2$  and  $C_{seed}/4$  respectively, with a clear difference of contrast between the core and the shell (Figures 2. 10 (a)-(c) and insets, Table 2.2). The corresponding size histograms show narrow size distributions, around 8% (figures. 2.10 (d)-(f)).

Furthermore, the thicknesses  $e$  of the silver layers for similar gold seed concentrations are greater than those obtained previously for smaller size seeds and identical [Ag precursor] / [Au seed] concentration ratios (see Tables 2.1 and 2.2).

Table 2.2. Experimental conditions used for the preparation of Au<sub>10nm</sub>(PC)@Ag NPs, where R is the [Ag precursor] / [Au seed] concentration ratio.

Samples	[Au seed ] ( $\mu\text{mol L}^{-1}$ )	[Ag <sup>+</sup> ] ( $\text{mmol L}^{-1}$ )	e (nm)	R
6	1.4	0.825	0.8	6
7	0.7	0.825	1.7	12
8	0.35	0.825	2.1	24

The silver growth process is thus faster and more efficient on Au<sub>10nm</sub>-C<sub>18</sub> compare to Au<sub>5nm</sub>-C<sub>12</sub>. Larger nanoparticle sizes offer indeed a larger surface area accessible to silver ions, which promotes the growth of the silver layer and gives a greater silver thickness than on smaller nanoparticle sizes. In addition, silver is deposited on Au area in presence of capping agent. The silver growth process thus requires a desorption of the capping layer, deposition of Ag on the exposed Au surface and subsequent re-encapsulation of the Au surface by the capping agents<sup>40</sup>. Oleylamine as a capping agent is more weakly binds to the gold surface and is very labile<sup>25,41</sup>, thereby promoting the growth of silver on the gold surface.

A typical HRTEM image of Au<sub>10nm</sub>(PC)@Ag NPs with overall size  $12.2 \pm 1.0$  nm after the silver shell growth is shown in figure 2.11. The icosahedral particle with rather rounded edges shows a dark central part and a bright outer part in agreement with a gold core and a silver shell. Moreover, the HRTEM image suggests an epitaxial growth relationship between the icosahedral Au core and Ag shell as the growth of the shell perfectly follows the morphology of the underlying gold core.

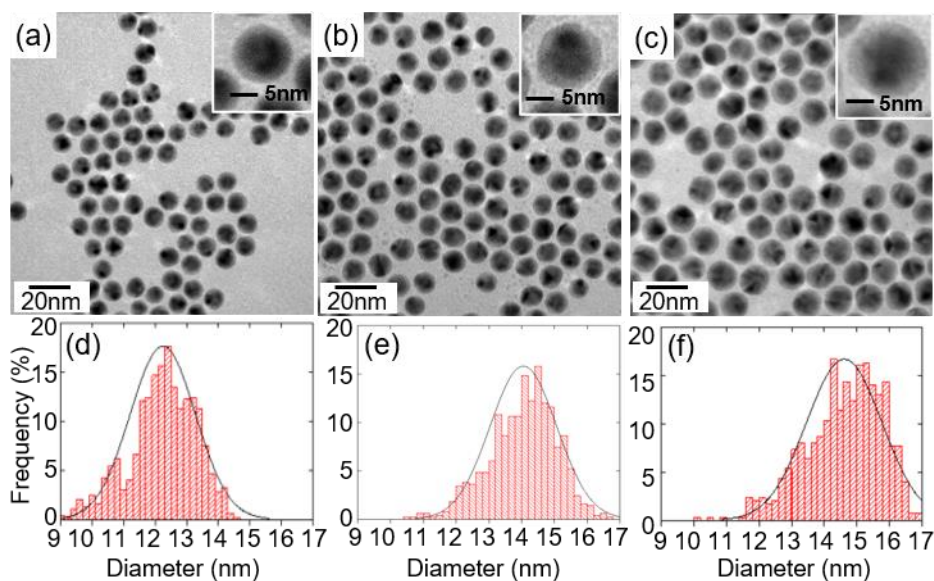


Figure 2.10. Representative TEM Images of  $Au_{10nm}(PC)@Ag$  core-shell NPs from different seed concentrations (a)  $C_{seed}$ , (b)  $C_{seed}/2$ , (c)  $C_{seed}/4$  where  $C = 1.4 \mu\text{mol L}^{-1}$  and (d, e, f) the corresponding size histograms. In inset: representative TEM images at higher magnification.

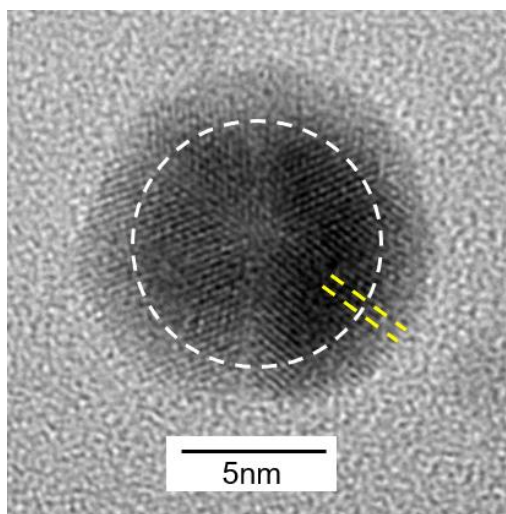


Figure 2.11. Typical HRTEM image of  $Au_{10nm}(PC)@Ag$  NPs obtained for  $C_{seed} = 1.4 \mu\text{mol.L}^{-1}$ . The white circle delineates the gold core of the silver layer and the yellow dotted lines show the epitaxial relationship between the heart and the shell.

### 3.2. Effect of Au seed crystallinity

Figure 2.12 (a) is a typical TEM image of SC  $Au_{5nm}$  NPs nm obtained after crystallinity selection (see experimental section). Most of the NPs shown exhibit indeed a homogeneous contrast which clearly indicates their single-crystalline structure. The corresponding high

resolution TEM image and Fourier transform of the image (figure 2.12 (b) and inset) show that these NPs are single crystal cuboctahedrons (or truncated octahedrons).

The silver shell overgrowth was induced as previously in a solution of Ag-oleylamine complex under annealing temperature at 90°C and with concentrations in Ag<sup>+</sup> ions and Au seed of C<sub>Ag<sup>+</sup></sub>=0.825 mmol L<sup>-1</sup> and C<sub>seed</sub>=1.4 μmol L<sup>-1</sup> respectively and R=[Ag precursor] / [Au seed] = 6. The size of the NPs is slightly increased, and the deduced average Ag thickness of 0.2 nm is around half that obtained on PC Au seeds in similar conditions (see figures 2.13 (a) and (b)).

**The silver shell appears thus to grow faster on PC Au seeds.** This is consistent with the fact that PC NPs present more corners and edges which are sub-coordinated atomic sites of higher energy and hence more active for the heterogeneous nucleation of Ag at the Au surface. When the Ag-oleylamine complex concentration is doubled (C<sub>Ag<sup>+</sup></sub>=1.65 mmol L<sup>-1</sup>, R=12), the SC nanoparticles flocculate after a reaction time of 1 hour due to a significant increase in their sizes and thus in van der Waals attractions but also due to a tendency to assemble originating from the atomic alignment between their facets<sup>29</sup>. A slight decrease of the heating temperature to 80°C (keeping C<sub>Ag<sup>+</sup></sub>=1.65 mmol L<sup>-1</sup>, R=12) was observed to slow down the growth of silver on the gold surface leading to an average silver thickness around 4 times greater than previously (e=0.85 nm) (Figure 2.13 (c)). Furthermore, the TEM image in inset figure 2.13 (c) confirms the formation of core-shell Au@Ag NPs via the difference of contrast between the core and the shell. The core-shell structure is further verified by the EELS map (figure 2.13 (d)). An average silver thickness *e* around 1 nm is estimated and is closed to the value deduced from TEM images.

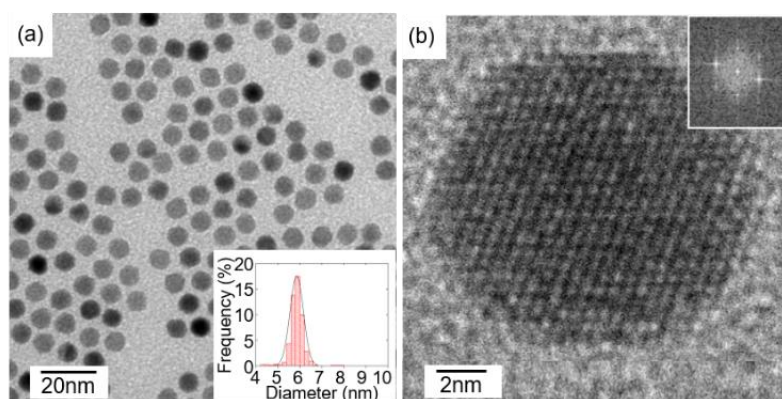


Figure 2.12. (a) TEM images of Au<sub>5nm</sub>(SC) seeds, (b) the corresponding HRTEM image and corresponding FFT image.

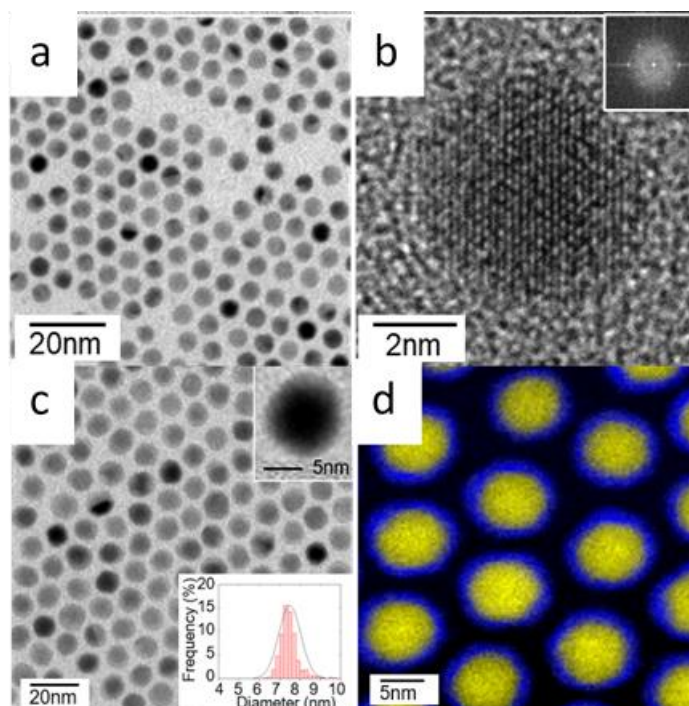


Figure 2.13. (a) typical TEM image of the corresponding  $Au_{5nm}(SC)@Ag$  NPs with a silver thickness  $e=0.2$  nm obtained for  $C_{Ag^+} = 0.825$  mmol  $L^{-1}$  and  $T=90^{\circ}C$  (b) HRTEM image of one corresponding single NP. (c) typical TEM image of  $Au_{5nm}(SC)@Ag$  core-shell NPs with a silver thickness  $e=0.85$  nm obtained for  $C_{Ag^+} = 1.65$  mmol  $L^{-1}$  and  $T=80^{\circ}C$  and (d) corresponding EELS map showing the Au core (yellow) and the silver shell (blue).

### 3.3. Effect of silver precursor initial concentration and reaction temperature

We have just seen that the seed concentration as well as the nature of the ligands coating the seeds had an influence on the final silver thickness in the core-shell structure. A low concentration of seeds and weakly bound ligands favored the growth of silver on the PC seed surface. In general, the overall core/shell particle size or shell thickness increases with increasing reactant concentration<sup>42,43</sup>. Subsequently, the effect of silver precursor concentration ( $C_{Ag^+}$ ) on silver overgrowth was investigated. The Au (PC) seeds used in this section were synthesized through chemical reduction of  $AuCl(PPh_3)$  complex by TBAB as described in section 2.1. The diameter of the Au PC seed is around 5nm (Figure 2.14 and table 2.3).

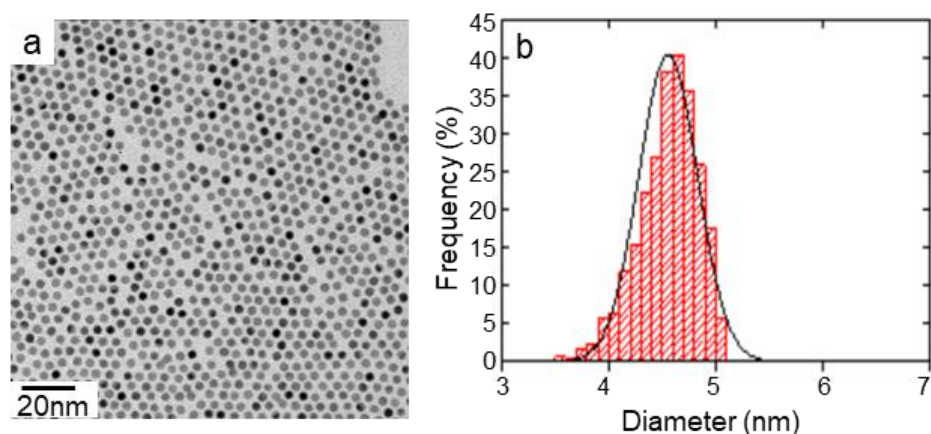


Figure 2.14. (a) Representative TEM images of  $Au_{5nm}$  NPs with an average diameter of  $4.6 \pm 0.3$  nm (b) the corresponding size histograms.

For the silver shell growth step, several concentrations of Ag-oleylamine complex were used:  $C_{Ag^+}=0.825$  mmol  $L^{-1}$ ,  $2C_{Ag^+}$  and  $4C_{Ag^+}$  for a fixed reaction temperature of  $90^\circ C$ . As Ag-oleylamine complex concentration was increased, the  $Au_{4.6nm}@Ag$  NP total diameter  $D_{CS}$  increases from 5.3 to 6.2 nm and keep the polydispersity as Au seed (Figure 2.15 a, b and c and Table 2.3). By multiplying the silver precursor concentration by 2, the silver shell thickness slightly increases, it is only by multiplying by 4 this concentration that we see a real thickness increase from 0.4 to 0.8 nm (Table 2.3 and Figure 2.17).

A second parameter that can influence the final composition of the core-shell NPs is the reaction temperature. Silver shell is grown on coated Au seeds via the reduction of  $[Ag(OLA)_n]^+$ . This process thus implies the desorption of the capping layer in order to allow the deposition of Ag on the Au surface then the re-encapsulation of the Au surface by the capping agent which can be dodecanethiol (initially present on the Au seeds) and/or oleylamine (present in the solution of  $Ag^+$ ). An increase of the reaction temperature can thermally activate the reduction of  $[Ag(OLA)_n]^+$  and also the desorption of the capping layer, that should favor the increase of the silver thickness shell<sup>44</sup>.



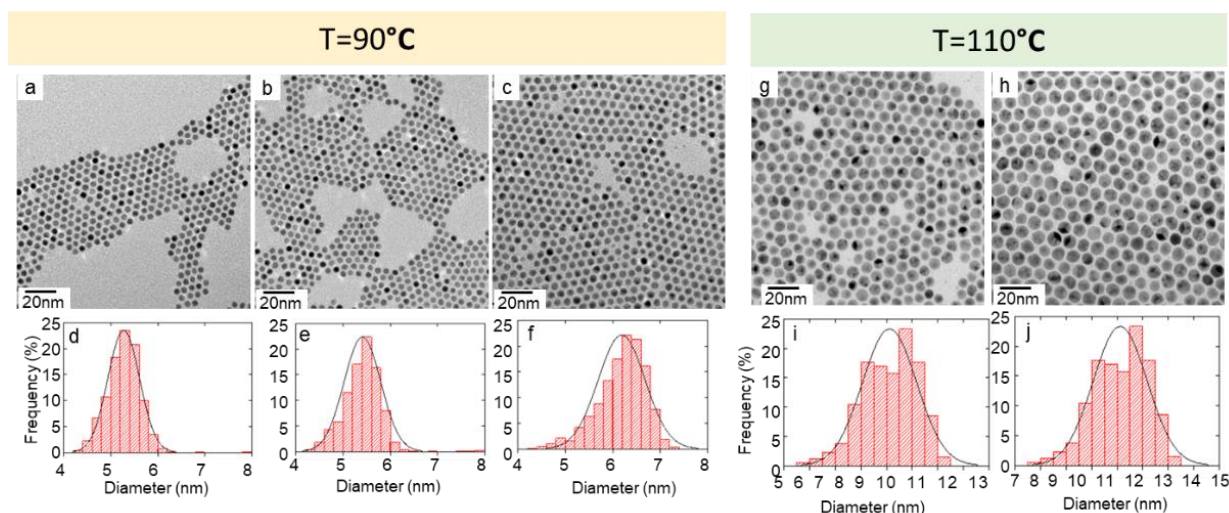


Figure 2.15. Representative TEM images of  $Au_{5nm}@Ag$  NPs obtained from two reaction temperatures  $T$  and different silver precursor concentration  $C_{Ag^+}$  ( $C_{Ag^+} = 0.825 \text{ mmol L}^{-1}$ ): (a) (b) and (c) for  $T=90^\circ\text{C}$ : and for  $C_{Ag^+}$ ,  $2C_{Ag^+}$  and  $4C_{Ag^+}$  respectively (d, e, f) the corresponding size histograms ; (g) and (h) for  $T=110^\circ\text{C}$  and for  $C_{Ag^+}$ , and  $2C_{Ag^+}$  respectively (i, j) the corresponding size histograms .

Table 2.3. Details of the diameter  $D_{core}$  of the Au seeds and of the total diameter  $D_{SC}$  of the corresponding  $Au@Ag$  core-shell NPs obtained from the different synthesis protocols (section 2.1). The concentration of Ag-oleylamine complex is varied from  $C_{Ag^+}=0.825 \text{ mmol L}^{-1}$ ,  $2C_{shell}$  and  $4C_{shell}$ . The reaction temperature is at  $90^\circ\text{C}$  and  $110^\circ\text{C}$  for the silver overgrowth. The initial seed concentration is fixed  $C_{seed} = 1.4 \mu\text{mol L}^{-1}$ .

		AgNO <sub>3</sub> concentration		
		$C_{Ag^+}$	$2C_{Ag^+}$	$4C_{Ag^+}$
Temperature ( $^\circ\text{C}$ )	$D_{core}$ (nm)	$D_{SC}$ (nm)	$D_{SC}$ (nm)	$D_{SC}$ (nm)
90	$4.6 \pm 0.3$	$5.4 \pm 0.4$	$5.5 \pm 0.5$	$6.2 \pm 0.6$
110		$9.1 \pm 1.1$	$11.1 \pm 1.2$	Precipitated

The reaction temperature was thus increased from 90 to  $110^\circ\text{C}$  for  $C_{Ag^+}$  and  $2C_{Ag^+}$  with reaction time maintains at 5 hours. The total diameter  $D_{SC}$  of the core-shell  $Au@Ag$  NPs was observed to increase drastically with the temperature and the silver precursor concentration (Figures 2.16 and 2.17). Furthermore, this temperature increase remains low enough to prevent the formation of separate silver NPs while increasing the thickness of the shell (Figure 2.16).

As previously observed, the increase in silver precursor concentration induces an increase of the silver thickness. Nevertheless, for a concentration of silver precursor multiplied by 4 ( $4C_{Ag^+}$ ) and a reaction temperature equal to  $110^\circ\text{C}$ , the formation of a bulk precipitate during the silver shell overgrowth was observed.

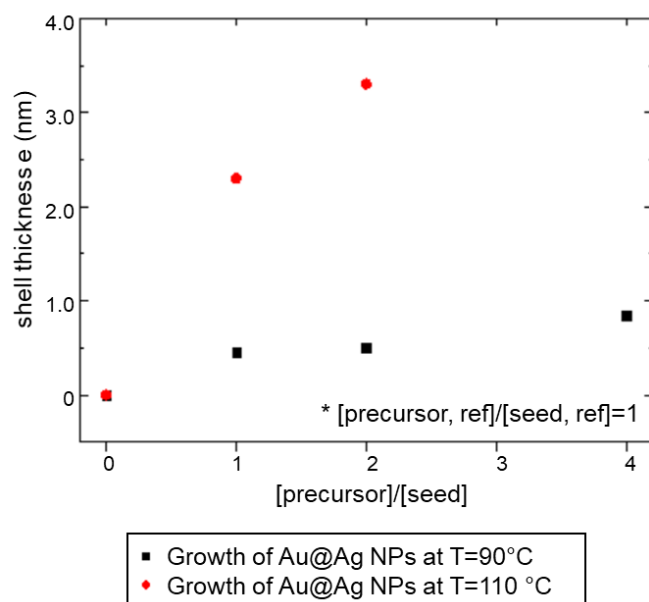


Figure 2.16. Temperature and silver precursor concentration effects on the final size of Au@Ag NPs.

Figure 2.17 reports the evolution of the final silver shell thickness in function of the initial silver precursor concentration or the initial Au seeds concentration but by maintaining the same [silver precursor] / [Au seed] concentration ratios. We observe a similar evolution of the silver shell thickness. This is in agreement with a general trend to observe an increase of the shell thickness with the reactant concentration <sup>45</sup>.

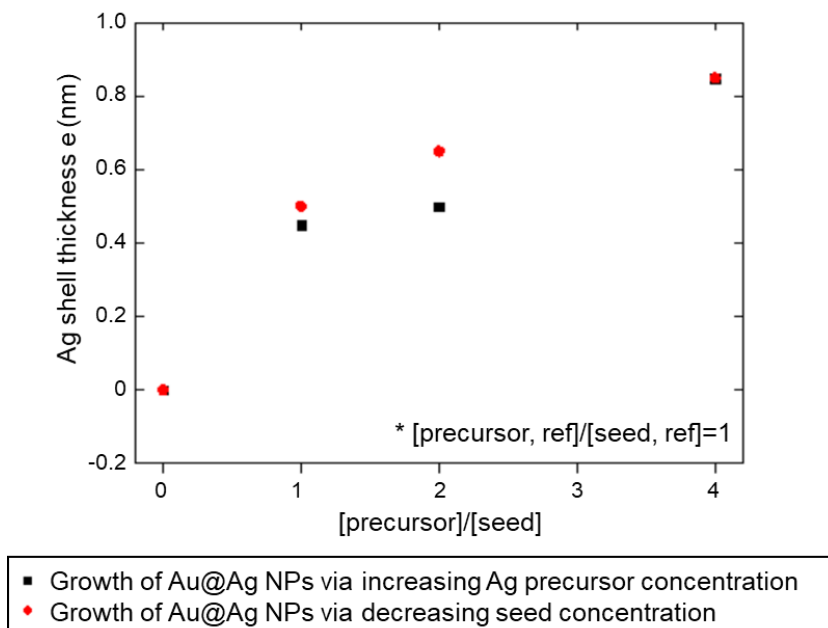


Figure 2.17. Comparison of silver precursor concentration and initial seed concentration effects on the final total diameter  $D_{SC}$  of Au@Ag NPs obtained for a reaction temperature of  $90^{\circ}\text{C}$ .

#### 4. Self-assembly of Au@Ag core-shell nanoparticles

We observed the 3D organization of NPs after drops deposition of colloidal solution on a silicon substrate and solvent evaporation (toluene in this case). Au NPs whatever their size ( $\sim 5$  or  $\sim 10$  nm), coating agent (dodecanethiol or oleylamine) or crystallinity (SC or PC) self-assembly in ordered well faceted 3D superlattices (SLs) as it is shown in the SEM images (see Figure 2.18(a), (d) and (g)). Similar SLs sizes are obtained whatever the NP size, capping agent, and crystallinity. Nevertheless, the SLs shapes are more well-defined with the appearance of triangular shaped SLs by increasing the NP sizes or considering single crystalline NPs. These well-defined shapes are characteristic of homogeneous growth in solution that could be favored by an increase in NP-NP interactions between larger NPs due to larger Van der Waals interactions or between SC NPs due to the presence of larger facets<sup>31,46</sup>. Furthermore, previous results showed that the nature of the interactions between NPs (attractive or repulsive) depend both on the nature of the capping agent and of the van der Waals attractions between the cores for a given solvent<sup>31,46</sup>. Although the interdigitation is partial for oleylamine molecules (unlike dodecanethiols) due to the C=C double bond<sup>47</sup>, a larger metal core size can still induce 3D organization into colloidal crystals. Ordered assemblies of gold NPs 16 to 21 nm in diameter

coated with oleylamine have indeed been reported in the literature<sup>25</sup> as well as 11 nm diameter  $\text{Fe}_x\text{O}/\text{CoFe}_2\text{O}_4$  NPs coated with oleic acids of molecular structure comparable to oleylamine<sup>48</sup>. After silver layer overgrowth, Au@Ag NPs form 3D SLs with similar sizes and shapes to those obtained from the Au<sub>5nm</sub> and Au<sub>10nm</sub> NPs, regardless of their overall size as shown in Figure 2.18. This is consistent with a uniform Ag overgrowth allowing to keep a narrow size and shape distribution of the core-shell NPs, which are well-known as key parameters for NP organization.

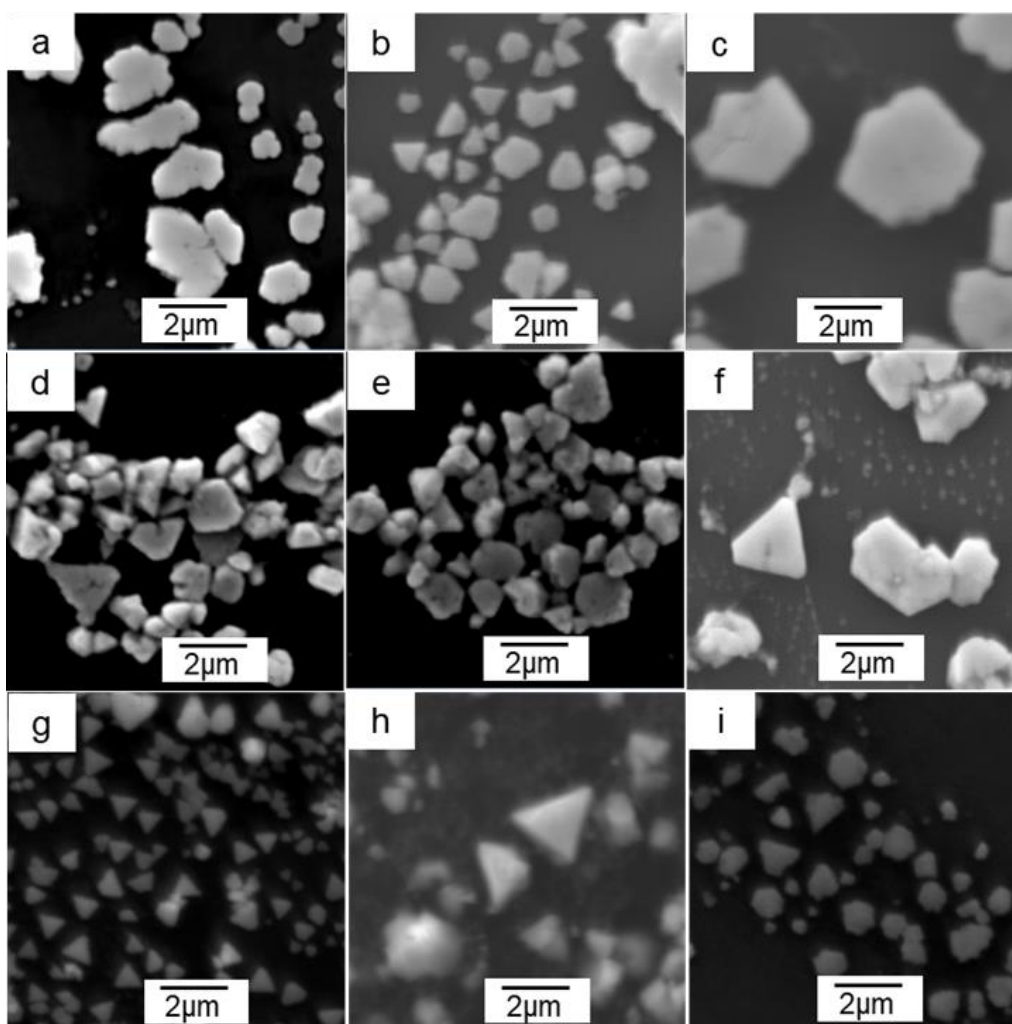


Figure 2.18. Typical SEM images of 3D superlattices made of (a) Au<sub>5nm</sub>(PC)-C<sub>12</sub> seeds and corresponding Au<sub>5nm</sub>(PC)@Ag NPs with (b)  $D_{CS} = 6.3$  nm and (c)  $D_{CS} = 6.6$  nm. (d) Au<sub>10nm</sub>(PC)-C<sub>18</sub> seeds and corresponding Au<sub>10nm</sub>(PC)@Ag NPs with (e)  $D_{CS} = 12.2$  nm and (f)  $D_{CS} = 14$  nm. (g) Au<sub>5nm</sub>(SC)-C<sub>12</sub> seeds and corresponding Au<sub>5nm</sub>(SC)@Ag NPs with (h)  $D_{CS} = 5.8$  nm and (i)  $D_{CS} = 7.5$  nm.

A HRSEM image and corresponding Fourier transform of a typical 3D superlattice made of  $\text{Au}_{10\text{nm}}(\text{PC})@\text{Ag}$  core-shell NPs with average overall size of 14 nm demonstrate that the nanoparticles are well ordered in a compact surface plane, which corresponds to the orientation  $[111]_{fcc}$  (Figure 2. 19 (a) and inset). At higher magnification, the HRSEM image (Figure 2. 19 (b)) clearly shows the stacking of NP monolayers organized in a hexagonal network.

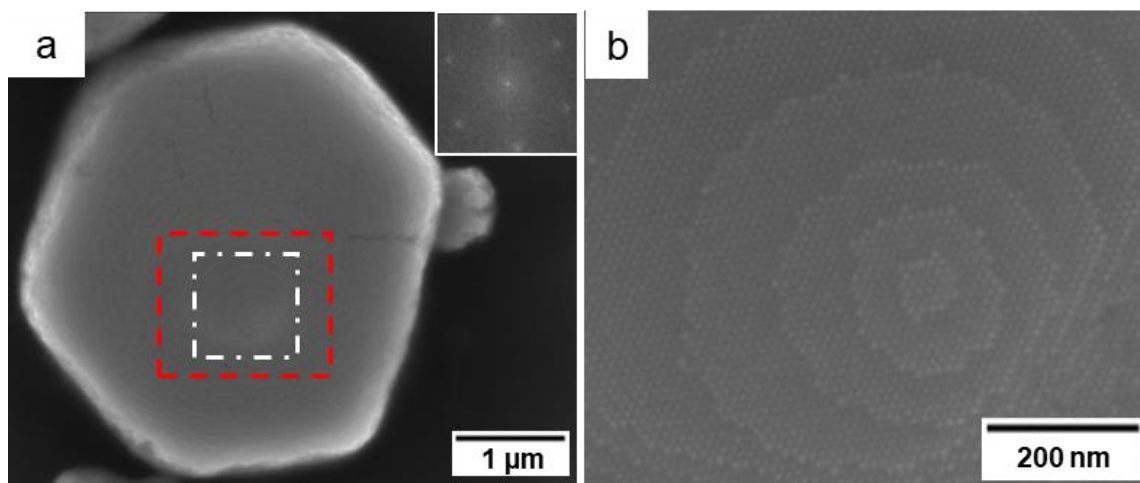


Figure 2.19. HRSEM image (a) of colloidal crystal made of core-shell  $\text{Au}_{10\text{nm}}(\text{PC})@\text{Ag}$  NPs with overall size of 14 nm after the shell growth. In inset the corresponding Fourier transform. (a) Magnified HRSEM image of the area delimited by red rectangle in (a).

All these samples were also analyzed by EDX in the SEM to determine the NP composition. When the measured error does not exceed one percent, we consider such NPs to be homogeneous in composition. EDX measurements confirm the homogeneous composition of the bimetallic nanoparticles everywhere on the substrate and agree with the atomic compositions calculated from the core-shell structures deduced from TEM images shown in table 2.4.

Table 2.4. Diameter  $D_{CS}$ , shell thickness  $e=(D_{CS}-D_{CORE})/2$  and atomic composition obtained through EDX measurements or calculations for  $Au_{5nm}(PC/SC)@Ag$  and  $Au_{10nm}(PC)@Ag$  core-shell NPs obtained from the different synthesis protocols.

Sample	$D_{CS}$ (nm)	$e$ (nm)	EDX composition		calculated composition	
			% Au	% Ag	% Au	% Ag
$Au_{5nm}(PC)@Ag$	6.3	0.50	64	36	61	39
	6.6	0.65	58	41	55	45
	7.0	0.85	26	73	40	60
$Au_{10nm}(PC)@Ag$	12.2	0.80	66	34	66	34
	14.0	1.70	40	60	43	57
$Au_{5nm}(SC)@Ag$	5.8	0.20	80	20	80	20
$Au_{5nm}(SC)@Ag$	7.5	0.85	50	50	54	46

## 5. Replacement of core and shell materials: towards new properties

The synthesis method of Au@Ag core-shell NPs that we developed in this Ph.D work is easily transposable to other bimetallic systems and yields core-shell NPs while keeping a narrow size dispersion and homogeneous shape. However, attention must be paid to the difference in redox potential ( $E$ ) between the material used for the core and for the shell in order to avoid galvanic replacements and the formation of alloys.  $E_{core}$  must be greater than  $E_{shell}$ . Temperature and reaction time can also be adapted. Our objectives were two synthesis bimetallic core-shell NPs combining different properties: a plasmonic core and a shell with strong catalytic activities. This combination – when efficiently tuned – can lead to plasmonic-driven enhancement of NPs catalytic activities. The idea is also to minimize synthesis costs for catalysis by using cheaper core materials than shell materials. Representative catalytic materials such as palladium (Pd) and platinum (Pt) were used for shell materials and gold or silver as core materials. Their application for catalysis is the subject of chapter III.

### 5.1. Replacement of shell material: synthesis of Au@Pd and Au@Pt core-shell nanoparticles

The Au<sub>10nm</sub> NPs coated by oleylamine and synthesized as reported in section 2.1 was used as seeds (Figure 2.7 (b)). Pd(acac)<sub>2</sub> and Pt(acac)<sub>2</sub> were used as metallic precursors. They were thus dispersed in 300 μl of OLA for a final concentration of 11 mM) and added to the Au NPs solution. The solution was then heated during 1 hours at 110°C or 140°C for Pd(acac)<sub>2</sub> or Pt(acac)<sub>2</sub> respectively (Figure 2.20). Once the mixture is cooled down to room temperature, 1 ml of ethanol is added to the solution, and then centrifuged at 5500 rpm during 5 min. The supernatant is removed, and the precipitate is dispersed in 1 ml of toluene.

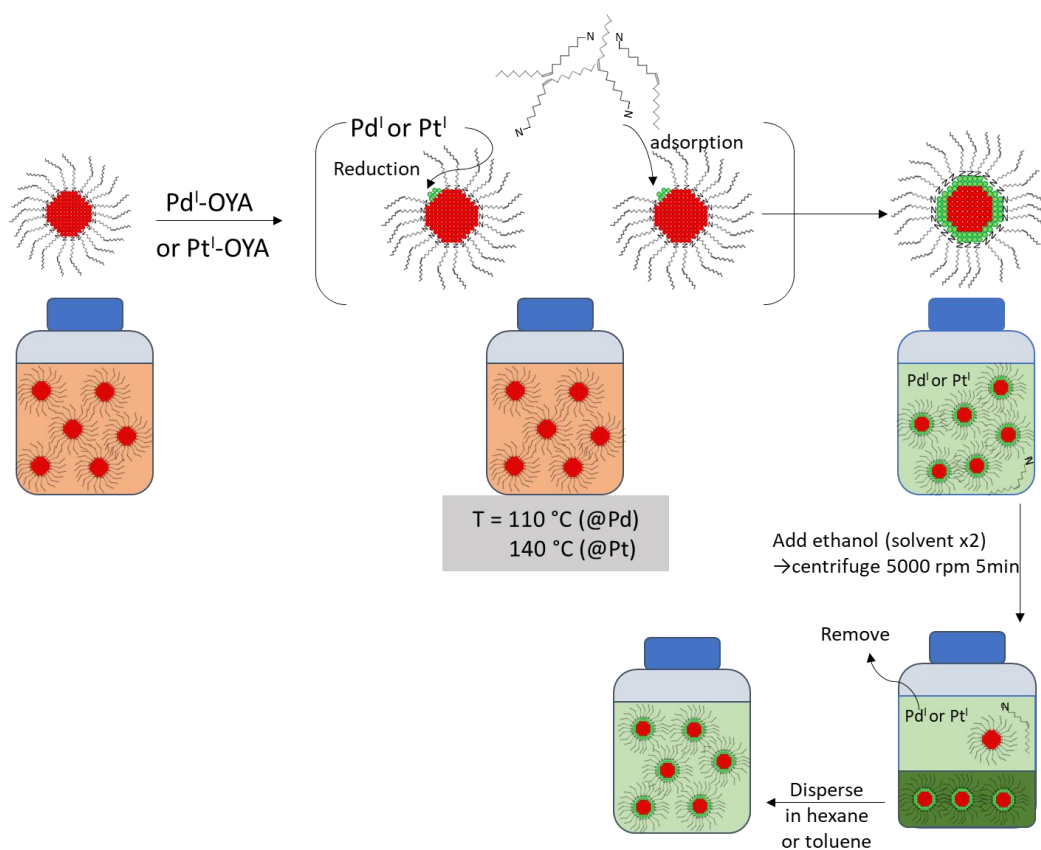


Figure 2.20. Schematic description to synthesize Au<sub>10nm</sub>@Pd or Au<sub>10nm</sub>@Pt core-shell NPs via seed mediated growth (Reaction condition can be varied from this to obtain different final size.)

In order to vary the thickness of the Pd or Pt shell, three Au seed concentration were used  $C_{seed}$ ,  $C_{seed}/2$ , and  $C_{seed}/4$  (with  $C_{seed}=1.4 \mu\text{mol L}^{-1}$ ), as described in table 2.5, the reference concentration for Pt or Pd precursors being  $C_{Pd^+}$  or  $C_{Pt^+}=0.825 \text{ mmol L}^{-1}$ . As a result, we could

obtain different sizes of core-shell NPs: Au<sub>10nm</sub>(PC)@Pd NPs with a total diameter  $D_{CS}$  from 11.4 to 12.5 or 13.7nm and Au<sub>10nm</sub>(PC)@Pt NPs with  $D_{CS}$  from 10.9 to 11.4 or 12.9 nm for different values of  $C_{seed}$  (Table 2.5). The average shell thicknesses  $e$  for palladium increases thus from 0.40 to 0.95 nm and for platinum layers from 0.25 to 0.55 nm by decreasing initial seed concentration.

The Au@Pd NPs present spherical shape with a narrow size distribution (Figure 2.21 (a)-(c)) whatever the initial seed concentration. While Au@Pt NPs present in majority spherical shapes with few dendritic shapes<sup>49</sup> (Figure 2.21 (d)-(f)). The amount of dendritic shapes is observed to increase with the increase of the concentration ratio [Pt precursor]/[seed]. The formation of such branched structures was already observed in oleylamine. Zhang et al<sup>50</sup> have reported indeed the synthesis of Pt branched NPs by reducing Pt(acac)<sub>2</sub> in oleylamine and modulating the growth kinetic through reaction temperature and time control.

Table 2.5. Details of the diameter  $D_{core}$  of the Au seeds and of the total diameter  $D_{SC}$  of the corresponding Au@Pd and Au@Pt core-shell NPs. The initial seed concentration Au NPs is varied from  $C_{seed}=1.4 \mu\text{mol L}^{-1}$  and  $1/2C_{seed}$ . The reaction temperature is varied up to the type of shell (Au@Pd at 110°C, Au@Pt at 140°C).

		Au seed concentration		
		$C_{seed}$	$C_{seed}/2$	$C_{seed}/4$
Temperature (°C)	$D_{core}$ (nm)	$D_{SC}$ (nm)	$D_{SC}$ (nm)	$D_{SC}$ (nm)
110	$10.6 \pm 0.8$	$11.4 \pm 0.9$	$12.5 \pm 1.0$	$13.7 \pm 1.0$
140		$11.1 \pm 2.2$	$11.7 \pm 2.5$	$12.9 \pm 2.3$



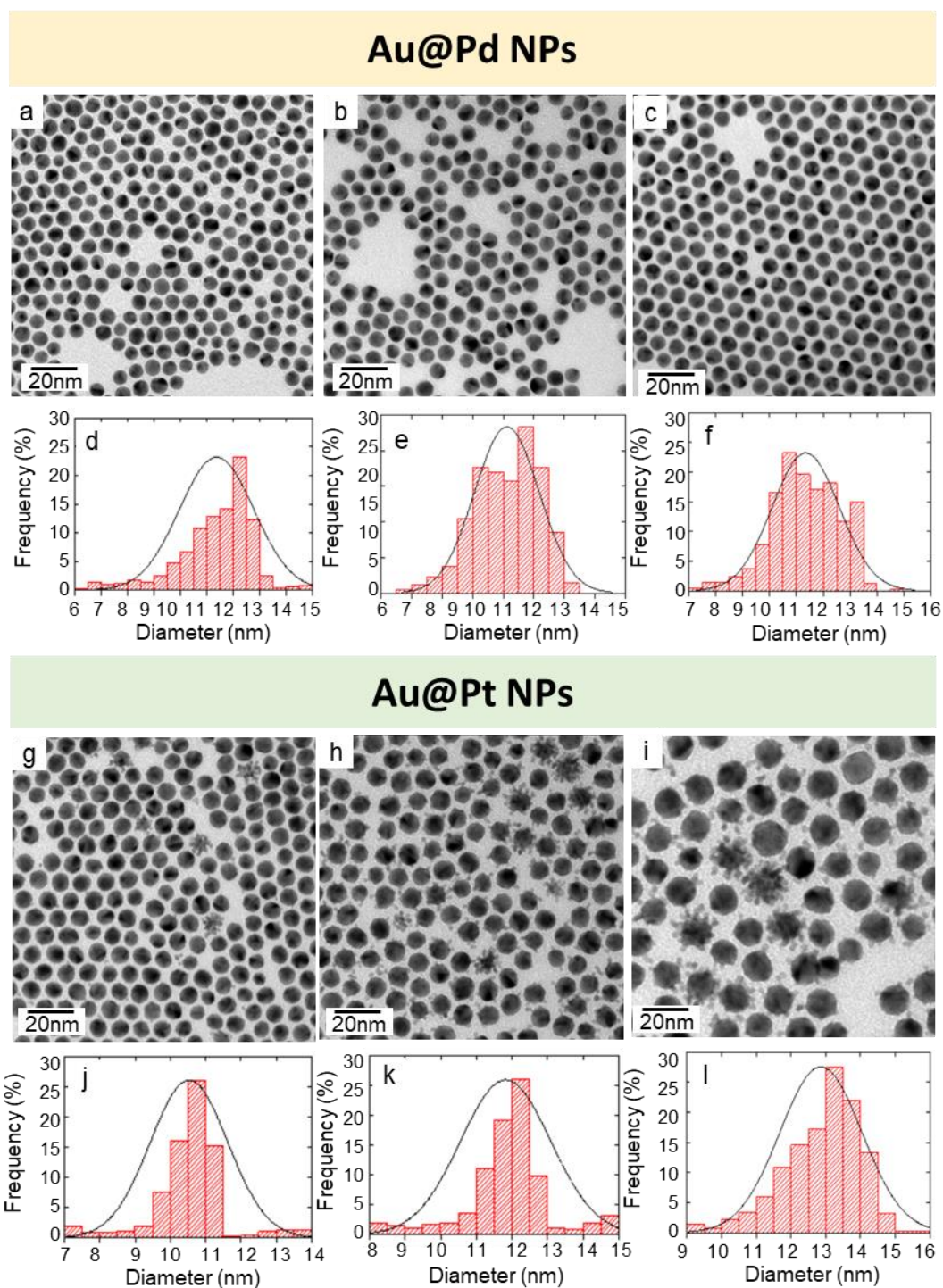


Figure 2.21. Representative TEM images of  $Au_{10nm}@Pd$  NPs obtained from different seed concentrations (a)  $C_{seed}$ , (b)  $1/2C_{seed}$  and (c),  $1/4C_{seed}$  where  $C_{seed} = 1.4 \mu\text{mol L}^{-1}$  (d, e, f) the corresponding size histograms and TEM images of  $Au_{10nm}@Pt$  NPs for similar seed concentrations (g, h, i) and the corresponding size histograms (j, k, l).

The efficiency of overgrowth as a function of the metal type (@Ag, Pd or Pt) is shown in Figure 2. 22. The Ag overgrowth appears to be the most effective, followed by the Pd and Pt overgrowths in order. Moreover, the thickness shells are well controlled by the concentration ratio [precursor]/[seed]. Ag and Au with low lattice mismatch (0.17%) generate smaller lattices strains, decrease the interfacial energy and thus form more easily core-shell structure compared to Au-Pt and Au-Pd with lattice mismatch of 3.70% and 4.60% respectively (Table 1.3 in chapter I). The difference of overgrowth efficiency between Pt and Pd could be attributed to higher Pt-Pt bond energy (Table 1.2 in chapter I) even though Au-Pt have a smaller lattice mismatch than Au-Pd50.

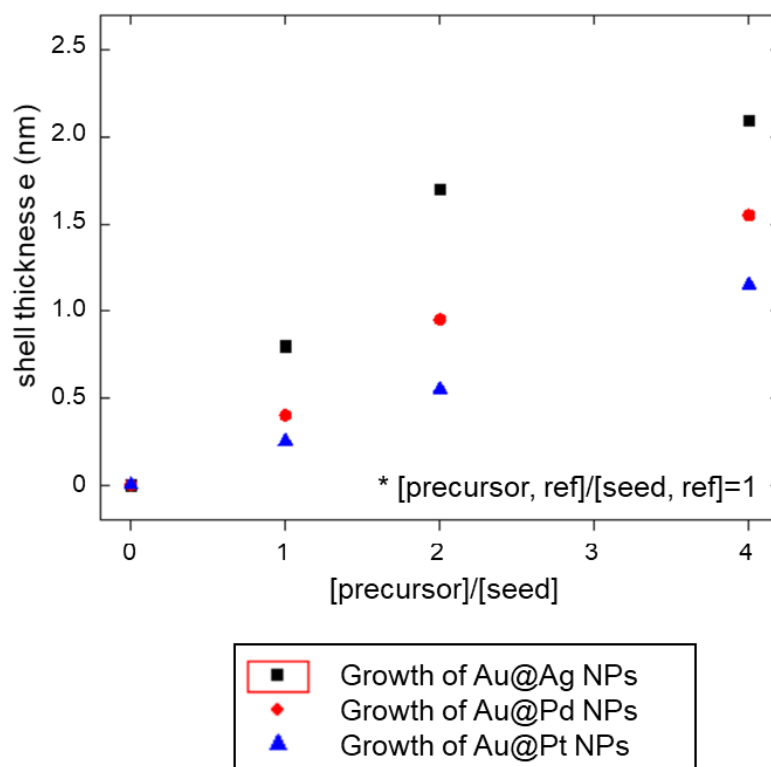


Figure 2.22. Comparison of final NPs sizes up to their shell materials type between Au@Ag NPs, Au@Pd and Au@Pt NPs in function of the ratio [precursor]/[seed].

## 5.2. Replacement of core materials: synthesis of Ag@Pt and Ag@Pd core-shell nanoparticles.

We succeeded in replacing the Ag shell by a material with a strong catalytic activity such as Pd and Pt so far. Here, we were interested by replacing the Au core by Ag. This is

because Ag NPs have a more intense and well-defined LSPR than Au NPs (corresponding UV-visible spectra are shown in chapter III). This work was done during a Master 2 internship (S. Hadoui) that I co-supervised.

To synthesize Ag NPs, direct reduction by oleylamine of  $\text{AgNO}_3$  was used and it basically followed same synthesis procedure as for Au NPs with 10.6nm diameter synthesized as described in section 1.1. 0.25mM of  $\text{AgNO}_3$  was thus dissolved in oleylamine which has a role as reducing agent, solvent and ligand. The temperature was increased with ramping ( $4^\circ\text{C}$  per minute) until it reached the reaction temperature  $240^\circ\text{C}$  during 30 minutes, then the solution was cooled down. TEM image of Ag core NPs shows their diameter is 12.4 nm and their histograms show their size distribution around 8% (Figure 2. 23 (b), (c)).

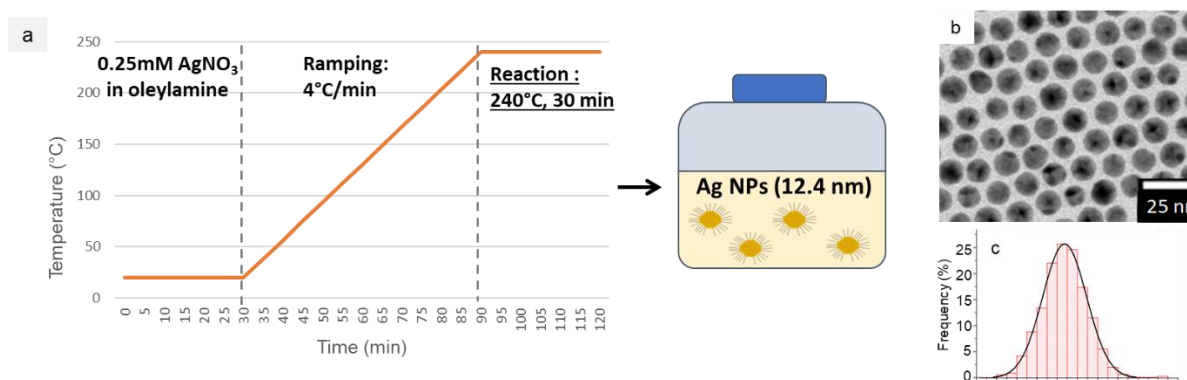


Figure 2.23. (a) . Description of synthesis process of Ag NPs via direct reduction of  $\text{AgNO}_3$  in oleylamine, (b) representative TEM image of Ag NPs with  $12.4 \pm 0.8$  nm diameter and (c) the corresponding histogram.

A palladium or platinum shell overgrowth was induced in a solution of  $\text{Pd}(\text{acac})_2$  or  $\text{Pt}(\text{acac})_2$  in oleylamine at a concentration of  $0.825 \text{ mmol L}^{-1}$  which is the same concentration as it is used for silver overgrowth in section 1 in Chapter II. The optimized reaction temperature is  $160^\circ\text{C}$  in case of Pd overgrowth and  $200^\circ\text{C}$  in case of Pt growth. Reaction time is fixed as 60 minutes (Figure 2. 24).

TEM images of the  $\text{Ag}_{12\text{nm}}@\text{Pt}$  NPs are reported in Figure 2. 25. Their mean diameter  $D_{\text{CS}}$  is controlled by the initial concentration of the Ag seed solution from  $C_{\text{seed}}$ ,  $C_{\text{seed}}/2$ ,  $C_{\text{seed}}/4$  and  $C_{\text{seed}}/8$ . As seed concentration decreases,  $\text{Ag}_{12\text{nm}}@\text{Pt}$  NPs  $D_{\text{CS}}$  increases to 12.9, 13.0, 13.2 and 13.7 nm in diameter with keeping low size polydispersity around 10% (table 2.6). We observe as for  $\text{Au}@\text{Pt}$  NPs a well control of the Pt thickness by adjustment of the Pt/Ag concentration ratios. Furthermore, Pt overgrowth on silver core do not lead to dendritic core-

shell NPs Island as observed for Au@Pt core-shell nanosphere (Figure 2.25). It could be explained by the use of a higher reaction temperature for the growth of Pt on Ag core (200°C) compared to Au core (140°C). It is coherent with the results obtained by Zhang et al<sup>50</sup> on the morphological control of Pt nanoparticles grown in oleylamine. The authors observed indeed that Pt nanostructure evolves from spheres to branched particles in OLA with decreasing the reaction temperature.

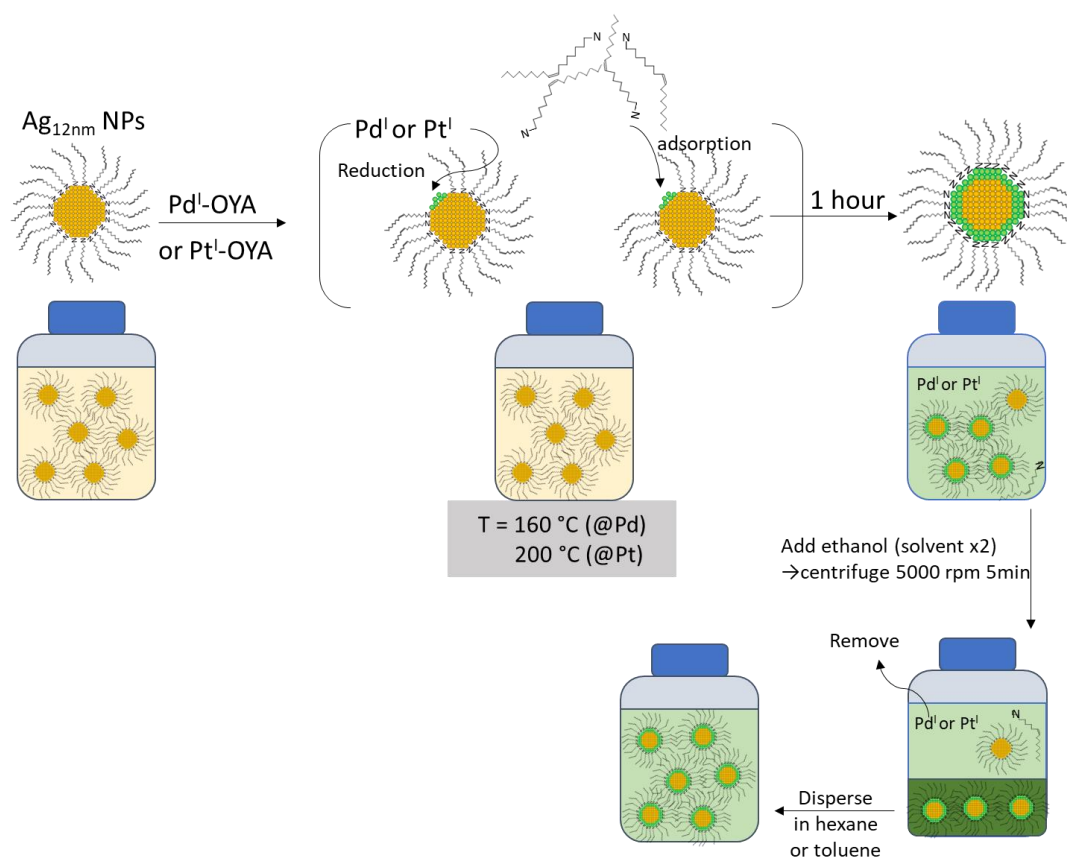


Figure 2.24. Schematic description to synthesize (a) Ag@Pd and Ag@Pt core-shell NPs via seed mediated growth (Reaction conditions can be varied from this to obtain different final size.)

Table 2.6. Details of the diameter  $D_{core}$  of the Ag seeds and of the total diameter  $D_{SC}$  of the corresponding Ag@Pd and Ag@Pt core-shell NPs. The concentration of Pd(or Pt)-oleylamine complex is fixed at  $0.825 \text{ mmol L}^{-1}$ . The initial seed concentration is alternatively  $C = 1.4 \text{ } \mu\text{mol L}^{-1}$ ,  $C/2$  or  $C/4$  or  $C/8$ .

Ag Core	Shell metal	Initial seed concentration			
		$C_{seed}$	$C_{seed}/2$	$C_{seed}/4$	$C_{seed}/8$

$D_{\text{core}}$ (nm)		$D_{\text{sc}}$ (nm)			
$12.4 \pm 0.8$	@Pd	12.8	13.2	13.6	14.6
	e (nm)	0.2	0.4	0.6	1.1
	@Pt	12.9	13.0	13.2	13.7
	e(nm)	0.25	0.3	0.4	0.65

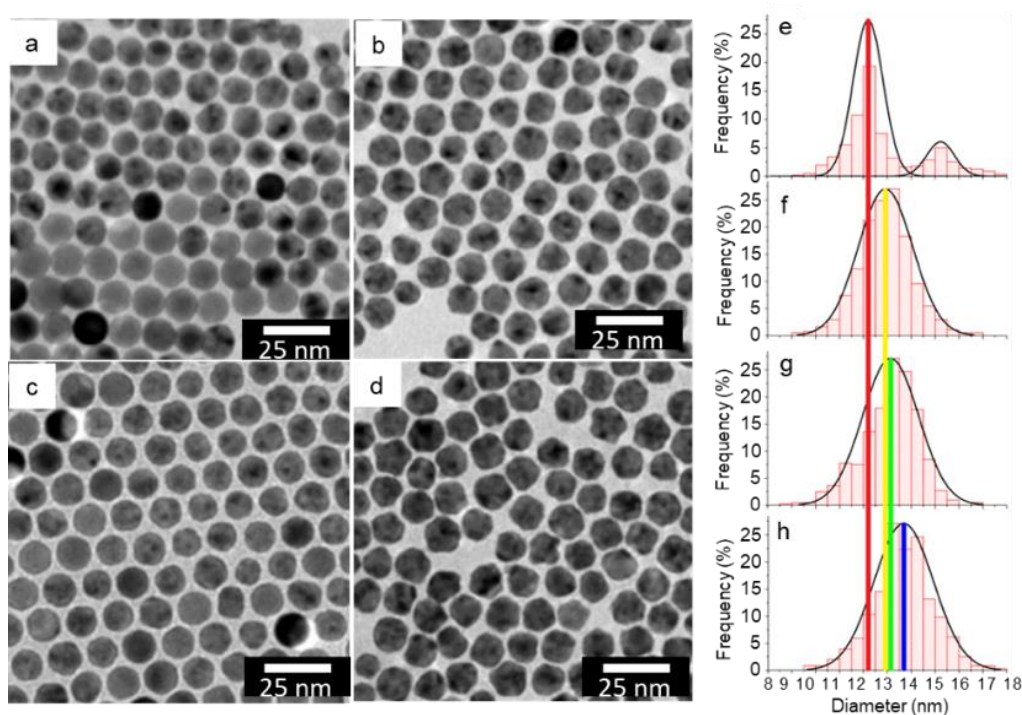


Figure 2.25. Representative TEM images of  $\text{Ag}_{12.4\text{nm}}\text{@Pt}$  NPs obtained from different seed concentrations (a)  $C_{\text{seed}}$ , (b)  $C_{\text{seed}}/2$ , (c)  $C_{\text{seed}}/4$  (d)  $C_{\text{seed}}/8$  where  $C = 1.4 \times 10^{-3} \text{ mmol L}^{-1}$  and (e-h) the corresponding size histograms.

Further observation to reveal the chemical composition and structural arrangement (core-shell structure) is done using HAADF-STEM in case of  $\text{Ag@Pt}$  NPs. Z-contrast imaging is capable of distinguishing the Ag and Pt within the nanoparticles because of the atomic number difference between Ag(47) and Pt(78). Typical HAADF-STEM images clearly show 13.7 nm core-shell  $\text{Ag}_{12\text{nm}}\text{@Pt}$  NPs with Ag core and Pt shell in a bright and dark contrast respectively (Figure 2.26 (a)). Core-shell structure is more precisely verified by corresponding EELS maps (Figure 2.26 (b)) in different color (Ag: blue, Pt: yellow). Finally, we could observe a hexagonal network of  $\text{Ag}_{12\text{nm}}\text{@Pt}$  NPs similar to  $\text{Au@Ag}$  NPs. The NPs spontaneously self-organized because of their narrow size distribution (less than 10%).

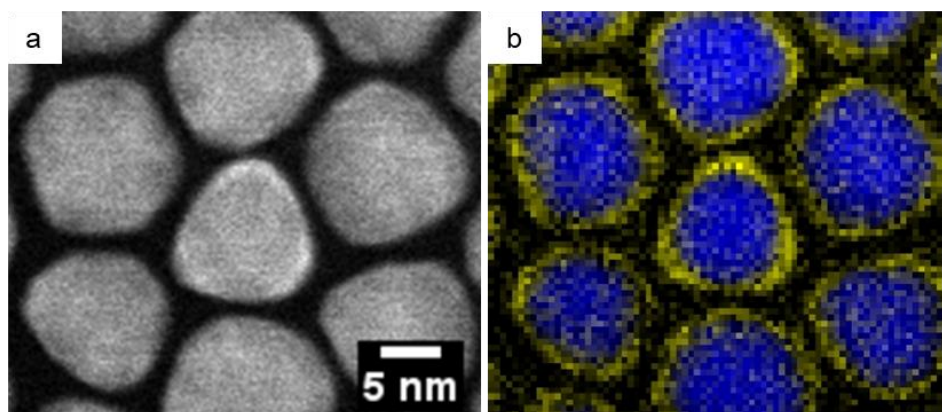


Figure 2.26. Electron microscopy characterization of  $\text{Ag}_{12\text{nm}}@Pt$  core-shell NPs (a) Typical HAADF-STEM dark field image of  $\text{Ag}_{12\text{nm}}@Pt$  NPs with a total diameter  $D_{CS} = 13.7$  nm, (b) corresponding EELS map showing the Ag core (blue) and the Pt shell (yellow).

**Pt shell replaced by Pd.** TEM images of the  $\text{Ag}_{12\text{nm}}@Pd$  NPs are reported in Figure 2.27 for different Ag seed concentrations  $C_{\text{seed}}$ ,  $C_{\text{seed}}/2$ ,  $C_{\text{seed}}/4$  and  $C_{\text{seed}}/8$ . As seed concentration decreases,  $\text{Ag}_{12\text{nm}}@Pd$  NPs  $D_{CS}$  increases from 12.8 to 14.6 nm in diameter and the obtained polydispersity remains low (around 10%) with a Gaussian profile characteristic of a homogeneous growth of palladium on the surface of the seeds. The thickness of Pd or Pt shells is well controlled by the [metallic precursor]/[seed] concentration ratio. Furthermore, Pt shell overgrowth on silver core is less effective than Pd overgrowth as was observed in the case of gold core (Table 2.6 and Figure 2.28).

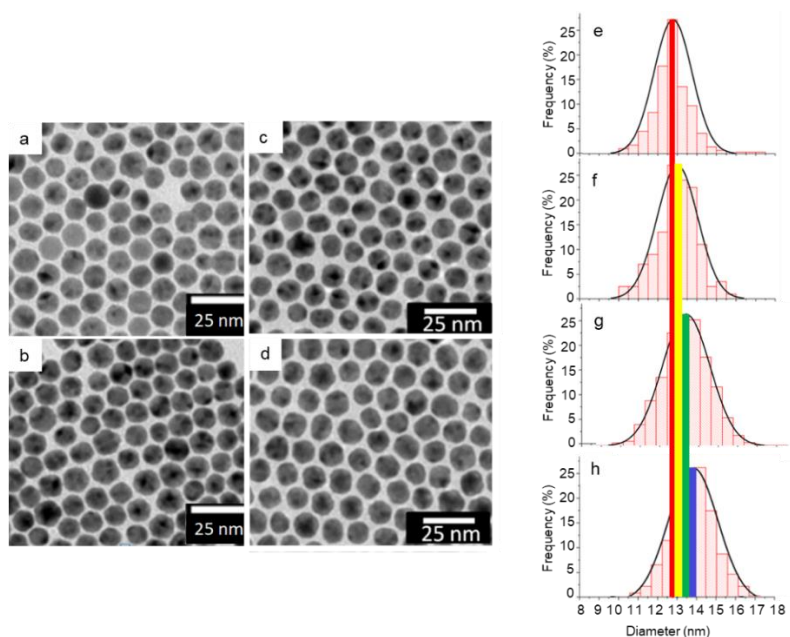


Figure 2.27. Representative TEM images of  $\text{Ag}_{12\text{nm}}@Pd$  NPs obtained from different seed concentrations (a)  $C_{\text{seed}}$ , (b)  $C_{\text{seed}}/2$ , (c)  $C_{\text{seed}}/4$ , (d)  $C_{\text{seed}}/8$  where  $C_{\text{seed}} = 1.4 \times 10^{-3} \text{ mmol L}^{-1}$  (e-h) the corresponding histograms.

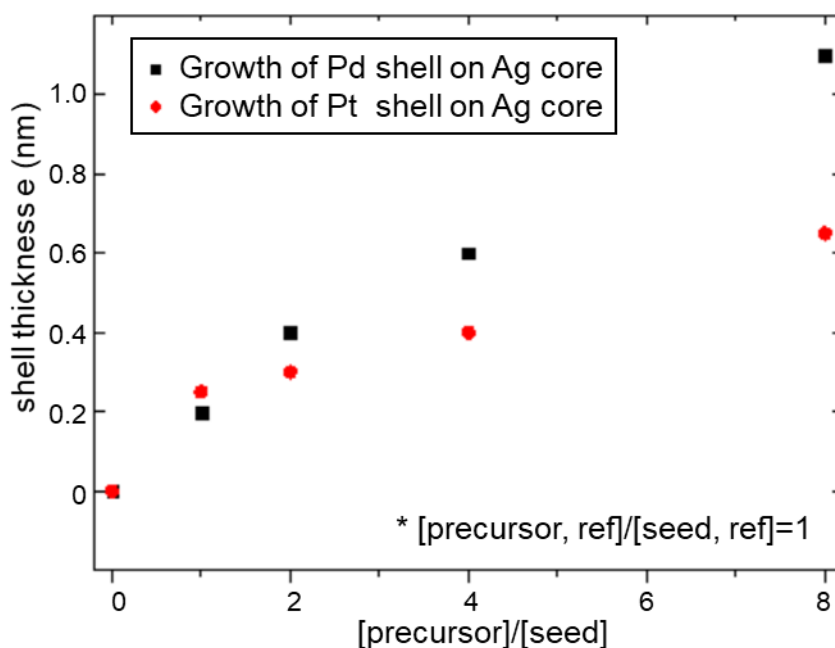


Figure 2.28. Shell thickness evolution of  $\text{Ag}_{12\text{nm}}@Pd$  (in black) and  $\text{Ag}_{12\text{nm}}@Pt$  (in red) NPs in function of the concentration ratio  $[\text{precursor}]/[\text{seed}]$ .

### 5.3. 3D organization of the metallic/catalytic core-shell nanoparticles

We studied the 3D self-assemblies of the core-shell NPs synthesized in this Ph.D work ( $\text{Au}_{10\text{nm}}@Pd$  or  $@Pt$  and  $\text{Ag}_{12\text{nm}}@Pd$  or  $@Pt$ ) core-shell NPs synthesized in this work. We have shown that they are all characterized by narrow size and shape polydispersity which is a key parameter for their organization (A. Courty, 2010)<sup>51</sup>. Deposition conditions are maintained in a same way as the one for  $\text{Au}@Ag$  self-assemblies (solvent: toluene, substrate: silicon wafer, method: drop deposition).

Both  $\text{Au}_{10\text{nm}}@Pd$  and  $\text{Au}_{10\text{nm}}@Pt$  NPs formed individual hexagonal shape 3D superlattices in micrometer scale (Figure 2.29). The presence of well-defined facets agrees with a *fcc* type crystalline structure due to their narrow size distribution (<10%)<sup>52</sup>.  $\text{Ag}@Pt$  and  $\text{Ag}@Pd$  NPs also exhibit homogeneous NPs size and shapes and after deposition on a solid substrate self-organized at 3D in well faceted superlattices. These self-assemblies were characterized by SEM and EDX cartography (Figure 2.30). The cartographies of two elements ( $\text{Au}/Pd$  or  $\text{Au}/Pt$  or  $\text{Ag}/Pt$  or  $\text{Ag}/Pd$ ) show a homogeneous repartition of the two metals in the 3D SLs. The atomic composition deduced from EDX analysis agrees with this one calculated from TEM images (Table 2.7). These results mean these SLs do not stem from the segregation of a specific population of NPs.

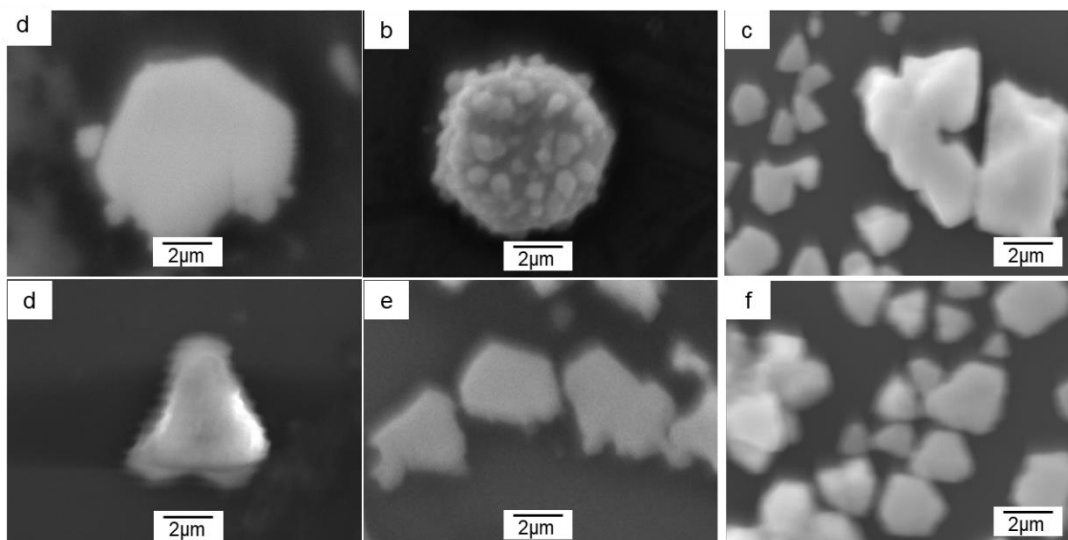


Figure 2.29. Typical SEM images of 3D superlattices made of  $\text{Au}_{10\text{nm}}@Pd$  with (a)  $D_{CS} = 11.4$  nm, (b) 12.5 nm, (c) 13.6 nm and  $\text{Au}_{10\text{nm}}@Pt$  with (d)  $D_{CS} = 10.9$  nm, (e) 11.4 nm, (f) 12.9 nm.



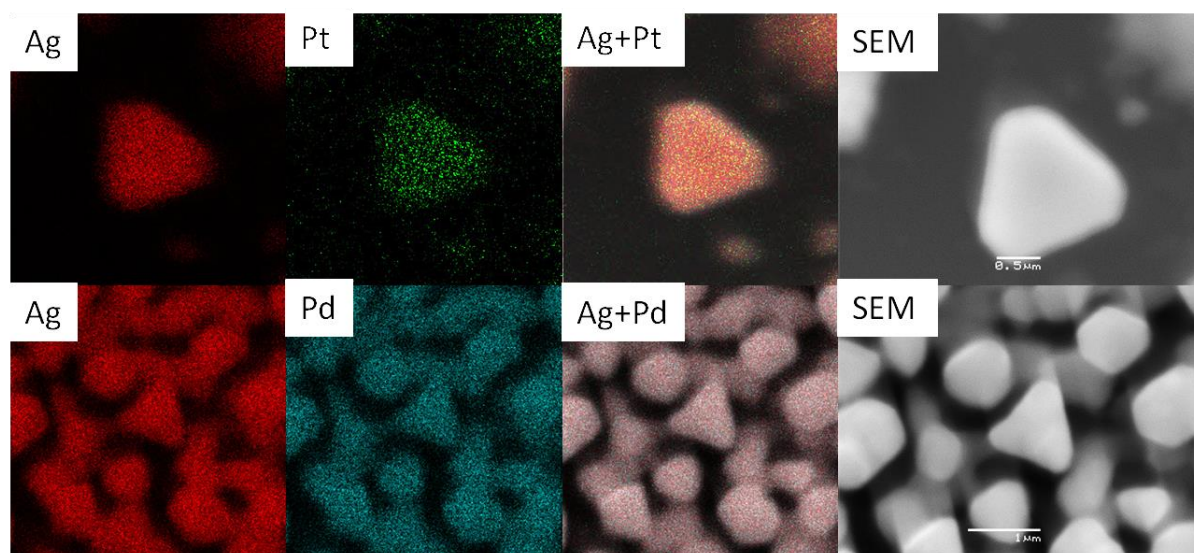


Figure 2.30. Typical SEM images of 3D superlattices made of  $\text{Ag}_{12\text{nm}}@Pt$   $D_{CS}=13.7$  nm and  $\text{Ag}_{12\text{nm}}@Pd$   $D_{CS}=13.0$  nm and cartography of each atom using EDX analysis.

Table 2.7. Diameter  $D_{CS}$ , shell thickness  $e=(D_{CS}-D_{CORE})/2$  and atomic composition obtained through EDX measurements or calculations for  $\text{Au}_{10\text{nm}}@Pd$ ,  $\text{Au}_{10\text{nm}}@Pt$  or  $\text{Ag}_{12\text{nm}}@Pd$ ,  $\text{Ag}_{12\text{nm}}@Pt$  core-shell NPs.

Sample	$D_{CS}$ (nm)	$e$ (nm)	EDX composition		Calculated composition	
			% Core	% Shell	% Core	% Shell
$\text{Au}_{10\text{nm}}@Pd$	11.4	0.4	76	24	80	20
	12.5	0.95	65	35	61	39
	13.7	1.55	51	49	46	54
$\text{Au}_{10\text{nm}}@Pt$	11.1	0.2	90	10	87	13
	11.7	0.4	74	26	74	26
	12.9	1.15	60	40	55	45
$\text{Ag}_{12\text{nm}}@Pd$	12.8	0.2	88	12	91	9
	13.2	0.4	80	20	87	13
	13.6	0.6	78	22	76	24

	14.6	1.1	57	43	61	39
<b>Ag<sub>12nm</sub>@Pt</b>	12.9	0.25	90	10	89	11
	13.0	0.3	86	14	87	13
	13.2	0.4	81	19	83	17
	13.7	0.65	70	30	74	26

The HR-SEM image and corresponding Fourier transform of a typical 3D superlattice made of Ag<sub>12nm</sub>@Pt core-shell NPs with a total diameter  $D_{SC}=13.7$  nm show the stacking of NP monolayers organized in a hexagonal network (Figure 2. 31). This is similarly to what was observed for Au@Ag core-shell NP SLs (Figure 2.19).

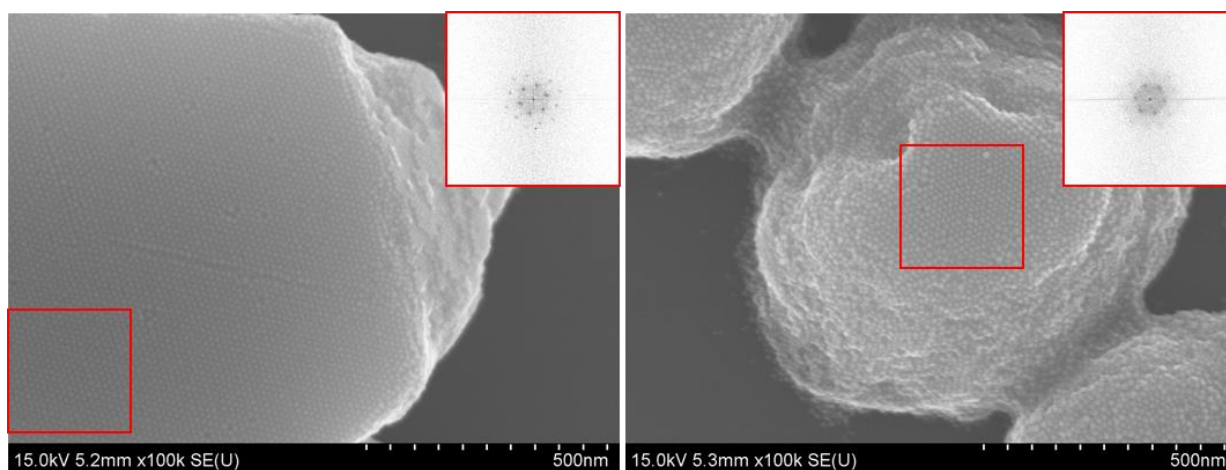


Figure 2. 31. HRSEM image of colloidal crystal made of core-shell Ag<sub>12nm</sub>@Pt NPs with a total diameter  $D_{CS} = 13.7$  nm. In inset the corresponding Fourier transform.

## 6. Conclusion

Au@Ag core-shell NPs were successfully synthesized with controlled size (size distribution < 10%), crystallinity of the core and chemical composition through a versatile approach using Au seeds with selected sizes and crystallinities, and coated by different ligands (oleylamine or dodecanthiol). The final size of the core-shell NPs was shown to depend on three main parameters: i) the [Ag precursor] / [Au seed] concentration ratio, ii) the nature of the ligands coating the seeds, and iii) the reaction temperature. Oleylamine as coating agent

and high temperature or low seed concentration (high silver precursor concentration) favors the growth of silver shells. Furthermore, micrometer-scale well-faceted 3D superlattices of ordered Au@Ag nanoparticles were obtained and imaged by HR-SEM.

Finally, we showed that this synthesis method is adaptable to different core and shell materials. Au core was exchanged by Ag, and Ag shell by Pt or Pd without strong modification of the synthesis process. Only reaction temperature and reaction time have to be optimized. The shell growth is always control by concentration ratio [metallic precursor]/[seed]. Pt and Pd shell growth on gold core are less efficient than Ag because of the higher lattice mismatch.

This thesis work show that we are able to design various core-shell NPs up to targeted new physical and chemical properties and new applications. The high degree of tunability of these nanostructures will facilitate their application in various domains such as SERS detection or catalysis. In chapter III, the optical, vibrational and catalytic of these core-shell NPs as a function of their composition, size and crystallinity are described. We will see that the high quality of the samples should make it possible to answer the question of the influence of shell thickness or crystalline defects on their properties.

## 7. References

- (1) Sytwu, K.; Vadai, M.; Dionne, J. A. Bimetallic Nanostructures: Combining Plasmonic and Catalytic Metals for Photocatalysis. *Adv. Phys. X* **2019**, *4* (1), 1619480. <https://doi.org/10.1080/23746149.2019.1619480>.
- (2) Lu, L.; Burkey, G.; Halaciuga, I.; Goia, D. V. Core–Shell Gold/Silver Nanoparticles: Synthesis and Optical Properties. *J. Colloid Interface Sci.* **2013**, *392*, 90–95. <https://doi.org/10.1016/j.jcis.2012.09.057>.
- (3) Ma, Y.; Li, W.; Cho, E. C.; Li, Z.; Yu, T.; Zeng, J.; Xie, Z.; Xia, Y. Au@Ag Core–Shell Nanocubes with Finely Tuned and Well-Controlled Sizes, Shell Thicknesses, and Optical Properties. *ACS Nano* **2010**, *4* (11), 6725–6734. <https://doi.org/10.1021/nn102237c>.
- (4) Gilroy, K. D.; Ruditskiy, A.; Peng, H.-C.; Qin, D.; Xia, Y. Bimetallic Nanocrystals: Syntheses, Properties, and Applications. *Chem. Rev.* **2016**, *116* (18), 10414–10472. <https://doi.org/10.1021/acs.chemrev.6b00211>.
- (5) Haidar, I.; Day, A.; Decorse, P.; Lau-Truong, S.; Chevillot-Biraud, A.; Aubard, J.; Félidj, N.; Boubekour-Lecaque, L. Tailoring the Shape of Anisotropic Core–Shell Au–Ag Nanoparticles in Dimethyl Sulfoxide. *Chem. Mater.* **2019**, *31* (8), 2741–2749. <https://doi.org/10.1021/acs.chemmater.8b04735>.
- (6) Dai, L.; Song, L.; Huang, Y.; Zhang, L.; Lu, X.; Zhang, J.; Chen, T. Bimetallic Au/Ag Core–Shell Superstructures with Tunable Surface Plasmon Resonance in the Near-Infrared Region and High Performance Surface-Enhanced Raman Scattering. *Langmuir* **2017**, *33* (22), 5378–5384. <https://doi.org/10.1021/acs.langmuir.7b00097>.
- (7) Nasrabadi, H. T.; Abbasi, E.; Davaran, S.; Kouhi, M.; Akbarzadeh, A. Bimetallic Nanoparticles: Preparation, Properties, and Biomedical Applications. *Artif. Cells Nanomedicine Biotechnol.* **2016**, *44* (1), 376–380. <https://doi.org/10.3109/21691401.2014.953632>.
- (8) Mao, K.; Zhou, Z.; Han, S.; Zhou, X.; Hu, J.; Li, X.; Yang, Z. A Novel Biosensor Based on Au@Ag Core-Shell Nanoparticles for Sensitive Detection of Methylamphetamine with Surface Enhanced Raman Scattering. *Talanta* **2018**, *190*, 263–268. <https://doi.org/10.1016/j.talanta.2018.07.071>.
- (9) Zhang, Y.-W. *Bimetallic Nanostructures Shape-Controlled Synthesis for Catalysis, Plasmonics, and Sensing Applications*, Ed by Ya-Wen Zhang.; Wiley: Beijing, 2018.
- (10) Wu, Y.; Jiang, P.; Jiang, M.; Wang, T.-W.; Guo, C.-F.; Xie, S.-S.; Wang, Z.-L. The Shape Evolution of Gold Seeds and Gold@silver Core–Shell Nanostructures. *Nanotechnology* **2009**, *20* (30), 305602. <https://doi.org/10.1088/0957-4484/20/30/305602>.
- (11) Tsuji, M.; Miyamae, N.; Lim, S.; Kimura, K.; Zhang, X.; Hikino, S.; Nishio, M. Crystal Structures and Growth Mechanisms of Au@Ag Core–Shell Nanoparticles Prepared by the Microwave–Polyol Method. *Cryst. Growth Des.* **2006**, *6* (8), 1801–1807. <https://doi.org/10.1021/cg060103e>.
- (12) Tsuji, M.; Matsuo, R.; Jiang, P.; Miyamae, N.; Ueyama, D.; Nishio, M.; Hikino, S.; Kumagae, H.; Kamarudin, K. S. N.; Tang, X.-L. Shape-Dependent Evolution of Au@Ag Core–Shell Nanocrystals by PVP-Assisted *N,N*-Dimethylformamide Reduction. *Cryst. Growth Des.* **2008**, *8* (7), 2528–2536. <https://doi.org/10.1021/cg800162t>.
- (13) Ji, Y.; Yang, S.; Guo, S.; Song, X.; Ding, B.; Yang, Z. Bimetallic Ag/Au Nanoparticles: A Low Temperature Ripening Strategy in Aqueous Solution. *Colloids Surf. Physicochem. Eng. Asp.* **2010**, *372* (1–3), 204–209. <https://doi.org/10.1016/j.colsurfa.2010.10.028>.

- (14) Xia, Y.; Gilroy, K. D.; Peng, H.-C.; Xia, X. Seed-Mediated Growth of Colloidal Metal Nanocrystals. *Angew. Chem. Int. Ed.* **2017**, *56* (1), 60–95. <https://doi.org/10.1002/anie.201604731>.
- (15) Fan, F.-R.; Liu, D.-Y.; Wu, Y.-F.; Duan, S.; Xie, Z.-X.; Jiang, Z.-Y.; Tian, Z.-Q. Epitaxial Growth of Heterogeneous Metal Nanocrystals: From Gold Nano-Octahedra to Palladium and Silver Nanocubes. *J. Am. Chem. Soc.* **2008**, *130* (22), 6949–6951. <https://doi.org/10.1021/ja801566d>.
- (16) Liu, Y.; Zhou, J.; Wang, B.; Jiang, T.; Ho, H.-P.; Petti, L.; Mormile, P. Au@Ag Core–Shell Nanocubes: Epitaxial Growth Synthesis and Surface-Enhanced Raman Scattering Performance. *Phys. Chem. Chem. Phys.* **2015**, *17* (10), 6819–6826. <https://doi.org/10.1039/C4CP05642F>.
- (17) Tong, Y.; Pu, J.; Wang, H.; Wang, S.; Liu, C.; Wang, Z. Ag–Pt Core–Shell Nanocomposites for Enhanced Methanol Oxidation. *J. Electroanal. Chem.* **2014**, *Complete* (728), 66–71. <https://doi.org/10.1016/j.jelechem.2014.06.030>.
- (18) Tedsree, K.; Li, T.; Jones, S.; Chan, C. W. A.; Yu, K. M. K.; Bagot, P. A. J.; Marquis, E. A.; Smith, G. D. W.; Tsang, S. C. E. Hydrogen Production from Formic Acid Decomposition at Room Temperature Using a Ag–Pd Core–Shell Nanocatalyst. *Nat. Nanotechnol.* **2011**, *6* (5), 302–307. <https://doi.org/10.1038/nnano.2011.42>.
- (19) Zhang, L.; Xie, Z.; Gong, J. Shape-Controlled Synthesis of Au–Pd Bimetallic Nanocrystals for Catalytic Applications. *Chem. Soc. Rev.* **2016**, *45* (14), 3916–3934. <https://doi.org/10.1039/C5CS00958H>.
- (20) Zheng, N.; Fan, J.; Stucky, G. D. One-Step One-Phase Synthesis of Monodisperse Noble-Metallic Nanoparticles and Their Colloidal Crystals. *J. Am. Chem. Soc.* **2006**, *128* (20), 6550–6551. <https://doi.org/10.1021/ja0604717>.
- (21) Andrieux-Ledier, A.; Tremblay, B.; Courty, A. Stability of Self-Ordered Thiol-Coated Silver Nanoparticles: Oxidative Environment Effects. *Langmuir* **2013**, *29* (43), 13140–13145. <https://doi.org/10.1021/la402916b>.
- (22) Goubet, N.; Yan, C.; Polli, D.; Portalès, H.; Arfaoui, I.; Cerullo, G.; Pileni, M.-P. Modulating Physical Properties of Isolated and Self-Assembled Nanocrystals through Change in Nanocrystallinity. *Nano Lett.* **2013**, *13* (2), 504–508. <https://doi.org/10.1021/nl303898y>.
- (23) Mourdikoudis, S.; Liz-Marzán, L. M. Oleylamine in Nanoparticle Synthesis. *Chem. Mater.* **2013**, *25* (9), 1465–1476. <https://doi.org/10.1021/cm4000476>.
- (24) Shen, C.; Hui, C.; Yang, T.; Xiao, C.; Tian, J.; Bao, L.; Chen, S.; Ding, H.; Gao, H. Monodisperse Noble-Metal Nanoparticles and Their Surface Enhanced Raman Scattering Properties. *Chem. Mater.* **2008**, *20* (22), 6939–6944. <https://doi.org/10.1021/cm800882n>.
- (25) Hiramatsu, H.; Osterloh, F. E. A Simple Large-Scale Synthesis of Nearly Monodisperse Gold and Silver Nanoparticles with Adjustable Sizes and with Exchangeable Surfactants. *Chem. Mater.* **2004**, *16* (13), 2509–2511. <https://doi.org/10.1021/cm049532v>.
- (26) Lavigne, A.; Sparfel, D.; Baranne-Lafont, J.; Cuong, N. K.; Maumy, M. MECHANISM OF PRIMARY ALIPI-IATIC AMINES OXIDATION TO NITRILES BY THE CUPROUS CHLORIDE - DIOXYGEN - PYRIDINE SYSTEM. *Tetrahedron Letters* **1990**, *31*, 3305.
- (27) Guo, H.; Chen, Y.; Cortie, M. B.; Liu, X.; Xie, Q.; Wang, X.; Peng, D.-L. Shape-Selective Formation of Monodisperse Copper Nanospheres and Nanocubes via Disproportionation Reaction Route and Their Optical Properties. *J. Phys. Chem. C* **2014**, *118* (18), 9801–9808. <https://doi.org/10.1021/jp5014187>.
- (28) Cooper, J. K.; Franco, A. M.; Gul, S.; Corrado, C.; Zhang, J. Z. Characterization of Primary Amine Capped CdSe, ZnSe, and ZnS Quantum Dots by FT-IR: Determination

- of Surface Bonding Interaction and Identification of Selective Desorption. *Langmuir* **2011**, *27* (13), 8486–8493. <https://doi.org/10.1021/la201273x>.
- (29) Portalès, H.; Goubet, N.; Sirotkin, S.; Duval, E.; Mermet, A.; Albouy, P.-A.; Pileni, M.-P. Crystallinity Segregation upon Selective Self-Assembling of Gold Colloidal Single Nanocrystals. *Nano Lett.* **2012**, *12* (10), 5292–5298. <https://doi.org/10.1021/nl3029009>.
- (30) Portales, H.; Goubet, N.; Saviot, L.; Adichtchev, S.; Murray, D. B.; Mermet, A.; Duval, E.; Pileni, M.-P. Probing Atomic Ordering and Multiple Twinning in Metal Nanocrystals through Their Vibrations. *Proc. Natl. Acad. Sci.* **2008**, *105* (39), 14784–14789. <https://doi.org/10.1073/pnas.0803748105>.
- (31) Goubet, N.; Richardi, J.; Albouy, P. A.; Pileni, M. P. How to Predict the Growth Mechanism of Supracrystals from Gold Nanocrystals. *J. Phys. Chem. Lett.* **2011**, *2* (5), 417–422. <https://doi.org/10.1021/jz200004f>.
- (32) Goubet, N.; Tempra, I.; Yang, J.; Soavi, G.; Polli, D.; Cerullo, G.; Pileni, M. P. Size and Nanocrystallinity Controlled Gold Nanocrystals: Synthesis, Electronic and Mechanical Properties. *Nanoscale* **2015**, *7* (7), 3237–3246. <https://doi.org/10.1039/C4NR06513A>.
- (33) Ko, F.-H.; Tai, M.; Liu, F.-K.; Chang, Y.-C. Au–Ag Core–Shell Nanoparticles with Controllable Shell Thicknesses for the Detection of Adenosine by Surface Enhanced Raman Scattering. *Sens. Actuators B Chem.* **2015**, *211*, 283–289. <https://doi.org/10.1016/j.snb.2015.01.047>.
- (34) Peng, S.; McMahon, J. M.; Schatz, G. C.; Gray, S. K.; Sun, Y. Reversing the Size-Dependence of Surface Plasmon Resonances. *Proc. Natl. Acad. Sci.* **2010**, *107* (33), 14530–14534. <https://doi.org/10.1073/pnas.1007524107>.
- (35) Srnová-Šloufová, I.; Lednický, F.; Gemperle, A.; Gemperlová, J. Core–Shell (Ag)Au Bimetallic Nanoparticles: Analysis of Transmission Electron Microscopy Images. *Langmuir* **2000**, *16* (25), 9928–9935. <https://doi.org/10.1021/la0009588>.
- (36) Guisbiers, G.; Mendoza-Cruz, R.; Bazán-Díaz, L.; Velázquez-Salazar, J. J.; Mendoza-Perez, R.; Robledo-Torres, J. A.; Rodríguez-Lopez, J.-L.; Montejano-Carrizales, J. M.; Whetten, R. L.; José-Yacamán, M. Electrum, the Gold–Silver Alloy, from the Bulk Scale to the Nanoscale: Synthesis, Properties, and Segregation Rules. *ACS Nano* **2016**, *10* (1), 188–198. <https://doi.org/10.1021/acsnano.5b05755>.
- (37) Shore, M. S.; Wang, J.; Johnston-Peck, A. C.; Oldenburg, A. L.; Tracy, J. B. Synthesis of Au(Core)/Ag(Shell) Nanoparticles and Their Conversion to AuAg Alloy Nanoparticles. *Small* **2011**, *7* (2), 230–234. <https://doi.org/10.1002/sml.201001138>.
- (38) Gao, C.; Hu, Y.; Wang, M.; Chi, M.; Yin, Y. Fully Alloyed Ag/Au Nanospheres: Combining the Plasmonic Property of Ag with the Stability of Au. *J. Am. Chem. Soc.* **2014**, *136* (20), 7474–7479. <https://doi.org/10.1021/ja502890c>.
- (39) Courty, A. Silver Nanocrystals: Self-Organization and Collective Properties. *J. Phys. Chem. C* **2010**, *114* (9), 3719–3731. <https://doi.org/10.1021/jp908966b>.
- (40) Wang, Luo, J.; Fan, Q.; Suzuki, M.; Suzuki, I. S.; Engelhard, M. H.; Lin, Y.; Kim, N.; Wang, J. Q.; Zhong, C.-J. Monodispersed Core–Shell Fe<sub>3</sub>O<sub>4</sub>@Au Nanoparticles. *J. Phys. Chem. B* **2005**, *109* (46), 21593–21601. <https://doi.org/10.1021/jp0543429>.
- (41) Ben Aissa, M. A.; Tremblay, B.; Andrieux-Ledier, A.; Maisonhaute, E.; Raouafi, N.; Courty, A. Copper Nanoparticles of Well-Controlled Size and Shape: A New Advance in Synthesis and Self-Organization. *Nanoscale* **2015**, *7* (7), 3189–3195. <https://doi.org/10.1039/C4NR06893A>.
- (42) Hu, J.-W.; Li, J.-F.; Ren, B.; Wu, D.-Y.; Sun, S.-G.; Tian, Z.-Q. Palladium-Coated Gold Nanoparticles with a Controlled Shell Thickness Used as Surface-Enhanced Raman Scattering Substrate. *J. Phys. Chem. C* **2007**, *111* (3), 1105–1112. <https://doi.org/10.1021/jp0652906>.

- (43) Bao, F.; Li, J.-F.; Ren, B.; Gu, R.-A.; Tian, Z.-Q. Synthesis and Characterization of Au@Co and Au@Ni Core–Shell Nanoparticles and Their Applications in Surface-Enhanced Raman Spectroscopy. *J. Phys. Chem. C* **2008**, *112* (2), 345–350. <https://doi.org/10.1021/jp075844k>.
- (44) Wang, J. Q.; Luo, J.; Fan, Q.; Suzuki, M.; Suzuki, I. S.; Engelhard, M. H.; Lin, Y.; Kim, N.; Wang, J. Q.; Zhong, C.-J. Monodispersed Core–Shell Fe<sub>3</sub>O<sub>4</sub>@Au Nanoparticles. *J. Phys. Chem. B* **2005**, *109* (46), 21593–21601. <https://doi.org/10.1021/jp0543429>.
- (45) Chen, Y.; Wu, H.; Li, Z.; Wang, P.; Yang, L.; Fang, Y. The Study of Surface Plasmon in Au/Ag Core/Shell Compound Nanoparticles. *Plasmonics* **2012**, *7* (3), 509–513. <https://doi.org/10.1007/s11468-012-9336-6>.
- (46) Ouhenia-Ouadahi, K.; Andrieux-Ledier, A.; Richardi, J.; Albouy, P.-A.; Beaunier, P.; Sutter, P.; Sutter, E.; Courty, A. Tuning the Growth Mode of 3D Silver Nanocrystal Superlattices by Triphenylphosphine. *Chem. Mater.* **2016**, *28* (12), 4380–4389. <https://doi.org/10.1021/acs.chemmater.6b01374>.
- (47) Borges, J.; Ribeiro, J. A.; Pereira, E. M.; Carreira, C. A.; Pereira, C. M.; Silva, F. Preparation and Characterization of DNA Films Using Oleylamine Modified Au Surfaces. *J. Colloid Interface Sci.* **2011**, *358* (2), 626–634. <https://doi.org/10.1016/j.jcis.2011.03.039>.
- (48) Talapin, D. V.; Lee, J.-S.; Kovalenko, M. V.; Shevchenko, E. V. Prospects of Colloidal Nanocrystals for Electronic and Optoelectronic Applications. *Chem. Rev.* **2010**, *110* (1), 389–458. <https://doi.org/10.1021/cr900137k>.
- (49) Wang, S.; Kristian, N.; Jiang, S.; Wang, X. Controlled Synthesis of Dendritic Au@Pt Core–Shell Nanomaterials for Use as an Effective Fuel Cell Electrocatalyst. *Nanotechnology* **2008**, *20* (2), 025605. <https://doi.org/10.1088/0957-4484/20/2/025605>.
- (50) Zhang, H.-T.; Ding, J.; Chow, G.-M. Morphological Control of Synthesis and Anomalous Magnetic Properties of 3-D Branched Pt Nanoparticles. *Langmuir* **2008**, *24* (2), 375–378. <https://doi.org/10.1021/la7032065>.
- (51) Courty, A. Silver Nanocrystals: Self-Organization and Collective Properties. *J. Phys. Chem. C* **2010**, *114* (9), 3719–3731. <https://doi.org/10.1021/jp908966b>.
- (52) Courty, A.; Richardi, J.; Albouy, P.-A.; Pileni, M.-P. How To Control the Crystalline Structure of Supracrystals of 5-Nm Silver Nanocrystals. *Chem. Mater.* **2011**, *23* (18), 4186–4192. <https://doi.org/10.1021/cm201313r>.

## **Chapter III. Physical and chemical properties of bimetallic core-shell nanoparticles.**

### **1. Introduction**

The optical, vibrational, and catalytic properties of bimetallic core-shell NPs are investigated in this Chapter. These core-shell NPs are synthesized by the two steps process described in chapter II, which allows to perform the synthesis under a variety of conditions (seed size, seed crystallinity, and seed surface chemistry). The core-shell NPs combine either two plasmonic materials: such as Au@Ag or plasmonic and catalytic materials such as Au@M or Ag@M with M=Pt or Pd. The LSPR effects can be control by the shell thickness or the core size. In addition, it is possible to enhance catalytic activities due to synergistic effects between two metals.

The optical properties of Au@Ag core-shell NPs are studied by UV-visible spectroscopy and discrete dipole approximation (DDA) calculations for different core sizes and shell thicknesses. Blue shift and increase of SPR band are expected by Ag shell overgrowth<sup>1</sup>. This study was then extended to other bimetallic core-shell NPs Au@M or Ag@M (M=Pt or Pd) NPs.

The vibrational properties of Au@Ag core-shell NPs are studied by low frequency Raman spectroscopy (LFRS) as a function of their chemical composition and crystalline structure. The LFRS studies were already reported to give various information of metallic NPs such as size, shape, crystallinity and chemical composition<sup>1-4</sup>. Furthermore, the vibrational frequency of Au@Ag core-shell NPs using LFRS should give information on coupling between both metals (core and shell)<sup>5</sup>.

The catalytic activity of Au@M (M=Ag, Pd or Pt) core-shell NPs, with different crystallinities (single crystalline (SC) or polycrystalline (PC)) and sizes of the Au core and different shell thicknesses, is tested through a model reaction based on the reduction in aqueous phase of 4-nitrophenol (4-NP) to 4-aminophenol (4-AP) by sodium borohydride (NaBH<sub>4</sub>). As the NPs are synthesized in organic solvent, a ligand exchange is necessary to transfer the NPs in water to test their catalytic activity with the model reaction. The choice of the ligand is governed by its ability to allow access to the reagents on the surface of the NPs. Physical-



chemical parameters such as the apparent rate constant ( $k_{app}$ ) and activation energy ( $E_a$ ) of the reactions are obtained for the different systems.

## 2. Optical properties

We succeeded to synthesize Au@Ag core-shell NPs from different Au core sizes (~5 and ~10 nm) and crystallinities (SC and PC) with various Ag shell thickness by the two steps process described in chapter II. Their structural characterization was confirmed by electron microscopy (HR-TEM, STEM HAADF, EELS). This synthesis method allowed also to replace the shell by other materials such as catalytic materials (Pt or Pd) or the core by a material with stronger plasmonic properties (Ag). This offer the opportunity to study the optical properties of core-shell NPs as a function of their size, composition. The optical properties of the colloidal dispersions were investigated by UV-visible absorption spectroscopy and DDA calculations.

### 2.1 Au@Ag core-shell nanoparticles

One of the main purposes of synthesize of core-shell NPs using Au and Ag is the exploring of their specific optical properties. Au and Ag have both representative plasmonic properties in visible range. In case of Au and Ag NPs the maximum of the plasmon resonance is ~500 nm, and ~400 nm, respectively. So, by integrating those two materials into one NP system, we expected to tune SPR in visible range between SPR of Au and Ag NPs. Moreover, the structural characteristics as a core-shell structure not random alloys are expected to be represented in their SPR band such as a separated influence from the core and the shell <sup>6</sup>. We studied the optical properties of Au@Ag NPs formed on one hand from polycrystalline (PC) Au cores with diameters ~5nm or ~10nm and various silver shell thicknesses and on the other hand from single crystalline (SC) Au core with diameters ~5nm and various silver shell thicknesses. The colloidal solutions were characterized through UV-visible absorption measurements (Figure 3.1). The spectra were recorded from colloidal solutions at room temperature with a fixed concentration of 0.14  $\mu\text{mol L}^{-1}$ .

**Au<sub>5nm</sub>(PC)@Ag NPs:** In figure 3.1 (a), Au<sub>5nm</sub>(PC) seeds exhibit an absorbance band at 520 nm corresponding to the surface plasmon resonance (SPR) of the NPs. For core-shell Au<sub>5nm</sub>(PC)@Ag NPs, a blue shift (30 nm) and an increase in the SPR band intensity are observed when the Ag shell grows to  $e = 0.5$  nm thickness (1~2 atomic layer). When the

thickness of the silver layer reaches 0.65 nm (2~3 atomic layers), the SPR band appears to be structured, with two components centered at 410 nm and 490 nm. The higher-wavelength SPR component is attributed to the Au core while the other one corresponds to the silver shell<sup>7-9</sup>. Finally, the absorption spectrum of Au<sub>5nm</sub>(PC)@Ag NPs with around 3-4 Ag atomic layers ( $e = 0.85$  nm) only exhibits the low-wavelength SPR component whose profile and wavelength correspond to the SPR of silver NPs of similar size. This experience was reproduced several times. It seems that the absorption of the silver shell is dominant despite the thin silver layer.

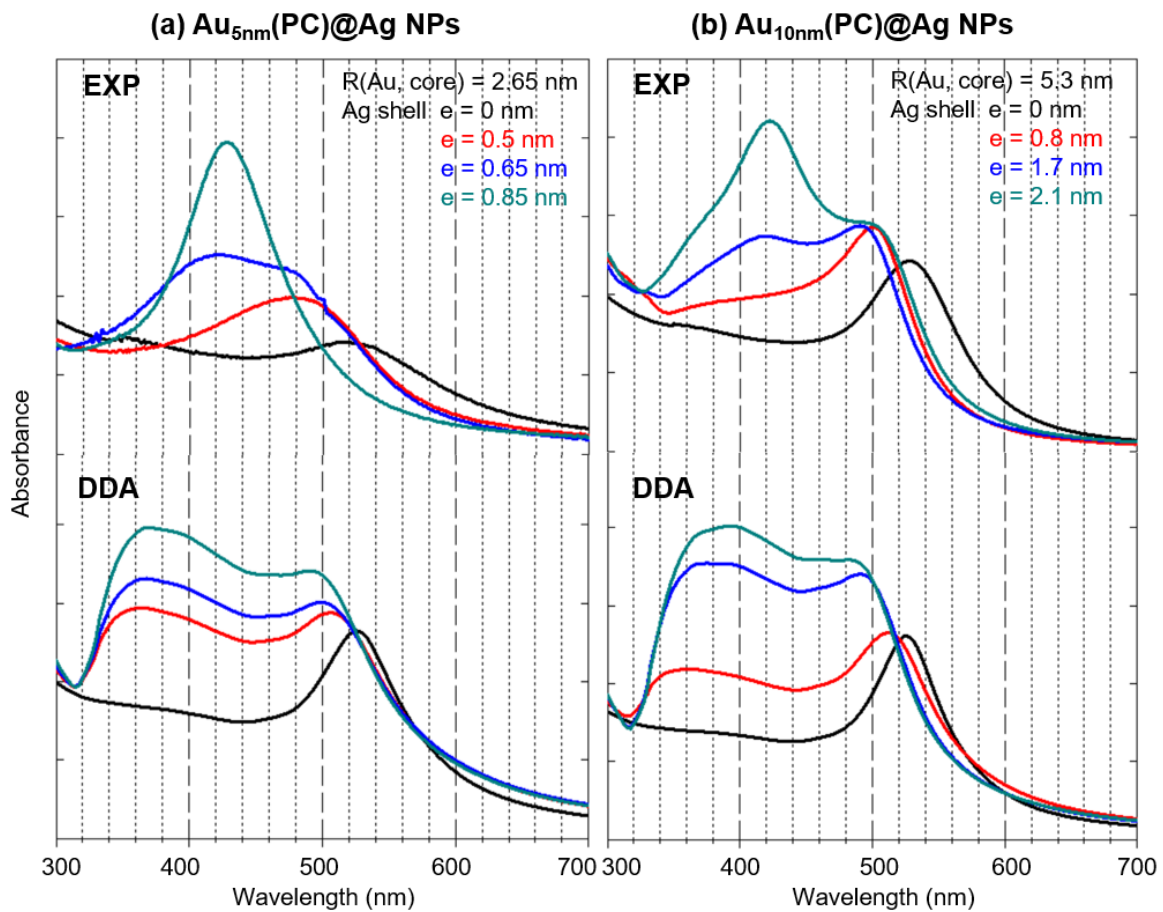


Figure 3.1. (a) Experimental and DDA calculated absorption spectra of core-shell Au<sub>5nm</sub>(PC)@Ag NPs and (b) Au<sub>10nm</sub>(PC)@Ag NPs with various shell thicknesses as indicated in both panels.

**Au<sub>10nm</sub>(PC)@Ag NPs:** Au<sub>10nm</sub>(PC) seed NPs a sharp and narrow SPR band centered at 530 nm is observed (Figure 3.1 (b) below). After the growth of a silver shell thickness of 0.8

nm ( $\sim 3$  atomic layers) the SPR band becomes more intense and shifts to the blue at 510 nm while a shoulder starts to grow on the low-wavelength side of the SPR. When the silver thickness is further increased to reach  $e = 1.7$  nm ( $\sim 5$  atomic layers), two SPR components are observed at 505 and 405 nm. As previously, the splitting into two components arises from the respective contributions of the gold core and the silver shell to the absorption. Finally, for a silver thickness of 2.1 nm ( $\sim 6$  atomic layers) the lower-wavelength SPR component attributed to the Ag shell becomes dominant. We experimentally observe that SPR features of Au@Ag NPs are significantly modulated by the layer thickness and core size in agreement with the literature<sup>10,11</sup>.

To gain deeper insights into the relationship between the SPR bands and the core size and shell thickness of the Au@Ag NPs, DDA calculations were carried out to simulate the absorption spectra of Au<sub>5nm</sub>(PC)@Ag and Au<sub>10nm</sub>(PC)@Ag core-shell NPs<sup>7</sup>. In these calculations, the refractive index of the surrounding medium is set to 1.5 to simulate the toluene used as the solvent<sup>12</sup>. The size-corrected complex dielectric functions for Ag shells and Au core were calculated according to the procedure described in Annex 3. The calculated spectra obtained for different Au core sizes and silver shell thicknesses are plotted in figure 3.1 (b) and are consistent with the general trend observed in experimental spectra. Nevertheless, for the Au<sub>10nm</sub>(PC)@Ag NPs spectra, the contribution from the silver component increases with the shell thickness but remains slightly smaller than in the experiment. For Au<sub>5nm</sub>(PC)@Ag NPs, in each calculated spectra, the contribution of the gold core remains more pronounced whatever the silver shell thickness, although it decreases with the thickness of silver layer as experimentally observed. The disagreement is all the greater as the number of silver layers reached is 3. The discrepancies between the experimental and calculated spectra may arise from the slight deviation from the ideal concentric spherical shape, as revealed in figure 2.9 in Chapter II by the EELS mapping of the core-shell NPs. And they also from a uniform shell thickness especially as it increases (see the HRTEM image of Au<sub>10nm</sub>@Ag NPs in figure 2.11 in Chapter II). The presence of pure Ag NPs in coexistence with core-shell Au@Ag NPs, which could explain the more pronounced contribution of silver component in the experimental spectra must be excluded according to the EDX results (see Table 2.4 in Chapter II) and LFRS spectra performed on these samples (Figure 3. 5). Finally, we can note that the peak corresponding to the contribution of silver to plasmon resonance appears at shorter wavelengths in all simulated spectra than in experimental ones. We cannot exclude an Au-Ag alloy layer at the interface according to EELS profiles (Figure A.4 in Annex). The interface in

the Au(SC)@Ag NPs (Figure 2.13 in chapter II) is thus no more than 1nm, with a likely value of half of this or less, corresponding to about 1 unit cell. The Au(PC)@Ag NPs are more difficult to analyze in this way, with some localized regions in which the silver layer penetrates further into the gold (figure 2.9 in chapter II). Nevertheless, there is no particular reason to believe the interface width here would be significantly different. This alloy layer could disturb the optical spectra and be at the origin of the disagreement with the DDA calculations.

The SPR evolution of Au<sub>5nm</sub>(PC)@Ag NPs covered with an even thicker layer of Ag obtained under higher temperature conditions (see Chapter II) are represented in Figure 3.2 (a). Both Au<sub>5nm</sub>(PC)@Ag NPs with thickness  $e = 2.5$  nm ( $\sim 7$  atomic layers), 3.5 nm ( $\sim 10$  atomic layers), shows SPR component whose profile and wavelength correspond to the SPR of Ag NPs of similar size ( $\lambda_{\max}=410$  nm). The corresponding DDA calculation is shown in figure 3.2 (b) and it shows a clear agreement with absorbance spectra obtained from experiment. Only difference is the broadening of the peak in case of experimental absorption spectra due to the size distribution of NPs.

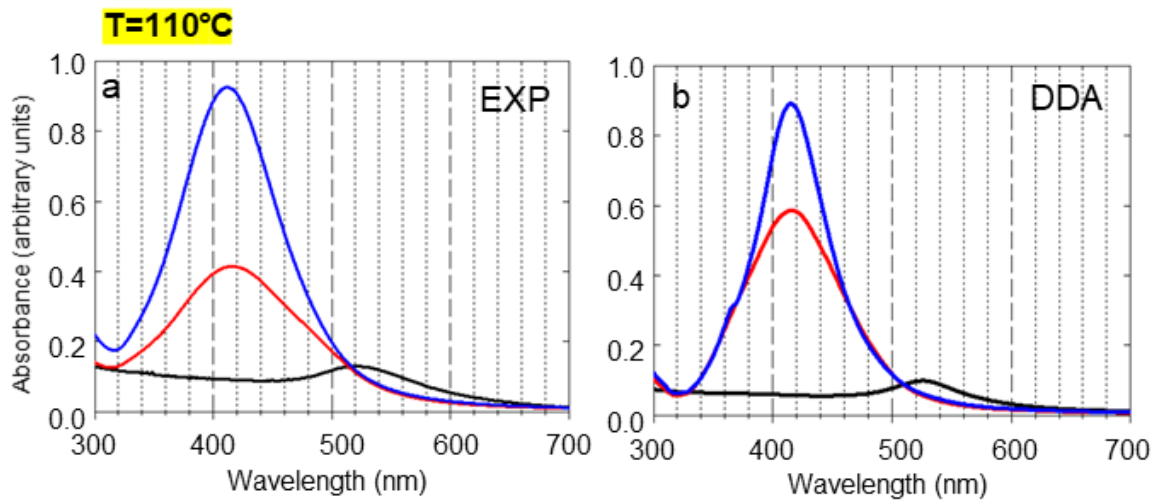


Figure 3.2. a) Experimental absorption spectra of core-shell Au<sub>5nm</sub>(PC)@Ag NPs with different Ag thicknesses  $e = 0$  (black curve),  $e = 2.5$  nm (red curve), and  $e = 3.5$  nm (blue curve). (b) Corresponding DDA calculated absorption spectra of Au@Ag NPs with shell thicknesses as those considered in (a).

## 2.2. Au@M (M=Pd or Pt) core-shell nanoparticles

We studied the optical properties of Au@Pd and Au@Pt core-shell NPs at visible wavelengths, which is essential for photocatalysis functionality. The objective is to have a clarified idea of the physical origin of enhanced catalysis functionality.

The replacement of shell materials from plasmonic materials (Ag) to catalytic materials (Pd or Pt) was able to synthesize because of the flexibility and robustness of the synthesis process developed in this work (see chapter II). The optical spectra for Au<sub>10nm</sub>(PC) seed solution and Au<sub>10nm</sub>(PC)@M NPs (M=Pt or Pd) were measured for different Pd or Pt thicknesses (Figure 3.3 (a) and (b) respectively). We observed only one resonance which is progressively blue shifted and damped in intensity with increasing Pt or Pd intake (see table 3.1). Our results show thus that Au@Pd and Au@Pt bimetallic NPs have their SPR in the visible range with a broad tunability, which is difficult for pure Pd and Pt NPs to achieve. For pure Pd or Pt NPs, there is indeed no SPR effect in this visible wavelength regime<sup>13</sup>. These spectral behaviors are in agreement with a core-shell structure.

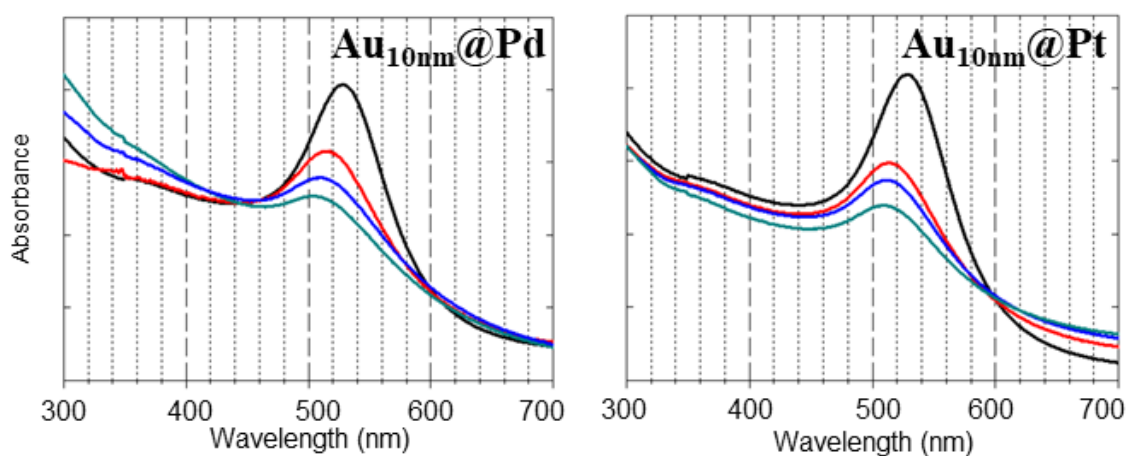


Figure 3.3. (a) Absorption spectra of core-shell Au<sub>10nm</sub>@Pd NPs with different thicknesses  $e = 0$  (black curve),  $e = 0.5$  nm (red curve),  $e = 0.65$  nm (blue curve),  $e = 0.95$  nm (green curve). (b) Absorption spectra of core-shell Au<sub>10nm</sub>@Pt NPs with different thicknesses  $e = 0$  (black curve),  $e = 0.25$  nm (red curve),  $e = 0.55$  nm (blue curve),  $e = 0.9$  nm (green curve).

Table 3.1. Maximum SPR wavelength and percentage of damping intensity of SPR calculated from the ratio between the intensity at the maximum of the SPR of core-shell NPs to that of the seed NPs for Au@M core-shell NPs (M=Pd or Pt) with a variable shell thickness(*e*).

Samples	Shell thickness <i>e</i> (nm)	Maximum SPR wavelength (nm)	Damping intensity %
Au <sub>10nm</sub>	0	529	0
Au <sub>10nm</sub> @Pd	0.4 (~1 atomic layer)	516	23
	0.55 (~2 atomic layer)	512	32
	0.95 (~3 atomic layers)	505	38
Au <sub>10nm</sub> @Pt	0.25 (~1 atomic layer)	515	29
	0.55 (~ 2 atomic layers)	513	35
	0.9 (~3 atomic layers)	509	43

### 2.3. Ag@M (M=Pd or Pt) core-shell nanoparticles.

The replacement of core material from Au to Ag with stronger plasmonic properties is beneficial to the enhancement of photocatalytic properties of both Pd and Pt. The optical spectra for Ag seed solution and Ag@ M (M=Pt or Pd) solutions (characterized by different Pd or Pt thickness) are measured by UV-visible absorption spectroscopy (Figures 3.4 (a) and (b)). The experimental spectra show progressive blue shift and intensity damping of the SPR maximum for increasing Pd and Pt thickness (see Table 3.2). The damping effect by the Pt or Pd shell appears stronger on silver core than gold core (see Tables 3.1 and 3.2).

To confirm the effect of shell thickness on the optical properties of Ag@Pt and Ag@Pd NPs, DDA calculations were performed. For calculated spectra, progressive blue shift and SPR intensity damping for increasing the shell thickness are also observed (see figures A.9 and A.10 in Annex 4). However, the widths of the SPR peaks between the calculated and experimental spectra differ. The experimental SPR peaks are indeed broader and this can be attributed to the size distribution of the NPs which is not considered in the DDA calculations.

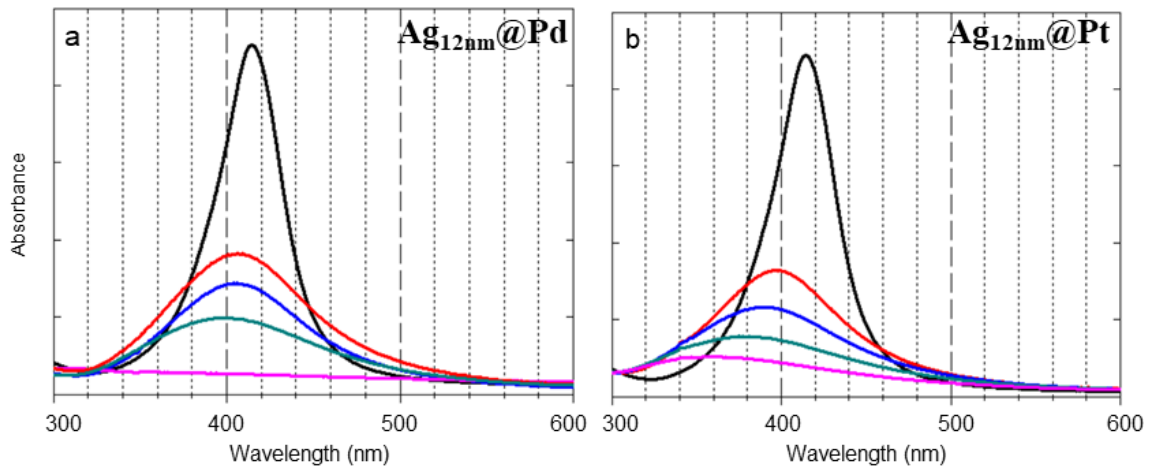


Figure 3.4. Experimental absorption spectra of core-shell  $\text{Ag}_{12\text{nm}}@M$  NPs. (a)  $\text{Ag}_{12\text{nm}}@Pd$  NPs with different thicknesses  $e = 0$  (black curve),  $e = 0.2$  nm (red curve) and  $e = 0.3$  nm (blue curve). (b)  $\text{Ag}_{12\text{nm}}@Pt$  NPs with different thicknesses  $e = 0$  (black curve),  $e = 0.2$  nm (red curve),  $e = 0.3$  nm (yellow curve),  $e = 0.4$  nm (green curve) and  $e = 0.65$  nm (blue curve).

Table 3.2. Maximum SPR wavelength and percentage of damping intensity of SPR calculated from the ratio between the intensity at the maximum of the SPR of core-shell NPs to that of the seed NPs for  $\text{Ag}@M$  core-shell NPs ( $M=Pd$  or  $Pt$ ) with a variable shell thickness( $e$ ).

Sample	Shell thickness $e$ (nm)	Maximum SPR wavelength (nm)	Damping intensity %
Ag	0	415	0
$\text{Ag}_{12\text{nm}}@Pd$	0.2	409	61
	0.3	405	71
	0.4	404	80
	0.65	399	99
$\text{Ag}_{12\text{nm}}@Pt$	0.25	399	74
	0.3	390	83
	0.4	380	88
	0.65	355	97

### 3. Vibrational properties of Au@Ag core-shell NPs

Low frequency Raman scattering (LFRS) of bimetallic particles is an area of investigation that has been little explored until recently. Raman scattering experiments carried out on Au@Ag particles lead on many points to results consistent with those already obtained with Au NPs<sup>3,14</sup>. They allow us to characterize the crystallinity of NPs between polycrystalline and monocrystalline, their size and shape.

Acoustic vibrations of Au<sub>5nm</sub>(PC)@Ag, Au<sub>5nm</sub>(SC)@Ag and Au<sub>10nm</sub>(PC)@Ag core-shell NPs with different silver shell thicknesses were investigated by LFRS to confirm the crystallinity of the Au core and to study the strength of the core-shell bond. The corresponding Stokes and anti-Stokes LFRS spectra are presented in figure 3.5. Each spectrum obtained from Au<sub>5nm</sub>(PC)@Ag and Au<sub>10nm</sub>(PC)@Ag core-shell NPs (figures 3.5 (a) and 3.5 (b)) exhibits an intense band ascribed to the Raman scattering by the quadrupolar vibrational mode of the NPs. Whatever the  $D_{CORE}$  value, this band shifts towards lower frequencies when the shell thickness is increased. Such a behavior qualitatively agrees with the usual dependence of the vibrational frequencies on the inverse of the NP diameter<sup>15</sup>. The measured frequencies at the maximum of the quadrupolar band are listed in Table 3.3 and compared to those calculated using a model based on Lamb's theory<sup>16</sup> and Eringen and Suhubi's equations<sup>17</sup>. The same approach was already described in a previous work<sup>5</sup> to numerically determine the frequencies of the free vibrational modes of core-shell and onion-like systems.



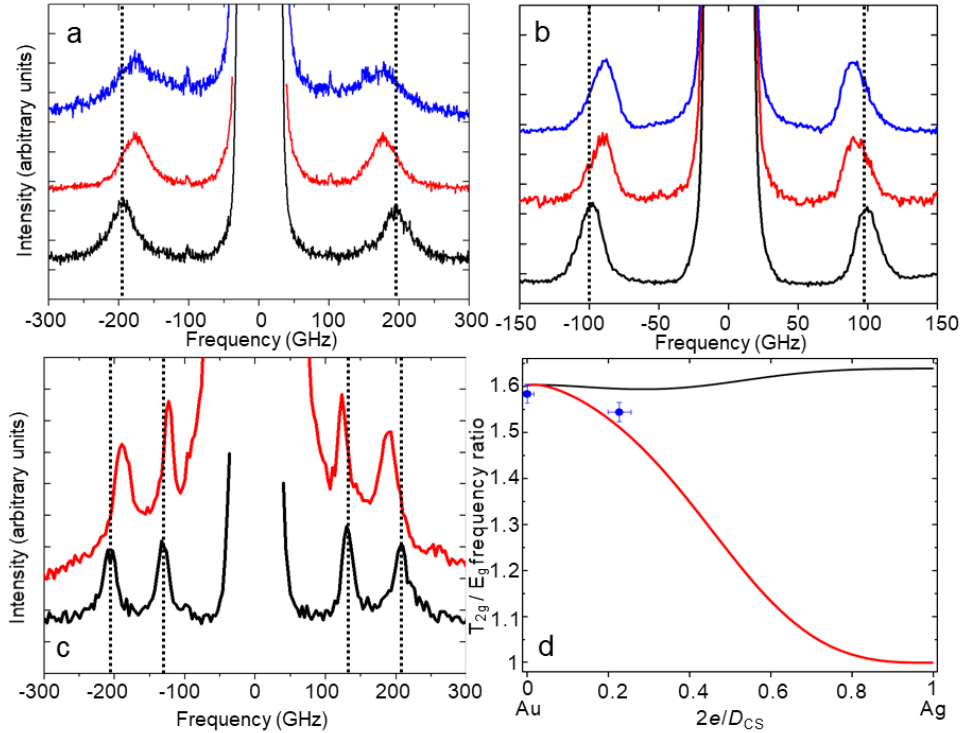


Figure 3.5. Stokes / anti-Stokes Raman scattering spectra of Au@Ag core-shell NPs with different Ag thicknesses  $e$  and core crystallinities (PC or SC). (a) Comparison of the spectrum of Au<sub>5nm</sub>(PC) NPs (black curve) with those of Au<sub>5nm</sub>(PC)@Ag with  $e = 0.5$  nm (red curve) or  $0.65$  nm (blue curve). (b) Comparison of the spectrum of Au<sub>10nm</sub>(PC) NPs (black curve) with those of Au<sub>10nm</sub>(PC)@Ag NPs with  $e = 0.8$  nm (red curve) or  $1.7$  nm (blue curve). (c) comparison of the spectrum of Au<sub>5nm</sub>(SC) NPs (black curve) with those of Au<sub>5nm</sub>(SC)@Ag NPs with  $e = 0.85$  nm (red curve). All the spectra are normalized and vertically shifted for clarity. (d) Calculated and measured (blue points)  $T_{2g}/E_g$  frequency ratio of Au<sub>5nm</sub>(SC)@Ag NPs in function of the relative shell thickness variation defined by  $2e/D_{CS}$  for epitaxial (black curve) and isotropic Ag shell (red curve).

For the Au(PC)@Ag NPs the calculated vibrational frequencies reported in Table 3.3 are in good agreement with the measured ones, especially for the largest values of  $D_{CORE}$ . Although the NPs self-assemble to form 3D superlattices, in which they are in contact with neighboring NPs via the coating molecules, their acoustic vibrations are successfully estimated in the frame of a free elastic sphere model. The calculated frequencies are determined by modeling the core-shell NPs as free elastic spheres made of an Au core and an Ag shell. Both materials are assumed to have isotropic elasticity. The transversal and longitudinal sound velocities used for Au and Ag are respectively  $v_t[\text{Au}] = 1250$  m/s,  $v_l[\text{Ag}] = 1740$  m/s,  $v_t[\text{Au}] =$

3330 m/s and  $v_1[\text{Ag}] = 3747$  m/s. In addition, to mimic a perfect contact between the core and shell materials, it is assumed that there is continuity of both the vibrational displacement and the force at the Au/Ag interface. The agreement between the measured and calculated vibrational frequencies supports therefore the core-shell structure of the NPs, i.e. the separation of the two metals. Moreover, it makes sense from this comparison to infer a strong contact between the Au core and the Ag shell.

Table 3.3. Measured quadrupolar vibrational mode frequencies of  $\text{Au}_{5 \text{ or } 10\text{nm}}(\text{PC})@\text{Ag}$  NPs compared to those calculated for a free elastic isotropic nanosphere with an Au core - Ag shell structure. The thickness  $e$  is equal to  $(D_{\text{CORE}}-D_{\text{CS}})/2$

$D_{\text{CORE}}$ (nm)	$D_{\text{CS}}$ (nm)	$e$ (nm)	Measured frequency (GHz)	Calculated frequency (GHz)
5.3	-	-	199	200
5.3	6.3	0.50	177	185
5.3	6.6	0.65	171	181
10.6	-	-	100	100
10.6	12.2	0.80	91	92
10.6	14.0	1.70	88	88

For the  $\text{Au}_{5\text{nm}}(\text{SC})$  seeds and the corresponding  $\text{Au}_{5\text{nm}}(\text{SC})@\text{Ag}$  NPs with a total diameter  $D_{\text{CS}}$  of 7.5 nm, two bands are observed and correspond to a splitting of the quadrupolar vibration into two components (figure 3.5 (c)) which was shown in previous papers as being an effect of crystallinity<sup>18-20</sup>. This quadrupolar mode splitting into  $E_g$  and  $T_{2g}$  modes is related to the variation of the transverse sound speeds with the propagation direction of phonons in the cubic lattice. The ratio of the calculated frequencies of the  $T_{2g}$  and  $E_g$  peaks is about 1.6 for gold which makes it a powerful indicator of the crystallinity of the NPs. Calculations for core-shell NPs were performed for an Au(SC) core surrounded by a shell made of either epitaxial silver or multiply-twinned silver (modeled as isotropic silver) with varying thicknesses using the elastic constants for bulk materials<sup>21</sup> and the sound speeds given above for the isotropic approximation of silver (see Table 3.4). We focus on the  $T_{2g}/E_g$  frequency ratio in the following

to monitor the elastic anisotropy of the core-shell NPs. The results are presented in figure 3.5 (d). The shell thickness variation is represented by  $2e/D_{CS}$ . On the left side of the graph ( $e = 0$ ) the NPs are  $Au_{5nm}(SC)$  NPs. On the right side ( $e \gg D_{CORE}$ ), the core can be neglected and the NPs are  $Ag(SC \text{ or } PC)$  NPs depending on the model. For an epitaxial silver shell, the  $T_{2g}/E_g$  frequency ratio hardly changes with  $e$  while in the case of a multiply twinned silver shell the splitting vanishes as  $e$  increases. The experimental ratios are also plotted in this graph with error bars considering the experimental accuracy. As already reported in previous works, calculations overestimate the experimental splitting for the  $Au(SC)$  NPs<sup>20</sup>. As we expect the same to be true for the  $Au_{5nm}(SC)@Ag$  core-shell NPs, we compare the variations of the  $T_{2g}/E_g$  frequency ratio as the shell thickness increases in the following. For the epitaxial silver shell, the variation of the calculated  $T_{2g}/E_g$  frequencies ratio between the  $Au$  NP and the  $Ag@Au$  NP is small ( $\sim 0.008$ ). For the isotropic silver shell, it is about ten times more ( $\sim 0.09$ ). The experimental variation falls in-between those two values ( $\sim 0.04$ ) but with non-negligible error bars. This intermediate value probably indicates that the actual structure of the core-shell  $Au_{5nm}(SC)@Ag$  NPs is more complex than previously thought. We assumed in these calculations an abrupt interface between the core and the shell and a shell having a constant thickness. These may be good first-order approximations only. As already discussed before, we cannot rule out the presence of interdiffusion between gold and silver. The presence of such an intermediate layer would modify the frequencies. Also, a thinner shell on the (110) facets of the  $Au_{5nm}(SC)@Ag$  core-shell NPs would increase the calculated  $T_{2g}$  frequencies and improve the agreement between the experimental data and the epitaxial model.

Table 3.4. Measured quadrupolar vibrational mode frequencies of  $Au_{5nm}(SC)@Ag$  NPs compared to those calculated using the Rayleigh-Ritz variational method.

$D_{core}$ (nm)	$D_{CS}$ (nm)	$e$ (nm)	measured frequency (GHz)		calculated frequency (GHz)		Ag shell growth
			$E_g$	$T_{2g}$	$E_g$	$T_{2g}$	
5.8	-	-	130.0	206.0	128.7	207.7	-
5.8	7.5	0.85	123.0	190.0	115.3	185.3	Cubic
					122.9	187.1	Isotropic

## 4. Catalytic properties of Au@M (M=Ag, Pt or Pd) core-shell NPs

Noble metal NPs, especially Au, Ag, Pt and Pd, are known to have a high catalytic activity in the reduction of different nitroaromatic compounds to the corresponding amino compounds in water in ambient conditions<sup>22-24</sup>. Core-shell Au@M (M=Ag, Pt or Pd), are expected to present enhanced catalytic activities due synergistic effects between both metals<sup>25</sup>. As observed previously the metallic shell whose thickness is finely controlled thanks to our two-step synthesis method, modifies the optical properties of the gold core. That is fundamental for photocatalysis functionality.

In this work, we have carried out a series of experiments in order to compare the catalytic reactivities of Au@M (M= Ag, Pt or Pd) core-shell NPs with different core size and crystallinity and shell thickness, in the reduction of 4-nitrophenol (4-NP) to 4-aminophenol (4-AP) in the aqueous phase in the presence of sodium Borohydride (NaBH<sub>4</sub>). From those experiments, we determined physical parameters such as the apparent rate constant ( $K_{app}$ ) and the activation energy ( $E_a$ ) of the reactions.

In chemical industries, the conversion from 4-nitrophenol (4-NP) to 4-aminophenol (4-AP) can be widely used in fabricating of analgesics and antipyretic drugs<sup>22,26</sup>. From that, there is great industrial demand for aromatic amino compounds. In addition, the model reaction of the reduction of 4-NP to 4-AP is selected, because it can easily monitor the reaction kinetics by UV-Vis spectroscopy during the color changes associated with the conversion of 4-NP to 4-AP.

### 4.1. Experimental setup

Catalytic properties of core-shell NPs were characterized by UV-Vis spectrometer by measuring the absorbance change of solution in quartz cell ( $l=1\text{ cm}$ ) by time from reactant (4-nitrophenol) to product (4-aminophenol) at controlled temperature by water flow (Figure 3.6). Detailed conditions will be explained below.

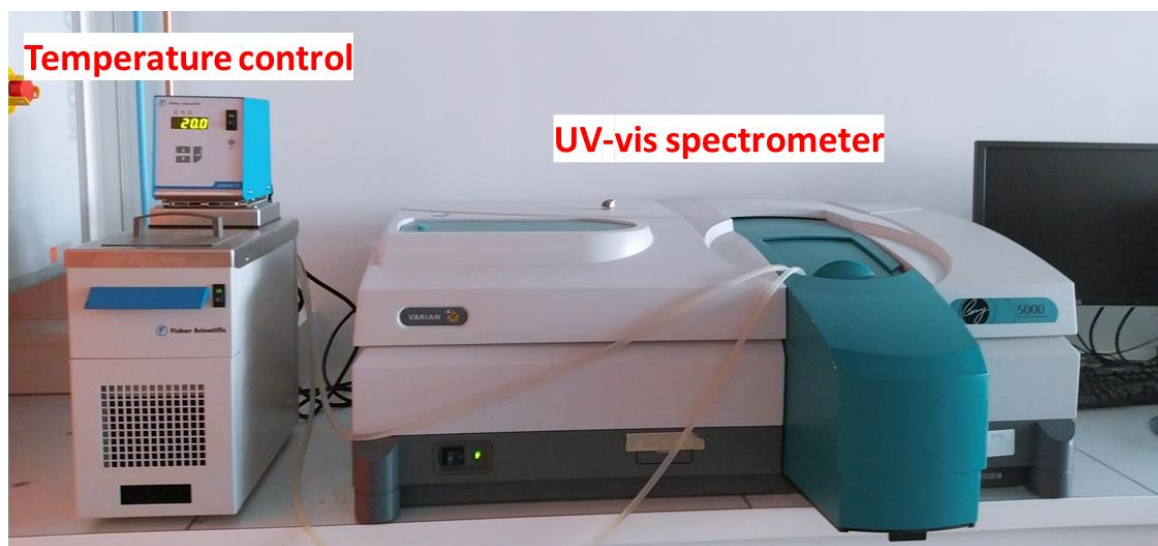


Figure 3.6. UV-Vis spectrometer experimental setup with controlled temperature setup.

#### 4.1.1. Preparation of NPs and ligand exchange

The characteristics (core size and crystallinity, final diameter, shell nature and thickness) of the different NPs (Au NPs and Au@M (M=Ag, Pt or Pd) core-shell NPs) that were the subjects of our study are shown in the table 3.5 and 3.6. The effects of shell thickness on one hand (see section 4.3) and core crystallinity on the other hand (see section 4.4) were tested on the catalytic response of the NPs.

Au seeds with 10 nm diameter are synthesized through direct reduction in oleylamine. Then, the growth of Ag, Pd or Pt shell was performed *via* the two steps methods described in chapter II. The obtained NPs are all reported in table 3.5. As reported in chapter II, Au seeds with 5 nm diameter were synthesized through organometallic route by reduction of AuClPPH<sub>3</sub> salt by TBAB complex at 100°C in presence of 1-dodecanethiols ligands. The crystallinity selection of Au<sub>5nm</sub>NPs was obtained then through the preferential self-assembly process of single crystal Au(SC) NPs which allowed to separate SC from PC NPs. The Au or Ag shell overgrowth on Au<sub>5nm</sub> seeds with different crystallinity was then performed through the two steps method (see table 3.6).

The concentrations of NPs (or number of NPs per unit volume) were precisely controlled to study their catalytic activity. It is known that the number of atoms at the surface plays an important role on catalytic properties<sup>11,27,28</sup>. All the NPs considered in this study are spherical, we thus adjusted the concentration in NPs to keep the same number of atoms at the surface. The total surface area for a given colloidal solution is defined as:

$$\text{Total surface area} = C_{\text{NPs}} \times \text{Surface area per NP (S)}$$

where  $C_{\text{NPs}}$  is concentration of NPs, S is surface area per spherical NP of diameter D.

In all the experiments, the total number of atoms at NP surface is expected to be the same in order to reveal synergistic effects between the core and the shell in relation to the nature of the shell and the crystallinity of the core. As a result, NPs concentration was adjusted. Table A.1 in Annex 5 shows the list of the characteristics of the NPs and their concentration used to catalyze the reaction.

Table 3.5. Final sizes, core crystallinity and chemical composition of Au NP seeds, and corresponding Au@M (M=Ag, Pt or Pd) core-shell NPs

<b>Au (PC) NPs</b>	<b>Au(PC)@Ag NPs</b>							
	<b>D (nm)</b>	<b>e (nm)</b>	<b>D (nm)</b>	<b>e (nm)</b>	<b>D (nm)</b>	<b>e (nm)</b>	<b>D (nm)</b>	<b>e (nm)</b>
10.6 ± 0.8	11.4±1.0	0.8	12.2±1.0	0.8	14±1.0	1.7	14.8±1.0	2.1
	1 atomic layer		2 atomic layers		5 atomic layers		6 atomic layers	
	<b>Au(PC)@Pd NPs</b>							
	<b>D (nm)</b>	<b>e (nm)</b>	<b>D (nm)</b>	<b>e (nm)</b>	<b>D (nm)</b>	<b>e (nm)</b>	<b>D (nm)</b>	<b>e (nm)</b>
	11.4±0.9	0.4	12.5±0.9	0.95	13.6±1.0	1.5	14.0±1.2	1.7
	1 atomic layer		2 atomic layers		4 atomic layers		5 atomic layers	
	<b>Au(PC)@Pt NPs</b>							
	<b>D (nm)</b>	<b>e (nm)</b>	<b>D (nm)</b>	<b>e (nm)</b>	<b>D (nm)</b>	<b>e (nm)</b>	<b>D (nm)</b>	<b>e (nm)</b>
	11.1±2.2	0.25	11.7±2.5	0.55	12.9±2.3	1.15	13.4±2.3	1.4
	1 atomic layer		2 atomic layers		3 atomic layers		4 atomic layers	

Table 3.6. Final sizes, core crystallinity and chemical composition of Au NPs and Au@Ag core-shell NPs

<b>Au<sub>7nm</sub> NPs</b>	<b>Au<sub>5nm</sub>@Ag NPs</b>		<b>Au seed (mixture PC/SC)</b>
<b>D (nm)</b>	<b>D (nm)</b>	<b>e (nm)</b>	<b>D (nm)</b>
7.0 ± 0.6 (PC)	7.0±0.5 (PC)	0.7	5.4±0.4
7.2 ± 0.5 (SC)	7.5±0.4 (SC)	0.6	5.8±0.4

growth  
←

The reaction of 4-nitrophenol (4-NP) with NaBH<sub>4</sub> to form 4-aminophenol (4-AP) takes place in water, however, all NPs synthesized in this thesis work are dispersed in organic solvent such as toluene or chloroform and coated by alkyl chain like oleylamine or 1-dodecanethiols (see Chapter II). So, it is necessary to exchange the hydrophobic ligands by hydrophilic ligands on NP surfaces to allow their dispersion in water. The objective of ligand exchange is to replace alkyl chains with a shorter, charged ligand to allow the transfer of the NPs into the polar solvent and to favor the adsorption of the reactants on the free NP surface for catalysis. The procedure of ligand exchange has been adapted from the literature<sup>29-31</sup>.

We decided to exchange oleylamine ligands by mercaptosuccinic acid (MSA) (Figure 3. 7). This concerns the case of 10 nm gold seeds and associated core-shells NPs. This acid has a thiol function that will have a stronger affinity for silver than the amine function of oleylamine. This will shift the equilibrium in favor of ligand exchange. In addition, MSA has two carboxylic acid functions that are easily deprotonated by the action of a base. The formation of carboxylates will thus favor the transfer into aqueous solution. MSA is therefore a good candidate for carrying out ligand exchange and simultaneous transfer of NPs into the aqueous phase<sup>32,33</sup>.

At first, 23 μmol of MSA and 26 μl of a base as tetramethylammonium hydroxide (TMAOH) were dispersed in 200 μl of methanol. Then, 1ml NPs solution dispersed in chloroform is added with a NP concentration C<sub>NPs</sub>=0.14 μmol·L<sup>-1</sup>. The color of solution

immediately changed into purple. After we sonicate them to favor the ligand exchange, the centrifugation was done for 5 minutes with 3500 rpm. The precipitates were re-dispersed in 1 ml methanol and repeated one more centrifugation (3500 rpm/ 5mins). Finally, the precipitate is dispersed in 1 ml of water. To help the NP stabilization, 10  $\mu$ l tetramethylammonium hydroxide ( $C_4H_{13}NO$ ) were added to the solution. To remove the excess of free ligands, 2 ml of acetone was added, and the solution was centrifuged at 3500 rpm during 5mins. Finally, the precipitate was dispersed in 1 ml water. After exchange, NPs are electrostatically dispersed in water. This decreases the interparticle distance, as observed on TEM images (Figures 3.8 (a) and (b)).

We observed that 1-dodecanethiol ligands could not be exchanged with MSA acid. This concerns the case of  $\sim 5$  nm gold seeds synthesized via organometallic route (see chapter II and Table 3.6) and coated by 1-dodecanethiols. 1-dodecanethiols are more strongly bound to the gold surface via their sulfur atoms than oleylamine via their nitrogen atoms<sup>34</sup>. In this case, the ligand exchange was performed in two steps: i) exchange of 1-dodecanethiol ligands by oleylamine via the overgrowth of gold or silver shell on  $Au_{5nm}\text{-}C_{12}$  seeds from the reduction of the  $[Au/Ag(OLA)_n]$  complexes (see chapter II) leading to  $Au_{7nm}$  or  $Au_{5nm}@Ag$  NPs, ii) exchange of oleylamine ligands by MSA by the procedure described above and Figure 3.7.

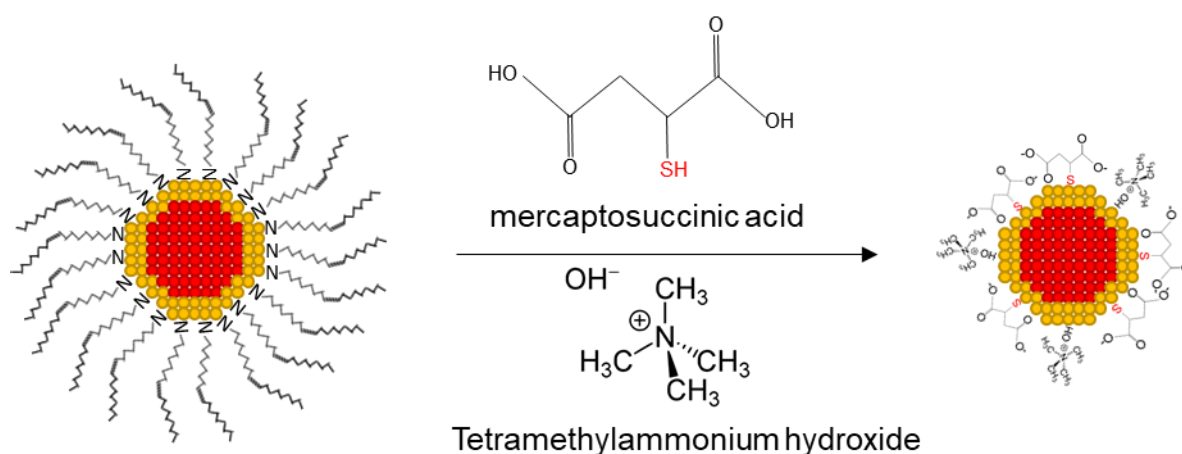


Figure 3.7. Ligand exchange reaction between oleylamine and MSA/TMAOH to lead water soluble NPs



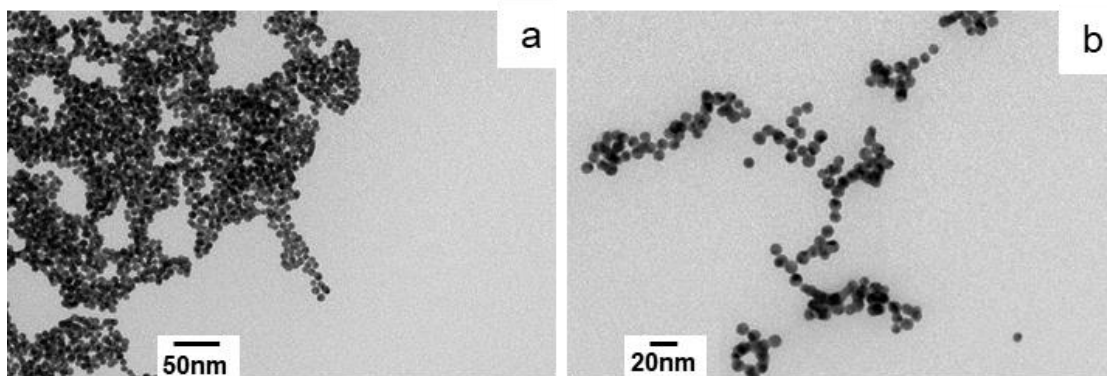


Figure 3.8. (a) and (b) Typical TEM Images at different magnifications of  $Au_{10nm}(PC)@Ag$  NPs with 12.2 nm as final diameter dispersed in water after ligand exchange.

The nature of the ligands adsorbed on the surface of core-shell NPs  $Au_{5nm}@Ag$  and  $Au_{10nm}@Ag$  was characterized by X-ray photoelectron spectrometry (XPS) measurements in collaboration with Pr. Vincent NOEL in the laboratory ITODYS (Paris University). Only main results are presented in Figure 3.9 and 3.10, and all detailed spectra are presented in Annex 6.

For  $Au_{10nm}@Ag$  NPs obtained just after synthesis and before ligand exchange, the XPS signals show the presence of nitrogen with a  $N_{1s}$  peak at 400 eV, as a signature of oleylamine. After the ligand exchange process,  $Au_{10nm}@Ag$  NPs show an S-Metal bond at 164 eV (at.% = 3.25) from the coordination of MSA (Figure 3.9 (i)). The XPS signals show two  $N_{1s}$  peaks, one at 400 eV is  $NH_2$  from the coordination of oleylamine (at.% = 0.44) and the other one at 404 eV is from  $NO_x$  (at.% = 2.25) which is originated from TMAOH (Figure 3.9(f)). The trace of residual oleylamine (at.% = 0.44) is relatively minor compared to the trace of  $NO_x$  (at.% = 2.25). The ratio between two major ligands (MSA/TMAOH) or (S /  $N_{at\ 400\ eV}$ ) is around 1.4 (= 3.25 / 2.25). Also,  $O_{1s}$  peak is observed at 533 eV (at % = 9.79), which is attributed to the C = O bond in MSA (Figure A.12 in annex 6). The atomic percentage of O is close to double the quantity of S, as expected regarding the crude formula of MSA. The chemical state of the silver shell was also studied by XPS. In the literature, the binding energy (BE) of the Ag  $3d_{5/2}$  peak from Ag(0) was reported at 368.24 eV [fwhm= 0.63 eV] and the Ag  $3d_{5/2}$  peak position of Ag(I) in  $Ag_2O$  was found to shift to lower BE than that of Ag(0) with BE= 366.8 eV [fwhm=0.8 eV] with a broad satellite at 368.2 eV [fwhm= 1.2 eV] attributed to Ag(III)<sup>35</sup>. In the experimental XPS spectra for Au@Ag NPs before and after ligand exchange (figure 3.10c and e), Ag  $3d_{5/2}$  peak is observed at 368 eV, with no evident supplementary peak around 366.8 eV. Furthermore, we do not observe the  $O_{1s}$  peak from AgO at 528.4 eV. Thus, we clearly demonstrate a ligand

exchange between oleylamine and a mixture of MSA and TMAOH leading to water soluble NPs, and in both cases the silver shell remains not oxidized.

For Au<sub>5nm</sub>(PC)@Ag NPs synthesized from Au<sub>5nm</sub> seeds coated by 1-dodecanethiols (Figure 3.10), there is no XPS signal of S and N<sub>1s</sub> peak at 400 eV is the signature of oleylamine. That confirms a first ligand exchange between 1-dodecanethiol and oleylamine during the silver shell overgrowth. After the second ligand exchange procedure to allow the NP transfer into water, the XPS signals show two N<sub>1s</sub> peaks, one at 400 eV is from NH<sub>2</sub> as a signature of residual oleylamine (at.%=0.44) and the other one at 404 eV is from NO<sub>x</sub> (at.%=2.25) which is originated from TMAOH. The ratio between two major ligands MSA:TMAOH deduced from the S and N<sub>1s</sub> peaks at 162 eV (at.%=3.44) and at 404 eV (at.%=2.25) respectively is around 1.5 (1.5:1) and is similar to that measured on Au<sub>10nm</sub>@Ag NPs Furthermore, O<sub>1s</sub> peak is observed at 533 eV (at.% =7.95), which is attributed to the C = O bond in MSA (see figure A.14 in annex 6). The atomic percentage of O is close to double ( $\approx 2.3$ ) the quantity of S whose peak is at 162 eV (at.%=3.44), It is in agreement with the crude formula of MSA and confirm its presence as ligands.

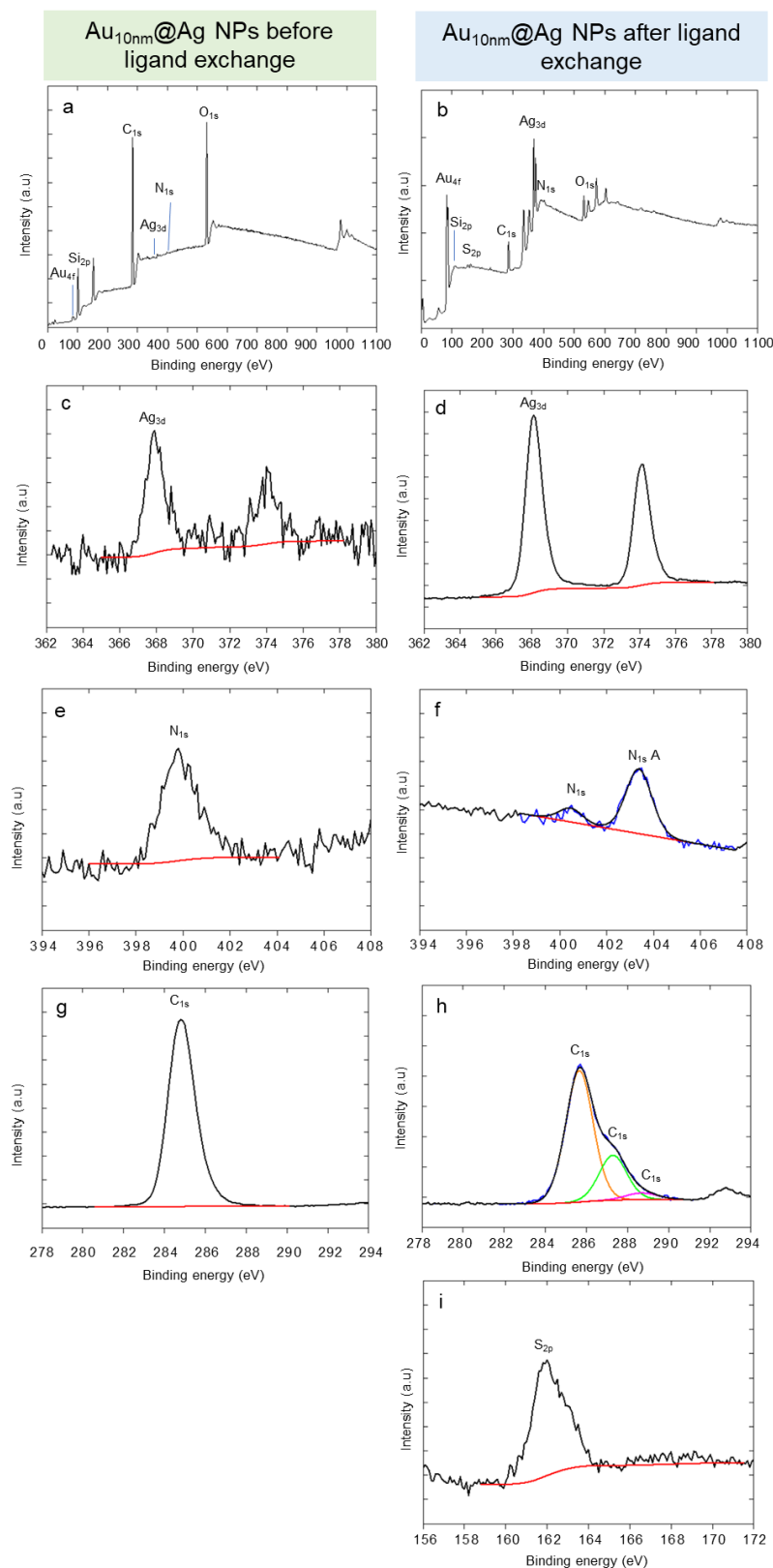


Figure 3.9. XPS spectra 2p for Au<sub>10nm</sub>@Ag core-shell NPs before ligands exchange and (left column) after ligand exchange (right column) in detail: (a, b) survey XPS spectra (c, d) Ag (3d), (e, f) N(1s), and (i) S(2p).

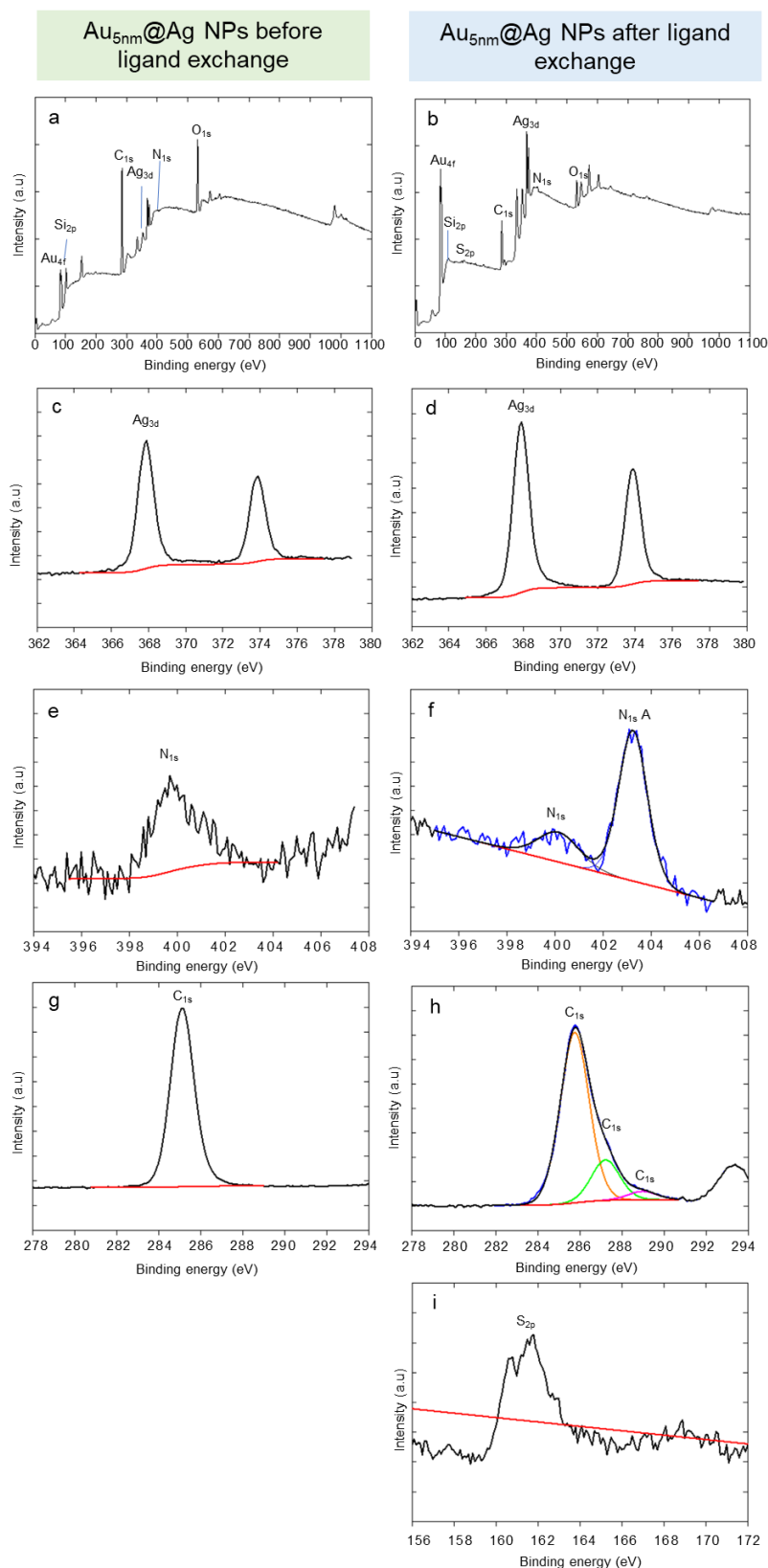


Figure 3.10. XPS spectra 2p for  $Au_{5nm}@Ag$  core-shell NPs before ligands exchange and (left column) after ligand exchange (right column) in detail: (a, b) survey XPS spectra (c, d) Ag (3d), (e, f) N(1s), and (i) S(2p).

#### 4.1.2. Catalytic reduction of 4-nitrophenol (4-NP) in 4-aminophenol (4-AP) by NPs

The catalytic capabilities of mono and bimetallic NPs considered in this Ph.D work (Tables 3.5 and 3.6) were ascertained in the reduction of 4-nitrophenol to 4-aminophenol in the presence of sodium borohydride in aqueous phase. The reaction mechanism can be explained by hydrogen adsorption by NPs that transported the hydrogen between  $\text{NaBH}_4$  and 4-NP (Figure 3. 11). That hydrogen is produced when  $\text{NaBH}_4$  reduces water. NPs adsorb hydrogen from  $\text{NaBH}_4$  and release it during the reduction process, therefore NPs is a hydrogen carrier in this reduction process<sup>36</sup>.

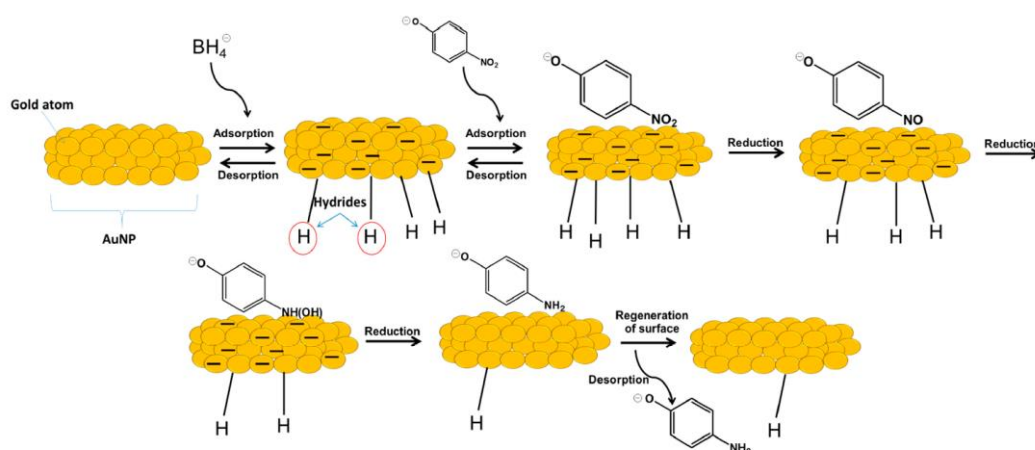


Figure 3.11. Schematic illustration of the reduction of 4-NP to 4-AP mechanism with NPs as catalysts [De Oliveira et al. 2016]<sup>27</sup>.

Optical measurement was performed using 1 cm quartz cell containing 150  $\mu\text{l}$  of 4-nitrophenol ( $C=4$  mM) to which 20  $\mu\text{l}$  of  $\text{Au}_{10\text{nm}}$ NPs solution. Then, 500  $\mu\text{l}$  of sodium borohydride ( $\text{NaBH}_4$ ,  $C=0.4$  M) used as reducing agent is added. Finally, water is added to make the total volume to 4 ml.

The 4-NP solution show a strong absorption peak at 317 nm<sup>37,38</sup>. The addition of the reducing agent  $\text{NaBH}_4$  induces the deprotonation of OH group of 4-NP and formed 4-nitrophenolate ion appearing at 400 nm in the UV-vis spectrum. The color of the 4-NP solution changed from light yellow to vivid yellow immediately after adding  $\text{NaBH}_4$  due to 4-nitrophenolate ion as it is shown in figure 3.12 a (left side)<sup>39</sup>. The reduction of 4-NP does not

occur without the presence of a catalyst as it was explained earlier<sup>40</sup>. The thermodynamically favorable reduction of 4-NP to 4-AP ( $E_0 = -0.76$  V vs. NHE) by  $\text{H}_3\text{BO}_3/\text{BH}_4^-$  ( $E_0 = -1.33$  V vs. NHE) produced large potential difference with negative free energy. The presence of a large energy between the mutually repelling negative ions of 4-NP and  $\text{BH}_4^-$  was responsible for the slow kinetics of the reaction.<sup>22</sup> Alternatively, NPs can absorb negative ions and able to act as electronic relay systems to transfer electrons donated by borohydride ions to the nitro groups of 4-NP, which is expected to lower the kinetic barrier and thus catalyze the reduction. Metallic NPs are known to catalyze the reduction reaction by facilitating the electron transfer process from the donor  $\text{BH}_4^-$  to the 4-NP acceptor.<sup>37</sup> With the presence of  $\text{Au}_{10\text{nm}}$  NPs as a catalyst, the absorption peak at 400 nm gradually decreased by time and a new peak appeared at 300 nm attributed to the 4-AP formation which is shown in figure 3.12 (b) (left side)<sup>40</sup>. The reduction reaction is also visible through color change with bleaching of yellow color, indicating complete reduction of 4-NP (see figure 3.12 (a), right side). This reduction process is a pseudo-first order reaction, therefore,  $\ln(A/A_0)$  versus time shows a linear tendency. The apparent reduction rate ( $k_{\text{app}}$ ) is a slope, directly calculated from the UV-vis spectra (figure 3.12 (b) right side).

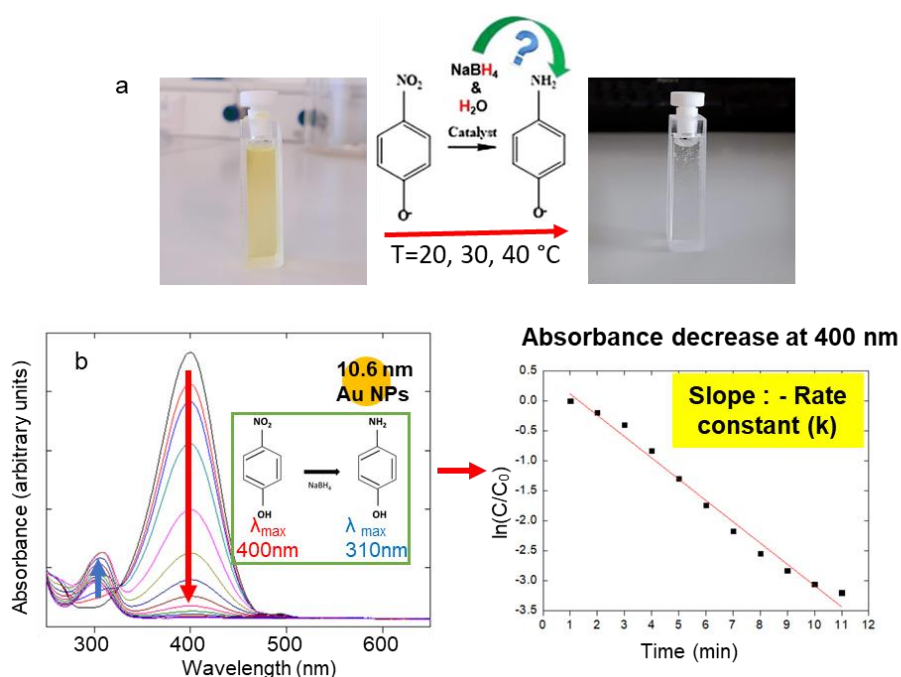


Figure 3.12. a) Images of quartz cells showing a change in color of the colloidal solution during the reduction of 4-nitrophenol to 4-aminophenol: before the reaction (left, yellow) and after the reaction (right, transparent) (b) corresponding UV-Vis spectrum and absorbance change at 400 nm by time to obtain the apparent rate constant of the conversion.

## 4.2. Catalytic activity of Au NPs: size effects

The catalytic activities of Au NP seeds were studied in function of their size and served as references for our study on corresponding Au@M NPs. To compare the size effect of the Au NPs on catalytic activities, the total number of gold atoms is kept the same for all colloidal solution. Atomic concentration of each NPs is thus fixed as  $C = 1.4 \times 10^{-3} \text{ mol L}^{-1}$ .

Herein, catalytic performances of Au NPs with different sizes were evaluated through the comparison of their reduction reaction rate by plotting  $\ln ([4\text{-NP}] / [4\text{-NP}]_0)$  versus reaction time (Figures 3. 13). A linear relationship between  $\ln ([4\text{-NP}] / [4\text{-NP}]_0)$  and reaction time (t) was obtained with linear coefficients all above 0.99, indicating that the reaction is pseudo first-order kinetics. In general, the higher the  $k_{app}$  value, the faster the catalytic reaction and the higher the efficiency of the nanocatalyst utilized.

The catalytic activities were compared with three different sizes of Au NPs (7 nm, 8.7 nm, and 10.6 nm). The rate constant of reduction process without NPs shows almost 0 indicating that the reduction of 4-NP requires catalyst (e.g. metallic NPs). The rate constant of three different sizes of Au NPs decreased with the increase of NPs diameter (Figure 3.13 and Table 3.6). We observed thus an increase of the catalytic activity with decreasing Au NP sizes. The size of the NPs was indeed demonstrated as pivotal for their catalytic activity<sup>41,42</sup>. A decrease of their size induces an increase surface to volume ratio, meaning more surface atoms become available for the reaction.

Table 3.6. Apparent rate constant ( $k_{app}$ ) for the reactions carried out in presence of different Au NP sizes

NPs	NP size (nm)	k (min <sup>-1</sup> )	Error (R <sup>2</sup> )
Au (PC)	7	0.48	0.99
	8.7	0.37	0.99
	10.6	0.27	0.99

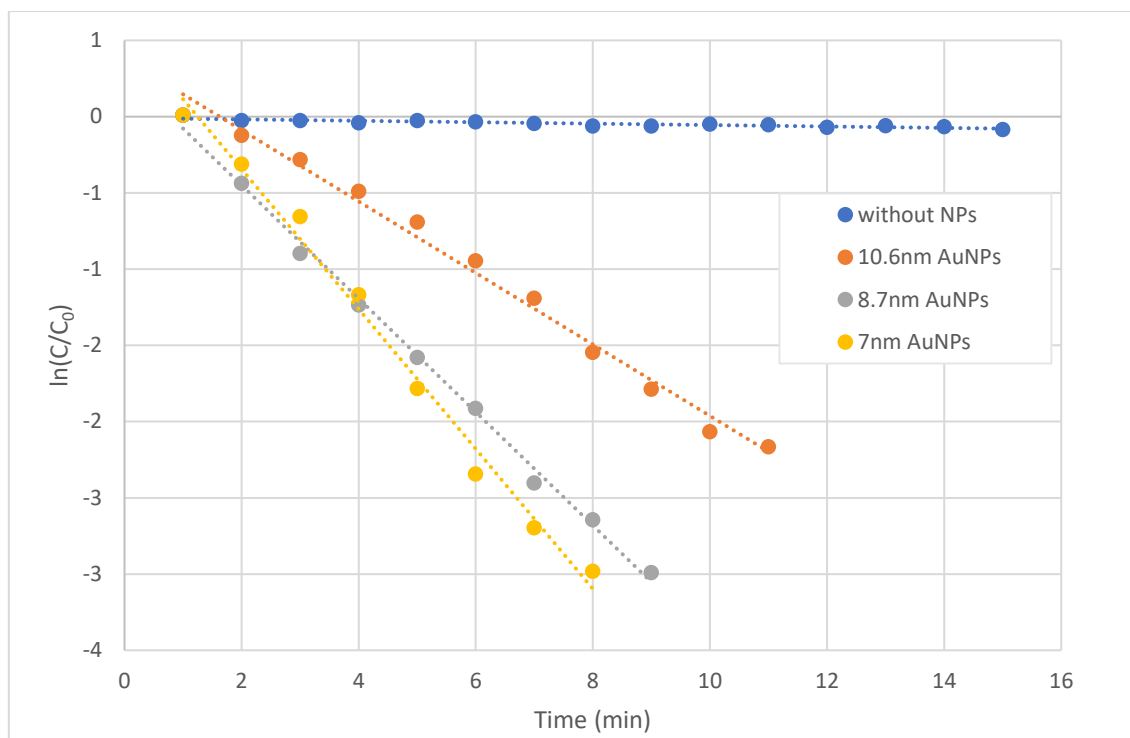


Figure 3.13. The comparison of catalytic activity between the catalysts 10.6 nm (red), 8.7 nm (gray) and 7 nm (yellow) Au NPs with the reduction reaction of 4-nitrophenol to 4-aminophenol.

#### 4.3. Catalytic activity of Au@M (M=Ag, Pd or Pt) core-shell nanoparticles

In the control reduction experiment, no clear change in the absorption intensity was observed at 400 nm for 4-NP in the absence of a catalyst (Figure A.15 in Annex 7). The spectra indicated that the 4-NP was not reduced by the NaBH<sub>4</sub>, and the mixture remained yellow. Au NPs or Au@Ag NPs were then used as catalysts, the peak at 400 nm decreased, until the peak ultimately disappears, and a new peak appear at 300 nm attributed to the 4-AP formation as described in experimental section (Figure A.15 in Annex 7). The comparison of rate constant between Au NPs and Au@Ag NPs with four different thicknesses is shown in Figure 3.14 and Table 3.7. The reduction reaction rate of bimetallic Au@Ag NPs appears to up to 1.6 times higher than that of monometallic Au NPs. These improved reduction rates can be explained by electronic synergistic effect between Au and Ag.<sup>22,37</sup> Electrons could transfer from Ag to Au leading to an increase in the electron density on the surface of the bimetallic Au@Ag NPs, which improved finally the catalytic activity.<sup>43</sup> The catalytic performance of the NPs appear also to depend on the shell thickness  $e$  (Figure 3.14 and Table 3.7). The reaction rate of 12.2nm



Au@Ag NPs with  $e = 0.8$  nm (around 2 Ag layers) is 1.2 times higher than the reaction rate of Au@Ag NPs with  $e = 0.4$  nm (around 1 Ag layer). Then, 14 nm Au@Ag NPs with  $e = 1.7$  nm (around 5 Ag layers) shows the same rate constant as Au@Ag NPs with 2 atomic layers. Finally, we observe a decrease in the reaction rate when the silver layer thickness reaches 2.2 nm (around 6 Ag layers). It can be assumed that the thickness of the silver layer is large enough for canceling ligand effects (electronic transfer) and decreasing the reactivity of NPs<sup>44</sup>.

Au@Pd NPs shows also better catalytic activities than Au NPs (UV-vis spectra in Figure A.16 in annex 7, Figure 3.15 and Table 3.7). Au@Pd NPs have indeed higher reaction rate than Au NPs and it increases with Pd thickness until a maximum thickness of 1.55 nm (around 4 Pd layers). Then it decreases slightly. Therefore, we can also adopt the synergetic effect between Pd and Au as Pd is well-known catalytic materials. Nevertheless, the catalytic performances of Au@Pd NPs appears lower than Au@Ag NPs. This results could be explained by hydrogen adsorption on Pd surfaces<sup>45,46</sup>. Pd has indeed the ability to absorb large volumetric quantities of hydrogen at room temperature and atmospheric pressure<sup>47</sup>. Moreover, a recent study showed that alloying Pd(110) surface with submonolayer of Au dramatically accelerates the hydrogen absorption, by a factor of more than 40.<sup>46</sup> This hydrogen adsorption on Pd surface can be an obstacle during the conversion reaction from 4-NP to 4-AP. The reducing agent  $\text{NaBH}_4$  in water produces hydrogen gas and it can remain trapped in the Pd shell surface and disrupt the activities as Au@Pd NPs catalyst.

Au@Pt NPs shows highest catalytic activities among the shell candidates (Ag, Pd) (UV-vis spectra in Figure A.15 in Annex 7, Figure 3.16, and Table 3.7). Pt is indeed a well-known metal as a candidate for catalyst with high catalytic activities<sup>25,48,49</sup>. It is also important to evaluate these results in terms of the NPs morphology. In case of Au@Pt NPs, their final morphologies of NPs are dendritic shape (Figure 2. 21 in Chapter II), so they have larger surface area than spherical Au@Ag or Au@Pd NPs. As they have different morphologies, they can display different number of atoms at their surfaces. Spheres show lower relative number of total atom than dendritic shape of NPs. It allows more efficient catalytic activities than spherical shape of NPs. The influence of shell thickness for Au@Pt NPs is coherent with other shell metal types, the catalytic activity increases indeed with the shell thickness and stabilize beyond 3 layers (Figure 3.16 and Table 3.7).

Table 3.7. Apparent rate constant ( $k_{app}$ ) for the reactions carried out in presence of 10.6 Au NPs, Au@Ag, Au@Pd and Au@Pt NPs with different shell thicknesses.

sample	NP size (nm)	Shell thickness (nm)	k (min <sup>-1</sup> )	Error, R <sup>2</sup>
Au	10.6	-	0.27	0.99
Au@Ag	11.4	0.4 (~1 layer)	0.36	0.95
	12.2	0.8 (~2 layers)	0.44	0.97
	14.0	1.7 (~5 layers)	0.44	0.99
	14.8	2.2 (~6 layers)	0.40	0.98
Au@Pd	11.4	0.4 (~1 layer)	0.30	0.99
	12.5	0.95 (~2 layers)	0.35	0.99
	13.7	1.55 (~4 layers)	0.40	0.99
	14.0	1.7 (~5 layers)	0.39	0.99
Au@Pt	11.1	0.25 (~1 layer)	0.44	0.98
	11.7	0.55 (~2 layers)	0.49	0.95
	12.9	1.15 (~3 layers)	0.52	0.96
	13.5	1.95 (~4 layers)	0.52	0.96

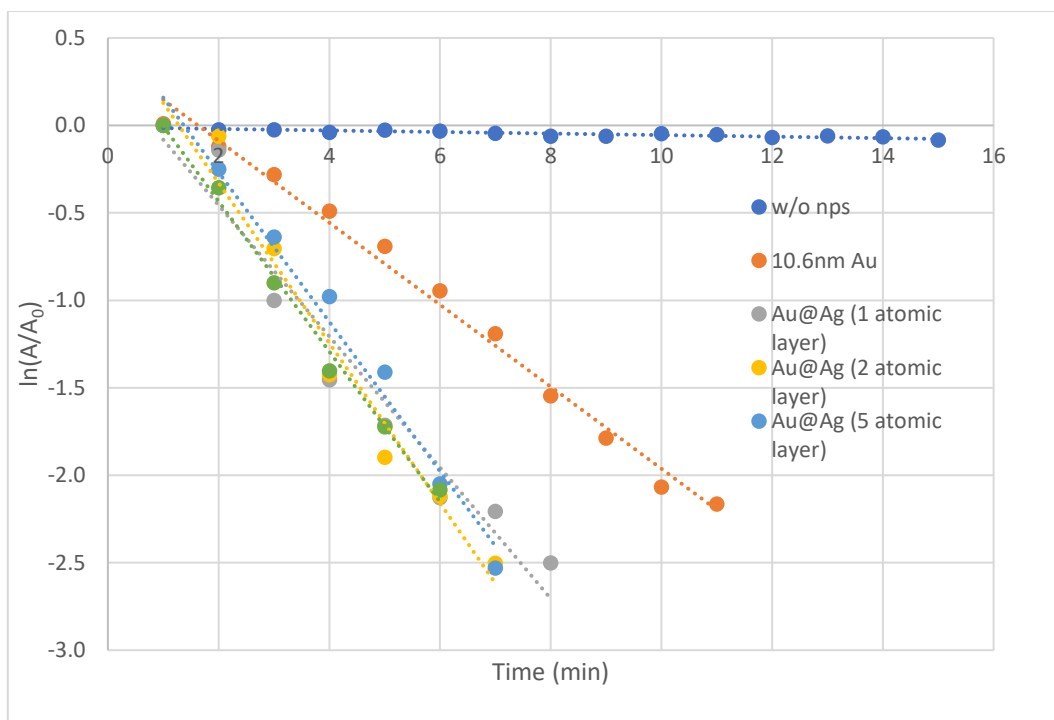


Figure 3.14. The comparison of catalytic activity between the catalysts 10.6 nm Au NPs and Au@Ag NPs with 11.4, 12.2, 14, and 14.8 nm diameters with the reduction reaction of 4-nitrophenol to 4-aminophenol.

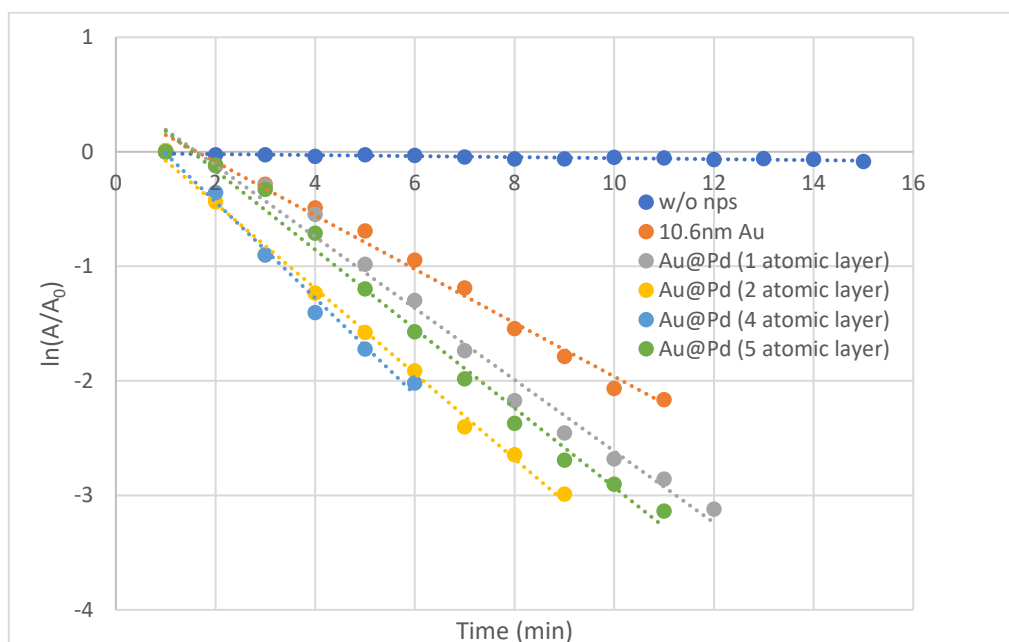


Figure 3.15. The comparison of catalytic activity between the catalysts 10.6 nm Au NPs and Au@Pd NPs with 11.4, 12.5, 13.6, and 14.0 nm diameters with the reduction reaction of 4-nitrophenol to 4-aminophenol.

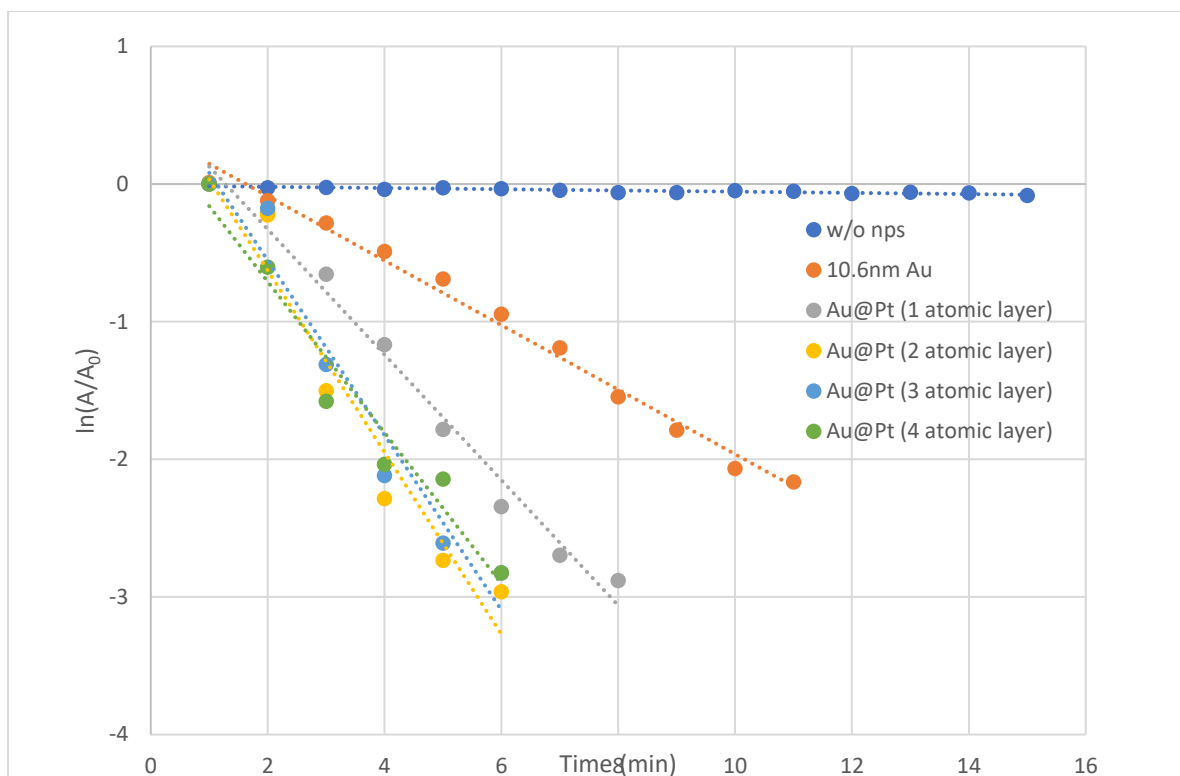


Figure 3.16. The comparison of catalytic activity between the catalysts 10.6 nm Au NPs and Au@Pt NPs with 11.1, 11.7, 12.9, and 13.4 nm diameters with the reduction reaction of 4-nitrophenol to 4-aminophenol.

#### 4.4. Influence of crystallinity of NPs on their catalytic performance

Herein, the NP crystallinity effects on their catalytic performance was studied. Single crystalline (SC) Au<sub>7nm</sub> NPs were separated from polycrystalline (PC) Au<sub>7nm</sub> NPs and Ag shell were grown on Au<sub>7nm</sub> (SC) or (PC) seeds with same sizes according to the process described in Chapter II. Their catalytic activities were evaluated in a same condition as previous experiment and the absorption spectra of 4-NP reduced by NaBH<sub>4</sub> are shown in Figure A.16 in Annex 7.

The crystallinity effect on Au NP catalytic performance is delicate to discuss. SC NPs characterized by electronic microscopy in Chapter II, are single crystal cuboctahedrons (or truncated octahedrons) with (100) and (111) facets with relatively large area (Figure 2.3 in Chapter II). Polycrystalline NPs correspond in large majority to multiply-twinned particles (MTP) with *fcc* tetrahedral sub-units and consist of smaller (111) facets with defects (figure 2.3 in Chapter II). For catalyst with a face-centred cubic (*fcc*) lattice, the coordination number of atoms on (111), (100), and (110) surfaces is 9, 8, and 7. The corresponding surface energy

was in the order of (111) < (100) < (110), which is the reason why (100) usually exhibited higher activity than (111) facets<sup>50,51</sup>. In case of monometallic Au<sub>7nm</sub> NPs, there is no significant difference in reaction rate between SC and PC NPs (Table 3.8 and Figure 3.17). The crystallinity effect is likely governed by a complex combination between coordination number of the different surfaces and the presence of defects like corners and edges which are sub-coordinated atomic sites of higher energies. SC NPs present (100) surfaces of higher energy than (111) facets present in PC NPs which however have more defects characterized by a high catalytic activity. As we can see in table 3.8, the rate constant k value for Au(SC) NPs is slightly higher than for Au(PC). The difference is not large enough to determine which is the most important parameter: the coordination number of the facets or the presence of defects.

The reduction rates with Au@Ag NPs are higher than Au NPs of similar sizes whatever the crystallinity of Au cores in agreement with previous results (see section 4.3). It is clearly due to a synergistic effect between both metals. The reduction rate of Au(SC)@Ag NPs is slightly higher than Au(PC)@Ag NPs (Table 3.8 and Figure 3.17). As the silver overgrowth is epitaxial (see chapter II), we can consider that the core-shell Au(SC)@Ag NPs are also single-crystalline.

In conclusion, the catalytic activities of SC (cuboctahedron) and PC (MTP) NPs are close whether mono- or bimetallic particles are involved.

Table 3.8. Apparent rate constant ( $k_{app}$ ) for the reactions carried out in presence of Au and Au@Ag of different crystallinities (SC or PC).

<b>NPs</b>	<b>NPs diameter (nm)</b>	<b>k (min<sup>-1</sup>)</b>	<b>Error, R<sup>2</sup></b>
Au (PC)	7	0.27	0.99
Au (SC)	7	0.29	0.98
Au@Ag (PC)	7.2 (4 layers)	0.43	0.98
Au@Ag (SC)	7.5 (4 layers)	0.46	0.98

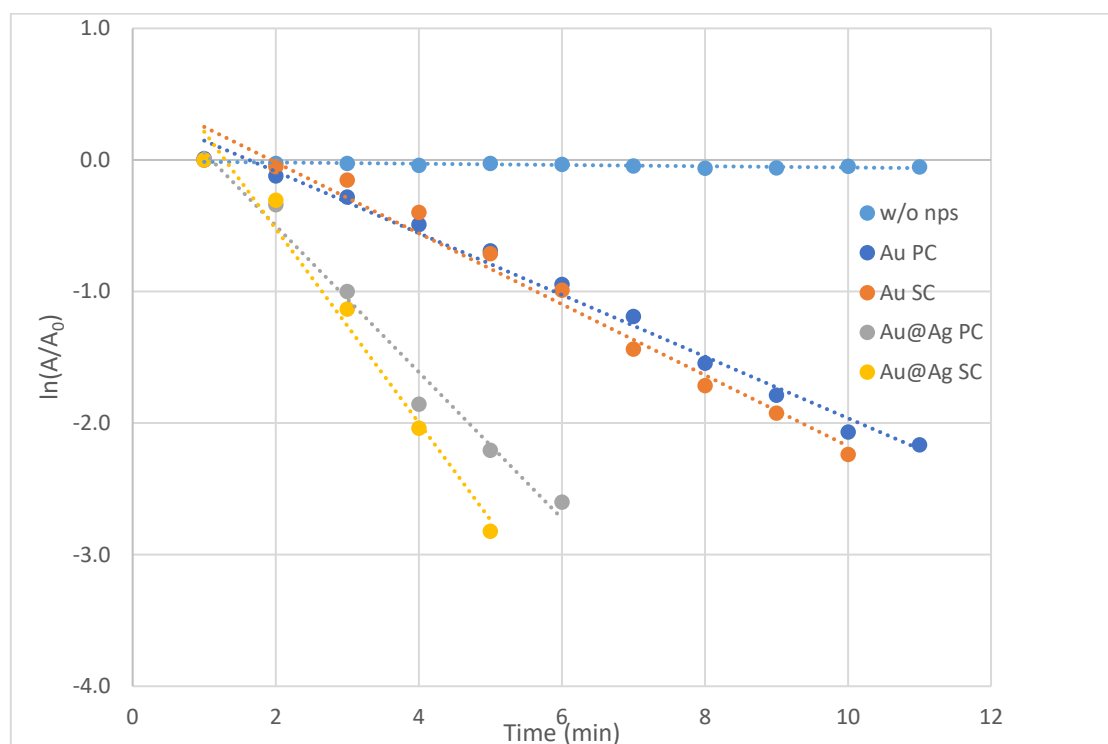


Figure 3.17. The comparison of catalytic activity between the catalysts between poly- and single crystalline Au NPs, Au@Ag NPs with the reaction in absence of any catalyst.

#### 4.5. Influence of reaction temperature on catalytic activity of Au and Au@Ag core-shell nanoparticles

In this part we carried out a series of reduction reactions of 4-NP in the presence of Au<sub>10.6nm</sub> NPs and Au<sub>10.6nm</sub>@Ag NPs to obtain thermodynamic parameters that show how the reaction temperature can affect the kinetic of such reaction. The reduction process of 4-NP to 4-AP is highly dependent on reaction temperature because it directly influences the rate constant (k) based on Arrhenius equation<sup>27,52</sup>;

$$k = -Ae^{-E_a/RT} \quad (3.1)$$

where k is the apparent rate constant, A is numerical constants characteristic of the reacting substances, E<sub>a</sub> is the activation energy, R is the thermodynamic gas constant, and T is the absolute temperature.

All of absorption spectra during the reduction of 4-NP to 4-AP were performed in same conditions with previous experiment except that the temperature is raised from 20 to 30 and

40°C. The temperature effect was studied on the catalytic performance of Au<sub>10nm</sub> NPs and Au<sub>10nm</sub>@Ag NPs with overall diameters of 11.4 nm, 12.2 nm, 14.0 nm, and 14.8 nm.

From figures 3.18, the reaction temperature has an important influence. In fact, at higher temperatures the conversion of 4-NP is faster. The catalytic activities of both mono and bimetallic NPs are improved with increasing temperature (Table 3.9). When Au@Ag particles are used as catalyst the conversion of 4-NP is significantly faster than for Au NPs whatever the reaction temperature is and when the silver thickness is increased until 0.8 nm. This trend shows that the core-shell structure improves the catalytic activity of the NPs. Based on the Arrhenius equation, by plotting the rate constant for each catalytic system versus the corresponding 1/T (see figure 3.18) we can obtain the activation energy ( $E_a$ , apparent)<sup>53</sup>. From the slopes of the lines, we obtained the  $E_a$  values for the different systems reported in Table 3.9. The lower  $E_a$  values for Au@Ag NPs compared to Au NPs demonstrate synergistic effects between Au and Ag in core-shell NPs, which lead to the improvement of their catalytic activity. It is important to note that  $E_a$  decreases with the thickness of the silver shell, but beyond a thickness of 2 nm (6 Ag layers) increases. As mention in the previous section, if the silver shell is too thick (around 6 atomic layers), the effects of electronic transfers are no longer possible, and the reactivity of the NPs decreases.

For comparison, apparent activation energy were estimated in the literature for 16 nm and 4 nm diameter Au NPs coated by PVP around 43.566 and 39.690 *kJ/mol* respectively, and for 10 nm Au NPs coated by glucose polymer (MBS) around 47.42 *kJ/mol*<sup>54,51</sup>. The apparent activation energy for Au<sub>10nm</sub> NPs that we calculated (30.9 *kJ/mol*) is thus lower than those reported in the literature for similar sizes. This may be due to a difference in the nature of the coating agents, which are consider having an influence the catalytic performance of the<sup>55</sup>. In case of Au@Ag core-shell NPs, few studies were performed. An activation energy around 14 (*kJ/mol*)<sup>56</sup> was reported in case 2-6 nm diameter Au@Ag NPs stabilized on porous MOF. An activation energy of 51 (*kJ/mol*)<sup>57</sup> in case of 21 nm diameter Au-Ag (5:5) alloyed NPs was also reported. The activation energies of Au@Ag NPs calculated in this work are around 22 *kJ/mol*. The prominent catalytic activity of Au@Ag core-shell NPs is ascribed to the electronic structure in a core-shell NP which is superior to that in an alloy or monometallic NP for the reduction of 4-NP.

Table 3.9. The comparison of rate constant ( $k$ ) of reduction reaction up to temperature change (20, 30 and 40 °C) and the apparent activation energy ( $E_a$ ) in presence of lists of NPs.

NPs	$k$ ( $\text{min}^{-1}$ )			$E_a$ ( $\text{kJ/mol}$ )	Error, $R^2$
	20°C	30°C	40°C		
10.6 nm Au NPs	0.24	0.35	0.54	30.9	0.99
11.4 nm Au@Ag NPs	0.36	0.56	0.76	24.4	0.99
12.2 nm Au@Ag NPs	0.44	0.63	0.84	22.1	0.99
14.0 nm Au@Ag NPs	0.44	0.6	0.81	21.5	0.99
14.8 nm Au@Ag NPs	0.40	0.57	0.78	22.7	0.99

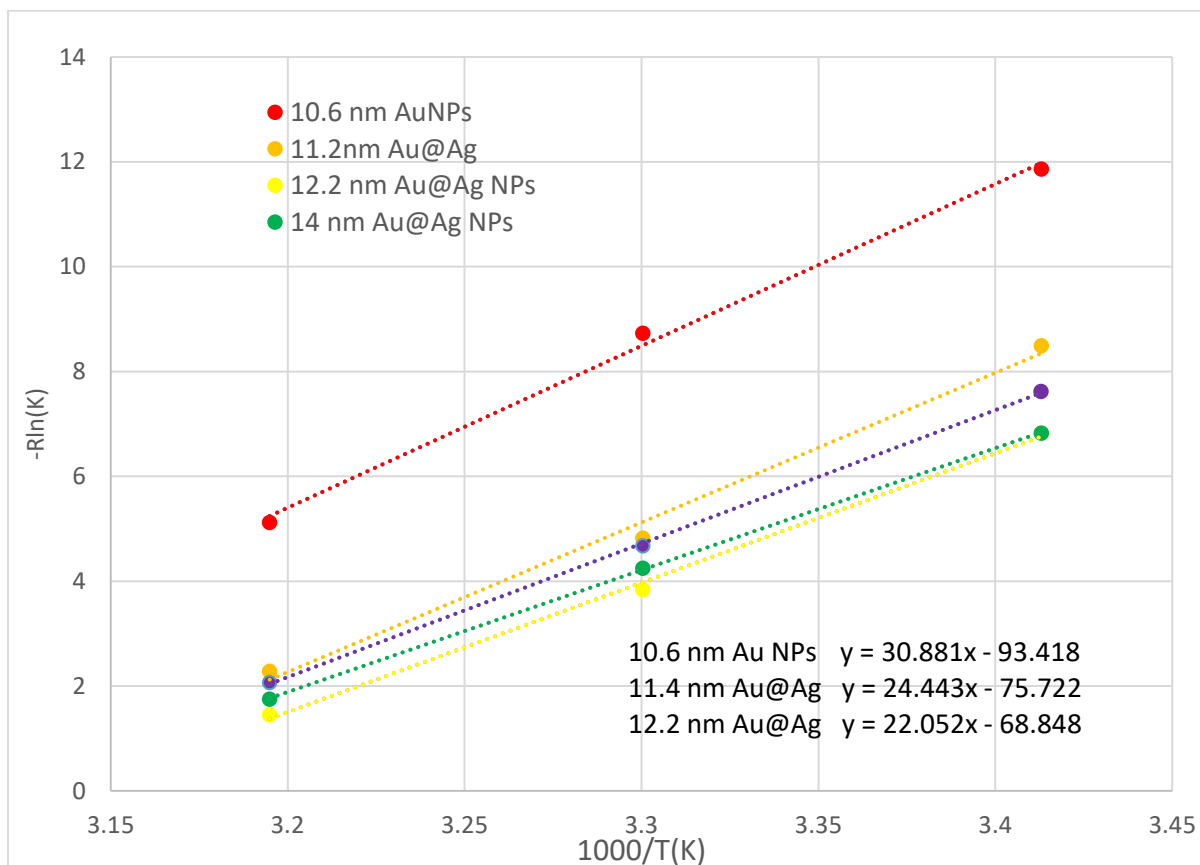


Figure 3. 18. The apparent activation energy ( $E_a$ ) are calculated from the slope of the linear fitting  $\ln k = f(1000/T(K))$  in each case.



## 5. Conclusion

In this Chapter, we characterized physical and chemical properties of bimetallic core-shell NPs synthesized through a two-steps protocol. Optical, vibrational, and catalytic properties were investigated according to their size, chemical composition, and crystalline structure.

First, the plasmonic properties of the  $\text{Au}_{5\text{nm}/10\text{nm}}(\text{PC})@\text{Ag}$  NPs were studied as a function of the Au core diameter and Ag shell thickness by UV-vis absorption spectroscopy and DDA calculations. One of the interests of synthesizing the core-shell NPs is to tune the optical properties by tuning the shell thickness. The tunability of the SPR band through shell overgrowth was observed. The study of SPR band after the replacement of shell from plasmonic materials to catalytic materials (Pd or Pt) or the replacement of core material from Au to Ag with stronger plasmonic properties were also performed. Our results show that  $\text{Au}(\text{Ag})@\text{Pd}$  and  $\text{Au}(\text{Ag})@\text{Pt}$  bimetallic NPs have their SPR in the visible range with a broad tunability, which is very difficult for pure Pd and Pt NPs to achieve. Nevertheless, a damping effect of the SPR band is also observed, which is more significant with the shell thickness.

The vibrational properties of  $\text{Au}_{5\text{nm}/10\text{nm}}(\text{PC})@\text{Ag}$  NPs were demonstrated by low frequency Raman spectroscopy (LFRS). Bimetallic core-shell NPs have their own vibrational frequency different from monometallic NPs. Core-shell NPs vibration modes are shifted to lower frequency by the increase of Ag shell thickness. Especially, one of the distinctive characteristics of single crystalline (SC) NPs is the splitting of quadrupolar vibrational mode into two peaks. It was verified that this splitting is maintained throughout  $\text{Au}(\text{SC})@\text{Ag}$  growth.

The catalytic performance of bimetallic core-shell NPs was evaluated via a model reaction of reduction of 4-NP to 4-AP in presence of  $\text{NaBH}_4$  in aqueous phase. First, catalytic activities of Au NPs are inversely proportional to diameter of NPs when we keep same atomic concentration due to the increase of their surface area. We show that the bimetallic  $\text{Au}@\text{Ag}$  NPs synergistically improves the catalytic activity compared to the monometallic Au NPs. It was also found that shell thickness in bimetallic  $\text{Au}@\text{M}$  ( $\text{M}=\text{Ag}$ , Pt or Pd) NPs influenced their catalytic properties. Ag, Pt or Pd shells with thicknesses below 5 atomic layers can maximize the synergetic effect between core and shell. Even though palladium is known for its catalytic performances, the catalytic performance of  $\text{Au}@\text{Pd}$  NPs was shown to be lower than that of  $\text{Au}@\text{Ag}$  NPs. This could be explained by the ability of Pd to absorb hydrogen which is

detrimental to the reduction of 4-NP by NaBH<sub>4</sub>. Finally, Pt shell shows the highest catalytic activities among all the shells studied.

The crystallinity effect on NP catalytic performance is trickier to discuss. This effect is likely governed by a complex combination between surface energy of the different crystalline facets and the presence of defects like corners and edges which are sub-coordinated atomic sites of high energies. The experiment shows that the crystallinity structure of mono or bimetallic NPs from SC to PC has a minor effect on their catalytic activities. Single crystalline (SC) NPs have indeed slightly higher rate constant than polycrystalline (PC) NPs.

From our results, we could estimate the activation energy of the reduction process of 4-NP to produce 4-AP. The lower  $E_a$  values for Au@Ag NPs compared to Au NPs, demonstrates synergistic effects between Au and Ag in core-shell NPs, which lead to the improvement of their catalytic activity.

## 6. Reference

- (1) Duval, E.; Portales, H.; Saviot, L.; Fujii, M.; Sumitomo, K.; Hayashi, S. Spatial Coherence Effect on the Low-Frequency Raman Scattering from Metallic Nanoclusters. *Phys. Rev. B* **2001**, *63* (7), 075405. <https://doi.org/10.1103/PhysRevB.63.075405>.
- (2) Portales, H.; Saviot, L.; Duval, E.; Fujii, M.; Hayashi, S.; Del Fatti, N.; Vallée, F. Resonant Raman Scattering by Breathing Modes of Metal Nanoparticles. *J. Chem. Phys.* **2001**, *115* (8), 3444–3447. <https://doi.org/10.1063/1.1396817>.
- (3) Portales, H.; Goubet, N.; Saviot, L.; Adichtchev, S.; Murray, D. B.; Mermet, A.; Duval, E.; Pileni, M.-P. Probing Atomic Ordering and Multiple Twinning in Metal Nanocrystals through Their Vibrations. *Proc. Natl. Acad. Sci.* **2008**, *105* (39), 14784–14789. <https://doi.org/10.1073/pnas.0803748105>.
- (4) Stephanidis, B.; Adichtchev, S.; Etienne, S.; Migot, S.; Duval, E.; Mermet, A. Vibrations of Nanoparticles: From Nanospheres to Fcc Cuboctahedra. *Phys. Rev. B* **2007**, *76* (12), 121404. <https://doi.org/10.1103/PhysRevB.76.121404>.
- (5) Portalès, H.; Saviot, L.; Duval, E.; Gaudry, M.; Cottancin, E.; Pellarin, M.; Lermé, J.; Broyer, M. Resonant Raman Scattering by Quadrupolar Vibrations of Ni-Ag Core-Shell Nanoparticles. *Phys. Rev. B* **2002**, *65* (16), 165422. <https://doi.org/10.1103/PhysRevB.65.165422>.
- (6) Malathi, S.; Ezhilarasu, T.; Abiraman, T.; Balasubramanian, S. One Pot Green Synthesis of Ag, Au and Au–Ag Alloy Nanoparticles Using Isonicotinic Acid Hydrazide and Starch. *Carbohydr. Polym.* **2014**, *111*, 734–743. <https://doi.org/10.1016/j.carbpol.2014.04.105>.
- (7) Wu, W.; Njoki, P. N.; Han, H.; Zhao, H.; Schiff, E. A.; Lutz, P. S.; Solomon, L.; Matthews, S.; Maye, M. M. Processing Core/Alloy/Shell Nanoparticles: Tunable Optical Properties and Evidence for Self-Limiting Alloy Growth. *J. Phys. Chem. C* **2011**, *115* (20), 9933–9942. <https://doi.org/10.1021/jp201151m>.
- (8) Mao, K.; Zhou, Z.; Han, S.; Zhou, X.; Hu, J.; Li, X.; Yang, Z. A Novel Biosensor Based on Au@Ag Core-Shell Nanoparticles for Sensitive Detection of Methylamphetamine with Surface Enhanced Raman Scattering. *Talanta* **2018**, *190*, 263–268. <https://doi.org/10.1016/j.talanta.2018.07.071>.
- (9) Samal, A. K.; Polavarapu, L.; Rodal-Cedeira, S.; Liz-Marzán, L. M.; Pérez-Juste, J.; Pastoriza-Santos, I. Size Tunable Au@Ag Core–Shell Nanoparticles: Synthesis and Surface-Enhanced Raman Scattering Properties. *Langmuir* **2013**, *29* (48), 15076–15082. <https://doi.org/10.1021/la403707j>.
- (10) Zhang, J.; Tang, Y.; Weng, L.; Ouyang, M. Versatile Strategy for Precisely Tailored Core@Shell Nanostructures with Single Shell Layer Accuracy: The Case of Metallic Shell. *Nano Lett.* **2009**, *9* (12), 4061–4065. <https://doi.org/10.1021/nl902263h>.
- (11) Ma, Y.; Li, W.; Cho, E. C.; Li, Z.; Yu, T.; Zeng, J.; Xie, Z.; Xia, Y. Au@Ag Core–Shell Nanocubes with Finely Tuned and Well-Controlled Sizes, Shell Thicknesses, and Optical Properties. *ACS Nano* **2010**, *4* (11), 6725–6734. <https://doi.org/10.1021/nn102237c>.
- (12) Forsythe, W. E.; Smithsonian Institution. *Smithsonian Physical Tables*; Knovel: Norwich, N.Y., 2003.
- (13) Zhang, C.; Chen, B.-Q.; Li, Z.-Y.; Xia, Y.; Chen, Y.-G. Surface Plasmon Resonance in Bimetallic Core–Shell Nanoparticles. *J. Phys. Chem. C* **2015**, *119* (29), 16836–16845. <https://doi.org/10.1021/acs.jpcc.5b04232>.
- (14) Portales, H. Étude Par Diffusion Raman de Nanoparticules Métalliques En Matrice Diélectrique Amorphe. These de doctorat, Lyon 1, 2001.

- (15) Courty, A.; Lisiecki, I.; Pileni, M. P. Vibration of Self-Organized Silver Nanocrystals. *J. Chem. Phys.* **2002**, *116* (18), 8074–8078. <https://doi.org/10.1063/1.1467049>.
- (16) Lamb, H. On the Vibrations of an Elastic Sphere. *Proc. Lond. Math. Soc.* **1881**, No. 1, 189–212. <https://doi.org/10.1112/plms/s1-13.1.189>.
- (17) Eringen, A. C.; Suhubi, E. S. *Elastodynamics. 1: Finite Motions*; Acad. Pr: New York, 1975.
- (18) Portalès, H.; Goubet, N.; Sirotkin, S.; Duval, E.; Mermet, A.; Albouy, P.-A.; Pileni, M.-P. Crystallinity Segregation upon Selective Self-Assembling of Gold Colloidal Single Nanocrystals. *Nano Lett.* **2012**, *12* (10), 5292–5298. <https://doi.org/10.1021/nl3029009>.
- (19) Portalès, H.; Goubet, N.; Saviot, L.; Yang, P.; Sirotkin, S.; Duval, E.; Mermet, A.; Pileni, M.-P. Crystallinity Dependence of the Plasmon Resonant Raman Scattering by Anisotropic Gold Nanocrystals. *ACS Nano* **2010**, *4* (6), 3489–3497. <https://doi.org/10.1021/nn1005446>.
- (20) Portales, H.; Goubet, N.; Saviot, L.; Adichtchev, S.; Murray, D. B.; Mermet, A.; Duval, E.; Pileni, M.-P. Probing Atomic Ordering and Multiple Twinning in Metal Nanocrystals through Their Vibrations. *Proc. Natl. Acad. Sci.* **2008**, *105* (39), 14784–14789. <https://doi.org/10.1073/pnas.0803748105>.
- (21) Neighbours, J. R.; Alers, G. A. Elastic Constants of Silver and Gold. *Phys. Rev.* **1958**, *111* (3), 707–712. <https://doi.org/10.1103/PhysRev.111.707>.
- (22) Berahim, N.; Basirun, W. J.; Leo, B. F.; Johan, M. R. Synthesis of Bimetallic Gold-Silver (Au-Ag) Nanoparticles for the Catalytic Reduction of 4-Nitrophenol to 4-Aminophenol. *Catalysts* **2018**, *8* (10), 412. <https://doi.org/10.3390/catal8100412>.
- (23) Yang, M.-Q.; Pan, X.; Zhang, N.; Xu, Y.-J. A Facile One-Step Way to Anchor Noble Metal (Au, Ag, Pd) Nanoparticles on a Reduced Graphene Oxide Mat with Catalytic Activity for Selective Reduction of Nitroaromatic Compounds. *CrystEngComm* **2013**, *15* (34), 6819–6828. <https://doi.org/10.1039/C3CE40694F>.
- (24) Liu, Y.; Zhou, J.; Wang, B.; Jiang, T.; Ho, H.-P.; Petti, L.; Mormile, P. Au@Ag Core-Shell Nanocubes: Epitaxial Growth Synthesis and Surface-Enhanced Raman Scattering Performance. *Phys. Chem. Chem. Phys.* **2015**, *17* (10), 6819–6826. <https://doi.org/10.1039/C4CP05642F>.
- (25) Zaleska-Medynska, A.; Marchelek, M.; Diak, M.; Grabowska, E. Noble Metal-Based Bimetallic Nanoparticles: The Effect of the Structure on the Optical, Catalytic and Photocatalytic Properties. *Adv. Colloid Interface Sci.* **2016**, *229*, 80–107. <https://doi.org/10.1016/j.cis.2015.12.008>.
- (26) Arora, N.; Mehta, A.; Mishra, A.; Basu, S. 4-Nitrophenol Reduction Catalysed by Au-Ag Bimetallic Nanoparticles Supported on LDH: Homogeneous vs. Heterogeneous Catalysis. *Appl. Clay Sci.* **2018**, *151*, 1–9. <https://doi.org/10.1016/j.clay.2017.10.015>.
- (27) De Oliveira, F. M.; Nascimento, L. R. B. de A.; Calado, C. M. S.; Meneghetti, M. R.; Da Silva, M. G. A. Aqueous-Phase Catalytic Chemical Reduction of p-Nitrophenol Employing Soluble Gold Nanoparticles with Different Shapes. *Catalysts* **2016**, *6* (12), 215. <https://doi.org/10.3390/catal6120215>.
- (28) Xie, S.; Choi, S.-I.; Xia, X.; Xia, Y. Catalysis on Faceted Noble-Metal Nanocrystals: Both Shape and Size Matter. *Curr. Opin. Chem. Eng.* **2013**, *2* (2), 142–150. <https://doi.org/10.1016/j.coche.2013.02.003>.
- (29) Callan, J. F.; Mulrooney, R. C. Luminescent Detection of Cu(II) Ions in Aqueous Solution Using CdSe and CdSe-ZnS Quantum Dots Functionalised with Mercaptosuccinic Acid. *Phys. Status Solidi C* **2009**, *6* (4), 920–923. <https://doi.org/10.1002/pssc.200880571>.
- (30) Bharali, D. J.; Lucey, D. W.; Jayakumar, H.; Pudavar, H. E.; Prasad, P. N. Folate-Receptor-Mediated Delivery of InP Quantum Dots for Bioimaging Using Confocal and

- Two-Photon Microscopy. *J. Am. Chem. Soc.* **2005**, *127* (32), 11364–11371. <https://doi.org/10.1021/ja051455x>.
- (31) Lin, G.; Wang, X.; Yin, F.; Yong, K.-T. Passive Tumor Targeting and Imaging by Using Mercaptosuccinic Acid-Coated near-Infrared Quantum Dots. *Int. J. Nanomedicine* **2015**, *10*, 335–345. <https://doi.org/10.2147/IJN.S74805>.
- (32) Maenosono, S.; Suzuki, T.; Saita, S. Mutagenicity of Water-Soluble FePt Nanoparticles in Ames Test. *J. Toxicol. Sci.* **2007**, *32* (5), 575–579. <https://doi.org/10.2131/jts.32.575>.
- (33) Salgueiriño-Maceira, V.; Liz-Marzán, L. M.; Farle, M. Water-Based Ferrofluids from FexPt1-x Nanoparticles Synthesized in Organic Media. *Langmuir* **2004**, *20* (16), 6946–6950. <https://doi.org/10.1021/la049300a>.
- (34) Abdou, H. E.; Mohamed, A. A.; Fackler, J. P. Gold(I) Nitrogen Chemistry. In *Gold Chemistry*; John Wiley & Sons, Ltd, 2009; pp 1–45. <https://doi.org/10.1002/9783527626724.ch1>.
- (35) Kaspar, T. C.; Droubay, T.; Chambers, S. A.; Bagus, P. S. Spectroscopic Evidence for Ag(III) in Highly Oxidized Silver Films by X-Ray Photoelectron Spectroscopy. *J. Phys. Chem. C* **2010**, *114* (49), 21562–21571. <https://doi.org/10.1021/jp107914e>.
- (36) Huang, J.; Li, Q.; Sun, D.; Lu, Y.; Su, Y.; Yang, X.; Wang, H.; Wang, Y.; Shao, W.; He, N.; Hong, J.; Chen, C. Biosynthesis of Silver and Gold Nanoparticles by Novel Sundried Cinnamomum Camphoraleaf. *Nanotechnology* **2007**, *18* (10), 105104. <https://doi.org/10.1088/0957-4484/18/10/105104>.
- (37) Haldar, K. K.; Kundu, S.; Patra, A. Core-Size-Dependent Catalytic Properties of Bimetallic Au/Ag Core-Shell Nanoparticles. *ACS Appl. Mater. Interfaces* **2014**, *6* (24), 21946–21953. <https://doi.org/10.1021/am507391d>.
- (38) Ahmed Zelekew, O.; Kuo, D.-H. A Two-Oxide Nanodiode System Made of Double-Layered p-Type Ag<sub>2</sub>O@n-Type TiO<sub>2</sub> for Rapid Reduction of 4-Nitrophenol. *Phys. Chem. Chem. Phys. PCCP* **2016**, *18* (6), 4405–4414. <https://doi.org/10.1039/c5cp07320k>.
- (39) Krishnamurthy, S.; Esterle, A.; Sharma, N. C.; Sahi, S. V. Yucca-Derived Synthesis of Gold Nanomaterial and Their Catalytic Potential. *Nanoscale Res. Lett.* **2014**, *9* (1), 627. <https://doi.org/10.1186/1556-276X-9-627>.
- (40) Dong, F.; Guo, W.; Park, S.-K.; Ha, C.-S. Controlled Synthesis of Novel Cyanopropyl Polysilsesquioxane Hollow Spheres Loaded with Highly Dispersed Au Nanoparticles for Catalytic Applications. *Chem. Commun. Camb. Engl.* **2012**, *48* (8), 1108–1110. <https://doi.org/10.1039/c1cc14831a>.
- (41) Zhou, X.; Xu, W.; Liu, G.; Panda, D.; Chen, P. Size-Dependent Catalytic Activity and Dynamics of Gold Nanoparticles at the Single-Molecule Level. *J. Am. Chem. Soc.* **2010**, *132* (1), 138–146. <https://doi.org/10.1021/ja904307n>.
- (42) Isaifan, R. J.; Ntais, S.; Baranova, E. A. Particle Size Effect on Catalytic Activity of Carbon-Supported Pt Nanoparticles for Complete Ethylene Oxidation. *Appl. Catal. Gen.* **2013**, *464–465*, 87–94. <https://doi.org/10.1016/j.apcata.2013.05.027>.
- (43) Xia, B.; He, F.; Li, L. Preparation of Bimetallic Nanoparticles Using a Facile Green Synthesis Method and Their Application. *Langmuir* **2013**, *29* (15), 4901–4907. <https://doi.org/10.1021/la400355u>.
- (44) Gao, F.; Goodman, D. W. Pd–Au Bimetallic Catalysts: Understanding Alloy Effects from Planar Models and (Supported) Nanoparticles. *Chem. Soc. Rev.* **2012**, *41* (24), 8009–8020. <https://doi.org/10.1039/C2CS35160A>.
- (45) Conrad, H.; Ertl, G.; Latta, E. E. Adsorption of Hydrogen on Palladium Single Crystal Surfaces. *Surf. Sci.* **1974**, *41* (2), 435–446. [https://doi.org/10.1016/0039-6028\(74\)90060-0](https://doi.org/10.1016/0039-6028(74)90060-0).

- (46) Namba, K.; Ogura, S.; Ohno, S.; Di, W.; Kato, K.; Wilde, M.; Pletikosić, I.; Pervan, P.; Milun, M.; Fukutani, K. Acceleration of Hydrogen Absorption by Palladium through Surface Alloying with Gold. *Proc. Natl. Acad. Sci.* **2018**, *115* (31), 7896–7900. <https://doi.org/10.1073/pnas.1800412115>.
- (47) Adams, B. D.; Chen, A. The Role of Palladium in a Hydrogen Economy. *Mater. Today* **2011**, *14* (6), 282–289. [https://doi.org/10.1016/S1369-7021\(11\)70143-2](https://doi.org/10.1016/S1369-7021(11)70143-2).
- (48) Rylander, P. N. Platinum Metals in Catalytic Hydrogenation. *Ann. N. Y. Acad. Sci.* **1967**, *145* (1), 46–51. <https://doi.org/10.1111/j.1749-6632.1967.tb52997.x>.
- (49) Wang, X.; Choi, S.-I.; Roling, L. T.; Luo, M.; Ma, C.; Zhang, L.; Chi, M.; Liu, J.; Xie, Z.; Herron, J. A.; Mavrikakis, M.; Xia, Y. Palladium–Platinum Core-Shell Icosahedra with Substantially Enhanced Activity and Durability towards Oxygen Reduction. *Nat. Commun.* **2015**, *6* (1), 1–8. <https://doi.org/10.1038/ncomms8594>.
- (50) Cao, S.; Tao, F. (Feng); Tang, Y.; Li, Y.; Yu, J. Size- and Shape-Dependent Catalytic Performances of Oxidation and Reduction Reactions on Nanocatalysts. *Chem. Soc. Rev.* **2016**, *45* (17), 4747–4765. <https://doi.org/10.1039/C6CS00094K>.
- (51) Zhang, L.; Xie, Z.; Gong, J. Shape-Controlled Synthesis of Au–Pd Bimetallic Nanocrystals for Catalytic Applications. *Chem. Soc. Rev.* **2016**, *45* (14), 3916–3934. <https://doi.org/10.1039/C5CS00958H>.
- (52) Esq, J. J. H. XLIX. On the Laws of Chemical Change.—Part I. *Lond. Edinb. Dublin Philos. Mag. J. Sci.* **1878**, *6* (38), 371–383. <https://doi.org/10.1080/14786447808639527>.
- (53) Ma, T.; Yang, W.; Liu, S.; Zhang, H.; Liang, F. A Comparison Reduction of 4-Nitrophenol by Gold Nanospheres and Gold Nanostars. *Catalysts* **2017**, *7* (2), 38. <https://doi.org/10.3390/catal7020038>.
- (54) Chairam, S.; Konkamdee, W.; Parakhun, R. Starch-Supported Gold Nanoparticles and Their Use in 4-Nitrophenol Reduction. *J. Saudi Chem. Soc.* **2017**, *21* (6), 656–663. <https://doi.org/10.1016/j.jscs.2015.11.001>.
- (55) Campisi, S.; Schiavoni, M.; Chan-Thaw, C. E.; Villa, A. Untangling the Role of the Capping Agent in Nanocatalysis: Recent Advances and Perspectives. *Catalysts* **2016**, *6* (12), 185. <https://doi.org/10.3390/catal6120185>.
- (56) Jiang, H.-L.; Akita, T.; Ishida, T.; Haruta, M.; Xu, Q. Synergistic Catalysis of Au@Ag Core–Shell Nanoparticles Stabilized on Metal–Organic Framework. *J. Am. Chem. Soc.* **2011**, *133* (5), 1304–1306. <https://doi.org/10.1021/ja1099006>.
- (57) Holden, M. S.; Nick, K. E.; Hall, M.; Milligan, J. R.; Chen, Q.; Perry, C. C. Synthesis and Catalytic Activity of Pluronic Stabilized Silver–Gold Bimetallic Nanoparticles. *RSC Adv.* **2014**, *4* (94), 52279–52288. <https://doi.org/10.1039/C4RA07581A>.



# Chapter IV. Fabrication of multifunctional binary nanoparticle superlattices: mixing plasmonic and magnetic or catalytic nanoparticles

## 1. Introduction

The term binary superlattices (BNSLs) refers to the assemblies of nanomaterials composed of two different cooperative complementary components. Normally, two or more individual components are synthesized separately, then binary superlattices can be fabricated through the methods like fabricate the 3D assemblies of one type of NPs as described previously (see chapter I). Monodisperse spherical particles can usually self-assemble into superlattices with either face centered cubic (*fcc*) or hexagonal close packed crystalline (*hcp*) structures<sup>1-5</sup>. Binary mixtures naturally provide a much richer class of compositions and structures. When two types of particles co-crystallize, they must meet, as far as possible, the requirements of certain geometrical principles. In the simplest approach, the formation of a binary assembly is expected only if its compactness exceeds that of single-component crystals in *fcc* or *hcp* (0.74)<sup>6</sup>. This principle of space filling is still widely used for predicting the behavior of particles in binary mixtures. Particle size ratio ( $R_{\text{small}}/R_{\text{large}}$ ) and concentrations are considered as factors determining the structure of binary assemblies<sup>7,8</sup>. By taking into account the geometric considerations, we can predict the formation of BNSLs structure such as AB, AB<sub>2</sub>, or AB<sub>13</sub>. The interparticle distance (between NPs A) can be increased through the insert of NPs B (with possible different sizes) in the BNSLs as compared to the single component superlattices (made of NPs A). Consequently, the strategy of the binary superlattices offers a possibility to tune the interactions between the NPs (NPs A), to control the collective properties of the assemblies<sup>9,10</sup>. The binary superlattices constitute ideal candidates to favor coupling between two types of NPs (NP A and NP B) (e.g. plasmonic/plasmonic, magnetic/magnetic and magnetic/plasmonic), which is expected to result in tunable and/or novel collective properties.

The distance between the two components is a main factor for the formation of binary superlattices. An understanding of the interaction between both components leads to the fabrication of appropriate and desired binary structure. The fabrication of binary superlattices



started in 1998<sup>11</sup>, hence the study of their physical properties in view of possible applications is still a challenge in nanoscience.

Fabrication of BNSLs is one other way to integrate two different metals into one system. The organization between two different types of NPs is obtained through a balance between van der Waals interaction and steric repulsion. In case of plasmonic or magnetic NPs, coupling between NPs may influence the interactions, which brings unique collective properties on binary assemblies<sup>12–14</sup>.

In first part of Chapter IV, we focus on structural study of binary assemblies made of Au and maghemite ( $\gamma$ -Fe<sub>2</sub>O<sub>3</sub>) NPs. The influence of different parameters like deposition temperature (Td),  $\gamma$ -Fe<sub>2</sub>O<sub>3</sub>/Au effective size ratio  $\gamma_{eff}$ , or  $[\gamma\text{-Fe}_2\text{O}_3]/[\text{Au}]$  concentration ratio was studied to optimize their organization. The Maghemite ( $\gamma$ -Fe<sub>2</sub>O<sub>3</sub>) and Au NPs used are characterized by narrow size distributions and their size can be tuned from 7.9 to 12.4 nm for maghemite NPs and fixed around 5 nm for gold NPs.

In a second part, we studied the BNSLs structure from Pd and Au NPs characterized by their well-known catalytic and plasmonic properties, respectively. The influence of Au/Pd effective size ratio  $\gamma_{eff}$ , and the deposition methods is studied to optimize their organization. All the BNLs structure were characterized by TEM (in the case of thin films), by high-resolution scanning electron microscopy (HR-SEM) and small angle X-ray scattering (SAXS). Finally, the magnetic properties of  $\gamma$ -Fe<sub>2</sub>O<sub>3</sub>/Au NP BNSLs were studied by SQUID magnetometer measurements and compared to those of  $\gamma$ -Fe<sub>2</sub>O<sub>3</sub> NPs superlattices.

## 2. Fabrication of binary superlattices by mixing $\gamma$ -Fe<sub>2</sub>O<sub>3</sub> and Au NPs

### 2.1. Preparation of nanoparticles (NPs)

The maghemite ( $\gamma$ -Fe<sub>2</sub>O<sub>3</sub>) NPs with 12.4 nm ( $\sigma=8\%$ ), 11.4 nm, ( $\sigma=8\%$ ) and 7.9 nm ( $\sigma=8\%$ ) were prepared by Anh-Tu Ngo (MONARIS)<sup>15</sup> using modified procedure from Park *et al*<sup>16</sup>. For the 12.4 nm diameter maghemite NPs, the reactants sodium oleate and oleic acid are replaced here by sodium laurate and lauric acid. The typical synthesis of the iron–laurate complex is prepared by mixing iron chloride (FeCl<sub>3</sub>6H<sub>2</sub>O) and sodium laurate in a solvent mixture composed of ethanol, distilled water, and hexane. The mixture is refluxed at

66 °C for 4 h and the organic phase is washed three times with ultrapure water in a separatory funnel. The remaining hexane in the organic phase is evaporated under vacuum in a rotavapor at 32 °C. The iron–laurate complex is then washed three times with a mixture of ethanol and hexane and evaporated at 40 °C. In a typical synthesis procedure of maghemite nanocrystals, 1.05 g of the iron–laurate complex is dissolved in a mixture of 10 ml of 1-octadecene and 0.64 g of lauric acid at room temperature. This mixture is heated to the boiling point of 1-octadecene (b.p: 317 °C) under vigorous stirring and is refluxed for 30 min and then cooled to room temperature. A black gel containing the nanocrystals is formed. The nanocrystals are separated and washed with a large excess of hexane, ethanol, and acetone.

For the 11.4 nm and 7.9 nm diameter maghemite NPs, we replaced the sodium laurate and lauric acid by sodium oleate and oleic acid. The procedures for synthesizing the reactant (sodium oleate) and particles are the same way as those described above. The 7.9 nm diameter maghemite NPs were synthesized using 1.42 g of iron–oleate complex dissolved in a mixture of 10 mL of 1-octadecene and 0.9 g of oleic acid. However, if we heated this mixture for 2h at 100°C before heating up to the boiling point of 1-octadecene under vigorous stirring and keeping under refluxed for 30 min, 11.4 nm maghemite NPs are obtained. The NPs are then dispersed in organic solvent such as chloroform or toluene.

The Au NPs were synthesized via organometallic route as described in chapter II. They are characterized by a mean diameter of 4.6 nm with a size distribution of 7% and are dispersed in organic solvent (chloroform or toluene). The binary samples were then prepared by mixing both colloidal solutions

In entropy-driven self-assemblies with hard-sphere approximation, it is possible to predict the most thermodynamically stable binary structure. The packing density of binary superlattices is mainly dependent on the effective size ratio between smaller and bigger NPs. The effective size ratio can be shown below.

$$\gamma_{eff} = \frac{D_{eff} \text{ of smaller NPs}}{D_{eff} \text{ of bigger NPs}} \quad (4.1)$$

The effective diameter ( $D_{eff}$  or  $D_{C-C}$ ) is the distance between NPs including ligands length and this distance can be estimated by TEM, the center to center distance between NPs organized in 2D or 3D network (Figure 4.1).

The introduction of soft repulsive potential allows a characterization of a significant morphological diversity in self-assembled superlattices. In the region where phase separation into A + B can be overcome<sup>17,18</sup>.

Thus, before mixing the NP concentrations of both colloidal solutions were determined by UV-vis absorption spectroscopy. The  $[\gamma\text{-Fe}_2\text{O}_3]/[\text{Au}]$  concentration ratio for mixing was tuned from 1:1 to 1:7 with fixed  $[\gamma\text{-Fe}_2\text{O}_3]=0.1$  wt. %, for example 1:1=0.1 wt. %:0.1 wt. % and 1:7=0.1 wt. % : 0.7 wt. %. Their volume ratio is always fixed to 1:1. The  $\gamma\text{-Fe}_2\text{O}_3$  and Au colloidal solutions were prepared separately and then mixed under sonication during 5 min.

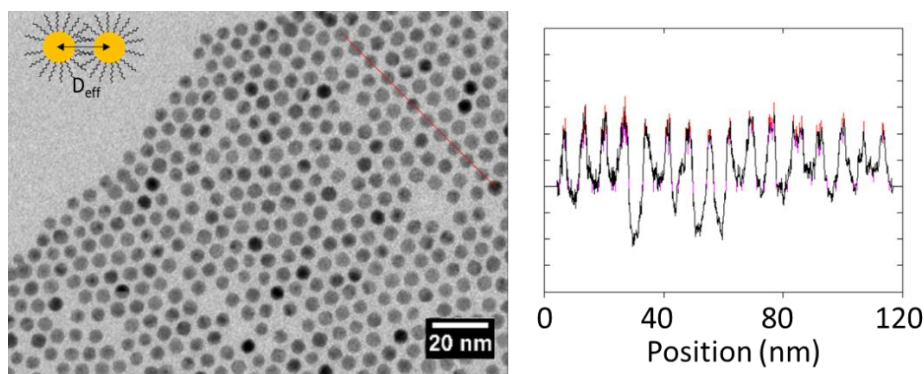


Figure 4. 1. TEM image of 4.6 nm diameter Au NPs with 7% polydispersity covered by 1-dodecanethiol (DDT) with a line profile showing an interparticle distance  $\approx 6.4$  nm.

## 2.2. Preparation of binary assemblies

There are various methods to fabricate the NP binary superlattices which are similar to those for the fabrication of one-component ordered assemblies (see Chapter I). Here, we used two deposition methods: i) immersion method, ii) liquid-liquid interface deposition (already mentioned in chapter I) (Figure 4.2).

### *i) immersion method*

The BNSLs growth process is performed via the evaporation of binary colloidal solutions<sup>19,20</sup>. Substrates (TEM grid or silicon) were placed in a glass vial in a temperature-controlled chamber through water circulation and the whole chamber is filled with flowing  $\text{N}_2$  gas. Then, fixed volume of binary colloidal solution was added: 20  $\mu\text{l}$  in case of TEM grids

used as substrates and 200  $\mu\text{l}$  for silicon substrates. Ordered binary assemblies formed upon solvent, such as Toluene, evaporation.

*ii) liquid-liquid interface deposition*

There is another way to obtain BNSLs which is liquid-liquid interface deposition method<sup>21,22</sup>. This assembly method is based on the use of a bad solvent, ethylene glycol (EG) in our case. It is called a bad solvent because it cannot solubilize the NPs which tend to agglomerate at its surface. EG is filled in a Teflon beaker, then 20  $\mu\text{l}$  of the binary colloidal solution is deposited on top of the bad solvent. This deposition is performed in a temperature-controlled chamber through water circulation and filled with flowing  $\text{N}_2$ . This heterogeneous growth mode of NP assemblies leads, after solvent evaporation, to the formation of a thin film made of ordered binary assemblies. The NPs film is collected and deposited on a solid substrate.

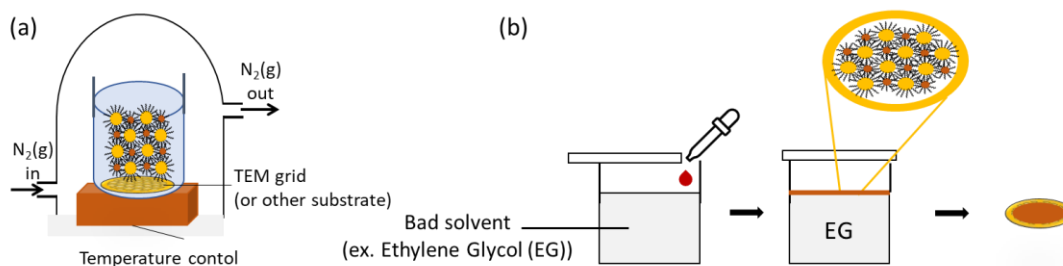


Figure 4. 2. Schemes of preparation methods used for growing ordered binary assemblies.

### 3. Control of binary superlattices structure: case of mixing $\gamma\text{-Fe}_2\text{O}_3$ and Au NPs

#### 3.1. Influence of effective nanoparticle size ratios

Here, we used only spherical NPs with low dispersion in size  $\approx 8\%$  favoring their self-assembly. The choice of both components (called  $\text{NP}_1$ ,  $\text{NP}_2$ ) to form binary assemblies is dependent on; i) their size distribution which must be narrow ( $\leq 10\%$ ) to favor their self-organization, ii) the need of second component with moderate sizes to obtain a reasonable effective size ratio. One of main parameter to control the binary assembly is the effective nanoparticle size ratio ( $\gamma_{eff}$ ) between smaller and larger binary components<sup>23</sup>. The hydrophobic long alkyl chain ligands covered each NPs make avoid the formation of

aggregates through short-range steric repulsion and favor a sphere-like crystallization<sup>24</sup>. These long alkyl chain ligands also prevent phase separation of NP<sub>1</sub>-NP<sub>1</sub>, NP<sub>2</sub>-NP<sub>2</sub> and lead to the NP<sub>1</sub>-NP<sub>2</sub> interactions as electrostatic repulsion and van der Waals attractions<sup>8</sup>.

In this work, three different sizes of  $\gamma$ -Fe<sub>2</sub>O<sub>3</sub> NPs (12.4, 11.4, and 7.9 nm) are expected to form binary assemblies with Au NPs (4.6 nm diameter). The corresponding effective diameter of both components are given in table 4.1, the nature of the ligands and the effective size ratio are also indicated. BNSLs of  $\gamma$ -Fe<sub>2</sub>O<sub>3</sub> and Au NPs were self-assembled from the toluene solution by using the immersion method (see table 4.2 for the details on the BNSLs growth conditions). During the evaporation process, the system is expected to adapt the crystal structure corresponding to the most efficient space filling system and reach the maximum packing density for a given effective size ratio.

TEM studies revealed that three different structural types of BNSLs: NaCl (Space Group Fm3m), AlB<sub>2</sub> (Space Group P6/mmm), NaZn<sub>13</sub> (Space Group Fm3c) could be obtained by varying the effective nanoparticle size ratio  $\gamma_{eff}$  keeping the other conditions constants ( $T_d=50$  °C and [ $\gamma$ -Fe<sub>2</sub>O<sub>3</sub>]: [Au]= 1:4) (figures 4. 3a, b and c). The TEM image in figure 4.3a show typical (111) crystal planes of NaCl-type binary superlattices with the corresponding model in the insets for an effective size ratio  $\gamma_{eff}=0.45$ . The size of the crystal domains of the NaCl-type binary structure is up to few  $\mu$ m (low magnification TEM image in Annex 9). Furthermore, a further increase of  $\gamma_{eff}$  to 0.48 and 0.65 induces the production of AlB<sub>2</sub> and NaZn<sub>13</sub> type binary structures respectively (Figure 4.3b and c). the corresponding model are in insets. The size of the crystal domains of both binary structures are up to a few hundred nm to 1-2  $\mu$ m (TEM image in Annex 9). For AlB<sub>2</sub>-type structure, the crystal orientation has the (110) plane parallel to the substrate as is observed in the TEM image (Figure 4.3b). For NaZn<sub>13</sub>-type structure, the TEM image represent the icosahedral NaZ<sub>13</sub> (Figure 4.3c) from the preferential crystal orientation with the (100) plane parallel to the substrate.

We could observe film formation with some cracks through the TEM images observation (Annex 9) that most probably indicates the layer by layer growth for such NaCl, AlB<sub>2</sub>, NaZn<sub>13</sub>-type superlattices<sup>25</sup>.

Table 4.1. Nanoparticles used as components for BNSLs composed of magnetic NPs of  $\gamma\text{-Fe}_2\text{O}_3$  NPs) and plasmonic NPs (Au NPs), as a result, three combinations of BNSL with different effective size ratios.

NP type	NP <sub>big</sub> : $\gamma\text{-Fe}_2\text{O}_3$ NPs			+	NP <sub>small</sub> : Au NPs
	1	2	3		4
Ligand	lauric acid (C <sub>12</sub> )	oleic acid (C <sub>18</sub> )	oleic acid (C <sub>18</sub> )		1-dodecanethiol (C <sub>12</sub> )
NPs diameter	12.4 nm	11.4 nm	7.9 nm		4.6 nm
Effective diameter (D <sub>C-C</sub> )	14.2 nm	13.4 nm	10 nm		6.4 nm

	BNSLs	NP1+NP4	NP2+NP4	NP3+NP4
Effective size ratio ( $\gamma_{\text{eff}}$ )		0.45	0.48	0.64

Table 4.2. Growth conditions of BNSLs assemblies.

Fixed parameter	Condition
Concentration ratio ([ $\gamma\text{-Fe}_2\text{O}_3$ ]:[Au])	1:4 (0.1 wt.% : 0.4 wt. %)
Solvent	Toluene
Volume of NPs	40 ( $\mu\text{l}$ )
deposition method	Immersion method
Deposition temperature (T <sub>d</sub> )	50 °C

According to hard sphere model, the system is expected to adopt the crystal structure corresponding to the most efficient space filling to reach the maximization of the packing density for a given effective nanoparticle size ratio<sup>26</sup>. The effective size ratio ( $\gamma_{\text{eff}}$ ) of three BNSL combinations between  $\gamma\text{-Fe}_2\text{O}_3$  and Au NPs has been increased ( $0.45 \leq 0.48 < 0.64$ ) with the decrease of the  $\gamma\text{-Fe}_2\text{O}_3$  diameter ( $12.4 \text{ nm} > 11.4 \text{ nm} > 7.9 \text{ nm}$ ). With the increase of size ratio, the BNSL type-structure has been changed from NaCl, AlB<sub>2</sub> and finally NaZn<sub>13</sub> structures.

The BNSLs structures observed in this work are in accordance with the phase diagram for binary hard spheres mixtures<sup>6-8,8,27</sup>. A transition of binary structure was observed by decreasing the nanoparticle effective size ratio. This confirms that at a fixed temperature (50 °C) and concentration ratio ( $[\gamma\text{-Fe}_2\text{O}_3]:[\text{Au}] = 1:4$ ), the hard-sphere model design for atoms can, to some extent, be used for NPs. Consequently, the binary superlattices can be simply predicted from the spacing filling curves. This is confirmed by Table 4.3, which compares the various structures of binary superlattices obtained for the different nanoparticle effective size ratio values claimed for these different structures in the paper given in reference.

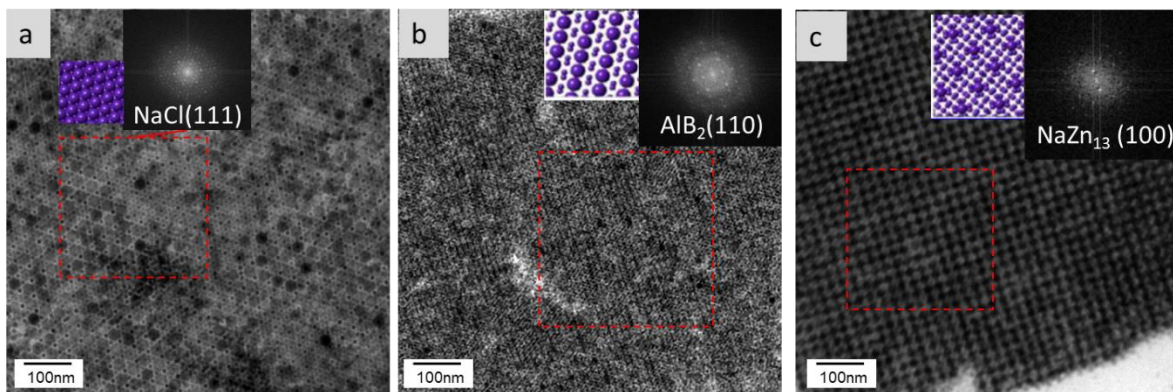


Figure 4. 3. TEM images of binary superlattices formed from  $\gamma\text{-Fe}_2\text{O}_3$  and Au NPs under different effective size ratio ( $\gamma_{eff}$ ) keeping the other conditions as a constant ( $[\gamma\text{-Fe}_2\text{O}_3]:[\text{Au}]=1:4$ ,  $T_d=50^\circ\text{C}$ ) (a) 0.45 (b) 0.48 (c) 0.64. Insets (right) indicate selected area FFT analysis. Representation of each BNSL structure corresponding to TEM image is presented in insets (left side from FFT diagram).

Table 4.3. Comparison of structures that are experimentally observed with the theoretical phase diagrams for binary hard spheres mixtures<sup>7,27</sup>.

	NaCl	AlB <sub>2</sub>	NaZn <sub>13</sub>
Ref. <sup>27</sup>	$0.421 \leq \gamma_{eff} \leq 0.45$	$0.45 \leq \gamma_{eff} \leq 0.54$	$0.54 \leq \gamma_{eff} \leq 0.625$
$D_{eff, Au}/D_{eff, Fe_2O_3}$	$\gamma_{eff} = 0.45$	$\gamma_{eff} = 0.48$	$\gamma_{eff} = 0.64$

### 3.2. Influence of $[\gamma\text{-Fe}_2\text{O}_3]/[\text{Au}]$ concentration ratio and deposition temperature.

The effective size ratio is not the only parameter to control the BNSLs structure. NPs mixture decide the BNSL structure which are thermodynamically stable for them. Previous studies showed that the change of the relative volume of colloidal solutions can induce the phase transformation in binary NP SLs<sup>25</sup>. Here, the  $[\gamma\text{-Fe}_2\text{O}_3]/[\text{Au}]$  concentration ratio and deposition temperature ( $T_d$ ) were modulated (table 4.2). We have chosen  $\gamma\text{-Fe}_2\text{O}_3$  NPs with 7.9 nm NP diameter and Au NPs with 4.6 nm NP diameter to fix the effective size ratio ( $\gamma_{\text{eff}}=0.64$ ).

TEM images in Figure 4.4 show that BNSL type-structures can change with the  $[\gamma\text{-Fe}_2\text{O}_3]:[\text{Au}]$  concentration ratio and deposition temperature ( $T_d$ ). First, at  $T_d=50^\circ\text{C}$ , the concentration ratio from 1:1 to 1:4 or 1:7 induced the change of BNSL structure from CuAu to NaZn<sub>13</sub> structure. A similar behavior is observed at  $T_d=65^\circ\text{C}$ . At  $T_d=35^\circ\text{C}$ , CuAu-type structure is observed for concentration ratios  $[\gamma\text{-Fe}_2\text{O}_3]:[\text{Au}]=1:1$  and 1:4. At high concentration ratio  $[\gamma\text{-Fe}_2\text{O}_3]:[\text{Au}]=1:7$  NaZn<sub>13</sub>-type with high density of Au NPs remains dominant. At the medium ratio  $[\gamma\text{-Fe}_2\text{O}_3]:[\text{Au}]=1:4$ , amorphous arrangements are also observed (figure 4.4 d). The deposition temperature influences the solvent evaporation velocity from the mixture of two NPs and the formation of superlattices. The formation of superlattices are typically required enough temperature for binary hard-sphere mixtures<sup>8</sup>. However, exceeding boiling point of solvent prevent the organization. This clearly shows that, for a given  $\gamma$  value, the well-known hard sphere model of atomic binary bulk material is valid for nanoparticles in a rather restrictive domain related to the relative concentration of large to small nanoparticles and depends on the deposition temperature ( $T_d$ ). Here, this is valid for  $\gamma_{\text{eff}}=0.64$  with  $1:4 \leq [\gamma\text{-Fe}_2\text{O}_3]:[\text{Au}] \leq 1:7$  for a substrate temperature  $T_d \geq 50^\circ\text{C}$ .



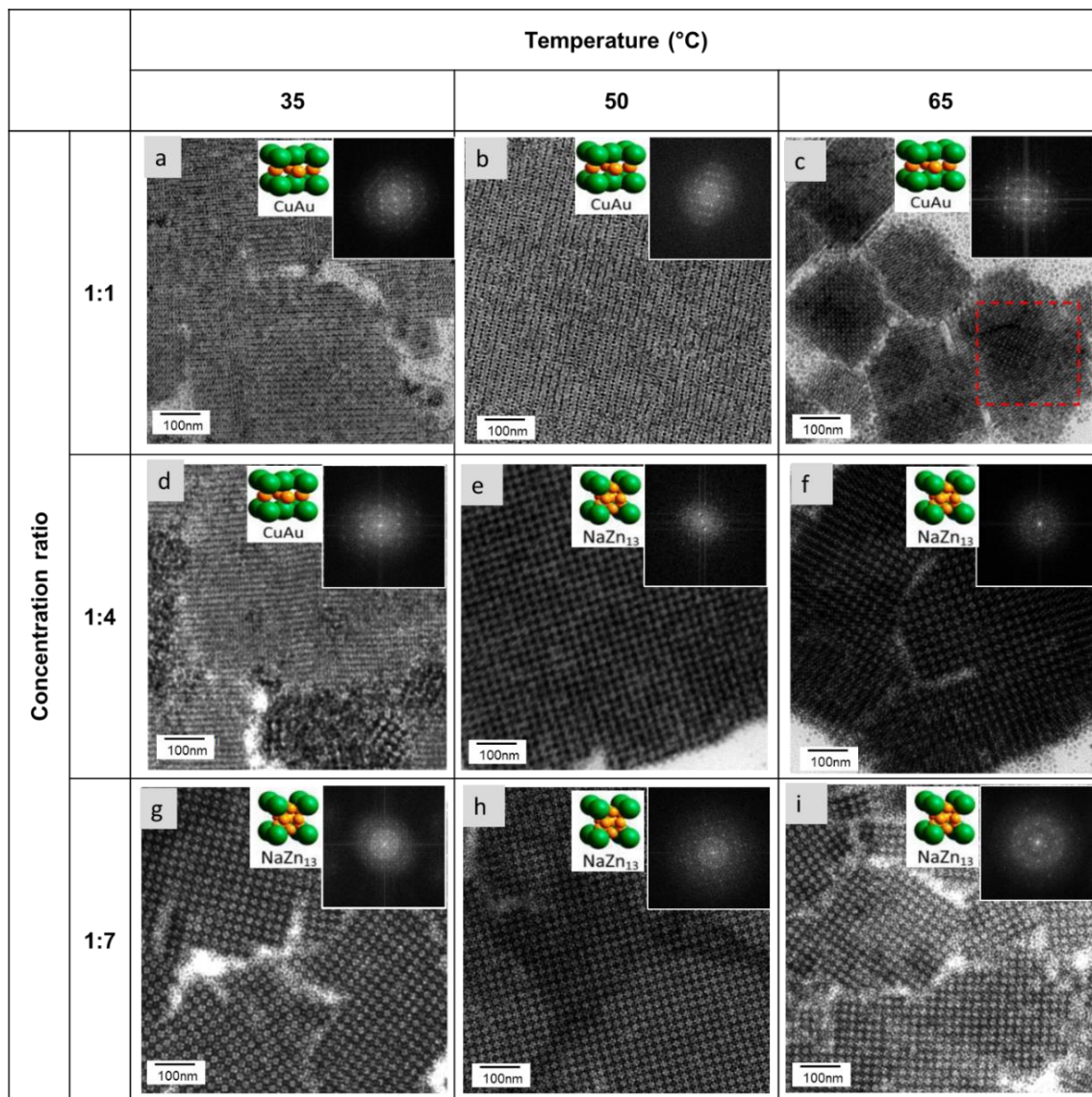


Figure 4. 4. TEM images of binary superlattices formed with 7.9nm  $\gamma$ -Fe<sub>2</sub>O<sub>3</sub> NPs and 4.6nm Au NPs and fixed effective size ratio ( $\gamma_{eff} = 0.64$ ) and different  $[\gamma\text{-Fe}_2\text{O}_3]/[\text{Au}]$  concentration ratios (in three rows : 1:1, 1:4, and 1:7 from top to below), and deposition temperatures (in three columns : 35 °C, 50°C, and 65 °C from left to right). Insets indicate selected area FFT analysis. Representation of unit cell of each BNSL structure corresponding to TEM image is presented as an inset (left side from FFT diagram).

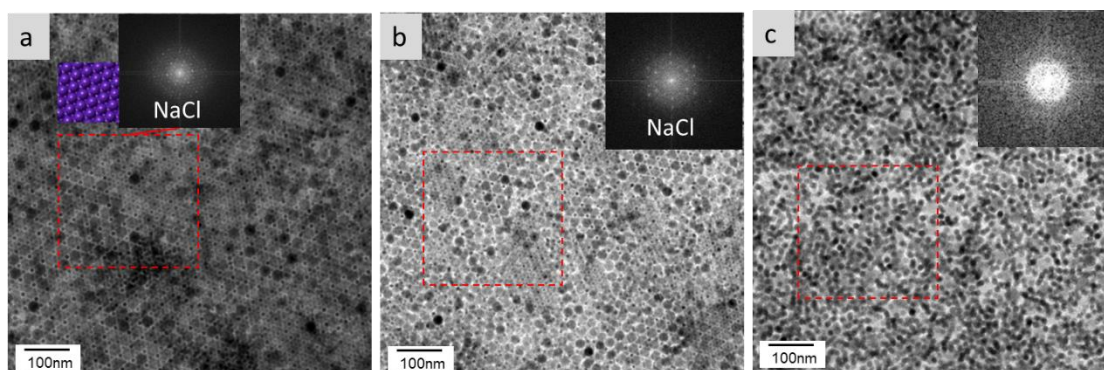
### 3.3. Influence of the nature of the solvent

The long hydrophobic alkyl chain ligands are attached on NPs surface through a headgroup linker, forming a soft corona around the NPs. The interaction between NPs and surface ligands are repulsive in some solvent, also can be attractive in other solvent. And it is

up to NPs diameter and chemical structure of ligands. During the self-assembly process, solvent evaporation densifies the NPs colloidal solution and force the solvated NPs to contact each other. It is shown that the phase diagram of a soft repulsive potential leads to the morphological diversity observed in experiments with binary nanoparticles, thus providing a general framework to understand their phase diagrams. Particular emphasis is given to the two most successful crystallization strategy which is the evaporation of solvent from nanoparticles with grafted hydrocarbon ligands<sup>17,28</sup>. Finally, complete evaporation of solvent makes the collection of NPs into a binary superlattices by the balance between van der Waals attraction and ligand elastic repulsion. Also, the formation of stable BNSL structure takes time along the evaporation of the solvent. The solvent with high boiling point is typically required to form well-ordered BNSL structures<sup>21</sup>.

So, we have chosen  $\gamma$ -Fe<sub>2</sub>O<sub>3</sub> NPs with 12.4 or 11.4 nm diameter and Au NPs with 4.6 nm diameter to fix the effective size ratios  $\gamma_{\text{eff}} = 0.45$  or  $0.48$ , respectively. We tested toluene, hexane, and chloroform as solvents. The NaCl and AlB<sub>2</sub> type binary structures are observed with hexane and toluene as solvent depending on the  $\gamma_{\text{eff}}$  value in agreement with the well-known hard sphere model of atomic binary bulk material (see table 4.3). Nevertheless, any BNSL organization were observed with chloroform as solvent in agreement with the Fast Fourier Transform (FFT) of the TEM image (inset figure 4.5 c). The Hildebrand parameter value for 1-dodecanethiol or lauric acid as coating agents for gold and ferrite NPs, respectively can be approximated by the Hildebrand parameter value for the solvent dodecane (16 MPa<sup>0.5</sup>)<sup>29</sup> and is thus close to this one of oleic acid coating agent (16.3 MPa<sup>0.5</sup>) (table 4.4). Hexane, whose Hildebrand parameter (14.9 MPa<sup>0.5</sup>) is expected to be a significantly better solvent for the coating agents than toluene or chloroform (18.2 and 18.7 MPa<sup>0.5</sup>) respectively (see table 4.4). This translates into interaction potentials that are repulsive or very weakly attractive for hexane, whereas they are highly attractive for toluene or chloroform for any NP sizes<sup>29</sup>. The BNSLs are thus more homogeneous with toluene (less defects) than with hexane. Nevertheless, the evaporation rate has also to be considered. The hexane evaporation rate is faster than toluene that could also prevent the NP diffusion, and thus their interaction. Thus, Chloroform whose has a Hildebrand parameter close to toluene leads to amorphous arrangement due to a too fast evaporation rate.

1)  $\gamma$ -Fe<sub>2</sub>O<sub>3</sub> NPs (12.4nm-C12) - Au NPs (4.6nm-C12)



2)  $\gamma$ -Fe<sub>2</sub>O<sub>3</sub> NPs (11.4nm-C18) - Au NPs (4.6nm-C12)

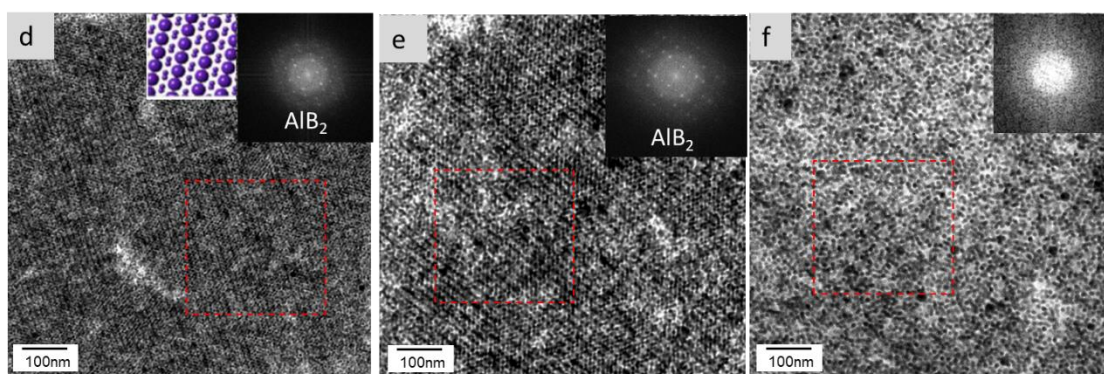


Figure 4. 5. TEM images of binary nanoparticle superlattices formed from  $\gamma$ -Fe<sub>2</sub>O<sub>3</sub> and Au NPs with effective size ratio of (1)  $\gamma_{eff} = 0.45$  and (2) 0.48 formed after evaporation of different nature of solvent (a) and (d) toluene, (b) and (e) hexane and (c) and (f) chloroform. Insets indicate selected area FFT analysis. Representation of unit cell of each BNSL structure corresponding to TEM image is presented as an inset (left side from FFT diagram).

Decane, cumene toluene and isooctane characterized by boiling points of 174, 152, 111 and 99°C respectively were tested in the case of mixing  $\gamma$ -Fe<sub>2</sub>O<sub>3</sub> NPs with 7.9 nm diameter and Au NPs with 4.6 nm diameter to fix the effective size ratio ( $\gamma_{eff} = 0.64$ ). For a concentration ratio of 1:4 and a deposition temperature  $T_d = 50^\circ\text{C}$ , NaZn<sub>13</sub> type binary structure was expected according to previous results and in agreement with hard-sphere model.

As expected, NaZn<sub>13</sub> type structure for BNSLs were observed whatever the nature of the solvent (Figure 4.6). However, by increasing the solvent evaporation time from toluene to cumene and decane, the BNSLs tend to exist as isolated islands scattered irregularly on the solid substrate. Nevertheless, if we consider isooctane having a close boiling point to toluene

(see table 4.4), we observed smaller BNSL island sizes with isooctane than with toluene. Isooctane (Hildebrand parameter =  $16.8 \text{ MPa}^{0.5}$ ) is expected to be a significantly better solvent for the NP coatings agent than toluene ( $18.2 \text{ MPa}^{0.5}$ ) (see table 4.4). Highly attractive interactions between NPs in toluene seems again to favor the NP organization into BNSLs of larger sizes.

The nature of the solvent is clearly shown not to influence the structure type of BNSLs but rather its coherence length which appears to depend both on the solvent evaporation rate and the Hildebrand parameters of the solvent and the ligands. Experiments under quasi-saturated conditions would allow us to better distinguish these two last effects.

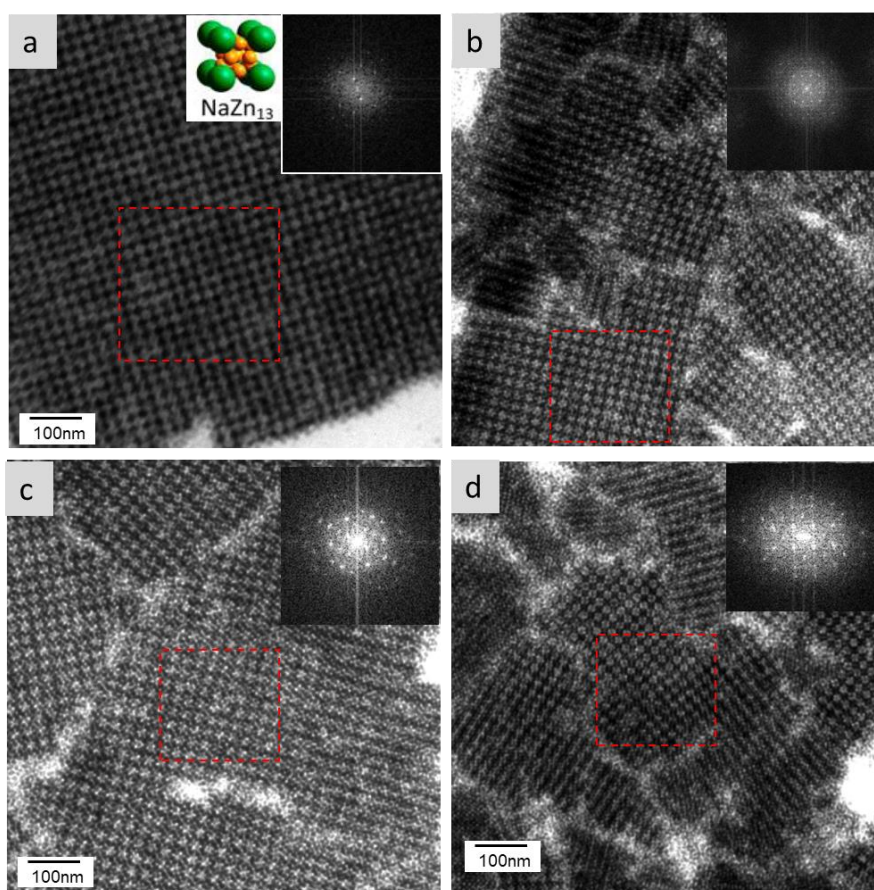


Figure 4. 6. TEM images of  $\text{NaZn}_{13}$  type binary superlattices formed with  $7.9 \text{ nm } \gamma\text{-Fe}_2\text{O}_3$  and  $4.6 \text{ nm Au}$  NPs with fixed effective size ratio ( $\gamma_{\text{eff}}=0.64$ ) and deposition temperature  $T_d=50^\circ\text{C}$  by using different solvents a) isooctane, b) toluene, c) cumene and d) decane . In Insets selected area FFT analysis. And representation of unit cell of  $\text{NaZn}_{13}$  type binary structure.

Table 4.4. Hildebrand parameters and boiling points of the different solvents and ligands used in this work<sup>29-31</sup>.

Solvent or (ligands)	Hildebrand solubility parameters (MPa <sup>0.5</sup> )	Boiling point (°C)	Evaporation time (hour)
toluene	18.2	111	4
chloroform	18.7	61	0.3
cumen	17.5	152	5
decane	15.6	174	6~7
isooctane	16.8	99	3~4
Oleic acid (ligands)	16.3	360	-
Dodecane (ligands)	16	216.2	-
hexane	14.9	68	0.5

### 3.4. Influence of deposition method

The as-grown BNSLs structure in immersion method typically exists as isolated, randomly scattered islands on the substrate in an optimized condition as it is shown in previous sections. The formation of isolated island is due to the formation of BNSL is a procedure typically leading to a low surface coverage during a solvent evaporation<sup>32</sup>. Here, we studied how BNSLs are influenced by the deposition method.

Liquid-liquid interface deposition is based on self-assemblies on an immiscible liquid surface, allowing the growth of macroscopic BNSL films with no substrate restrictions under ambient conditions. Another major benefit of our approach is that BNSL films formed on the liquid surface can be easily transferred to another substrate.

We have chosen  $\gamma$ -Fe<sub>2</sub>O<sub>3</sub> NPs with 7.9 nm NP diameter and Au NPs with 4.6 nm NP diameter to fix the effective size ratio ( $\gamma_{\text{eff}}=0.64$ ), and solvent as toluene. The TEM images (figures 4.7 a and b) allowed to identify CuAu binary type structure of BNSL domains in case of a concentration ratio  $[\gamma\text{-Fe}_2\text{O}_3]/[\text{Au}]=1:1$  whatever the deposition method. Nevertheless, the BNSLs appear clearly thicker by using immersion method than interface deposition.

The structure and stoichiometry of BNSL film is tuned by changing the concentration ratio between both NPs components. The BNSL structure in case of 1:4 concentration ratio is  $\text{NaZn}_{13}$  type whatever the deposition method. For this concentration ratio the binary crystal domains appear clearly thicker and larger in size by using immersion method than interface deposition.

Thus, there is no difference in BNSL type binary structure depending on the deposition method, which appears to influence only the thickness and size of the crystal domains.

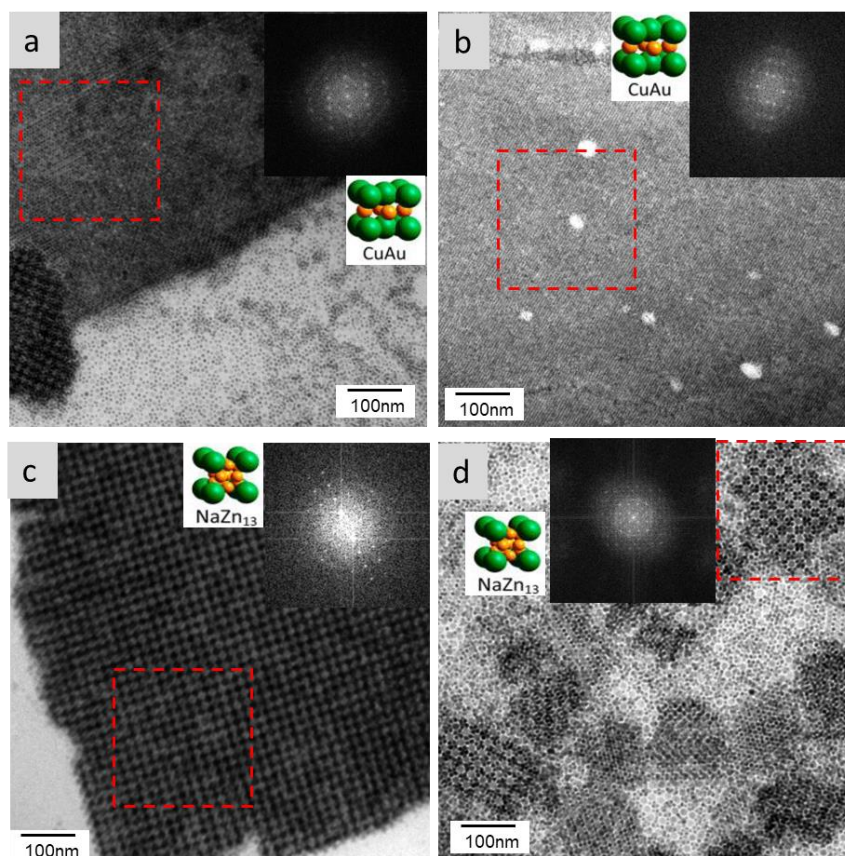


Figure 4. 7. TEM images of binary superlattices formed with 7.9nm  $\gamma\text{-Fe}_2\text{O}_3$  and 4.6nm Au NPs with fixed effective size ratio ( $\gamma_{\text{eff}} = 0.64$ ), different concentration ratio and deposition method: a) and c) by immersion method for  $T_d = 50^\circ\text{C}$  and concentration ration of 1:1 and 1:4 respectively, b) and d) by liquid-liquid interface method and concentration ration of 1:1 and 1:4 respectively Insets indicate selected area FFT analysis. Representation of unit cell of each BNSL structure corresponding to TEM image is presented as an inset (left side from FFT diagram).

### 3.5. Structural and magnetic characterizations of 2D organization of BNSLs ( $\gamma$ -Fe<sub>2</sub>O<sub>3</sub> NPs-Au NPs) and $\gamma$ -Fe<sub>2</sub>O<sub>3</sub> NPs

#### 3.5.1. Structural characterization of 2D organization of BNSLs ( $\gamma$ -Fe<sub>2</sub>O<sub>3</sub> NPs-Au NPs) and $\gamma$ -Fe<sub>2</sub>O<sub>3</sub> NPs

In the previous section, the successful coassembly of spherical 7.9 nm maghemite ( $\gamma$ -Fe<sub>2</sub>O<sub>3</sub>) and gold (4.6 nm) NPs is demonstrated. The different type structures of BNSL obtained according to the deposition conditions (temperature, solvent, effective size and concentration ratios) correspond to the stacking of a few layers of nanoparticles (3-4 layers) which is thus fine enough to be observed by MET but need the use of a superconducting quantum interface device (SQUID) magnetometer for the characterization of their magnetic properties in order to optimize the signal. In order to anticipate the evolution of the magnetic properties between assemblies of pure maghemite NPs and binary assemblies of maghemite and golds NPs, it is interesting to determine the core to core interparticle distances  $D_{c-c}$  between maghemite in both types of assemblies.

We focused our study on one type of BNSL structure. For this purpose, the effective size ratio was set at  $\gamma_{\text{eff}} = 0.64$  and all other deposition conditions listed in Table 2.2 were set to obtain a structure of NaZn<sub>13</sub> type binary structure. From TEM image, we confirm the cubic lattices (Figure 4.8a) and from a closer view (Figure 4.8 b and c) we can distinguish the  $\gamma$ -Fe<sub>2</sub>O<sub>3</sub> (light grey) and the Au (black) NPs since gold atoms scatter electrons more strongly than iron oxide. The core to core interparticle distance  $D_{c-c}$  between maghemite in BNSL is deduced from TEM image (see profile in figure 4.8 d) and is around 13.8 nm (table 4.5). For pure  $\gamma$ -Fe<sub>2</sub>O<sub>3</sub> assemblies, the TEM image show close packed arrangement of these NPs. From the profile performed on the TEM image we deduce the core to core interparticle distance  $D_{c-c}$  between maghemite which is around 10 nm (table 4.5). From this  $D_{c-c}$  value and maghemites size, we deduce an edge to edge distance around 2.2 nm that imply no interdigitation of the OA chains (effective length 1.1nm) in agreement with previous results<sup>24</sup>. Thus, the maghemite NPs assemblies are distorted by the presence of gold that induces an increase in interparticle  $D_{c-c}$  distance. Here, we can thus anticipate that magnetic dipole-dipole interactions between maghemite NPs should be modified in the BNSL.

Table 4. 5. Interparticle distance  $D_{C-C}$  between magnetic NPs ( $\gamma\text{-Fe}_2\text{O}_3$  NPs) in thin BNSLs and pure  $\gamma\text{-Fe}_2\text{O}_3$  NP assemblies.

	<b>Binary superlattices formed with 7.9 nm <math>\gamma\text{-Fe}_2\text{O}_3</math> and 4.6 nm Au NPs</b>	<b>Pure 7.9 nm <math>\gamma\text{-Fe}_2\text{O}_3</math> NP superlattices</b>
$D_{C-C}$	13.8 nm	10 nm
crystalline structure	$\text{NaZn}_{13}$	<i>fcc</i>

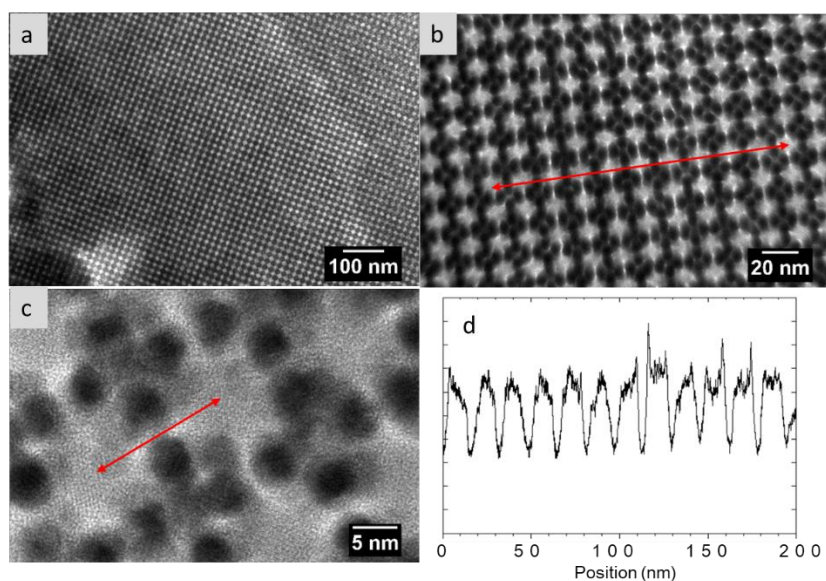


Figure 4. 8. (a-c) HR-TEM images of  $\text{NaZn}_{13}$  BNSL structure with different magnification, scale bar indicated in each TEM image. (d) the line profiles from (c) indicate interparticle distances  $D_{C-C} \approx 13.8$  nm, respectively.

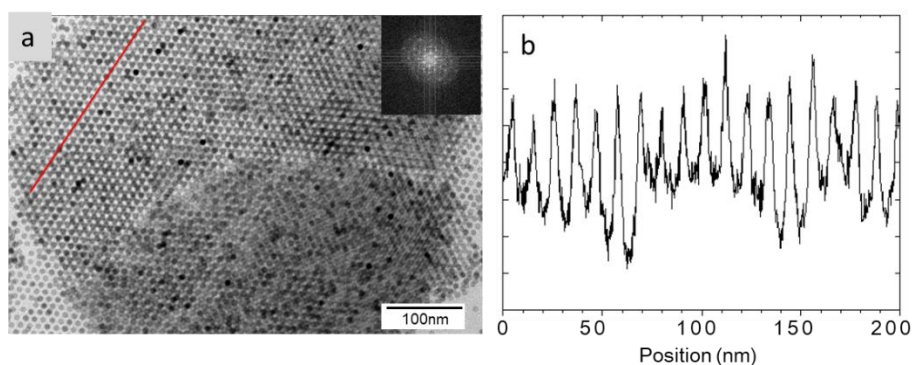


Figure 4. 9. (a) TEM image of thin layers of  $\gamma\text{-Fe}_2\text{O}_3$  NPs with their FFT image inset and (b) the line profiles from (a) indicate interparticle distances  $D_{C-C} \approx 10$  nm, respectively.



### 3.5.2. Magnetic characterization of 2D organization of BNSLs ( $\gamma$ -Fe<sub>2</sub>O<sub>3</sub> NPs-Au NPs) and $\gamma$ -Fe<sub>2</sub>O<sub>3</sub> NPs

In order to study the effect of the presence of Au NPs in the superlattices of  $\gamma$ -Fe<sub>2</sub>O<sub>3</sub> on the magnetic properties, a comparative study at low field and high field have been performed involving (1) the thin superlattices composed of  $\gamma$ -Fe<sub>2</sub>O<sub>3</sub> NCs (Figure 4.9) and (2) the thin NaZn<sub>13</sub> binary superlattices composed of  $\gamma$ -Fe<sub>2</sub>O<sub>3</sub> and Au NCs (Figure 4.8). The measurements have been performed on the samples deposited on a TEM grid by using a SQUID magnetometer.

It must be noted that maghemite NPs with a mean diameter of 7.9 nm, are small enough to have a single magnetic domain. In that case, in an assembly of NPs, each nanoparticle acts like a giant or “superspin”. In sufficiently concentrated systems as this is the case in superlattices, these superspins can interact via long-range dipolar interactions<sup>33</sup>. The magnetic measurements we performed, allow to learn about these dipolar interactions, which are, in light of the structural characterizations, expected to change between the two samples.

Figure 4.10 shows the field-cooled (FC) and zero field cooled (ZFC) magnetization versus temperature curves for pure  $\gamma$ -Fe<sub>2</sub>O<sub>3</sub> superlattices and NaZn<sub>13</sub> binary  $\gamma$ -Fe<sub>2</sub>O<sub>3</sub>-Au superlattices. In a general trend, as the sample has been cooled in zero field, there is no net alignment of the superspins (here at 3 K) and hence the magnetization is close to zero. A small magnetic field (here of 20 Oe) is applied. As the temperature is increased, the superspins become progressively ‘unblocked’, aligning towards the field direction and the magnetization increases until it reaches a maximum which we define here as the blocking temperature,  $T_B$ . Above  $T_B$  the behavior is paramagnetic i.e. the thermal energy increases to such an extent that the increased dynamic rotation of the superspins prevents alignment in the field direction and the magnetization decreases with increasing temperature. In the FC curve, the magnetization is high from 5 K to  $T_B$ . Above  $T_B$  the behavior is paramagnetic, and the magnetization decreases with increasing temperature in line with the ZFC curve.

The pure  $\gamma$ -Fe<sub>2</sub>O<sub>3</sub> superlattices are characterized by a  $T_B$  of around 84 K. This value is in good agreement with the values reported in the literature for the same size of NPs<sup>24</sup>. The blocking temperature accounts of the energy barriers of the magnetic nanoparticles ( $E_b$ ), which depend on both the anisotropy energy (size, nanocrystallinity and shape)  $E_a = k_a V$  and the dipole interaction energy,  $E_{dd}$ <sup>5</sup>. The narrowness of the ZFC peak indicates here, a narrow distribution of energy barriers, that is to say a low size distribution of the maghemite NCs in the sample. The low slope of the FC curve, at low temperature, is indicative of rather strong

dipolar interactions between the nanoparticles.

For the binary superlattices, we observe a significant decrease in the  $T_B$  from 84 K to 76 K. As the two sample are made with the same batch of maghemite NCs, this change in  $T_B$  cannot result from a change in the anisotropy energy, that is in the NP size. The  $T_B$  decrease is explained by the decrease in the dipolar interactions between the maghemite NPs. This behavior is in good agreement with the decrease in the distance (from 13.8 nm to 10 nm) between the magnetic NPs in the binary superlattices compared to the pure maghemite superlattices<sup>24,34</sup>. Besides, we see that there is a slight increase in the field cooled magnetization with temperature below  $T_B$  for the binary sample compared to the pure maghemite superlattices. This feature is explained by the decrease in the NP dipolar interaction in the assembly, and well agree with the  $T_B$  decrease.

Figure 4.10 shows the magnetization as a function of field for pure  $\gamma$ -Fe<sub>2</sub>O<sub>3</sub> superlattices and NaZn<sub>13</sub> binary  $\gamma$ -Fe<sub>2</sub>O<sub>3</sub>-Au superlattices. The measurements have been performed at  $\underline{\leq}$  3 K. The magnetic signatures (at high field) of both samples appear similar. Independently of the presence of Au NPs in the thin superlattices, the coercive field is found equal to around 360 Oe. The change in the dipolar interaction, expected to impact  $H_c$ , and observed in the ZFC curves could be compensated by a coupling between the Au and  $\gamma$ -Fe<sub>2</sub>O<sub>3</sub> NPs.

In conclusion, both the structural and magnetic studies clearly evidence an effect of the insertion of Au NPs in the superlattices of  $\gamma$ -Fe<sub>2</sub>O<sub>3</sub>. As a result of an increase in the interparticle distance in the binary sample compared to the pure  $\gamma$ -Fe<sub>2</sub>O<sub>3</sub> sample, we observe a decrease in the dipolar magnetic interactions between magnetic NPs. So, 4.6 nm Au NPs can be used as spacer between 7.9nm  $\gamma$ -Fe<sub>2</sub>O<sub>3</sub> NPs in binary assemblies to tune the dipole interactions between  $\gamma$ -Fe<sub>2</sub>O<sub>3</sub> NPs. However, a coupling between Au and  $\gamma$ -Fe<sub>2</sub>O<sub>3</sub> cannot be excluded.

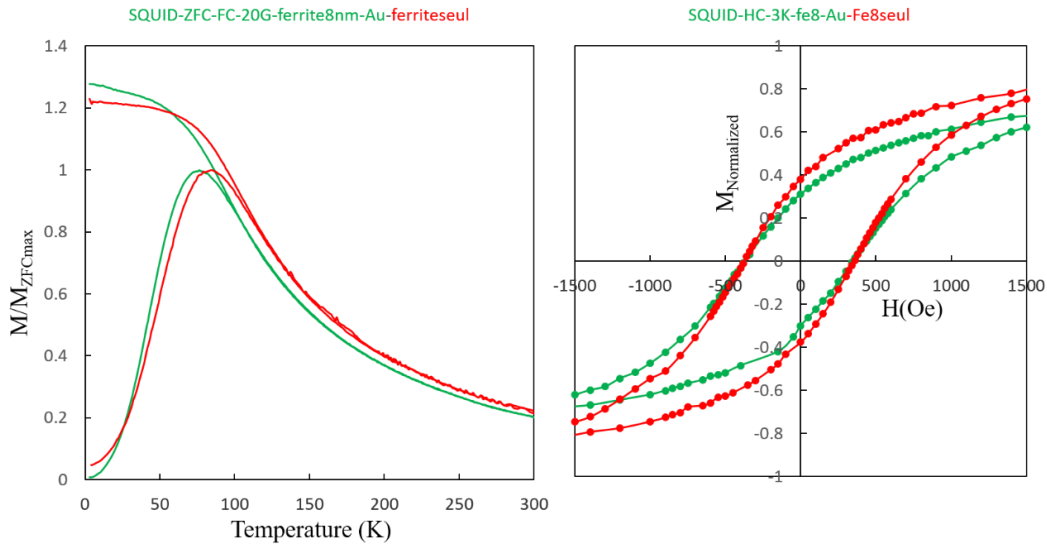


Figure 4. 10. SQUID measurements in thin layers of NaZn<sub>13</sub> binary structure composed of 7.9 nm  $\gamma$ -Fe<sub>2</sub>O<sub>3</sub> and 4.6 nm Au NPs (green curve) compared with 7.9 nm  $\gamma$ -Fe<sub>2</sub>O<sub>3</sub> NPs 2D organization (red, reference). (a) zero field cooled/field cooled (ZFC/FC) measurements of magnetization vs. temperature, (b) the in-plane field dependence (measured at 3K).

Table 4. 6. Comparison of blocking temperature and coercivity values of SQUID measurements. All values are deduced from Figure 4. 10.

	SQUID	
	Blocking temperature, T <sub>b</sub> (K)	Coercivity, H <sub>c</sub> (Oe)
$\gamma$ -Fe <sub>2</sub> O <sub>3</sub> alone	84	360
$\gamma$ -Fe <sub>2</sub> O <sub>3</sub> -Au BNSLs	76	360

#### 4. Fabrication of binary superlattices by mixing Pd and Au NPs

We studied also the formation of BNSLs by mixing Pd and Au NPs well known for their catalytic and plasmonic properties<sup>13,35</sup>. The self-assembly of two types of NPs show great interest design of new functional materials. Some BNSLs can be an ideal model for investigating catalytic process, providing a unique approach to link information gained from the superlattices<sup>35</sup>. We exploited the ability to control the relative size ratio, deposition method to vary the BNSL type structure.

We considered the binary mixture in which 7.5 nm Pd NPs coated by oleylamine ( $C_{18}$ ) were used as large NPs ( $NP_1$ ), whereas small NPs ( $NP_2$ ) were replaced by Au NPs with diameter between 4 and 5 nm and coated with dodecanethiols ( $C_{12}$ ). 7.5 nm Pd NPs were synthesized through direct reduction in oleylamine of  $PdCl_2(PPh_3)_2$  metallic salt. Briefly 36 mg  $PdCl_2(PPh_3)_2$  are dissolved in 10 ml of oleylamine (OLA,  $C_{18}$ ). Then, the solution is heated until 240°C with ramping 450°C/h. The reaction has been performed during 1 hour at 240°C, then it is cooled down to room temperature. The washing step is like this one of 10 nm Au NPs (see Chapter II). The final Pd NP size is 7.5 nm in diameter with 7% polydispersity.

For BNSL formation, we used three different sizes of Au NPs ( $NP_2$ ). All Au NPs are synthesized through the reduction of  $ClAuPPh_3$  salt in presence of 1-dodecanethiols ( $C_{12}$ ) by TBAB complex as described in Chapter II. The control of size from 4nm to 4.6 nm and 5nm was done through the amount of added ligand during the synthesis (from 600, 500 and 400  $\mu$ l). The effective size ratio ( $\gamma_{eff}$ ) of the three BNSL combinations between Pd and Au NPs was increased ( $0.6 < 0.67 < 0.73$ ) with the increase of the Au NP diameter ( $4 \text{ nm} < 4.6 \text{ nm} < 5 \text{ nm}$ ). The BNSL structure was observed to change with the effective size ratio and deposition method. The concentration ratio  $[Pd]:[Au]$  is fixed to 1:4.

Table 4. 7. Nanoparticles used as components for BNSLs composed of catalytic NPs (Pd NPs) and plasmonic NPs (Au NPs), as a result, three combinations of BNSL with different effective size ratios.

$NP_{big}$ : Pd NPs	+	NP type	$NP_{small}$ : Au NPs		
1			2	3	4
oleylamine ( $C_{18}$ )		Ligand	1-dodecanethiol ( $C_{12}$ )		
7.5 nm		NPs diameter	4.0 nm	4.6 nm	5.0 nm
9.6 nm		Effective diameter ( $D_{C-C}$ )	5.8 nm	6.3 nm	7.0 nm

	BNSLs	$NP_1+NP_2$	$NP_1+NP_3$	$NP_1+NP_4$
Effective size ratio ( $\gamma_{eff}$ )		0.60	0.67	0.73

By using immersion method for the BNSL fabrication ( $T_d=50^\circ\text{C}$ ), the BNSL structure was changed with the effective size ratio from CuAu for  $\gamma_{\text{eff}}=0.6$  to a mixture of AlB<sub>2</sub> and NaZn<sub>13</sub> type structures for  $\gamma_{\text{eff}}=0.67$ . NaZn<sub>13</sub> is the expected product for  $0.54 \leq \gamma_{\text{eff}} \leq 0.67$ <sup>36</sup> whereas the CuAu and AlB<sub>2</sub> are not predicted to appear at this size ratio. Finally, MgZn<sub>2</sub> structure, which is a highly stable phase in the hard-sphere model, was not produced at large  $\gamma_{\text{eff}}$  values (0.73), and only the formation of separated monometallic superlattices was observed (more than 80 % of area) instead with some amorphous states (10-20%). These data clearly show that in this case, the binary structures produced with two different coating agents (dodecanethiols and oleylamine) can differ from the hard-sphere model as observed previously by Wei et al in the case of binary nanocrystal superlattices made of Ag–Ag binary mixtures with two distinct nanocrystal sizes<sup>25</sup>.

By using liquid-liquid interface method for the BNSL fabrication, the BNSL structure was changed with the effective size ratio from AlB<sub>2</sub> ( $\gamma_{\text{eff}}=0.6$ ), NaZn<sub>13</sub> structure ( $\gamma_{\text{eff}}=0.67$ ), and finally pure separated monometallic superlattices formation ( $\gamma_{\text{eff}}=0.73$ ). The unstable CuAu structure is thus no more observed. The binary structure appears also to depend on the deposition method. Detailed fixed deposition conditions are same as listed in table 4.2.

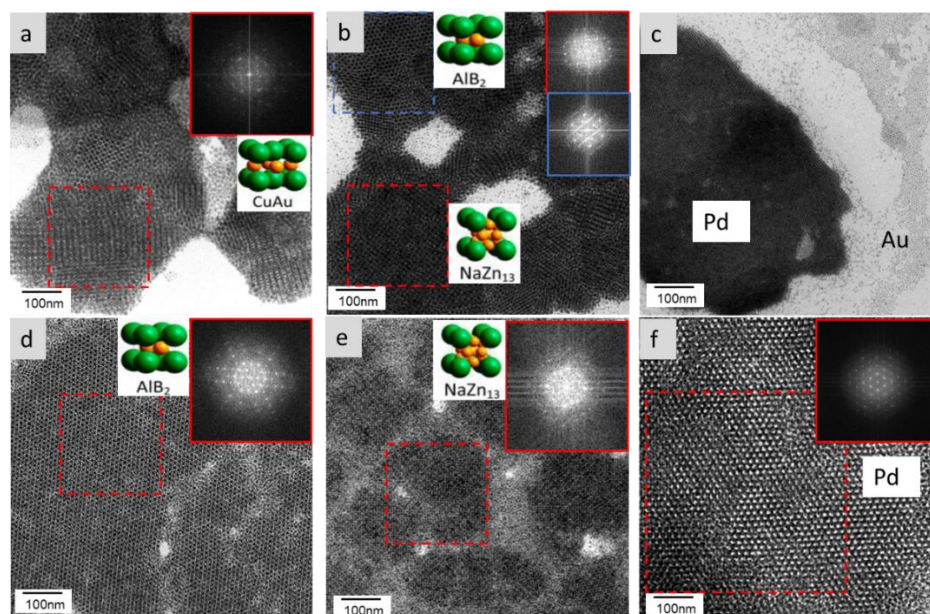


Figure 4. 11. TEM images of BNSL formed with Pd NPs and Au NPs at a fixed concentration ratio  $[\text{Pd}]/[\text{Au}] = 1/4$  with different effective size ratio ( $\gamma_{\text{eff}}$ ) 0.6, 0.67, and 0.75 (in column) and different deposition methods: immersion ( $T_d=50^\circ\text{C}$ ), and liquid-liquid interface mode (in row). Insets indicate selected area FFT analysis. Representation of unit cell of each BNSL structure corresponding to TEM image is presented as an inset (left side from FFT diagram).

## 5. Macroscopic 3D organization of binary superlattices formed by mixing $\gamma$ -Fe<sub>2</sub>O<sub>3</sub> and Au nanoparticles

We prepared thick binary assemblies on silicon substrate (approximately hundred layers of binary  $\gamma$ -Fe<sub>2</sub>O<sub>3</sub> /Au). The effective size ratio is fixed to  $\gamma_{\text{eff}} = 0.64$  and all other deposition conditions listed in Table 4.8 are fixed to get NaZn<sub>13</sub> type structure according to our previous results. The SEM images performed after solvent evaporation, show predominantly individual faceted SLs with cubic shape with 2-7  $\mu\text{m}$  long edges (Figure 4.12 a-f) characteristic of homogenous growth in toluene. The SLs was also analyzed by energy dispersive X-ray spectroscopy (EDX) in the SEM to obtain quantitative information on the chemical composition of the deposition. EDX measurement confirmed that the SLs are composed by gold and iron with an atomic ratio of Fe and Au around 20% and 80% in agreement with the initial concentration ratio ( $[\gamma\text{-Fe}_2\text{O}_3]:[\text{Au}] = 1:4$ ). The composition in Au and Fe remains similar in all 3D cubic binary assemblies. Few less faceted thin films composed of pure Au NPs are also observed (see an arrow on the SEM image Figure 4.12 d). Around 80% superlattices were found out to be BNSLs, and around 20% of Au SLs (Figures 4.12 f, g, h).

The high resolution HRSEM image and corresponding Fourier transform of a typical cubic 3D BNSL demonstrates that the nanoparticles are well ordered in close packed arrangements (Figure 4.13) in agreement with NaZ<sub>13</sub> type binary structure from the preferential crystal orientation with the (100) plane parallel to the substrate.

Table 4. 8. Growth conditions of NaZn<sub>13</sub> structure BNSLs assemblies.

Fixed parameter	Condition
Effective size ratio ( $\gamma_{\text{eff}}$ )	0.64
Concentration ratio ( $[\gamma\text{-Fe}_2\text{O}_3]:[\text{Au}]$ )	1:4 (0.1 wt.% : 0.4 wt. %)
Solvent	Toluene
Volume of NPs	200 ( $\mu\text{l}$ )
deposition method	Immersion method
Deposition temperature ( $T_d$ )	50 °C

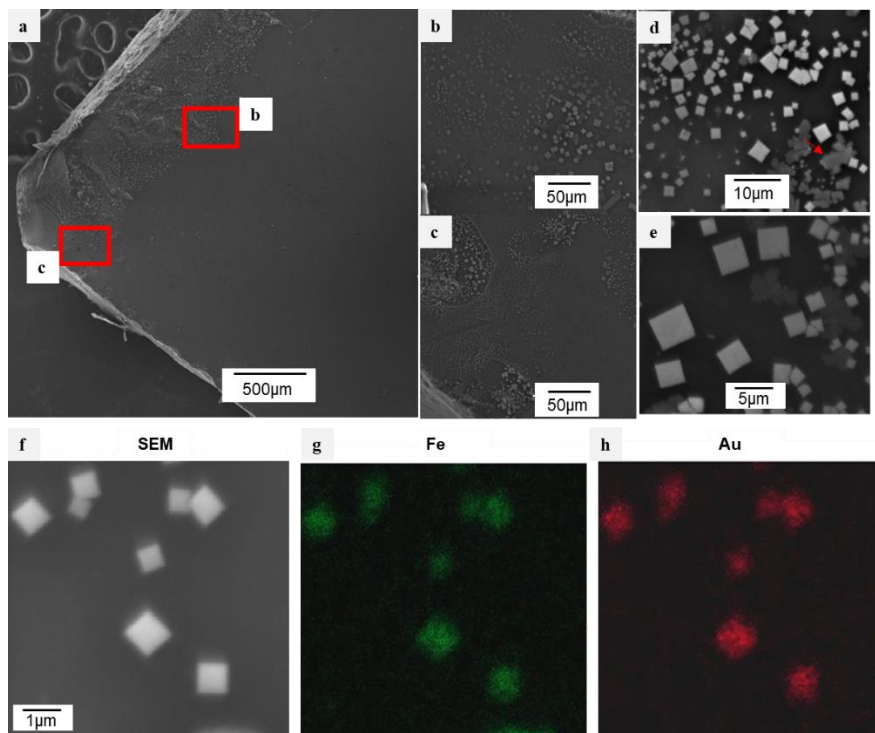


Figure 4. 12. (a-d) SEM images at different magnifications of  $\text{NaZn}_{13}$  BNSLs formed with 7.9 nm  $\gamma\text{-Fe}_2\text{O}_3$  NPs and 4.6 nm Au NPs for effective size and concentration ratios fixed to 0.64 and 1:4, respectively and (e, f) corresponding cartography of Fe in green, and Au in red using EDX analysis.

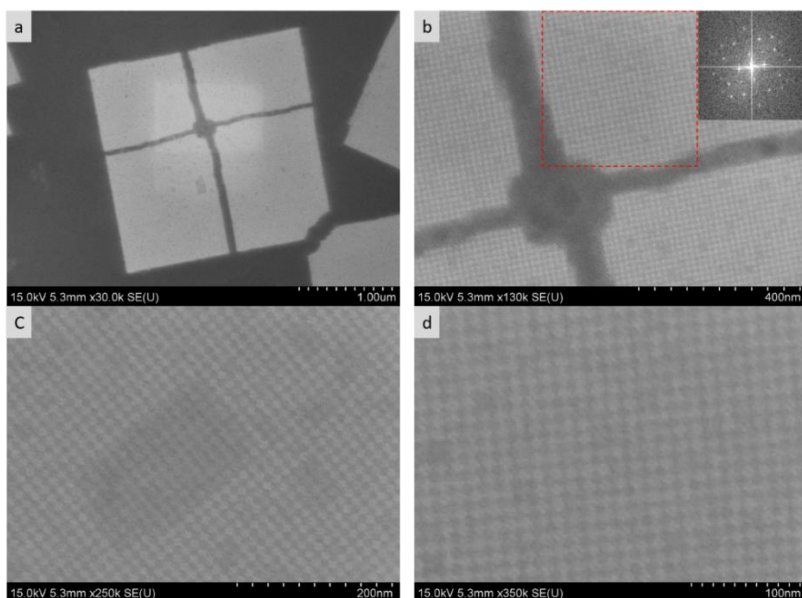


Figure 4. 13. (a-d) HR-SEM images at different magnification of  $\text{NaZn}_{13}$  BNSL formed with 7.9 nm  $\gamma\text{-Fe}_2\text{O}_3$  NPs and 4.6 nm Au NPs for effective size and concentration ratios fixed to  $[\gamma\text{-Fe}_2\text{O}_3]:[\text{Au}]=1:4$ , respectively. Magnification is indicated in each image. (b) FFT image shown as an inset which are obtained from selected area (marked as a dotted red square).

In comparison, pure  $\gamma$ -Fe<sub>2</sub>O<sub>3</sub> NPs 3D assemblies prepared in the same conditions (see table 4.8) were formed as a thin film (Figure 4. 14), characteristic of a heterogeneous layer-by-layer growth. The Au NPs inserted in the maghemite cubic arrangement appear to strengthen the film cohesion and favor the homogeneous growth of binary superlattices in colloidal crystals of cubic shape<sup>37</sup>.

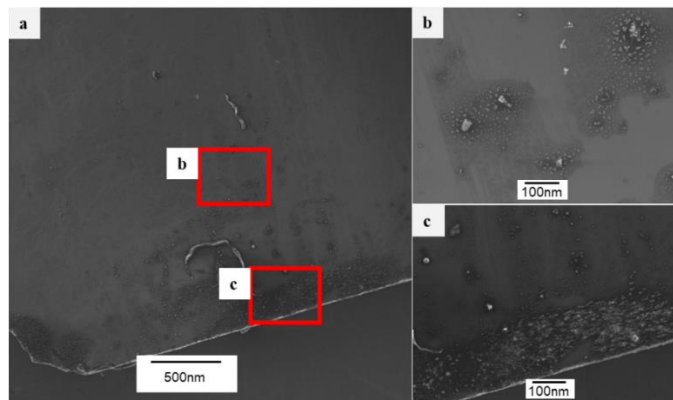


Figure 4. 14. SEM images at low magnification of pure 7.9 nm  $\gamma$ -Fe<sub>2</sub>O<sub>3</sub> NPs 3D deposition on silicon substrate (mostly existed as film state).

The crystalline structure of BNSL obtained by mixing  $\gamma$ -Fe<sub>2</sub>O<sub>3</sub> (7.9 nm) and Au (4.6nm) NPs was further investigated by grazing incidence small angle X-ray scattering (GISAXS). Binary and pure  $\gamma$ -Fe<sub>2</sub>O<sub>3</sub> NPs superlattices lead to similar GIXAS patterns as shown in figures 4.15a and 4.16a. Both patterns reveal rings and d periodicity pointing to an *fcc* cubic structure (Table 4.9).

Table 4. 9. Summary of the binary and pure maghemite superlattices properties deduced from GISAXS pattern

Rings	$\gamma$ -Fe <sub>2</sub> O <sub>3</sub> and Au NP BNSLs		pure $\gamma$ -Fe <sub>2</sub> O <sub>3</sub> SLs	
	q <sub>z</sub>	periodicity d(nm)	q <sub>z</sub>	periodicity d (nm)
1	0.73	8.60	0.77	8.16
2	0.83	7.53	1.47	4.27
3	1.40	4.48		



For pure maghemite superlattices, the rings show marked equatorial reinforcement of (111) and (222) diffraction lines (numbered 1 and 2 respectively on figure 4.16a and b), this suggest that the films have (111) planes preferentially oriented parallel to the substrate. We also pointed out the presence of elongated spots that is due to the presence of stacking faults. These observations agree with a layer by layer growth.

For BNSLs (figure 4.15a and b), the GISAXS pattern show continuous rings with discontinuous reinforcements. The rings are characteristics of small randomly oriented BNSLs and the reinforcements are attributed to large well-developed BNSLs sitting on their larger flat facets. This agree with the SEM images shown in figure 4.12, and 4.13. These observations can be explained by a homogenous growth of binary SLs<sup>31,37</sup>. To our knowledge this is the first experimental evidence that the incorporation of Au NPs in *fcc*  $\gamma$ -Fe<sub>2</sub>O<sub>3</sub> NP Superlattices tune the SLs growth mechanism from a heterogenous to a homogenous one.

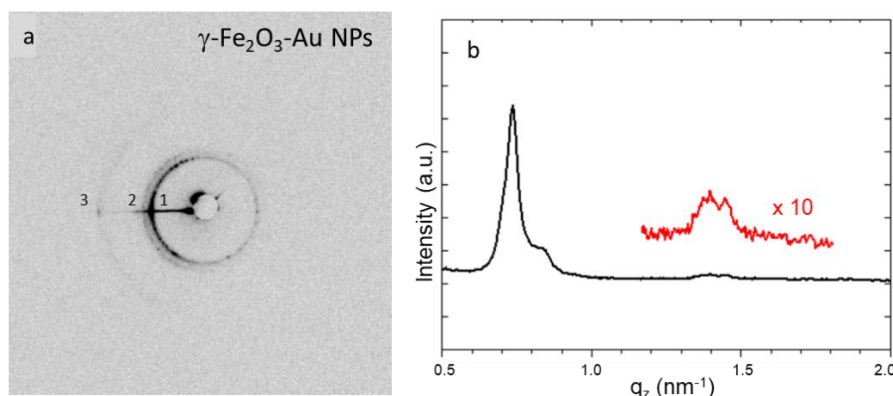


Figure 4. 15. GISAXS patterns of (a) NaZn<sub>13</sub> structure BNSLs of 7.9 nm  $\gamma$ -Fe<sub>2</sub>O<sub>3</sub> NPs and 4.6 nm Au NPs, respectively. (b) normalized intensity vs.  $q_z$  from (a).

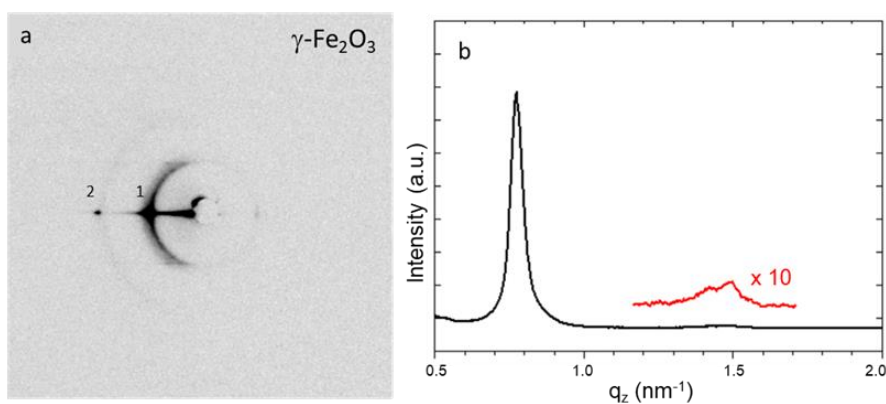


Figure 4. 16. GISAXS patterns of (a) 7.9 nm  $\gamma$ -Fe<sub>2</sub>O<sub>3</sub> NPs 3D assemblies and (b) normalized intensity vs.  $q_z$  from (a).

From the sample-detector distance and the spot coordinates, we determine the Bragg angle  $2\theta_B$  and therefore the modulus of the diffracted vector  $q_z$  from the Bragg relation. We also can estimate the core-to-core interparticle distance  $D_{c-c}$  between maghemite NPs calculated from the positions of the Bragg reflections, i.e., from the interplanar stacking periodicities  $d$  along the normal to the surface  $q_z$  (in case of *fcc* arrangement  $D_{c-c} = d \times \sqrt{(3/2)}$ )<sup>24,38</sup>. The line profiles along  $q_z$  (figure 4.16b) give a stacking periodicity of  $d \sim 8.16$  nm ( $D_{c-c} \sim 10$  nm) for pure maghemite superlattices, similar with previous results deduced from TEM images on thin pure maghemite SLs. For binary superlattices, the line profiles along  $q_z$  (figures 4.15b) give a stacking periodicity of  $d \sim 8.60$  nm ( $D_{c-c} \sim 10.54$  nm). The  $D_{c-c}$  values obtained by SAXS deviate up to a few nm from those obtained by TEM analysis. This observation can be explained on one hand by the limits of the TEM analysis accuracy<sup>39</sup> |and by a difference of SLs growth mode. To obtain thick binary SLs, a higher volume of colloidal solution is used inducing a higher evaporation time, which may cause the growth mode of BNSLs to change from heterogeneous to homogeneous. The presence of less defects in faceted binary lattices due to the homogenous growth mode could explain a shorter average interparticle distance  $D_{c-c}$  compared to this one determined in binary thin films characteristic of a heterogeneous layer by layer growth.

Consequently, complementary SAXS measurements on Thin binary SLs should be considered in the future.

## 6. Conclusion

In this Chapter, it is shown that binary superlattices obtained by mixing  $\gamma$ -Fe<sub>2</sub>O<sub>3</sub> and Au NPs or Pd and Au NPs, allow to integrate different types of NPs and to get synergistic effect between the binary constituents for magnetic, plasmonic or catalytic applications. At first, different parameters were optimized the form binary superlattices made of  $\gamma$ -Fe<sub>2</sub>O<sub>3</sub> NPs (bigger size) and Au NPs (smaller size) with controlled crystalline structure. One of the main factors to control BNSL structure was the effective size ratio. By increasing the effective size ratio, the BNSL type-structure changes from NaCl to AIB<sub>2</sub> and NaZn<sub>13</sub> in accordance with the phase diagram for binary hard spheres mixtures. The effects of concentration ratio ([Fe<sub>2</sub>O<sub>3</sub>]:[Au]) and deposition conditions such as deposition temperature, deposition method, and nature of the solvent were also investigated. It is shown that they can influence the final structure of the binary superlattice, alone or combined with each other. For binary superlattices obtained by

mixing Pd and Au NPs, the final type structures appear to differ from the hard-sphere model depending on the deposition conditions. Thick binary superlattices were prepared. Binary faceted superlattices characteristic of homogeneous growth were obtained, whereas same deposition condition of only  $\gamma$ -Fe<sub>2</sub>O<sub>3</sub> NP lead to superlattices in the form of films. To our knowledge, we get evidence for the first time that the incorporation of Au NPs in *fcc*  $\gamma$ -Fe<sub>2</sub>O<sub>3</sub> NP Superlattices tune the SLs growth mechanism from a heterogenous to a homogenous one.

Finally, the difference in the magnetic properties has been investigated in thin Au NPs /  $\gamma$ -Fe<sub>2</sub>O<sub>3</sub> NPs binary and pure  $\gamma$ -Fe<sub>2</sub>O<sub>3</sub> NPs SLs using SQUID experiments. We clearly evidenced an effect of the insertion of Au NPs in the superlattices of  $\gamma$ -Fe<sub>2</sub>O<sub>3</sub>. As a result of an increase in the interparticle distance in the binary sample compared to the pure  $\gamma$ -Fe<sub>2</sub>O<sub>3</sub> sample, we observe a decrease in the dipolar magnetic interactions between magnetic NPs.

## 7. Reference

- (1) Meziane, L.; Salzemann, C.; Aubert, C.; Gérard, H.; Petit, C.; Petit, M. Hcp Cobalt Nanocrystals with High Magnetic Anisotropy Prepared by Easy One-Pot Synthesis. *Nanoscale* **2016**, *8* (44), 18640–18645. <https://doi.org/10.1039/C6NR05792F>.
- (2) Courty, A.; Richardi, J.; Albouy, P.-A.; Pileni, M.-P. How To Control the Crystalline Structure of Supracrystals of 5-Nm Silver Nanocrystals. *Chem. Mater.* **2011**, *23* (18), 4186–4192. <https://doi.org/10.1021/cm201313r>.
- (3) Wan, Y. F.; Goubet, N.; Albouy, P. A.; Pileni, M. P. Hierarchy in Au Nanocrystal Ordering in Supracrystals: A Potential Approach to Detect New Physical Properties. *Langmuir* **2013**, *29* (24), 7456–7463. <https://doi.org/10.1021/la3045187>.
- (4) Wan, Y.; Goubet, N.; Albouy, P.-A.; Schaeffer, N.; Pileni, M.-P. Hierarchy in Au Nanocrystal Ordering in a Supracrystal: II. Control of Interparticle Distances. *Langmuir* **2013**, *29* (44), 13576–13581. <https://doi.org/10.1021/la403583q>.
- (5) Parker, D.; Lisiecki, I.; Salzemann, C.; Pileni, M.-P. Emergence of New Collective Properties of Cobalt Nanocrystals Ordered in Fcc Supracrystals: II, Magnetic Investigation. *J. Phys. Chem. C* **2007**, *111* (34), 12632–12638. <https://doi.org/10.1021/jp071821u>.
- (6) Murray, M. J.; Sanders, J. V. Close-Packed Structures of Spheres of Two Different Sizes II. The Packing Densities of Likely Arrangements. *Philos. Mag. A* **1980**, *42* (6), 721–740. <https://doi.org/10.1080/01418618008239380>.
- (7) Boles, M. A.; Talapin, D. V. Many-Body Effects in Nanocrystal Superlattices: Departure from Sphere Packing Explains Stability of Binary Phases. *J. Am. Chem. Soc.* **2015**, *137* (13), 4494–4502. <https://doi.org/10.1021/jacs.5b00839>.
- (8) Evers, W. H.; Nijs, B. D.; Fillion, L.; Castillo, S.; Dijkstra, M.; Vanmaekelbergh, D. Entropy-Driven Formation of Binary Semiconductor-Nanocrystal Superlattices. *Nano Lett.* **2010**, *10* (10), 4235–4241. <https://doi.org/10.1021/nl102705p>.
- (9) Chen, J.; Dong, A.; Cai, J.; Ye, X.; Kang, Y.; Kikkawa, J. M.; Murray, C. B. Collective Dipolar Interactions in Self-Assembled Magnetic Binary Nanocrystal Superlattice Membranes. *Nano Lett.* **2010**, *10* (12), 5103–5108. <https://doi.org/10.1021/nl103568q>.
- (10) Wang, K.; Li, F.; Jin, S.-M.; Wang, K.; Tian, D.; Hussain, M.; Xu, J.; Zhang, L.; Liao, Y.; Lee, E.; Yi, G.-R.; Xie, X.; Zhu, J. Chain-Length Effect on Binary Superlattices of Polymer-Tethered Nanoparticles. *Mater. Chem. Front.* **2020**, *4*. <https://doi.org/10.1039/D0QM00194E>.
- (11) Kiely, C. J.; Fink, J.; Brust, M.; Bethell, D.; Schiffrin, D. J. Spontaneous Ordering of Bimodal Ensembles of Nanoscopic Gold Clusters. *Nature* **1998**, *396* (6710), 444–446. <https://doi.org/10.1038/24808>.
- (12) Cheon, J.; Park, J.-I.; Choi, J.; Jun, Y.; Kim, S.; Kim, M. G.; Kim, Y.-M.; Kim, Y. J. Magnetic Superlattices and Their Nanoscale Phase Transition Effects. *Proc. Natl. Acad. Sci.* **2006**, *103* (9), 3023–3027. <https://doi.org/10.1073/pnas.0508877103>.
- (13) Ye, X.; Chen, J.; Diroll, B. T.; Murray, C. B. Tunable Plasmonic Coupling in Self-Assembled Binary Nanocrystal Superlattices Studied by Correlated Optical Microspectrophotometry and Electron Microscopy. *Nano Lett.* **2013**, *13* (3), 1291–1297. <https://doi.org/10.1021/nl400052w>.
- (14) Shevchenko, E. V.; Ringler, M.; Schwemer, A.; Talapin, D. V.; Klar, T. A.; Rogach, A. L.; Feldmann, J.; Alivisatos, A. P. Self-Assembled Binary Superlattices of CdSe and Au Nanocrystals and Their Fluorescence Properties. *J. Am. Chem. Soc.* **2008**, *130* (11), 3274–3275. <https://doi.org/10.1021/ja710619s>.

- (15) Ngo, A.-T.; Richardi, J.; Pileni, M. P. Crack Patterns in Superlattices Made of Maghemite Nanocrystals. *Phys. Chem. Chem. Phys.* **2013**, *15* (26), 10666–10672. <https://doi.org/10.1039/C3CP50276G>.
- (16) Park, J.; An, K.; Hwang, Y.; Park, J.-G.; Noh, H.-J.; Kim, J.-Y.; Park, J.-H.; Hwang, N.-M.; Hyeon, T. Ultra-Large-Scale Syntheses of Monodisperse Nanocrystals. *Nat. Mater.* **2004**, *3* (12), 891–895. <https://doi.org/10.1038/nmat1251>.
- (17) Travasset, A. Binary Nanoparticle Superlattices of Soft-Particle Systems. *Proc. Natl. Acad. Sci.* **2015**, *112* (31), 9563–9567. <https://doi.org/10.1073/pnas.1504677112>.
- (18) Waltmann, C.; Horst, N.; Travasset, A. Potential of Mean Force for Two Nanocrystals: Core Geometry and Size, Hydrocarbon Unsaturation, and Universality with Respect to the Force Field. *J. Chem. Phys.* **2018**, *149* (3), 034109. <https://doi.org/10.1063/1.5039495>.
- (19) Pileni, M. P. Nanocrystal Self-Assemblies: Fabrication and Collective Properties. *J. Phys. Chem. B* **2001**, *105* (17), 3358–3371. <https://doi.org/10.1021/jp0039520>.
- (20) Yang, Z.; Altantzis, T.; Bals, S.; Tendeloo, G. V.; Pileni, M.-P. Do Binary Supracrystals Enhance the Crystal Stability? *J. Phys. Chem. C* **2018**, *122* (25), 13515–13521. <https://doi.org/10.1021/acs.jpcc.7b12373>.
- (21) Dong, A.; Chen, J.; Vora, P. M.; Kikkawa, J. M.; Murray, C. B. Binary Nanocrystal Superlattice Membranes Self-Assembled at the Liquid–Air Interface. *Nature* **2010**, *466* (7305), 474–477. <https://doi.org/10.1038/nature09188>.
- (22) Wu, Y.; Li, S.; Gogotsi, N.; Zhao, T.; Fleury, B.; Kagan, C. R.; Murray, C. B.; Baxter, J. B. Directional Carrier Transfer in Strongly Coupled Binary Nanocrystal Superlattice Films Formed by Assembly and in Situ Ligand Exchange at a Liquid–Air Interface. *J. Phys. Chem. C* **2017**, *121* (8), 4146–4157. <https://doi.org/10.1021/acs.jpcc.6b12327>.
- (23) Eldridge, M. D.; Madden, P. A.; Frenkel, D. Entropy-Driven Formation of a Superlattice in a Hard-Sphere Binary Mixture. *Nature* **1993**, *365* (6441), 35–37. <https://doi.org/10.1038/365035a0>.
- (24) Breitwieser Romain; Auvray Thomas; Volatron Florence; Salzemann Caroline; Ngo Anh-Tu; Albouy Pierre-Antoine; Proust Anna; Petit Christophe. Binary Superlattices from {Mo132} Polyoxometalates and Maghemite Nanocrystals: Long-Range Ordering and Fine-Tuning of Dipole Interactions. *Small* **2016**, *12* (2), 220–228. <https://doi.org/10.1002/sml.201502127>.
- (25) Wei, J.; Schaeffer, N.; Pileni, M.-P. Ligand Exchange Governs the Crystal Structures in Binary Nanocrystal Superlattices. *J. Am. Chem. Soc.* **2015**, *137* (46), 14773–14784. <https://doi.org/10.1021/jacs.5b09959>.
- (26) Parthé, E. Space Filling of Crystal Structures A Contribution to the Graphical Presentation of Geometrical Relationships in Simple Crystal Structures. *Z. Für Krist. - Cryst. Mater.* **1961**, *115* (1–2), 52–79. <https://doi.org/10.1524/zkri.1961.115.1-2.52>.
- (27) Fillion, L.; Dijkstra, M. Prediction of Binary Hard-Sphere Crystal Structures. *Phys. Rev. E* **2009**, *79* (4), 046714. <https://doi.org/10.1103/PhysRevE.79.046714>.
- (28) Li, H.; Hu, D.; Zheng, Z.; Jiang, H.; Lu, J.; Geng, X.; Zhang, X.; Wan, Y.; Yang, P. Primary Growth of Binary Nanoparticle Superlattices with Distinct Systems Contingent on Synergy: Softness and Crystalline Anisotropy. *Appl. Nanosci.* **2020**, *10* (5), 1653–1666. <https://doi.org/10.1007/s13204-019-01244-6>.
- (29) Goubet, N.; Richardi, J.; Albouy, P.-A.; Pileni, M.-P. Which Forces Control Supracrystal Nucleation in Organic Media? *Adv. Funct. Mater.* **2011**, *21* (14), 2693–2704. <https://doi.org/10.1002/adfm.201100382>.
- (30) Bertouche, S.; Sahraoui, N.; Hellal, A. Determining Hansen Solubility Parameters by StefanisPanayiotou Method for Fatty Acids Extraction by Petrochemical and Green Solvents. *Int. J. Sci. Res. Eng. Technol. IJSET* **6**, 14–20.

- (31) Goubet, N.; Richardi, J.; Albouy, P. A.; Pileni, M. P. How to Predict the Growth Mechanism of Supracrystals from Gold Nanocrystals. *J. Phys. Chem. Lett.* **2011**, *2* (5), 417–422. <https://doi.org/10.1021/jz200004f>.
- (32) Smith, D. K.; Goodfellow, B.; Smilgies, D.-M.; Korgel, B. A. Self-Assembled Simple Hexagonal AB<sub>2</sub> Binary Nanocrystal Superlattices: SEM, GISAXS, and Defects. *J. Am. Chem. Soc.* **2009**, *131* (9), 3281–3290. <https://doi.org/10.1021/ja8085438>.
- (33) Parker, D.; Lisiecki, I.; Pileni, M. P. Do 8 Nm Co Nanocrystals in Long-Range-Ordered Face-Centered Cubic (Fcc) Supracrystals Show Superspin Glass Behavior? *J. Phys. Chem. Lett.* **2010**, *1* (7), 1139–1142. <https://doi.org/10.1021/jz1001874>.
- (34) Costanzo, S.; Ngo, A. T.; Russier, V.; Albouy, P. A.; Simon, G.; Colombari, P.; Salzemann, C.; Richardi, J.; Lisiecki, I. Enhanced Structural and Magnetic Properties of Fcc Colloidal Crystals of Cobalt Nanoparticles. *Nanoscale* **2020**. <https://doi.org/10.1039/D0NR05517D>.
- (35) Kang, Y.; Ye, X.; Chen, J.; Qi, L.; Diaz, R. E.; Doan-Nguyen, V.; Xing, G.; Kagan, C. R.; Li, J.; Gorte, R. J.; Stach, E. A.; Murray, C. B. Engineering Catalytic Contacts and Thermal Stability: Gold/Iron Oxide Binary Nanocrystal Superlattices for CO Oxidation. *J. Am. Chem. Soc.* **2013**, *135* (4), 1499–1505. <https://doi.org/10.1021/ja310427u>.
- (36) Yang, Z.; Wei, J.; Pileni, M.-P. Metal–Metal Binary Nanoparticle Superlattices: A Case Study of Mixing Co and Ag Nanoparticles. *Chem. Mater.* **2015**, *27* (6), 2152–2157. <https://doi.org/10.1021/acs.chemmater.5b00123>.
- (37) Ouhenia-Ouadahi, K.; Andrieux-Ledier, A.; Richardi, J.; Albouy, P.-A.; Beaunier, P.; Sutter, P.; Sutter, E.; Courty, A. Tuning the Growth Mode of 3D Silver Nanocrystal Superlattices by Triphenylphosphine. *Chem. Mater.* **2016**, *28* (12), 4380–4389. <https://doi.org/10.1021/acs.chemmater.6b01374>.
- (38) Henry, A.-I.; Courty, A.; Pileni, M.-P.; Albouy, P.-A.; Israelachvili, J. Tuning of Solid Phase in Supracrystals Made of Silver Nanocrystals. *Nano Lett.* **2008**, *8* (7), 2000–2005. <https://doi.org/10.1021/nl8010947>.
- (39) Schulz, F.; Pavelka, O.; Lehmkuhler, F.; Westermeier, F.; Okamura, Y.; Mueller, N. S.; Reich, S.; Lange, H. Structural Order in Plasmonic Superlattices. *Nat. Commun.* **2020**, *11* (1), 3821. <https://doi.org/10.1038/s41467-020-17632-4>.



## Conclusion and future work

These 3 years of study have allowed us to design multifunctional nanomaterials including bimetallic nanoparticles and binary nanoparticles superlattices. These nanomaterials offer the possibility of combining the properties of individual components and to evidence new ones arising from their interactions. Multifunctional nanomaterials combining two cooperative and complementary components such as plasmonic-plasmonic, plasmonic-magnetic, plasmonic-catalytic were studied. They attract much interest for their promising potentials in fields such as optical detection, catalysts, or magnetic sensors.

In chapter II, we developed a protocol to synthesize core-shell NPs. First, Au@Ag core-shell NPs with controlled final size (size distribution < 10%) and crystallinity of the core through a versatile approach using Au seeds with selected sizes and crystallinities and coated by different ligands (oleylamine or dodecanthiol). The final size of the core-shell NPs was shown to depend on three main parameters: i) the [Ag precursor]/[Au seed] concentration ratio, ii) the nature of the ligands coating the seeds, and iii) the reaction temperature. Furthermore, micrometer-scale well-faceted 3D superlattices of ordered Au@Ag nanoparticles were obtained and imaged by HR-SEM. The final narrow size distribution of core-shell NPs favored their organization.

We also showed that this two-step synthesis method is adaptable to different core and shell materials. Au core was exchanged by Ag, and Ag shell by Pt or Pd without strong modification of the synthesis process. Only reaction temperature and reaction time have to be optimized. The shell growth is always controlled by [metallic precursor]/[seed] concentration ratio. Still, more precise approaches are necessary to obtain fine control of size and shape of Ag core and thus to control the final morphology of Ag@M (M=Pd, Pt) NPs. Depending on the morphology of the seeds, and the growth conditions of the metallic overlayer (temperature, concentration of reagents...), bimetallic nanoparticles of different crystalline structures and morphologies should be obtained Dendritic morphologies are for example expected to be more efficient for catalysis.

In Chapter III, optical and catalytic properties of bimetallic core-shell NPs, which were synthesized through the two-steps protocol described in previous chapter, were investigated as a function of their size, chemical composition, and crystalline structure. First, the plasmonic properties of the Au<sub>5nm/10nm</sub>@Ag NPs were studied as a function of the Ag shell thickness and Au polycrystalline (PC) core size by UV-vis absorption spectroscopy and DDA calculations.



The evolution of SPR band through shell overgrowth was observed. Blue shift and enhancement of the SPR band were evidenced. The SPR band of bimetallic core-shell NPs obtained after the replacement of shell materials to catalytic materials (Pd or Pt) were investigated. Finally, replacement of core material by Ag with stronger plasmonic properties were also studied. Our results show thus that Au(Ag)@Pd and Au(Ag)@Pt bimetallic nanoparticles have their SPR in the visible range with a broad tunability, which is very difficult for pure Pd and Pt nanoparticles to achieve. Nevertheless, a damping effect of the SPR band is also observed, which is more significant with the shell thickness.

The vibrational properties of Au<sub>5nm/10nm</sub>(PC)@Ag NPs were demonstrated by low frequency Raman spectroscopy (LFRS). Bimetallic core-shell NPs have their specific vibrational frequency different from monometallic NPs. Core-shell NPs vibration modes are shifted to lower frequency by the increase of Ag shell thickness. Especially, one of the distinctive characteristics of single crystalline (SC) NPs is the split of quadrupolar vibrational mode into two peaks. It was verified that this split is maintained throughout Au(SC)@Ag growth.

The catalytic activity of bimetallic core-shell NPs was evaluated via a model reaction of reduction of 4-NP to 4-AP in presence of NaBH<sub>4</sub> in aqueous phase. First, catalytic activities of Au NPs are inversely proportional to diameter of NPs when we keep same atomic concentration due to the increase of their surface area. We show that synergistic interaction between Au and Ag in bimetallic core-shell Au@Ag NPs improves their catalytic activity compared to the monometallic Au NPs. It was also found that shell thickness in bimetallic Au@M (M=Pt or Pd) NPs influenced their catalytic properties. Pt or Pd shells with thicknesses less than 6 atomic layers can maximize the synergetic effect between core and shell. Even though palladium is known for its catalytic performances, the catalytic performance of Au@Pd NPs was shown to be lower than that of Au@Ag NPs. This could be explained by the capability of Pd to absorb hydrogen which is detrimental to the reduction of 4-NP by NaBH<sub>4</sub>. Finally, Pt shell shows the highest catalytic activities among the different shell materials.

The crystallinity effect on NP catalytic performance is more delicate to discuss. The crystallinity effect is likely governed by a complex combination between surface energy of the different crystalline facets and the presence of defects like corners and edges which are sub-coordinated atomic sites of high energies. We observed that the change in crystallinity of Au

NPs from SC to PC has a minor effect on their catalytic activities. SC NPs have indeed slightly higher rate constant than PC NPs.

From our results we could estimate the activation energy of the reduction process of 4-NP to produce 4-AP. The lower  $E_a$  values for Au@Ag NPs compared to Au NPs demonstrate synergistic interactions between Au and Ag in core-shell NPs, which lead to the improvement of their catalytic activity. So far, catalytic activities of core-shell NPs were only studied as a colloidal state in water. The investigation of catalytic activities as a solid state is necessary to get closer to the applications: heterogenous catalyst. The catalytic activities and electrochemical study of 3D-assemblies of core-shell NPs on solid substrate will be done as a future work to get closer to the application as a catalyst. Furthermore, these bimetallic Au/Ag@M NPs are of interest for the study of LSPR catalytic interactions.

In Chapter IV, the formation of binary nanoparticle superlattices (BNSLs) were investigated. We focused on structural study of binary assemblies made of Au and maghemite ( $\gamma$ -Fe<sub>2</sub>O<sub>3</sub>) NPs. The influence of different parameters like temperature, effective size ratio, and concentration ratio were studied to favor the growth of BNSLs with controlled crystalline phase (NaZn<sub>13</sub>, NaCl or AlB<sub>2</sub>). Furthermore, depending on deposition conditions faceted BNSLs were obtained, the Au NPs inserted in the maghemite cubic arrangement appear to strengthen the film cohesion and favor the homogeneous growth of binary superlattices in colloidal crystals with cubic shape. In a second part, we studied the formation of binary superlattices obtained by mixing Pd and Au NPs characterized by their well-known catalytic and plasmonic properties, respectively. Their final type structures appear to differ from the hard-sphere model depending on the deposition conditions.

Finally, the change of magnetic properties in BNSLs was observed compared to pure  $\gamma$ -Fe<sub>2</sub>O<sub>3</sub> ordered assemblies. It is due to an increase in the interparticle distance in the binary sample compared to the pure  $\gamma$ -Fe<sub>2</sub>O<sub>3</sub> sample. Resulting from this structural change, we observe a decrease in the dipolar magnetic interactions between magnetic NPs. Still, the deeper investigation of various physical properties is necessary in future. The blocking temperature of BNSL is expected to be controlled through the control of their structure. Also, the study of other physical properties such as change of optical, and catalytic properties will be investigated in future. BNSLs formed by mixing plasmonic active metals (Au) with traditionally catalytic metal (Pd) should promote an optical coupling between the plasmonic and catalytic metals to

enhance reactivity. For example, the measure performance of such BNSL on hydrogen dissociation for different illumination wavelength and polarization could be considered.

## Annex

### Annex 1. Electronic microscopy techniques

#### 1.1. Transmission Electron Microscopy (TEM)

The transmission electron microscope (TEM) is the conventional electronic optical microscope in transmission mode. The first TEM was built in 1932 by Ruska (Nobel Prize in 1986). The conventional lenses of optical microscope are replaced by electromagnetic lenses. A schematic illustration of a TEM column is shown in Figure A.1.

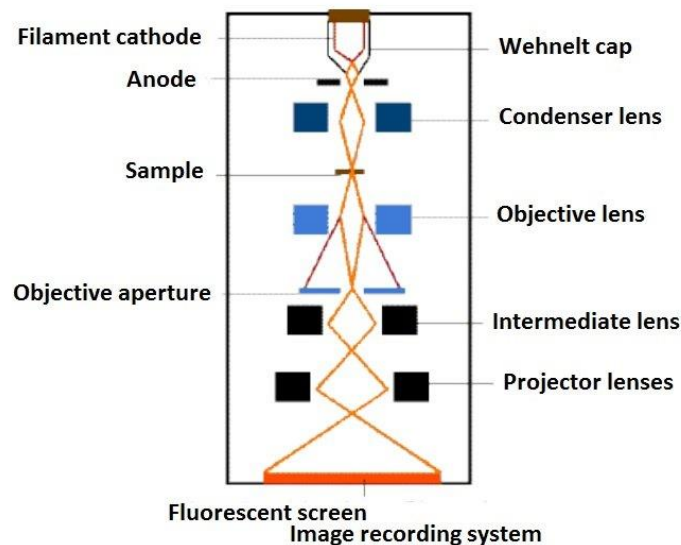


Figure A.1. Schematic illustration of TEM.

TEM image images can be obtained through different image modes (Figure A.2).

- Bright field image mode: Electrons are diffracted on the crystalline planes at  $2\theta$  angle to the direction of the incident electrons. The objective diaphragm passes transmitted electrons which have not interacted with the sample and blocks diffracted electrons. The diffraction planes appear as dark compared to background. The principle is equivalent for scattered electrons in a different from the incident direction.

- Dark field image mode: The incident electron beam cannot arrive in normal incidence but with an incidence such that the diffracted electrons stand out in the direction of the objective diaphragm. The diffraction planes can appear on dark background.

- Conical dark field image mode: this mode consists of applying a precession motion, at angular velocity, on the primary electron beam tilted at an angle. This will induce a rotational

movement of the diffraction pattern with the optical axis of the column as its center. By placing the objective diaphragm on the optical center, we pass through an entire ring of a plane type. In this way, we get a dark field made up of all the electrons diffracted at a certain angle. The image is accumulated for a while to obtain a minimum angle of  $360^\circ$  on the illumination.

- High resolution: Imaging of the sample is obtained from both transmitted and diffracted beams. This is possible by a much larger opening of the objective diaphragm and in some cases without any objective diaphragm. The high-resolution comes from the interference of transmitted and diffracted beams.

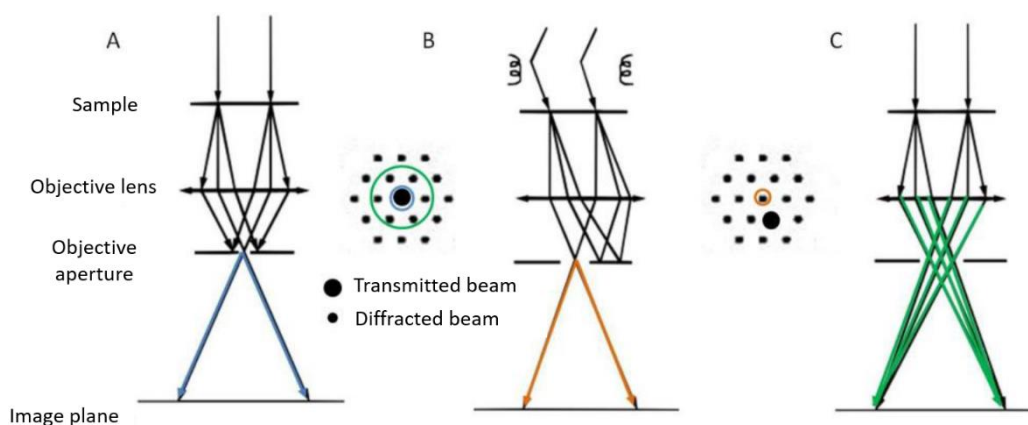


Figure A.2. Types of TEM imaging modes: (A) bright-field mode, (B) dark-field mode, (C) high-resolution image.

Transmission electron microscopy (TEM) images of Au seeds and Au@Ag NPs were acquired with a JEOL 1011 (100kV) instrument. High resolution TEM(HRTEM) observations and chemical analyses were performed using a JEOL JEM-2011 UHR operating at 200 kV and fitted with an energy-dispersive X-ray spectroscopy (EDX) microanalyser (PGT-IMIX PC). The size distributions of NPs are determined with NIH ImageJ software (1.37v) by measuring the diameters of at least 500 NPs. The samples are prepared by depositing a 20 mL drop of NP solution on a carbon-coated copper grid.

## 1.2. Scanning Transmission Electron Microscopy (STEM)

Scanning Transmission Electron microscopy (STEM) is a powerful tool for imaging nanostructures. STEM works in the same way as scanning electron microscopy by forming a concentrated beam of high energy ( $> 200$  kV) electrons that scans the surface of the sample while the desired signal is collected to form an image. This achieves atomic resolution. The

samples, as in the case of TEM, must be thin and are prepared by depositing on a conventional MET grid. Figure A.3 shows the main components of STEM. The electrons are accelerated from the source and concentrated at a point via a set of lenses. There are several types of detector to form the image.

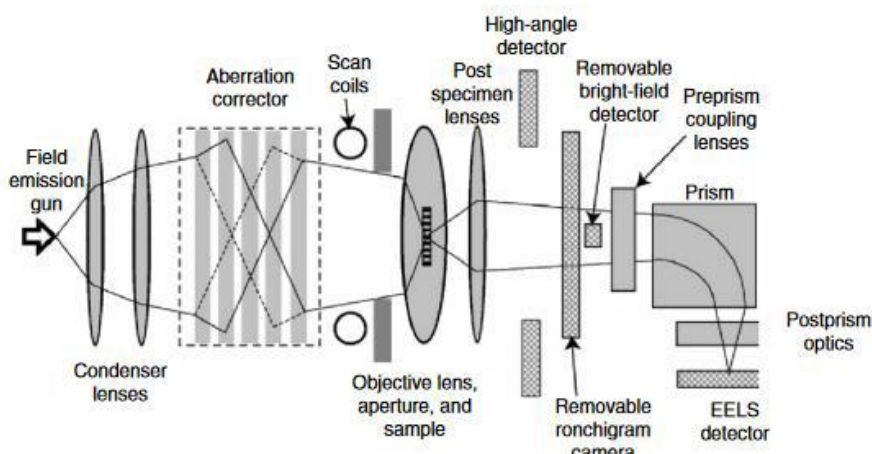


Figure A.3. Schematic illustration of STEM.

STEM images were taken using a high-angle annular dark field (HAADF) detector in a Nion Ultrastem 200 Cs-corrected microscope operating at 100kV with a probe size of about 0.07 nm. The probe convergence and HAADF detector minimum collection semi-angles were 35 and 75mrad respectively, meaning that HAADF images were dominated by Z-contrast, although some diffraction contrast is possible. Elemental maps were obtained using electron energy-loss spectroscopy (EELS) in the spectrum-image collection mode using the Ag M- and Au M-edges. More detail and typical spectra are included in the supplementary information.

EELS is one of the major advantages of STEM is the possibility of recovering the EELS signal and simultaneously with the HAADF image with atomic resolution. The EELS make it possible to obtain information by elemental analysis from measurements of loss of energy of the incident electrons, corresponding to the state transitions of the inner shell with the available unoccupied states. EELS is like energy dispersive x-ray spectroscopy commonly used in SEM but has atomic resolution. To obtain an EELS mapping corresponding to the corresponding HAADF image, an EELS spectrum is collected for each pixel and the mapping is thus reconstructed. The atomic mapping using EELS spectrum of Au@Ag core-shell NPs is shown in Figure A.4.

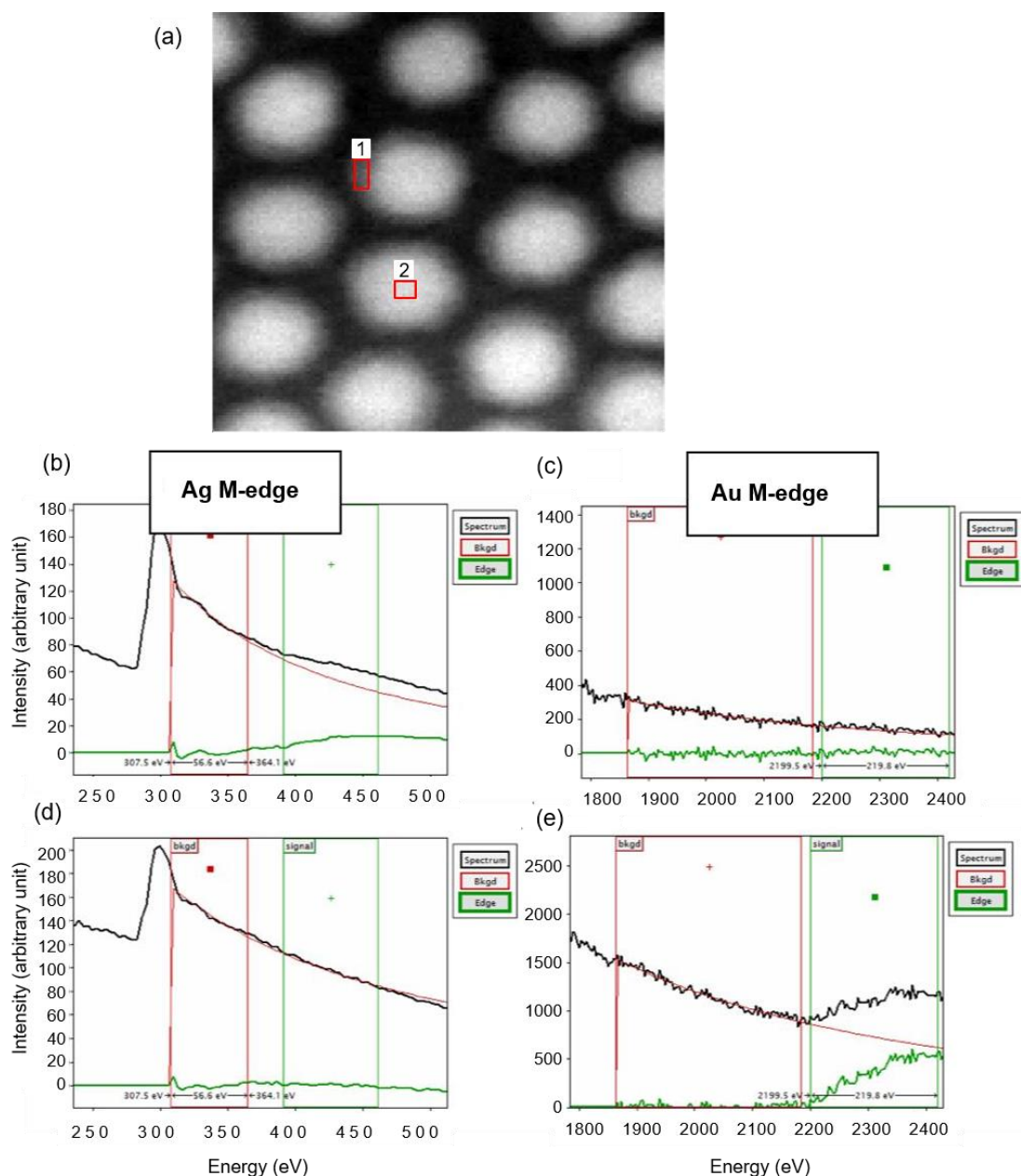


Figure A.4. EELS mapping details: (a) Typical spectrum image showing regions (1 and 2) over which the displayed spectra are summed, (b) and (c) Ag M- and Au M-edge signals in the shell region (1), (c) and (e) Ag M- and Au M-edge signals in the core region (2). Background and signal ranges are those used to generate the chemical maps. The channel width was 3.3 eV, convergence, and collection angles 35 and 44 mrad, respectively. The standard power-law background subtraction is not accurate for the delayed Ag M-edge and the intensities are not quantitative, but they suffice to localise the silver layer. The Au M-edge onset is blurred because of spectrometer defocus (it is not possible to be in focus across the entire > 2000 eV energy range). Dwell times per pixel were 20 to 50 ms.

### *1.3. Scanning Electron Microscopy (SEM)*

The first scanning electron microscopy (SEM) was built by Zworykin in 1942. This type of instrument is widely used in fields as diverse as electronics, materials, and life sciences. The basic principle of SEM is shown in Figure A.5. The SEM image is a reconstructed image: a probe, the electron beam, scans the surface of the sample, a detector synchronously recovers a signal induced by this probe to form an image, intensity mapping of this signal.

The SEM consists of a source of electrons that a set of “condenser” lenses focuses on a diaphragm. A second “objective” lens refocuses this beam on the sample in a fine spot (15 to 200 Å). A set of deflection coils makes it possible to move the beam and therefore sweep the sample. This forms the probe. Under the impact of the electron beam, there are essentially: i) electron backscattering of the incident beam with energy loss, ii) emission of low energy secondary electrons from the outer layers of the atoms of the sample, iii) X-ray emission, competitively with Auger electrons, iv) UV-visible photon emission, v) flow of a current towards the mass.

All these signals can be used to form an image. The SEM base detector recovers a mixture in variable proportion of secondary electrons and backscattered electrons, proportion depending on the primary energy, the sample-objective distance, the angle of incidence of the primary beam, the material observed. Other detectors make it possible to discriminate the secondary electrons from the backscattered electrons.

The contrast (i.e. the local variation of the electronic emission) of the image comes from topographical, chemical, and structural effects, governing back scattering and secondary emission. The magnification is determined by the ratio between the area scanned on the sample (a rectangle of dimension varying between a few mm and a fraction of micrometers on the side) and the dimension of the final document on the observation screen.

The secondary electron image is characterized by very good definition, up to magnifications between x20,000 and x50,000 in conventional, up to > 500,000 in high resolution, with lateral resolutions of 10 to 200 Å, depending on the sample, the apparatus and the observation parameters. Mounting the detector in the objective lens makes it possible to eliminate most of the backscattering, and to obtain a better-defined image of the surface, particularly at low primary energy.

The backscattered electron image has a lateral resolution at best of the order of 0.1 µm. The use of a specialized detector (semiconductor or scintillator) makes it possible to bring out



a contrast which is a function of the atomic number of the elements present. A heavy element will give an intense signal and therefore a clear area; a light element will give a weak signal and therefore a dark area, sort of an atomic number map. This mode of operation requires a flat surface to minimize the contrast due to the relief. On the other hand, the identification of the elements present requires the use of another method, typically X-ray microanalysis.

Scanning electron microscopy (SEM) images associated with energy dispersive X-ray spectroscopy (EDX) on the NPs 3D superlattices were performed with a JEOL-5510LV. The samples were prepared by depositing several drops of colloidal solution on a silicon wafer.

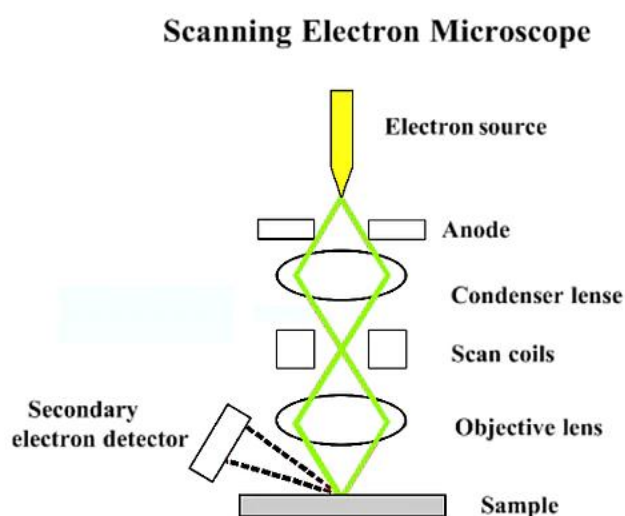


Figure A.5. Schematic illustration of SEM principle.

## ***Annex 2. Spectroscopy techniques***

### *2.1. IR spectroscopy*

This technique is based on the absorption of infrared radiation by the material. An analysis of the chemical functions present in the material is made possible by detecting the vibrations characteristic of chemical bonds. In practice, medium infrared radiation (between 4000 and 400  $\text{cm}^{-1}$ ), of frequency close to frequency of vibration of the molecule, is sent on the sample to be analyzed. These radiations are absorbed by the molecule and save us-rans a decrease in the intensity of the transmitted or reflected beam. The main modes of vibration of molecules are the modes of elongation and deformation. The vibration of elongation, also called "stretching", concerns the variation of the interatomic distance. When the molecule has symmetries, we can distinguish between symmetrical or antisymmetric modes of elongation. The deformation modes relate to the variation of the angles between adjacent links. They can be symmetrical or asymmetrical and occur in the plane or out of the plane.

The infrared spectra are recorded on a Bruker Equinox 55 spectrometer, equipped with a Ge / KBr separator (semi-reflecting mirror) and an MCT detector (Mercury Cadmium Tellurium) cooled by liquid nitrogen. They are produced either in solution in an optically transparent CaF<sub>2</sub> cell of length  $l = 200 \mu\text{m}$ , or in transmission-reflection mode, by depositing drops of solution on a horizontal mirror (silicon substrate covered with a layer of aluminum). The different modes of vibration of molecules are known and referenced in databases. The interpretation of infrared spectra is therefore based on the detection of characteristic peaks and their attribution to specific chemical groups.

We saw in Chapter II that infrared spectroscopy allows us to obtain information on the environment. local NPs, on the adsorbed molecules on their surface [KORGEL 1998] as well as their arrangement. Infrared (IR) spectra of oleylamine, Au- and Ag-oleylamine complexes were recorded using an ATR diamond crystal accessory on a Bruker Equinox 55 spectrometer equipped with a Ge/KBr beamsplitter and a liquid nitrogen-cooled MCT detector. Au- and Ag-oleylamine complexes samples are prepared as a solution as same concentration as the synthesis protocol.

### *2.2. UV-visible spectroscopy*

The extinction spectrum of NP solutions with a fixed concentration of 0.14  $\mu\text{mol L}^{-1}$  was measured at room temperature with a CARY 5000 double-beam UV-visible spectrophotometer between 300 and 700 nm using a quartz cell, with optical path( $l = 1 \text{ mm}$ ).

All the Au(PC) and Au(PC)@Ag NPs were dispersed in toluene. Spectrum processing is performed via CARY and ORIGIN 8.0 software. The directly measured quantity is absorbance  $A$ , defined by Beer-Lambert law:

$$A = -\log \frac{I}{I_0} = \varepsilon Cl \quad (3.1)$$

with  $A$ : absorbance at a given wavelength,

$I/I_0$ : transmittance of the solution (without unit)

$\varepsilon$ : molar extinction coefficient ( $\text{L}\cdot\text{mol}^{-1}\cdot\text{cm}^{-1}$ )

$l$ : length of the optical path which means thickness of the cell (cm)

$C$ : molar concentration of the solution ( $\text{mol}\cdot\text{L}^{-1}$ )

This law determines the concentration of the solutions of NPs.

### 2.3. Low Frequency Raman Spectroscopy (LFRS)

Samples for LFRS measurements were prepared by depositing several drops of colloidal solution onto a silicon wafer. The spectra are recorded with a six-pass tandem Fabry-Perot interferometer coupled with an Si avalanche photodiode for the detection of the scattered light. Because of the weak signal from the samples an acquisition time of several hours is required for each spectrum to obtain a sufficient signal-to-noise ratio. The 647.1 nm line of a  $\text{Kr}^+$  laser is used as excitation source. To prevent damage of the sample during the long irradiation time, the laser beam is focused on the sample surface at a low optical intensity of about  $10^{10} \text{ W m}^{-2}$ . This system allows us to record inelastic light scattering spectra with low frequency shifts ( $\nu < 300 \text{ GHz}$ ). To facilitate and support our interpretation of the LFRS spectra, the measured frequencies are compared with analytical calculations based on Lamb theory.<sup>1</sup>

A Fabry-Pérot multi-pass tandem (6 pass) was used in a classic backscattered geometry. Due to the weak signal detected on the samples, an integration time of several hours was typically required for each spectrum to obtain a suitable signal-to-noise ratio. To prevent any damage to the sample that could result from long laser irradiation, the laser beam was focused on the surface of the sample at low optical intensity in the order of  $10^7 \text{ W / m}^2$ . The laser excitation wavelength was 647 nm. This system allows measurement of inelastic scattering signals for wave numbers between 0.1 and  $15 \text{ cm}^{-1}$ .<sup>2,3</sup>

When the diameter of the spherical NP is small compared to the wavelength of the incident light  $D \ll \lambda$  it has been shown on the basis of symmetry arguments that only the breathing modes  $l=0$  and quadrupolar mode  $l=2$  are active in the Raman diffusion process (Chapter I). In most Raman experiments, only the fundamental mode of these two modes is

thus observed, which does not exclude the observation of  $n > 1$  harmonics<sup>4</sup>. This is mainly because the activity of the quadrupole modes is generally more important than that of the breathing modes in the case of a Raman scattering resonating with the surface plasmon. For a gold sphere of 5 nm in diameter [longitudinal sound speed  $v_L = 3330 \text{ ms}^{-1}$  and transverse  $v_T = 1250 \text{ ms}^{-1}$ ] the wave numbers expected for the quadrupole mode and the breathing mode are  $6.5 \text{ cm}^{-1}$  and  $19.2 \text{ cm}^{-1}$ , respectively<sup>5</sup>.

#### 2.4. X-ray photoelectron spectroscopy (XPS)

X-ray photoelectron spectroscopy (XPS) is a surface-sensitive quantitative spectroscopic technique based on the photoelectric effect. We can identify the elements that exist in a material or cover the surface, their chemical state, the overall electronic structure and density of the electronic states in the material. XPS analysis shows what elements are present, also what they are bonded to. A typical XPS spectrum is a plot of the number of electrons detected at a specific binding energy. Each element produces a set of characteristic XPS peaks which correspond to the electron configuration of the electrons within the atoms (e.g., 1s, 2s, 2p, 3s, etc). These are quantified by the elements based on peak intensity.

The ligand on the surface of Au NPs and Au@Ag NPs were quantified by in situ X-ray photoelectron spectroscopy (XPS) using a  $K\alpha\text{Al}$  source ( $h\nu = 1486,6 \text{ eV}$ ), and analyzed with the CASAXPS software). The measurement was performed by Vincent Noël in ITODYS, University of Paris. All XPS spectra are presented in Annex 6.



## ***Annex 3. Discrete dipole approximation (DDA) simulations and size-corrected dielectric functions of Au and Ag***

### *3.1. Discrete dipole approximation (DDA) simulations*

All the calculations of the extinction spectra performed in this work were carried out using the discrete dipole approximation (DDA) method. This method is based on the theory originally developed by Purcell and Pennypacker for the study of interstellar dust grains.<sup>6</sup> Subsequent improvements have enabled its use for calculating the extinction, absorption and scattering cross sections of other fine particles.<sup>7-9</sup> Due to its versatility this method has been widely used in the last few years to simulate the optical response of various metallic systems composed of either individual or multiple objects of any size and shape.<sup>10-15</sup> Here, the extinction spectra of Au(PC) and Au(PC)@Ag NPs are calculated using the free software DDSCAT 7.3 written by Draine and Flatau.<sup>16</sup> Size-corrected dielectric functions were calculated using the procedures described elsewhere for the spherical core<sup>17,18</sup> and the shell geometries.<sup>19</sup> This correction aims to account for the reduction of the effective electron mean free path  $L_{eff}$  due to the scattering of the conduction electrons from the particle surface as well as the core-shell interface. The size-correction aforementioned was performed on the dielectric functions of bulk Au and Ag taken from Palik's handbook.<sup>20</sup> Further information on the calculation of the size-corrected dielectric functions and their graphs are presented in Annex 3.2.

### *3.2. Au core and Ag shell size-corrected dielectric functions in Au@Ag core-shell NPs*

The optical properties of homogeneous metallic NPs are well-known to sensitively depend on their size<sup>4</sup>. A damping of the plasmon resonance is noticed when reducing the NP size to a few nanometers. In a purely classical approach, the origin of such a line shape broadening of the plasmon resonance is essentially geometric. The intrinsic bulk width of the dipole plasmon polariton,  $\gamma_0$  is due to the scattering of the electrons with phonons, electrons, lattice defects, or impurities. At variance, in a particle whose size is comparable to or smaller than the mean free path of conduction electrons in the bulk material, the scattering of the electrons from the particle surface results in a reduced effective mean free path,  $L_{eff}$ , and an increased homogeneous line width of the dipole plasmon polariton,  $\gamma(eff)$ . Through the Mathiessen's rule,<sup>4</sup> this latter is expressed as:

$$\gamma(eff) = \gamma_0 + A \frac{v_F}{L_{eff}}$$

where  $v_F$  is the Fermi velocity and  $A$  is a dimensionless factor, usually assumed to be close to unity.

The surface dispersion effect on the plasmon polariton described above gives rise to the size dependence of the dielectric function, according to the following relationship:<sup>5</sup>

$$\varepsilon(\omega, L_{eff}) = \varepsilon_{bulk}(\omega) + \frac{\omega_p^2}{\omega^2 + i\omega\gamma_0} - \frac{\omega_p^2}{\omega^2 + i\omega\gamma_{(eff)}}$$

where  $\varepsilon_{bulk}(\omega)$  is the bulk metal dielectric function and  $\omega_p$  is the plasma angular frequency. In this work, the Au and Ag bulk dielectric functions were taken from Palik's handbook.<sup>6</sup> The experimental values used for the Fermi velocity, the plasma energy and the intrinsic bulk width of the plasmon polariton of each metal are from Ref. [7]:

- For Au:  $v_F = 1.40 \times 10^6 \text{ m s}^{-1}$ ,  $\hbar\omega_p = 9.02 \text{ eV}$ ,  $\gamma_0 = 0.024 \text{ eV}$ .
- For Ag:  $v_F = 1.39 \times 10^6 \text{ m s}^{-1}$ ,  $\hbar\omega_p = 8.98 \text{ eV}$ ,  $\gamma_0 = 0.018 \text{ eV}$ .

Following a geometrical probability approach,<sup>8</sup> the effective mean free path of the conduction electrons inside a spherical particle of radius  $R$  is stated as  $L_{eff} = 4R/3$ , as used for correcting the dielectric function of the Au core. In Figure 6, one shows the size-corrected dielectric functions calculated for Au nanospheres of two different diameters, which are compared to the bulk one.

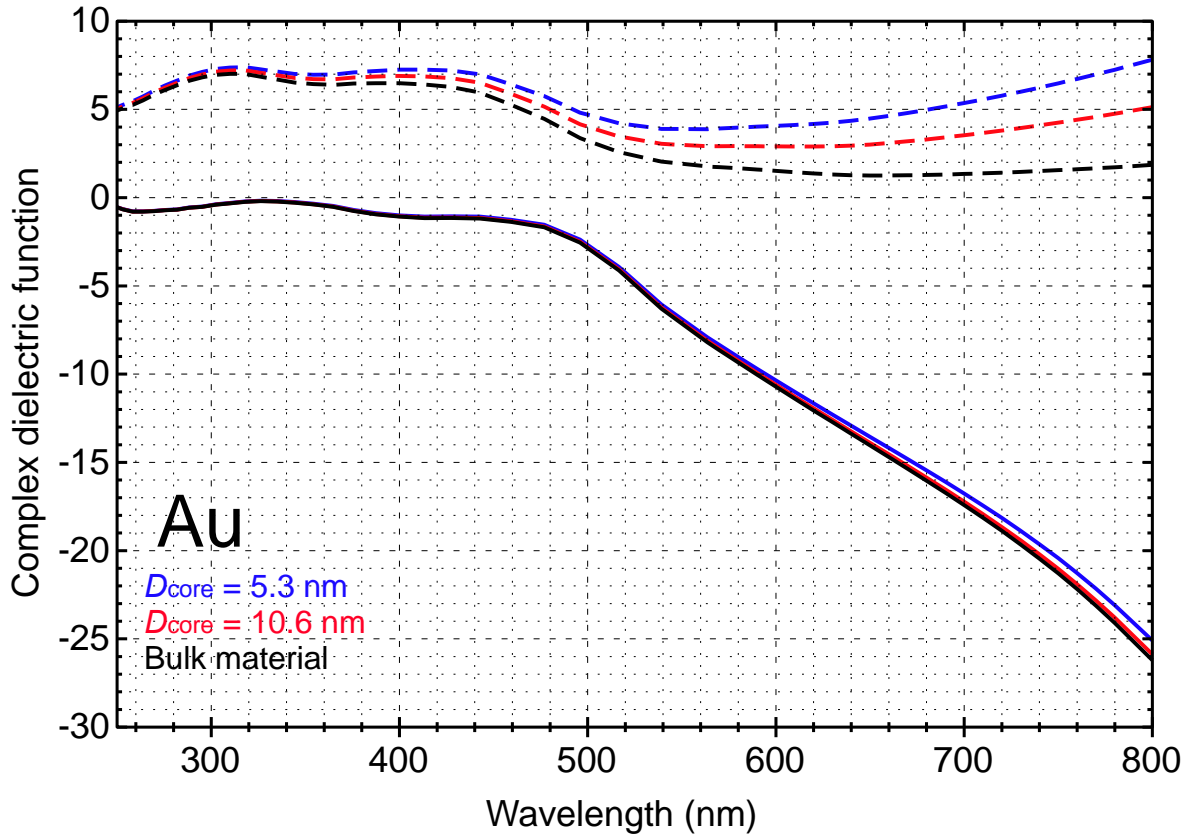


Figure A.6. Real (solid lines) and imaginary (dashed lines) components of the size-corrected complex dielectric function of Au nanospheres of 5.3 nm (blue curves) and 10.6 nm (red curves) in diameter compared to those of the bulk material (black curves) issued from Ref. [6].

Regarding the size dependence of the Ag dielectric function, one uses the reduced effective mean free path derived for a spherical shell geometry from the billiard formula:<sup>9</sup>

$$L_{eff} = \frac{4(R_{CS}^3 - R_{core}^3)}{3(R_{CS}^2 - R_{core}^2)} = \frac{2(D_{CS}^3 - D_{core}^3)}{3(D_{CS}^2 - D_{core}^2)}$$

where  $R_{CS}$  and  $R_{core}$  ( $D_{CS}$  and  $D_{core}$ ) are the radii (diameters) of the inner and outer surfaces of the shell, respectively. The dielectric functions calculated for Ag shells of various inner surface diameters and thicknesses,  $e = (D_{CS} - D_{core})/2$ , are presented below in Figure A.7-8.



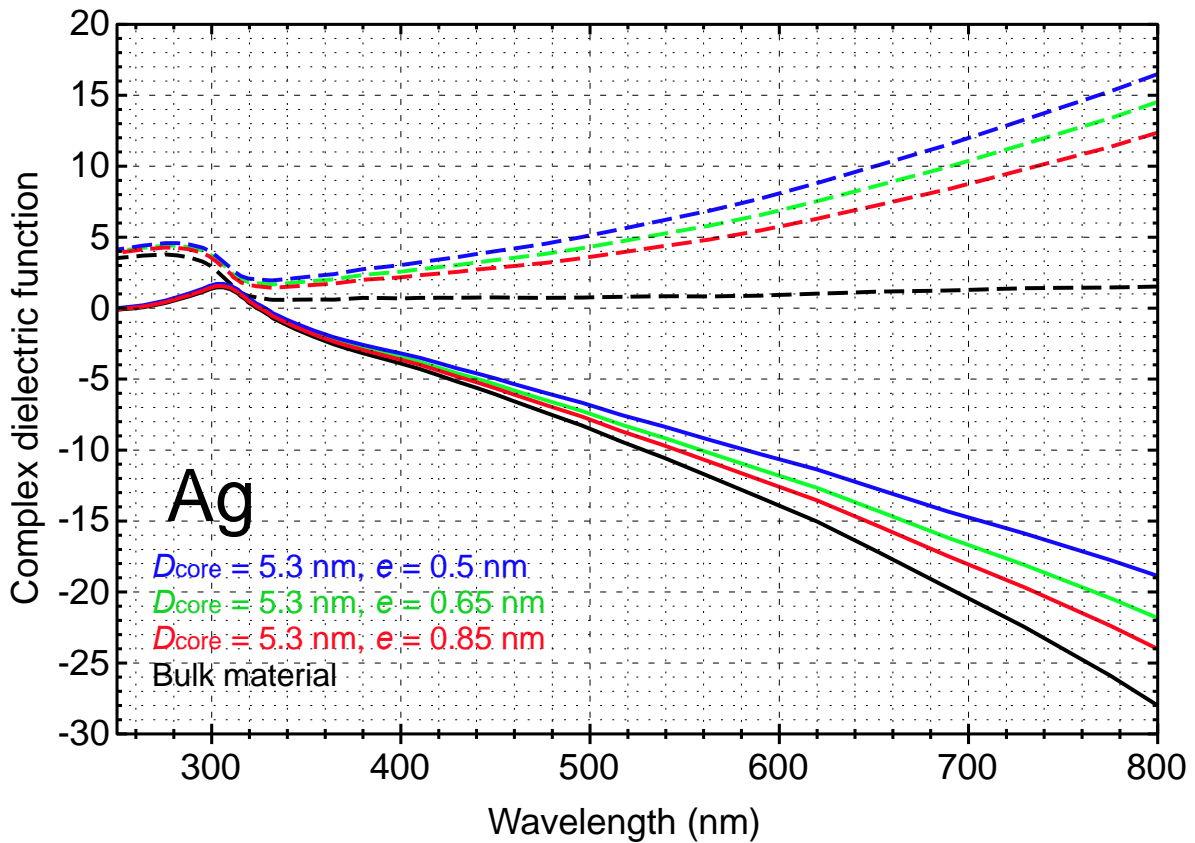


Figure A.7. Real (solid lines) and imaginary (dashed lines) components of the size-corrected complex dielectric function of various Ag shells compared to those of the bulk material (black curves) issued from Ref. [6]. The shells have the same internal diameter  $D_{\text{core}} = 5.3 \text{ nm}$  and three different thicknesses:  $e = 0.5 \text{ nm}$  (blue curves),  $e = 0.65 \text{ nm}$  (green curves) and  $e = 0.85 \text{ nm}$  (red curves).

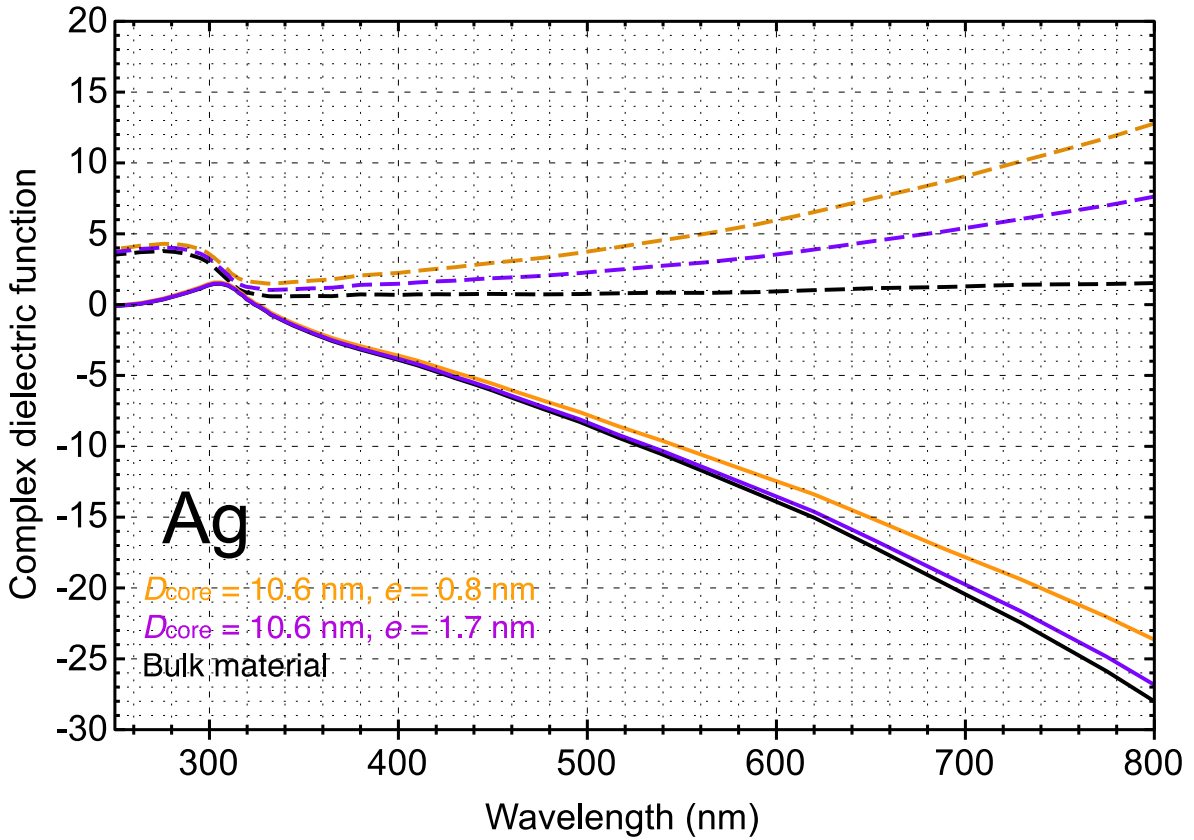


Figure A.8. Real (solid lines) and imaginary (dashed lines) components of the size-corrected complex dielectric function of various Ag shells compared to those of the bulk material (black curves) issued from Ref. [6]. The shells have the same internal diameter  $D_{\text{core}} = 10.6 \text{ nm}$  and two different thicknesses:  $e = 0.8 \text{ nm}$  (orange curves) and  $e = 1.7 \text{ nm}$  (violet curves).



## Annex 4. Comparison of experimental and DDA calculated absorption spectra of core-shell NPs

### 4.1. $Au_{10nm}(PC)@Pd$ and $Au_{10nm}(PC)@Pt$ NPs

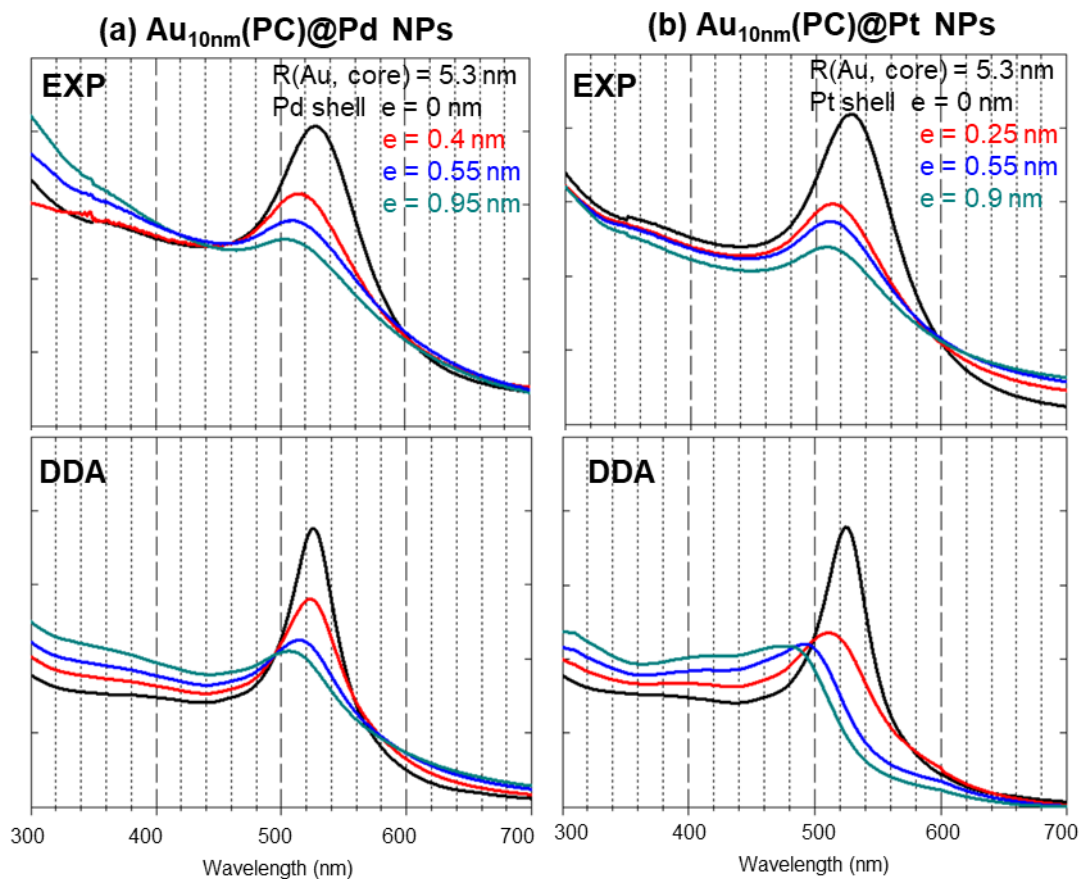


Figure A. 9. Experimental and DDA calculated absorption spectra of core-shell (a)  $Au_{10nm}(PC)@Pd$  NPs and (b)  $Au_{10nm}(PC)@Pt$  NPs with various shell thickness as indicated in both panels.

4.2.  $Ag_{12nm}(PC)@Pd$  and  $Ag_{12nm}(PC)@Pt$  NPs

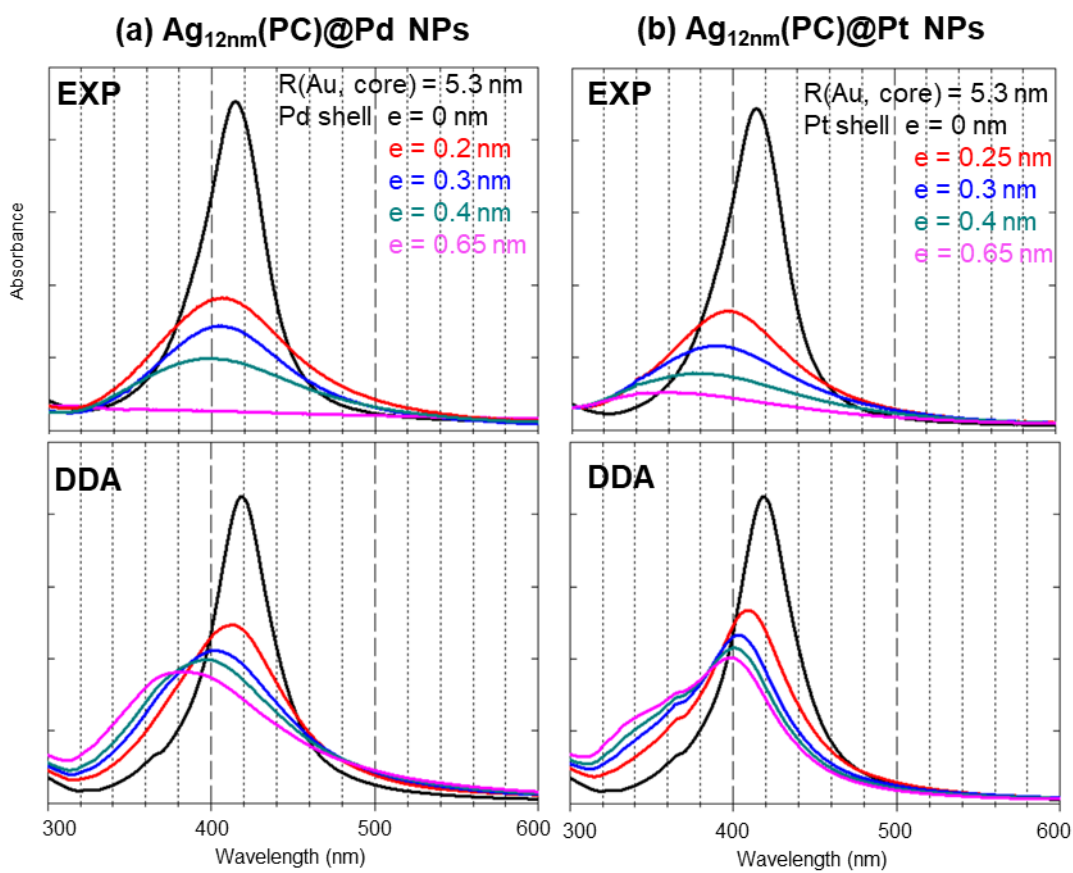


Figure A. 10. Experimental and DDA calculated absorption spectra of core-shell (a)  $Ag_{12nm}(PC)@Pd$  NPs and (b)  $Ag_{12nm}(PC)@Pt$  NPs with various shell thickness as indicated in both panels.

**Annex 5. NPs control conditions of catalytic activity test**

Table A.1. List of NPs and their concentration used in catalytic activity test.

NPs type	Diameter (nm)	Surface area per NP (S) (nm <sup>2</sup> )	NPs concentration (C <sub>NPs</sub> ) (μmol L <sup>-1</sup> )	Total surface area (S x C <sub>NPs</sub> ) (nm <sup>2</sup> μmol L <sup>-1</sup> )
Au NPs	10.6	353.0	0.0350	49.39
Au@Ag	11.4	408.3	0.0303	
	12.2	467.6	0.0264	
	14	615.8	0.0201	
	14.8	688.1	0.0180	
Au@Pd	11.4	408.3	0.0303	
	12.5	490.9	0.0252	
	13.7	589.6	0.0210	
	14	615.8	0.0201	
Au@Pt	11.1	387.1	0.0319	
	11.7	430.1	0.0287	
	12.9	522.8	0.0236	
	13.5	572.6	0.0216	
Au PC	7	153.9	0.0803	
Au SC	7.2	162.9	0.0759	
Au@Ag PC	7	153.9	0.0803	
Au@Ag SC	7.5	176.7	0.0699	



## Annex 6. Ligands on core-shell NPs in XPS analysis

Sample 1 : Au<sub>10nm</sub>(PC)@Ag NPs

Peaks					
Name	Peak BE	FWHM eV	Area (P) CPS.eV	At. %	Q
Ag3d	367.91	1.05	3046.09	0.08	Y
Au4f	83.72	1.11	3186.68	0.08	Y
C1s	284.82	1.53	161098.38	74.93	Y
N1s	399.80	1.60	2117.83	0.56	Y
O1s	532.39	1.51	144586.37	24.35	Y
Si2p	102.21	1.46	52999.48	0.00	

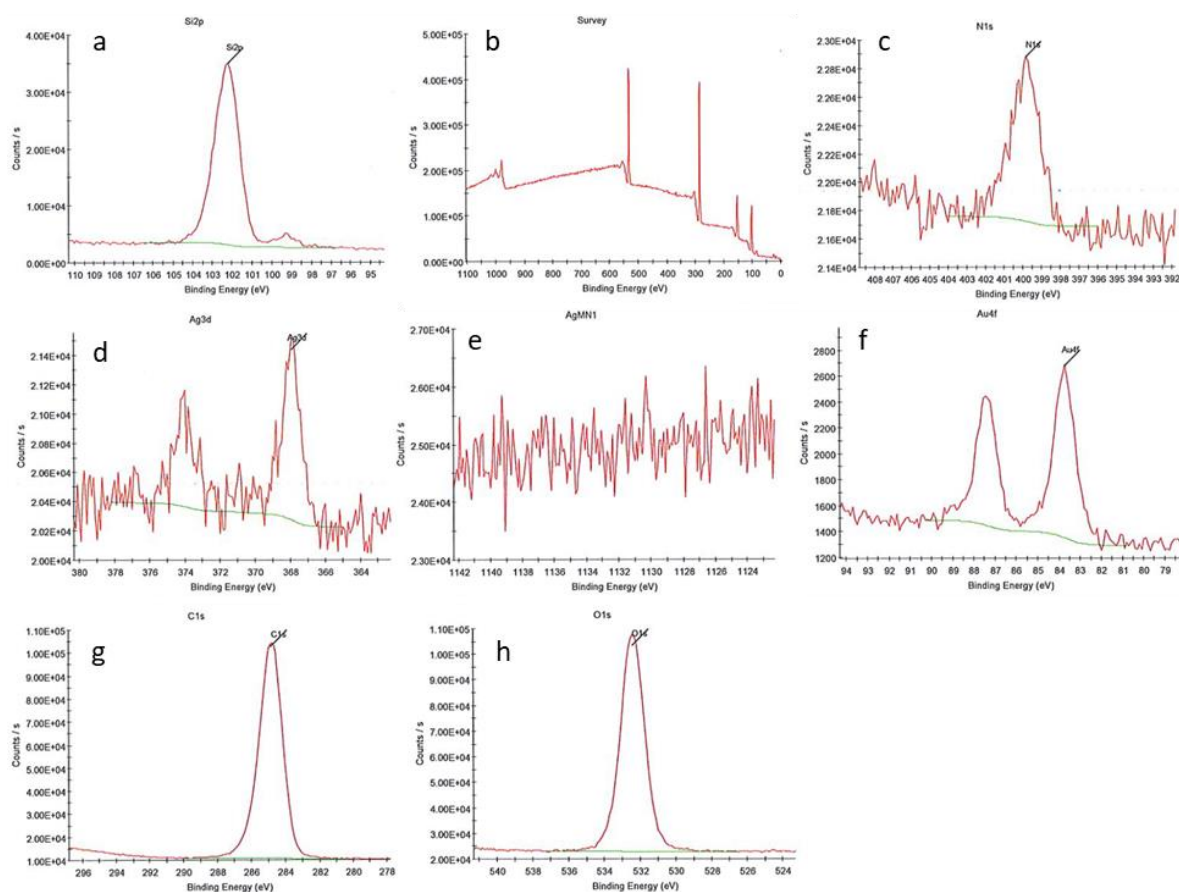


Figure A. 11. XPS spectra for Au<sub>10nm</sub>@Ag core-shell NPs before ligands exchange in detail: (a) Si(2p), (b) survey XPS spectra (c) N (1s), (d) Ag (3d), (e) Ag (MN1), (f) Au (4f), (g) C (1s), and (h) O (1s).



Sample 2: Au<sub>10nm</sub>(PC)@Ag NPs after ligand exchange

Peaks					
Name	Peak BE	FWHM eV	Area (P) CPS.eV	At. %	Q
Ag MN1	1134.05	4.08	107254.40	0.00	
Ag3d	367.89	1.09	429620.20	11.36	Y
Au4f	83.76	1.00	550440.82	14.56	Y
Cl s	285.58	1.69	81399.04	38.17	Y
Cl s A	287.22	1.58	25450.82	11.94	Y
Cl s B	288.82	1.77	4313.44	2.02	Y
N1s	400.20	1.54	1464.56	0.39	Y
N1s A	403.23	1.34	9586.54	2.56	Y
O1s	531.01	1.69	44793.71	7.60	Y
O1s A	532.88	1.76	46854.74	7.95	Y
S2p	161.78	2.10	12535.78	3.44	Y
Si2p	102.82	1.59	9795.65	0.00	

Peak Fit							
Name	Peak BE	Height CPS	Height	Area CPS.eV	Area	FWHM fit eV	L/G Mix (%)
N1s	400.20	875.64	0.13	1464.56	0.15	1.61	30.00
N1s A	403.23	6624.09	1.00	9586.54	1.00	1.39	30.00
O1s	531.01	24457.16	1.00	44793.71	0.96	1.76	30.00
O1s A	532.88	24571.98	1.00	46854.74	1.00	1.83	30.00
Cl s	285.58	44555.53	1.00	81399.04	1.00	1.75	30.00
Cl s A	287.22	14854.43	0.33	25450.82	0.31	1.64	30.00
Cl s B	288.82	2249.80	0.05	4313.44	0.05	1.84	30.00

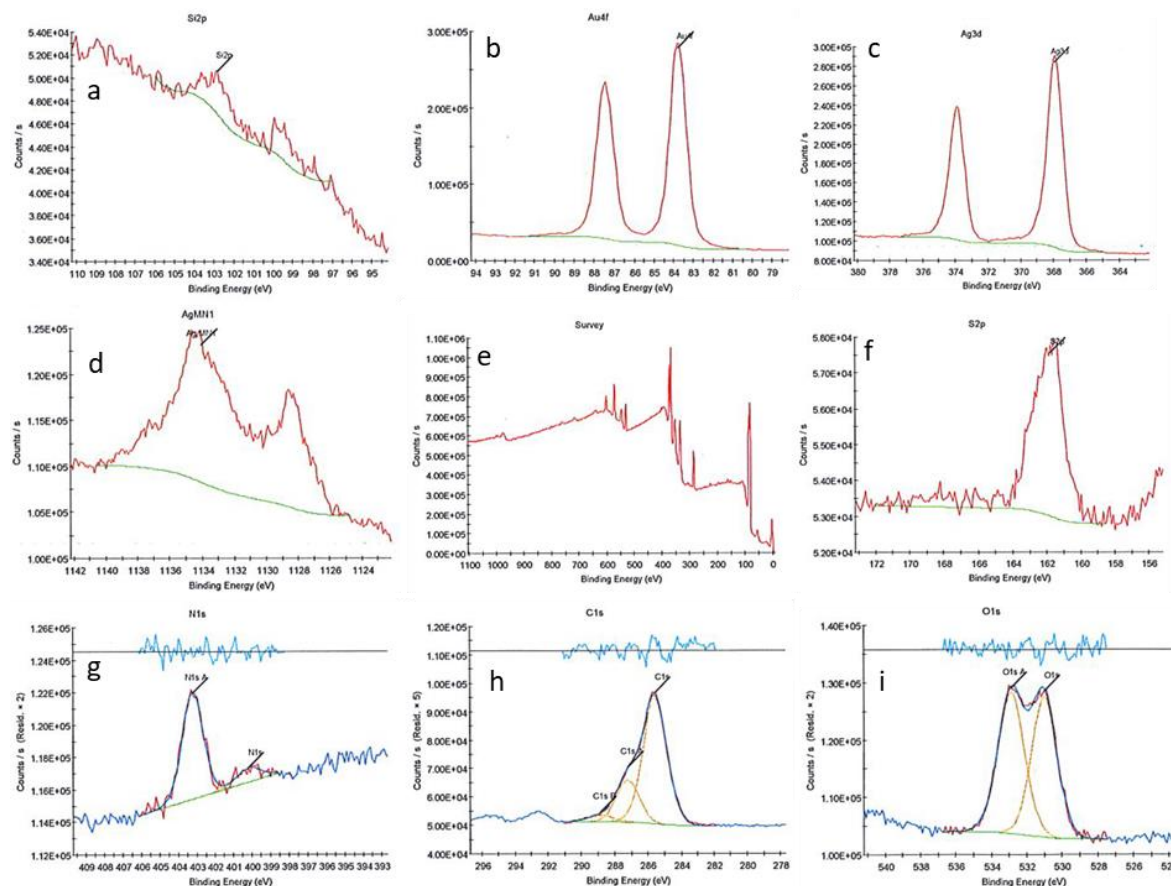


Figure A. 12. XPS spectra for Au<sub>10nm</sub>@Ag core-shell NPs after ligands exchange in detail: (a) Si(2p), (b) Au (4f), (c) Ag (3d), (d) Ag (MN1), (e) survey XPS spectra, (f) S (2p), (g) N (1s), (h) C (1s), and (i) O(1s).

Sample 3 : Au<sub>5nm</sub>(PC)@Ag NPs

Peaks					
Name	Peak BE	FWHM eV	Area (P) CPS.eV	At. %	Q
Ag MN1	1134.15	0.68	6612.46	0.00	
Ag3d	367.86	1.02	106648.11	2.62	Y
Au4f	83.74	0.99	122031.51	3.00	Y
C1s	285.13	1.32	171052.56	74.57	Y
N1s	399.72	1.24	3294.26	0.82	Y
O1s	532.58	1.35	120289.11	18.99	Y
Si2p	102.19	1.34	46193.71	0.00	

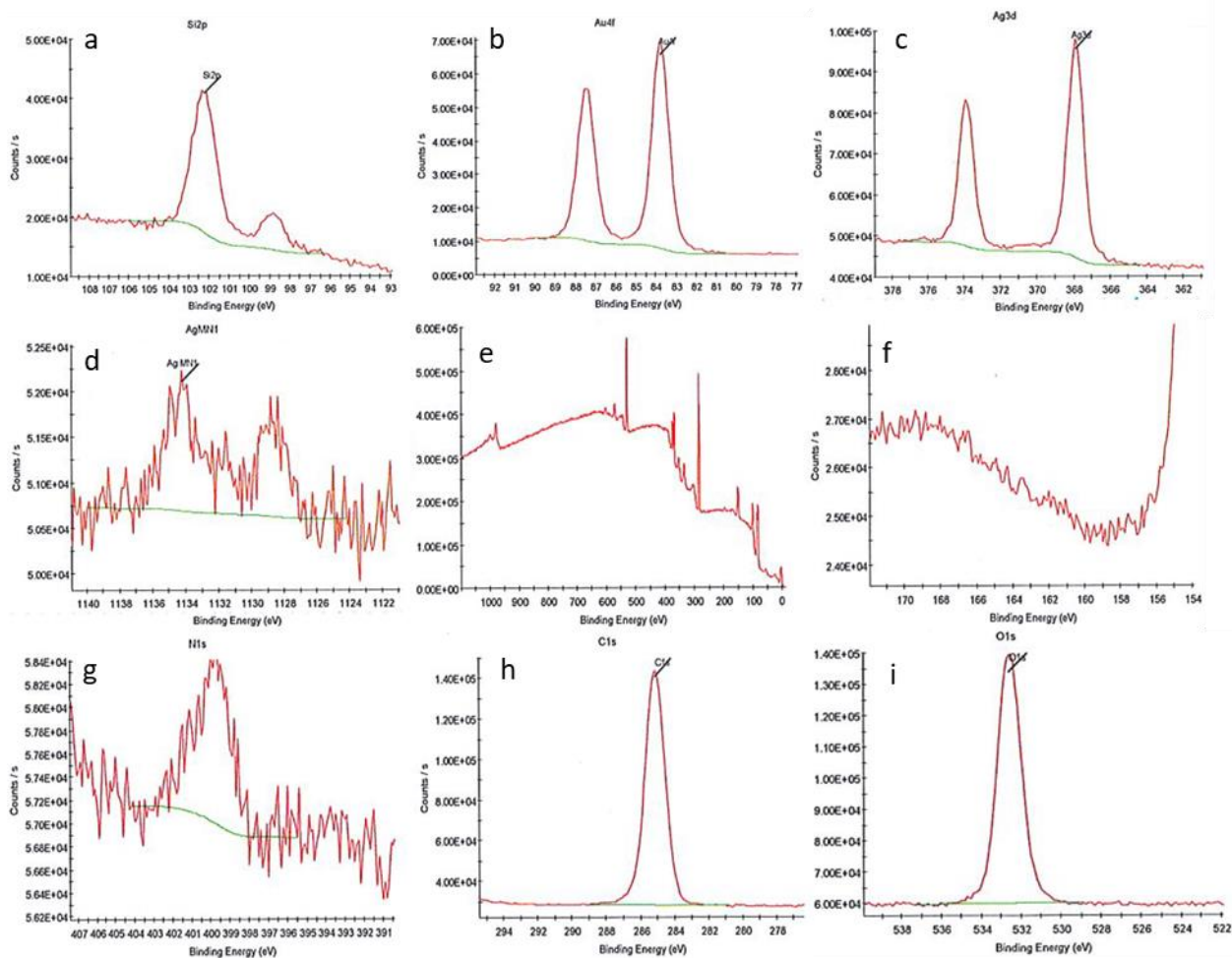


Figure A.13. XPS spectra for Au<sub>5nm</sub>@Ag core-shell NPs before ligands exchange in detail: (a) Si (2p), (b) Au (4f), (c) Ag (3d), (d) Ag (MN1), (e) survey XPS spectra, (f) S (2p), (g) N (1s), (h) C (1s), and (i) O(1s).

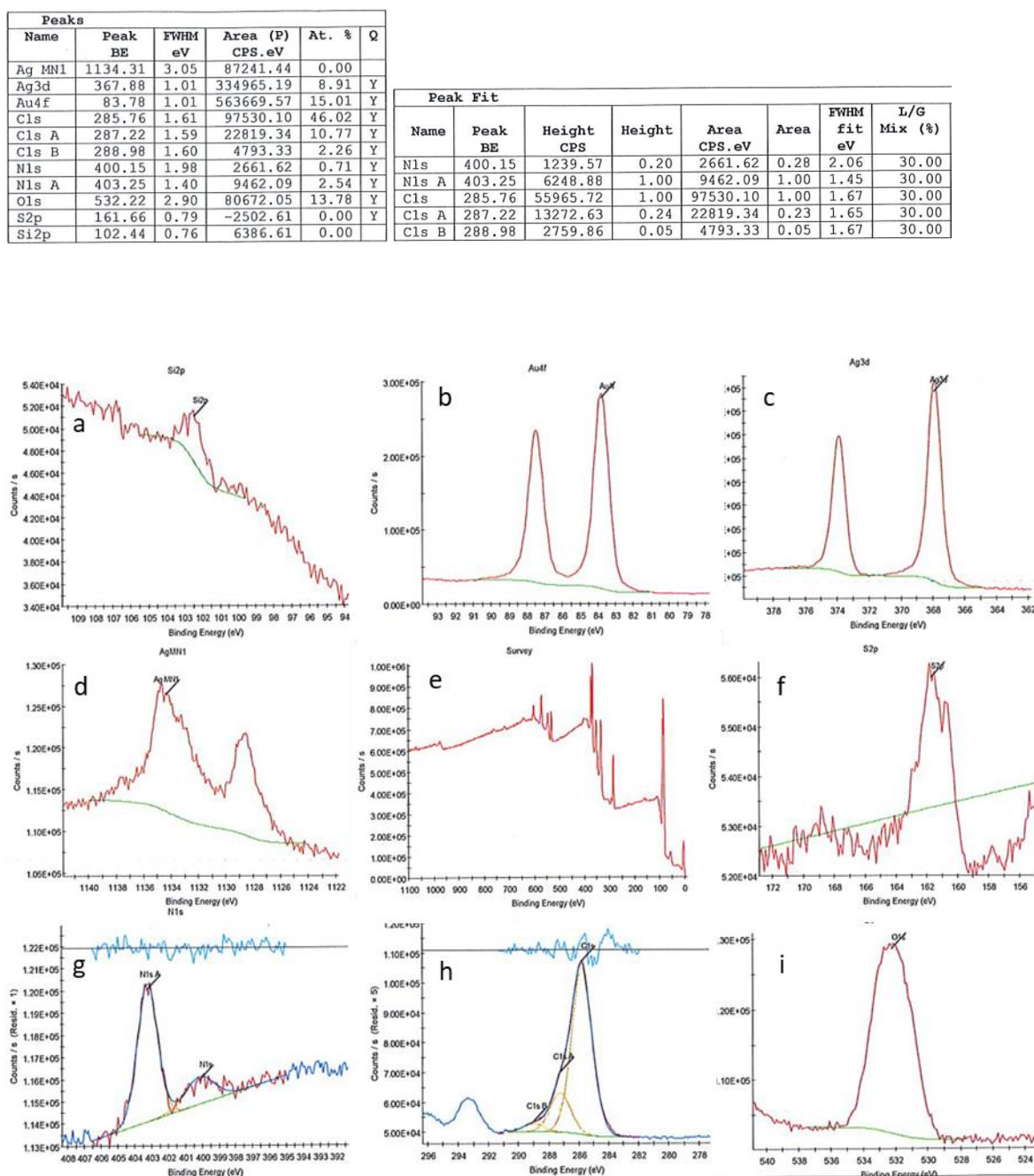
Sample 4 : Au<sub>5nm</sub>(PC)@Ag NPs after ligand exchange

Figure A. 14. XPS spectra for Au<sub>5nm</sub>@Ag core-shell NPs after ligands exchange in detail: (a) Si (2p), (b) Au (4f), (c) Ag (3d), (d) Ag (MN1), (e) survey XPS spectra, (f) S (2p), (g) N (1s), (h) C (1s), and (i) O(1s).

## Annex 7. Catalytic test of 4-NP to 4-AP UV-visible absorption spectrum

## 7.1. Absorption spectra change of Au@M NPs (M=Ag, Pd, Pt)

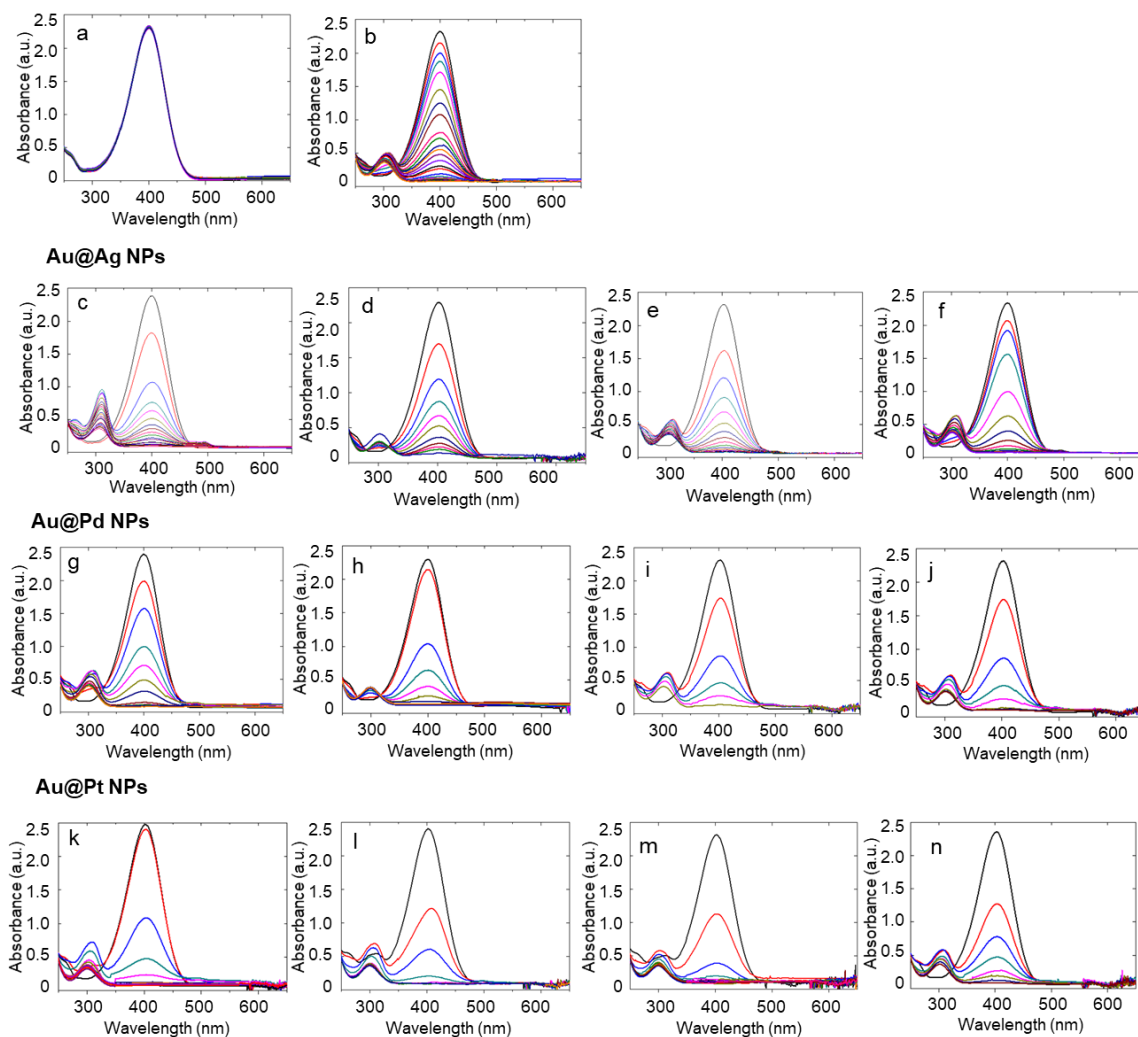


Figure A. 15. Absorption spectrum during the reduction of 4-nitrophenol to 4-aminophenol by time (a) without NPs, in presence of (b)  $Au_{10.6nm}$  NPs, (c-f)  $Au_{10.6nm}@Ag$  NPs with (c) 1 (d) 2 (e) 5 (f) 6 atomic layers, (g-j)  $Au_{10.6nm}@Pd$  NPs with (g) 1 (h) 2 (i) 4 (j) 5 atomic layers, (k-n)  $Au_{10.6nm}@Pt$  NPs with (k) 1 (l) 2 (m) 3 (n) 4 atomic layers,.

7.2. Absorption spectra change on crystallinity effect

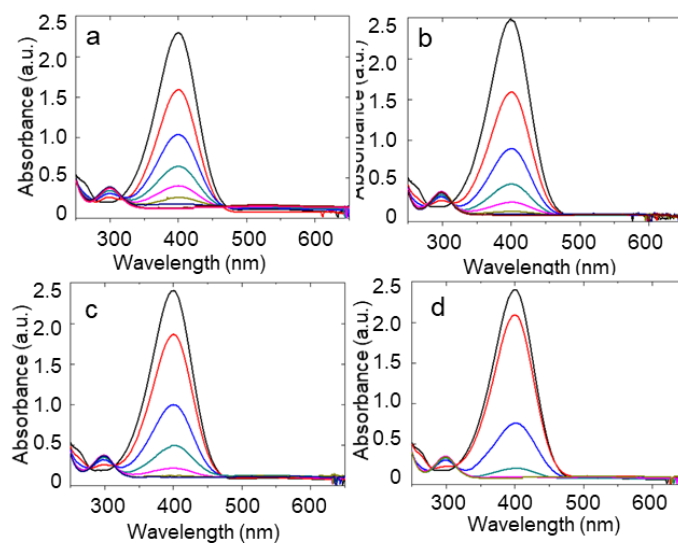
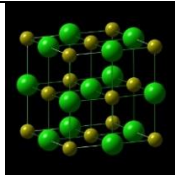


Figure A. 16. Absorption spectrum during the reduction of 4-nitrophenol to 4-aminophenol by time in presence of (a)  $Au_{7nm}(PC)$  NPs, (b)  $Au_{7nm}(SC)$  NPs with (c)  $Au_{5nm}(PC)@Ag$  NPs with 4 atomic layers of Ag (d)  $Au_{7nm}(SC)@Ag$  NPs with 4 atomic layers of Ag .

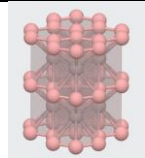
**Annex 8. Crystalline structure information of representative types of BNSLs**

All crystalline structure information is deduced from <https://materialsproject.org/materials>.

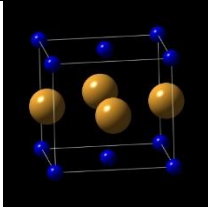
**NaCl-type BNSL structure**

<b>Crystal Structure Data</b>	
Spacegroup Symbol	Fm3c
Lattice Type	cubic
<b>Unit Cell Parameters</b>	
Unit cell display	
a [Å]	5.6400
b [Å]	5.6400
c [Å]	5.6400
alpha [deg]	90
beta [deg]	90
Gamma [deg]	90

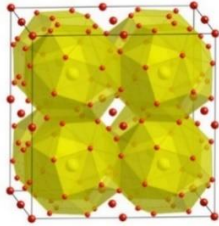
**AlB<sub>2</sub>-type BNSL structure**

<b>Crystal Structure Data</b>	
Spacegroup Symbol	P6/mmm
Lattice Type	tetragonal
<b>Unit Cell Parameters</b>	
Unit cell display	
a [Å]	3.007
b [Å]	3.007
c [Å]	3.274
alpha [deg]	90
beta [deg]	90
Gamma [deg]	120

**CuAu-type BNSL structure**

<b>Crystal Structure Data</b>	
Spacegroup Symbol	P4/mmm
Lattice Type	tetragonal
<b>Unit Cell Parameters</b>	
Unit cell display	
a [Å]	2.864
b [Å]	2.864
c [Å]	3.662
alpha [deg]	90
beta [deg]	90
Gamma [deg]	90

**NaZn<sub>13</sub>-type BNSL structure**

<b>Crystal Structure Data</b>	
Spacegroup Symbol	Fm3c [226]
Lattice Type	cubic
<b>Unit Cell Parameters</b>	
Unit cell display	
a [Å]	12.2836
b [Å]	12.2836
c [Å]	12.2836
alpha [deg]	90
beta [deg]	90
Gamma [deg]	90

**Annex 9. TEM image of NaCl, AlB<sub>2</sub>, and NaZn<sub>13</sub>-type of BNSL structure.**

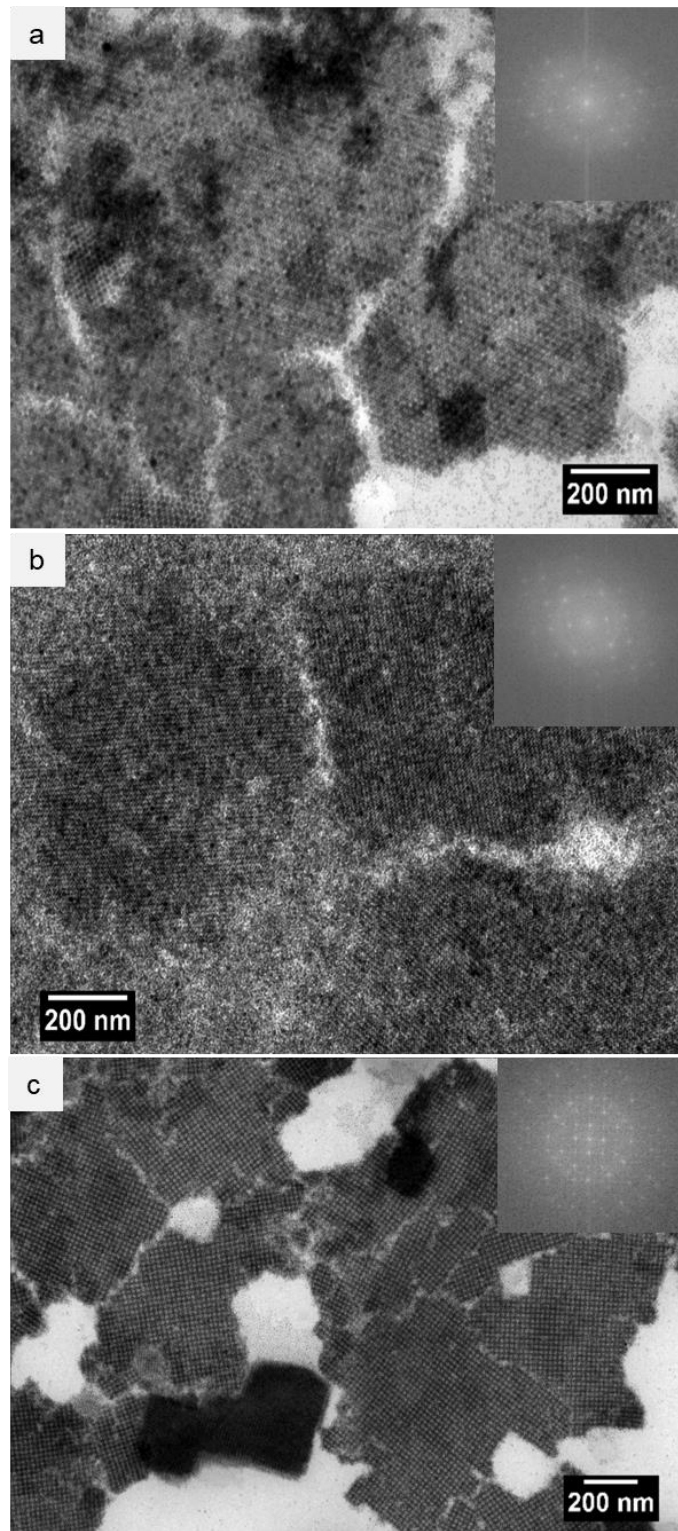


*Figure A. 17. TEM images of (a) NaCl, (b) AlB<sub>2</sub>, and (c) NaZn<sub>13</sub> type of BNSL structure in lower magnification. FFT images are shown in inset. Deposition condition is described in section 3.1, Chapter IV.*



## References

- (1) Portalès, H.; Saviot, L.; Duval, E.; Gaudry, M.; Cottancin, E.; Pellarin, M.; Lermé, J.; Broyer, M. Resonant Raman Scattering by Quadrupolar Vibrations of Ni-Ag Core-Shell Nanoparticles. *Physical Review B* **2002**, *65* (16), 165422. <https://doi.org/10.1103/PhysRevB.65.165422>.
- (2) Portales, H. Étude Par Diffusion Raman de Nanoparticules Métalliques En Matrice Diélectrique Amorphe. These de doctorat, Lyon 1, 2001.
- (3) Chapus, L. Organisation de Nanoparticules de Métaux Nobles : Application à La Spectroscopie Raman Exaltée de Surface et à l'électrochimie. These de doctorat, Paris 6, 2017.
- (4) Addison, C. J.; Konorov, S. O.; Brolo, A. G.; Blades, M. W.; Turner, R. F. B. Tuning Gold Nanoparticle Self-Assembly for Optimum Coherent Anti-Stokes Raman Scattering and Second Harmonic Generation Response. *J. Phys. Chem. C* **2009**, *113* (9), 3586–3592. <https://doi.org/10.1021/jp809579b>.
- (5) Murray, D. B.; Dhara, S.; Ravindran, T. R.; Nair, K. G. M.; Kalavathi, S.; Saviot, L.; Duval, E. Acoustic Vibrations of a Silica-Embedded Gold Nanoparticle: Elastic Anisotropy. *arXiv:cond-mat/0407548* **2004**.
- (6) Purcell, E. M.; Pennypacker, C. R. Scattering and Absorption of Light by Nonspherical Dielectric Grains. *The Astrophysical Journal* **1973**, *186*, 705. <https://doi.org/10.1086/152538>.
- (7) Draine, B. T.; Flatau, P. J. Discrete-Dipole Approximation For Scattering Calculations. *Journal of the Optical Society of America A* **1994**, *11* (4), 1491. <https://doi.org/10.1364/JOSAA.11.001491>.
- (8) Draine, B. T.; Flatau, P. J. Discrete-Dipole Approximation for Periodic Targets: Theory and Tests. *Journal of the Optical Society of America A* **2008**, *25* (11), 2693. <https://doi.org/10.1364/JOSAA.25.002693>.
- (9) Gutkovicz-Krusin, D.; Draine, B. T. Propagation of Electromagnetic Waves on a Rectangular Lattice of Polarizable Points. *Optics Express* **2012**, *20*, 1247.
- (10) Yang, W.; Schatz, G. C.; Van Duyne, R. P. Discrete Dipole Approximation for Calculating Extinction and Raman Intensities for Small Particles with Arbitrary Shapes. *The Journal of Chemical Physics* **1995**, *103* (3), 869–875. <https://doi.org/10.1063/1.469787>.
- (11) Wei, J. J.; Yang, P.; Portalès, H.; Albouy, P.-A.; Pileni, M. P. Collective Surface Plasmon Resonances in Two-Dimensional Assemblies of Au and Ag Nanocrystals: Experiments and Discrete Dipole Approximation Simulation. *The Journal of Physical Chemistry C* **2016**, *120* (25), 13732–13738. <https://doi.org/10.1021/acs.jpcc.6b03397>.
- (12) Sosa, I. O.; Noguez, C.; Barrera, R. G. Optical Properties of Metal Nanoparticles with Arbitrary Shapes. *The Journal of Physical Chemistry B* **2003**, *107* (26), 6269–6275. <https://doi.org/10.1021/jp0274076>.
- (13) Brioude, A.; Pileni, M. P. Silver Nanodisks: Optical Properties Study Using the Discrete Dipole Approximation Method. *The Journal of Physical Chemistry B* **2005**, *109* (49), 23371–23377. <https://doi.org/10.1021/jp055265k>.
- (14) Shuford, K. L.; Ratner, M. A.; Schatz, G. C. Multipolar Excitation in Triangular Nanoprisms. *The Journal of Chemical Physics* **2005**, *123* (11), 114713. <https://doi.org/10.1063/1.2046633>.
- (15) Yang, P.; Portalès, H.; Pileni, M.-P. Dependence of the Localized Surface Plasmon Resonance of Noble Metal Quasispherical Nanoparticles on Their Crystallinity-Related Morphologies. *The Journal of Chemical Physics* **2011**, *134* (2), 024507. <https://doi.org/10.1063/1.3523645>.

- (16) Draine, B. T.; Flatau, P. J. User Guide for the Discrete Dipole Approximation Code DDSCAT 7.3. *arXiv:1305.6497 [astro-ph, physics:cond-mat, physics:physics]* **2013**.
- (17) Hövel, H.; Fritz, S.; Hilger, A.; Kreibig, U.; Vollmer, M. Width of Cluster Plasmon Resonances: Bulk Dielectric Functions and Chemical Interface Damping. *Physical Review B* **1993**, *48* (24), 18178–18188. <https://doi.org/10.1103/PhysRevB.48.18178>.
- (18) Coronado, E. A.; Schatz, G. C. Surface Plasmon Broadening for Arbitrary Shape Nanoparticles: A Geometrical Probability Approach. *The Journal of Chemical Physics* **2003**, *119* (7), 3926–3934. <https://doi.org/10.1063/1.1587686>.
- (19) Moroz, A. Electron Mean Free Path in a Spherical Shell Geometry. *The Journal of Physical Chemistry C* **2008**, *112* (29), 10641–10652. <https://doi.org/10.1021/jp8010074>.
- (20) *Handbook of Optical Constants of Solids*, 6. Nachdr.; Palik, E. D., Ed.; Acad. Press: Boston, 2004.